



School of Chemistry

**Ultrahigh-Vacuum and  
Ambient-Pressure Characterisation of  
Nickel Model Catalysts for  
Enantioselective Hydrogenation  
Reactions**

Submitted in partial fulfilment of the requirements for the degree  
of Doctor of Philosophy

**Panayiotis Tsaousis**

August 2018

Supervised by Professor Georg Held

# Declaration

I confirm that this is my own work and the use of all material from other sources has been properly and fully acknowledged

Signed

Panayiotis Tsaousis

The experiments leading to this thesis were done in collaboration. Some parts of this thesis are essentially identical to work already published, in particular chapter 6. The extent of my contribution is stated in the relevant chapters.

# Abstract

The adsorption of (R,R) tartaric acid (TA) on clean and oxidised Ni{100}, (S)-alanine and MAA on Ni{100} and the co-adsorption of (S)-alanine and water on Ni{110} was investigated, under UHV conditions, to obtain fundamental insights into the enantioselective sites of the chirally modified nickel catalyst, which causes the asymmetric hydrogenation of  $\beta$ -ketoesters. The TA/Ni{100} and (S)-alanine/Ni{100} system was also investigated under ambient pressure conditions. The characterisation of these adsorbed complexes was performed using XPS, NEXAFS, TPD, LEED and DFT.

The temperature of the crystal, the dosing rate of the TA molecule and its surface coverage influence the chemical state and adsorption geometry of TA on Ni{100} ( $\mu_4/\text{TA}^{2-}$  or  $\mu_2/\mu_3/\text{HTA}^-$ ) with the latter being favoured, also, at elevated pressures of  $\text{H}_2$  and  $\text{H}_2\text{O}$ . Deposition of TA on oxidised Ni{100}, causes the formation of tartrate species which fully decompose on the nickel surface at  $T > 650$  K (200 degrees higher than on clean Ni{100}).

(S)-alanine chemisorbs on Ni{100} and Ni{110}, in its anionic and neutral form with coexistence of zwitterionic species which might not be a part of the chemisorbed layer, since these zwitterionic species are dominating the multilayer regime. The presence of  $P_{\text{H}_2} = 6.3$  mbar destabilises thermally the alanine molecule on Ni{100} and cause the formation of neutral and (perhaps zwitterionic species) of alanine. The presence of multilayer water does not influence the decomposition temperature of alanine on Ni{110} ( $T_{\text{decomposition}} \approx 400\text{-}420$  K) but causes the formation of zwitterionic species.

Finally DFT, XPS and NEXAFS results suggest that MAA adsorbs on Ni{100} in a tilted bidentate enolate geometry. The full decomposition of MAA on Ni{100} occurs at  $\sim 350$  K.

The contribution of these studies into the understanding of the mechanism of the chiral modification of the nickel catalyst is thoroughly discussed in the thesis.

# Acknowledgements

I would like to express my sincere gratitude to several people who helped me during this PhD:

To Andy Whittam, Gary Yeo, Mike Charij and Mark McClemont in the University of Reading for providing technical support.

To the IT support of the University of Reading.

To Rob Haigh for providing support in administrative safety issues.

To Catherine O'Hare, Judy Butler, Barbara Laura Parr, and Heather for providing administrative support.

To Gez Griffin and Phil Mason in the stores of the department, for dealing with our orders.

To the finance office of the University of Reading and to Sarah Hartrampf and Laura Attewell in Diamond Light Source for dealing with our orders and travel arrangements.

To the University of Reading and Diamond Light Source for co-funding my PhD project

To staff members in the B07 beamline, especially Rosa Arrigo, Federica Venturini, Pilar Ferrer Escorihuela and Dave Grinter for providing any kind of help during my stay in Diamond.

To Silvano Lizzit, Paolo Lacovig and Luca Bignardi in the SUPERESCA beamline (Elettra synchrotron, Trieste, Italy), to Alexei Preobrajenski and Karsten Handrup in the D1011 beamline (MAX-Lab synchrotron, Lund, Sweden), to Alexei Nevedov in the HE-SGM beamline (BESSY II synchrotron, Berlin, Germany), to Samuli Urpelainen and Andrey Shavorskiy in the SPECIES endsation (MAX-Lab synchrotron, Lund, Sweden) and to Alex Walton in the NAP-XPS facility in the University of Manchester for their tremendous technical and scientific support.

To Andrey Shavorskiy for writing some useful Igor macros.

To Jorge Ontaneda and Ricardo Grau-Crespo (University of Reading) for an amazing collaboration and for their DFT calculations in the MAA/Ni{100} project.

To Dr. Ricardo Grau-Crespo and Dr. Adam Squires, my examiners in 1st year viva for their valuable suggestions and comments.

To Georg Held, Roger Bennett, Chanan Euaruksakul, Rachel Price, Alix Cornish, Ed Nicklin, Jacopo Ardini, Silvia Baldanza, David Watson, Alex Large and Tom Statham for helping me collecting the data for this thesis. A special thanks:

- To Chanan Euaruksakul for being the best labmate anyone can ever have, for teaching me with patience everything he knows about UHV and surface science and for helping me with every scientific and technical issue I had.
- To Rachel Price for helping me with the lab, for helping me to learn Igor and Latex, for being the best beamtime partner and for always smiling, even during the night shifts.
- To Alix Cornish for collecting the TPD data of alanine on Ni{110}.
- To Ed Nicklin for his long talks about nickel.
- To Silvia Baldanza for welcoming me and for helping me to adjust in my first days in Reading, her advices and her friendship.
- To Jacopo Ardini for being my first “mentor” at the beginning of my studies and helping me to learn about UHV equipment.
- To Alex Large for helping me in the lab.
- To Roger Bennett for being my second supervisor, providing me with technical and scientific feedback and support at any time needed.
- To Georg Held, my first supervisor for always trusting, inspiring, advising, supporting and encouraging me with patience, for offering me amazing research opportunities and for sharing his knowledge and expertise with me.

To my friends in and out of Reading for being there for me. A special thanks to my friends Tolis, Vicky and Fotis for supporting me in all the possible ways throughout this period (especially the last year of my PhD project), for listening to all my complains and for offering me unlimited hospitality.

To Georgia and my big brother Tasos, for giving me a place to stay in Canterbury during my last year and for their amazing cooking skills. I cannot thank enough Tasos for being the best big brother anyone can ever have, taking care of me throughout my life with tremendous support while sharing his experiences and advices with me.

To my family back in Cyprus, my brother Avgoustinos and especially my parents Dimitris and Irene, the people I owe everything I am, for their unconditional love, for believing in me, supporting me and sharing their wisdom with me.

# Contents

<b>Contents</b>	<b>vii</b>
<b>1 Introduction</b>	<b>1</b>
1.1 Enantioselective heterogeneous catalysis . . . . .	1
1.2 Chiral modification of metals for enantioselective heterogeneous catalysis . . . . .	2
1.3 The hydrogenation of $\beta$ -ketoesters using chirally modified nickel catalysts . . . . .	5
1.3.1 The catalytic reaction . . . . .	5
1.3.2 Surface chemistry of tartaric acid and methyl acetoacetate (MAA) on nickel single crystals . . . . .	9
1.3.3 Surface chemistry of amino acids and methyl acetoacetate (MAA) on Ni{111} and polycrystalline nickel . . . . .	11
1.3.4 Possible models . . . . .	14
1.4 The pressure and complexity gap . . . . .	17
1.5 Aim of the project . . . . .	18
<b>2 Experimental techniques</b>	<b>20</b>
2.1 X-ray Sources . . . . .	20
2.2 X-ray photoelectron spectroscopy (XPS) . . . . .	22
2.2.1 The XPS process . . . . .	22
2.2.2 Experimental set-up . . . . .	26
2.2.3 XPS Data Analysis . . . . .	28
2.2.4 Temperature programmed-X-ray photoelectron spectroscopy (TP-XPS) . . . . .	30
2.3 Near edge X-ray absorption fine structure (NEXAFS) spectroscopy	31
2.3.1 The NEXAFS-Process . . . . .	31
2.3.2 Experimental set-up . . . . .	35
2.3.3 NEXAFS Data Analysis . . . . .	35
2.4 Temperature programmed desorption (TPD) . . . . .	37

2.5	Low energy electron diffraction (LEED) . . . . .	39
<b>3</b>	<b>Interaction of (R,R)-tartaric acid (TA) on clean and oxidised Ni{100} under UHV and ambient pressure (AP) conditions</b>	<b>42</b>
3.1	Introduction . . . . .	43
3.2	Experimental Methods . . . . .	47
3.3	Results . . . . .	49
3.3.1	Tartaric acid on clean Ni{100}/UHV . . . . .	49
3.3.2	Tartaric acid on oxidised Ni{100}/UHV . . . . .	63
3.3.3	Tartaric acid on clean Ni{100}/Elevated H <sub>2</sub> pressures . . .	76
3.3.4	Tartaric acid on clean Ni{100}/Elevated H <sub>2</sub> O pressures . .	81
3.4	Discussion . . . . .	83
3.5	Conclusions . . . . .	86
<b>4</b>	<b>Interaction of (S)-alanine on clean Ni{100} under UHV and elevated hydrogen pressures</b>	<b>88</b>
4.1	Introduction . . . . .	89
4.2	Experimental methods . . . . .	91
4.3	Results . . . . .	93
4.3.1	Alanine on clean Ni{100}/UHV . . . . .	93
4.3.2	Alanine on clean Ni{100}/Elevated H <sub>2</sub> pressures . . . . .	105
4.4	Discussion . . . . .	110
4.5	Conclusions . . . . .	111
<b>5</b>	<b>Co-adsorption of (S)-alanine and water on Ni{110}</b>	<b>113</b>
5.1	Introduction . . . . .	114
5.2	Experimental methods . . . . .	118
5.3	Results . . . . .	120
5.3.1	TPD Results . . . . .	120
5.3.2	XPS Results . . . . .	121
5.3.3	NEXAFS Results . . . . .	137
5.4	Discussion . . . . .	142
5.5	Conclusions . . . . .	147
<b>6</b>	<b>Adsorption of methyl acetoacetate (MAA) on Ni{100}</b>	<b>148</b>
6.1	Introduction . . . . .	149
6.2	Methodology . . . . .	151
6.3	Results . . . . .	152
6.3.1	XPS Results . . . . .	152

6.3.2	NEXAFS Results . . . . .	155
6.3.3	DFT results . . . . .	157
6.4	Discussion . . . . .	159
6.4.1	Comparison of Modelling and Experimental Data . . . . .	159
6.4.2	Implications for Heterogeneous Catalysis . . . . .	164
6.5	Summary . . . . .	165
<b>7</b>	<b>Conclusions</b>	<b>166</b>
	<b>Bibliography</b>	<b>173</b>

# Chapter 1

## Introduction

### 1.1 Enantioselective heterogeneous catalysis

Enantioselectivity is defined as the capability of generating a surplus of one enantiomer of a chiral molecule in a chemical reaction. Enantioselectivity is a key aspect in the field of life sciences, since some particular properties, which differ between the enantiomers, influence their biological activity and response. Such compounds are used as flavours and fragrances in addition to their use in the pharmaceutical and agrochemical industry [1–5].

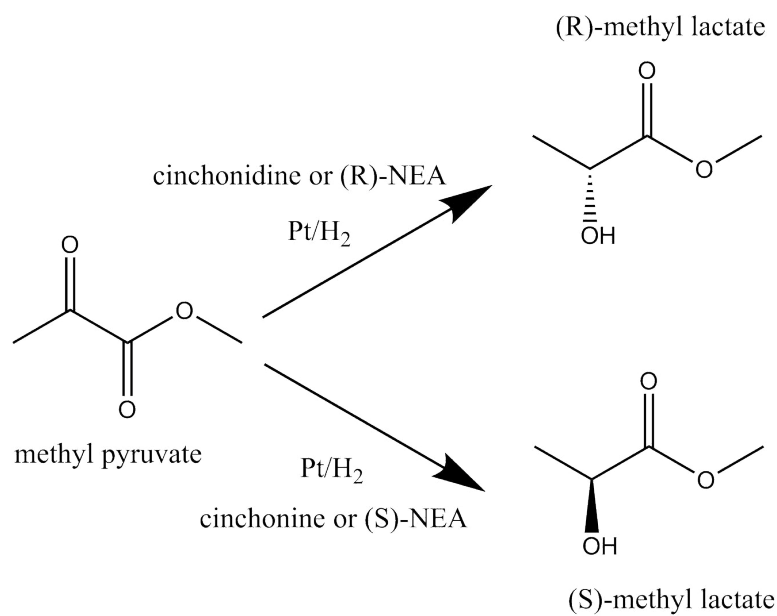
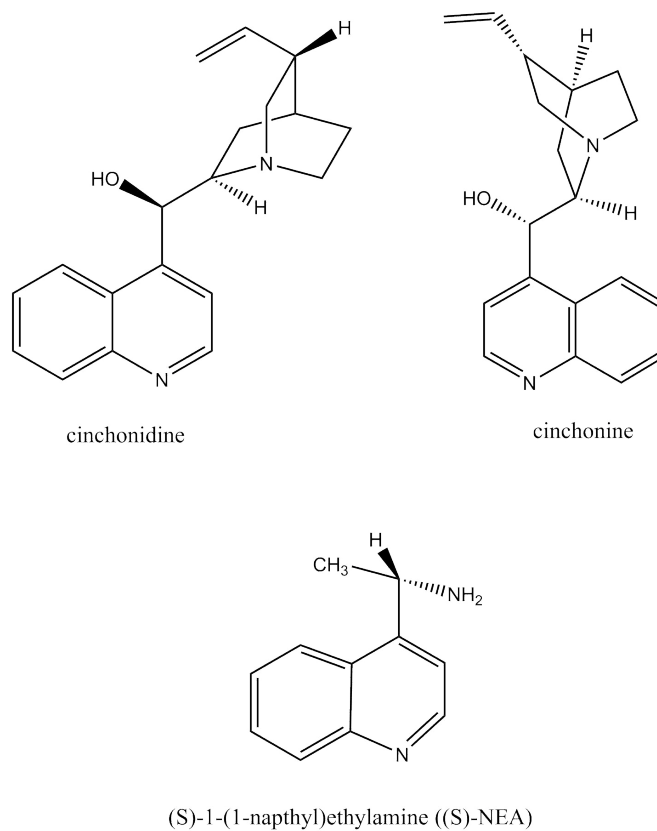
In homogeneous catalysis, the reactants and the catalysts are in the same phase, in contrast with heterogeneous processes where the reactant and the catalysts are in different phase. Homogeneous catalysts present high selectivities and activities and they are dominating the area of industrial enantioselective catalysis. These catalysts are typically metal complexes with chiral ligands and their reactive sites are better explained and defined compared to the corresponding heterogeneous catalysts, increasing the ability to control the enantioselectivity. Nevertheless, there is a great interest in the area of enantioselective heterogeneous catalysis, since heterogeneous catalysts can be easily separated and recycled, can reduce the presence of metal traces in the product, can be easily controlled during their use making the overall process cheaper and greener with respect to the homogeneous one. Sometimes, heterogeneous catalysts, present higher selectivities than the corresponding homogeneous. [2, 6, 7]. Ideally, the designing and development of an heterogeneous catalyst must combine the selectivity and activity of homogeneous and the described advantages of the heterogeneous catalysts [6].

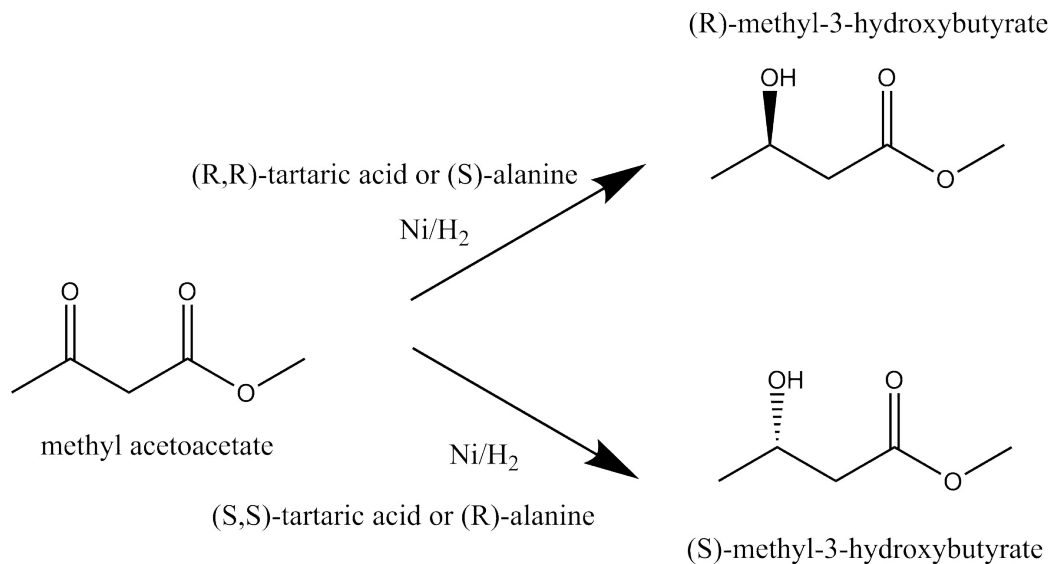
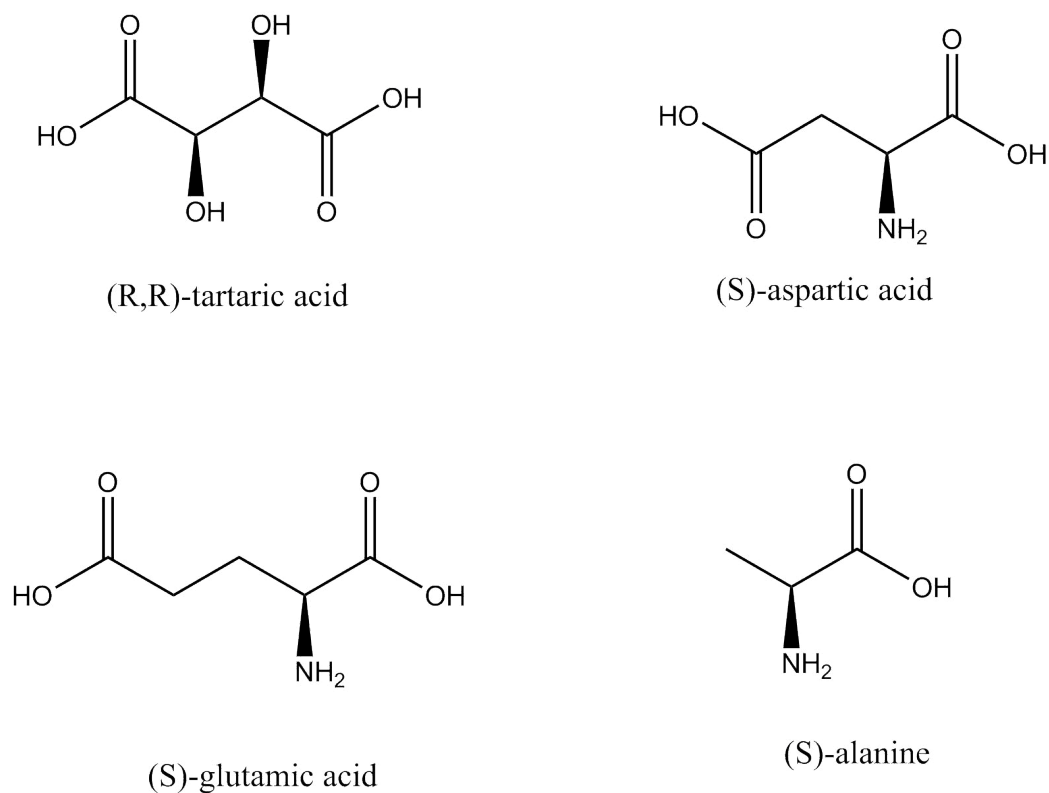
There are many approaches for designing an enantioselective heterogeneous catalyst. A single crystal can produce intrinsically chiral surfaces if it is cut to expose high Miller indices planes. If at these high Miller indices, the step lengths

on either side of the kink site are uneven, then the kink sites can be considered chiral [8]. Another approach is the transfer (or as it is called “immobilisation”) of a chiral homogeneous catalyst in pore materials/solid surfaces/polymers [4, 9, 10]. Finally, an enantioselective heterogeneous catalyst could be generated by attaching the active site (metal) to a chiral support, or attaching a chiral auxiliary to a metal (chiral modification). In the latter approach the chiral modification takes place either before or during the catalysed reaction [4] and the understanding of this process is the focus of this PhD thesis.

## 1.2 Chiral modification of metals for enantioselective heterogeneous catalysis

Two of the most important reactions in the area of enantioselective heterogeneous catalysis are the hydrogenation of  $\alpha$ -ketoesters using platinum group metals as catalysts (Fig. 1.1) and the hydrogenation of  $\beta$ -ketoesters (such as methyl acetoacetate) using nickel as a catalyst (Fig. 1.3). Typical chiral modifiers used in the hydrogenation of  $\alpha$ -ketoesters (Fig. 1.1) are cinchonidine, cinchonine, (R) and (R) and (S)-1-(1-naphthyl)ethylamine ((R) and (S)-NEA) (Fig. 1.1-1.2). Cinchonidine and (R)-NEA as chiral modifiers generate R-product in excess whereas cinchonine and (S)-NEA will generate (S)-product in excess. The nickel catalyst (Fig. 1.3-1.4) is chirally modified using either  $\alpha$ -hydroxyacids (such as (R,R) tartaric acid) or  $\alpha$ -amino acids (such as aspartic acid, glutamic acid and alanine). The current project is focusing on the latter reaction. (S)-hydroxy or (R)-amino acids as modifiers will produce (S)-product in excess, whereas (R)-hydroxy and (S)-amino acid modifiers will generate (R)-products in excess (Fig. 1.3)[2, 11–15].

Figure 1.1: The enantioselective hydrogenation of  $\alpha$ -ketoesters [2, 14].Figure 1.2: Typical modifiers used in the enantioselective hydrogenation of  $\alpha$ -ketoesters [2, 14].

Figure 1.3: The enantioselective hydrogenation of  $\beta$ -ketoesters [2, 14].Figure 1.4: Typical modifiers used in the enantioselective hydrogenation of  $\beta$ -ketoesters [2, 14].

## 1.3 The hydrogenation of $\beta$ -ketoesters using chirally modified nickel catalysts

### 1.3.1 The catalytic reaction

The asymmetric hydrogenation of  $\beta$ -ketoesters using chiral modifiers has been studied extensively. Much of the characterisation of this reaction in terms of enantiomeric excess, kinetics, modifier, solvent and temperature dependence is reported in Ref. [12, 16–18]. Here we report more recent (dated between 1997-2014) catalytic results of the asymmetric hydrogenation of  $\beta$ -ketoesters [19–31], in which tartaric acid was used as a chiral modifier. Hydroxy–dicarboxylic acids such as tartaric acid (TA) have been proven to be the most effective modifiers for hydrogenation of MAA (methyl acetoacetate) to MHB (methyl-3-hydroxybutyrate) [18]. Work of Osawa et al. (2011) [19], showed that 3  $\mu$ m powder nickel catalysts modified with (R,R) tartaric acid preserve high durability and enantioselectivity for the hydrogenation of methyl acetoacetate for almost 3 months under dry conditions, providing high applicability for industrial use.

#### **Effect of the nature of the reactant**

Osawa et al. (2014) [20] compared the asymmetric hydrogenation of different acetoacetate esters using (R,R)-tartaric acid and NaBr in the modification solution and nickel powder as a catalyst. The use of ethyl esters as reactants increase the enantiomeric excess (ee) with respect to the use of methyl acetoacetate as a reactant. The use of ethyl ester as a reactant generated products with up to 94% ee. On the other hand, the increase in the molecular mass of the ester group in the different acetoacetate esters decrease its conversion percentage. The addition of an aromatic group, instead of an alkyl group, did not influence the conversion of the reactant (100% conversion), however it decreased the ee value of the product [20].

#### **Effect of sodium bromide (NaBr) and in situ modification**

Sodium bromide is often used in the reaction mixture, to enhance the selectivity, since according to Ref.[18, 32], it adsorbs on some non-selective centers and therefore increases the enantioselectivity of the system. Osawa et al. (2001) [21] investigated the hydrogenation of methylacetoacetate (MAA) by in situ modification of fine Ni powder and reduced Ni catalyst. The in situ modification was performed by adding directly (R,R) tartaric acid and NaBr to the reaction mixture. Ref.[21] achieved 89% optical yield after the in situ modification of the reduced nickel catalyst. The addition of a small amount of NaBr in the reaction

mixture enhances the enantioselectivity and the reaction rate, whereas it decreases the hydrogenation rate when the NaBr is used in the conventional modification procedure [21]. NaBr added to the reaction medium during in situ modification plays the subsequent roles:  $\text{Na}^+$  enhances the enantioselectivity and the reaction rate, whereas  $\text{Br}^-$  enhances the enantioselectivity and decreases the reaction rate [21]. Osawa et al. (2002) [22] used in situ modification to compare the durability of three kind of chirally modified nickel catalysts: Raney nickel catalyst, reduced Ni from Ni oxide and reduced Ni powder. Reduced Ni from Ni oxide and reduced Ni powder showed more optimised behaviour in terms of durability and enantioselectivity ability compared to Raney nickel. The desorption of tartaric acid during the hydrogenation reaction is responsible for the lower durability of the nickel catalysts using the conventional modification procedure [22]. Chen et al. (2007) [23] prepared chirally modified Raney nickel catalysts using only tartaric acid during the modification procedure, while the NaBr was added directly to the reaction medium. The catalysts modified with this procedure present lower presence of alumina on the Raney nickel, while at the same time showed greater total surface area and higher acid corrosion on the surface in comparison with conventional modified Raney nickel catalyst prepared by adding both tartaric acid and NaBr in the modification solution. The highest optical yield and hydrogenation rate was achieved when methanol was used as a solvent using the new modification procedure. The maximum enantioselectivity (85% optical yield) was attained under less extreme conditions (Hydrogen pressure=0.6 MPa, T=333 K, and t=60 minutes), while the reaction rate was even more improved [23]. Finally this improved Raney catalyst presents high durability, maintaining 60% optical yield even after 11 runs, if 15mg of NaBr was added in every cycle [23]. Kukula et al. (2001) [25] found that the presence of NaBr in the modifying solution during the chiral modification of Raney nickel using (R,R)-tartaric acid causes decrease in the leaching of the catalyst. Similar results were obtained from Keane (1997) [24] upon co-modification of Ni/SiO<sub>2</sub> catalyst with NaBr and (R,R) tartaric acid. The author of Ref.[24] found that the presence of NaBr in the modifying solution causes decrease in the amount of leached Ni and the amount of adsorbed TA on the nickel surface.

### **Effect of modification procedure**

Kukula et al. (2001) [25] explored different modification variables during the chiral modification of Raney nickel using (R,R)-tartaric acid. Increase in the modification temperature, concentration of tartaric acid and modification times, causes increase in the amount of adsorbed tartaric acid on the nickel surface [25]. Increasing the temperature during modification of TA on Raney nickel and the

time, increases the optical yield. In addition, Ref.[25] suggested that the optimum pH for the chiral modification is 5 that the enantioselectivity as a function of TA concentration goes through a maximum. At pH=5, a minimum amount of the catalyst is transferred to the modifying solution. Keane (1997) [24] explored different modification variables during the modification of Ni/SiO<sub>2</sub> catalyst with (R,R) tartaric acid. The amount of adsorbed TA on the nickel catalyst increases and leaching of the nickel catalyst decreases in the following order of modifier solvents: water, methanol, ethanol, 1-butanol [24]. In addition, according to Ref.[24] the use of alcoholic solvents as modification medium increases the activity and the enantioselectivity of the catalyst [24]. The results of Keane (1997) [24] using Ni/SiO<sub>2</sub> as a catalyst suggested that the enantioselectivity of the catalyst as a function of modification temperature and tartaric acid concentration goes through a maximum. As in the case of Raney nickel [25], increase in the modification temperature, concentration of tartaric acid and modification time, causes increase in amount of the adsorbed tartaric acid on the nickel surface [24]. Modification of Ni/SiO<sub>2</sub> catalyst with tartaric acid, does not only improve the enantioselectivity of the catalyst, but increases the hydrogenation rate of the MAA reactant [24].

#### **Effect of reaction variables**

Kukula et al. (2002)[26], investigated the influence of temperature, pressure, solvent type and concentration of the substrate on the enantioselectivity of Raney nickel catalyst modified with (R,R)-tartaric acid [26]. Increase in the hydrogen pressure, increases the enantioselectivity of the catalyst, whereas decrease in methyl acetoacetate concentration influences negatively the enantioselectivity. The reaction solvent influences both the hydrogenation reaction rate and the enantioselectivity. Based on the authors results[26], the optimum conditions for attaining the highest enantioselectivity are: high hydrogen pressures (10MPa), T=60°C and THF or no solvent as a reaction medium. Keane (1997) [24] investigated the influence of reaction temperature and reaction medium on the enantioselectivity of the Ni/SiO<sub>2</sub> modified with (R,R) tartaric acid. According to the results of Ref.[24] and under the reported modification conditions the enantioselectivity as a function of temperature, goes through a maximum between 340-350 K. The use of alcoholic solvents as reaction medium, caused the highest hydrogenation rate of MAA reactant. The hydrogenation rate was increased and the enantioselectivity was decreased with increasing polarity of the alcohol solvent [24].

#### **Effect of the nature of the nickel catalyst**

Osawa et al. (2000)[27] prepared nickel catalysts with different support, using nickel acetylacetonate as a precursor, and studied the support influence on the enantioselectivity of the catalyst after chiral modification with tartaric acid. The

catalyst with sumico rundum ( $\alpha$ -alumina) or zeolite (pentasil powder) as support, generated products with 87% optical yield. The modified supported nickel catalyst prepared with this method (nickel acetylacetonate as a precursor) generated higher optical yield products compared to the supported catalysts prepared with usual method (in a nickel ion solution) [27]. Work of Jo et al. (2004) [28], showed that nickel catalysts supported on aluminum oxide present higher enantioselectivities compared to the silica supported catalysts. The reaction was studied after modification of the surface with (R,R) tartaric acid and NaBr [28]. Osawa et al. (2004) [29] compared the enantioselectivity of nickel catalysts, prepared from nickel hydroxide and nickel carbonate on the hydrogenation of methyl acetoacetate. The modification was in situ and took place using (R,R) tartaric acid and NaBr. The catalysts were prepared by calcination of the precursors to nickel oxides and subsequent reduction to nickel. The results suggested that the calcination temperature influences significantly the enantioselectivity of the nickel catalyst, while at the same time there was not a clear link between the crystallite size and the enantio-differentiating ability of the catalyst [29]. The authors proposed that the highest enantioselectivities will be presented in a nickel surface with the minimum lattice defects [29]. Work on the asymmetric hydrogenation of MAA using (R,R)-tartaric acid as a chiral modifier on nickel catalysts supported on graphite or activated carbon [30] found a direct correlation between the calcination and reduction temperature of the catalyst and its crystallite size and by extension the performance of the catalyst. The combustion of the carbon during calcination is responsible for the increase in the nickel loading and the crystallite size of the catalyst. The increase in the crystallite size causes the enhancement in the enantioselectivity of the catalyst but it also causes reduction in the catalytic activity. The higher crystallite size of the graphite supported nickel catalyst, compared to the one supported on activated carbon was the reason that the former presented greater performance (up to 91% enantiomeric excess) [30]. Lopez et al (2012) [31] produced Ni supported particles of approximately 20 nm size using hydrotalcite-like compounds (HLCs) as precursors, modified with tartaric acid. These chirally modified catalysts show enantioselectivity towards the hydrogenation of MAA. On the other hand, reduction in the particle size to 10nm did not show any enantioselectivity at all. Two series of HLCs were used based on the combination of cations: HLCs containing Ni/Mg/Al and HLCs containing Ni/Zn/Al using either urea hydrolysis or coprecipitation method as synthesis method for the HLCs. For catalyst with the same combination of cations, only the catalysts generated using the urea hydrolysis showed any enantioselectivity. In addition the Ni/Mg/Al series presented the higher catalyst activity, while the

Ni/Zn/Al series presented the higher enantioselectivity. Furthermore, according to the results the pH and the concentration of tartaric acid does not affect the enantioselectivity of the aforementioned catalysts, suggesting that in these catalysts, preparation method and the nature of the support is the controlling factor of the enantioselectivity [31].

### 1.3.2 Surface chemistry of tartaric acid and methyl acetoacetate (MAA) on nickel single crystals

Tartaric acid can exist in three different forms, according to the protonation or not of its two carboxyl groups: neutral biacid form, monotartrate form (one deprotonated carboxyl group) and bitartrate form (both carboxyl groups are deprotonated) [33]. The adsorption of tartaric acid on Ni{110} [33–35] and on Ni{111} [36–39], and its co-adsorption with MAA on Ni{111} [37, 38] was explored in previous studies to obtain fundamental insights into the mechanism of chiral modification of nickel catalyst.

#### Ni{110}

The adsorption of (R,R) tartaric acid on Ni{110} was studied using a combination of experimental techniques (RAIRS and STM), and theoretical calculations (DFT)[33–35]. The chemical state of the TA molecule on the Ni{110} [33] changes as a function of temperature and coverage. According to Ref.[33], tartaric acid is present, in the multilayer, in its biacid form regardless from the adsorption temperature. At 90-120 K, tartaric acid is in its biacid form at all coverages. Adsorption at higher temperatures (170-270 K) causes chemisorption of tartaric acid through the one deprotonated carboxyl group. At these temperatures, tartaric acid is presented in its monotartrate form. The other protonated carboxyl group is directed outside the surface plane, presenting also hydrogen bonding interactions. Above room temperature, tartaric acid exists in two forms up to the saturation coverage: at lower coverages it is found in its bitartrate form and at higher coverages tartaric acid is converted to its monotartrate form[33]. In the bitartrate form [34], tartaric acid is bound to 4 nickel atoms, with the oxygen atoms of the two corresponded carboxylate groups positioned above the Ni atoms, in a short bridge site. Based on DFT calculations, this geometrical orientation of the molecule, causes relaxation and reconstruction of the nickel surface, resulting in chiral footprint on the surface. Calculations propose that one chiral footprint is preferred energetically over the other suggesting that at room temperature the same mirror motif will be expected to dominate the surface by 90% ensuring the creation of an enantiospecific system [34]. Studies of the electronic structure of

the (R,R) tartaric acid on Ni{110} system [35], showed that bitartrate tartaric acid in the gas phase presents an intrinsic chirality not only in terms of atomic arrangement but also in its electronic structure, due to the uneven charge distribution between the four oxygen atoms of the two carboxylate groups which is transferred to the Ni-O bonds and by extension to all the nickel surface through the bonds between the nickel atoms [35].

### Ni{111}

Jones et al. (2002)[36], explored the adsorption of (R,R)-tartaric acid on the Ni{111} surface using RAIRS, STM and TPD techniques. The authors found that tartaric acid can adsorb on the Ni{111} surface either in its monotartrate or bitartrate form. The former structure is more stable at 300 K, where the latter is favoured at 350 K. In the bitartrate structure, the individual carboxylate groups of tartaric acid can interact with the nickel surface either in a monodentate or bidentate geometry. Co-adsorption with carbon monoxide (CO), causes reduction in the population of tartaric acid on the surface, shifting the desorption/decomposition of the tartaric to lower temperatures, compared to higher coverages of tartaric acid, where the CO is displaced from the surface [36].

Co-adsorption of (R,R)-tartaric acid and MAA on Ni{111} produced two ordered arrays with 0.113 ML (one tartrate and one MAA molecules per unit cell) and 0.167 ML (one tartrate and two MAA molecule per unit cell) local coverage [37], stabilised via hydrogen bonding between the modifier and the  $\beta$ -ketoester reactant. According to Ref.[37], in the low coverage structure, the hydrogenation will be enantiospecific and generate the R-product in excess whereas the high coverage structure will produce a racemic mixture of products [37]. High coverages of pre-adsorbed tartaric acid forbid the interaction of the MAA molecule on the Ni{111} surface [37].

Jones et al. (2007)[38], using RAIRS spectroscopy, examined the effect of different modification temperatures and pH on the interaction of MAA with Ni{111} which was pre-modified with (R,R) tartaric acid. Modification of Ni{111} with a solution of (R,R)-tartaric acid [38] show evidence of generation of nickel tartrate species on the Ni{111} surface at low modifying pH and nickel and sodium tartrate species at higher pH. The formation of these salt species points to a widespread etching of the nickel crystal. The etching of the surface is believed to cause the chiral modification of the surface, since it creates step-kink sites. A large quantity of the adsorbed species is removed from the surface, after washing it with water [38]. The remaining coverage is important for the chiral modification of the surface, since as it was shown in previous studies [37], high coverages of modifiers forbid the interaction of MAA with the nickel surface, while absence

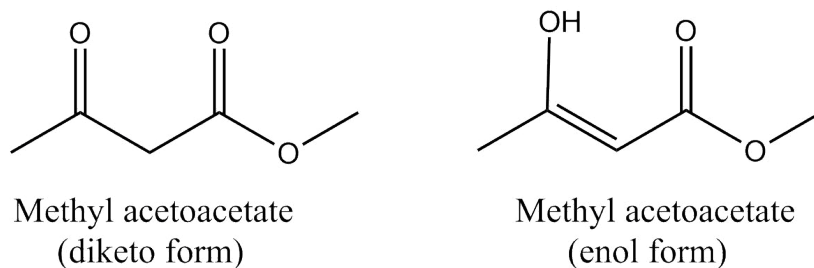


Figure 1.5: The two possible tautomers of the methylacetoacetate [37].

of modifiers generates product without optical activity [38]. Since this quantity depends on the pH and modification temperature, the pH of the tartaric acid solution controls the enantioselectivity of the surface by controlling the coverage of the modifier [38]. Modification of Ni{111} with (R,R)-tartaric acid from solution at 350 K (which according to Ref.[37, 38] is the optimum modification temperature for attaining the highest enantioselectivity using TA as modifier) following washing of the catalyst, caused generation of HTA<sup>-</sup> species on the nickel surface [38]. Subsequent immersion of the crystal in a MAA solution caused enhancement of the diketone/enol ratio of MAA substrate (Fig. 1.5) with respect to the modification at 300 K [38]. According to Ref.[38] the origin of the enantioselectivity of this system might be due to the formation of hydrogen bonds between the diketone and the HTA<sup>-</sup> species, in orientation that will preferably generate the R-enantiomer as a product during the hydrogenation reaction. Sodium bromide, on the other hand does not affect the RAIRS spectra of tartaric acid at 350 K modification temperature, whereas at 300 K, it enhances the diketo-enol form, thus increasing the enantioselectivity [38]. RAIRS data, obtained upon adsorbing (R,R) tartaric acid on oxidised Ni{111} as well as the decomposition temperature of the molecule on the NiO/Ni{111} substrate, suggest also the formation of species similar to nickel tartrate [39].

### 1.3.3 Surface chemistry of amino acids and methyl acetoacetate (MAA) on Ni{111} and polycrystalline nickel

Amino acids are carboxylic acids with an amino group on the other end of the chain. Depending on their protonation state, they exist in three different forms: neutral, anionic (deprotonated carboxyl group) and zwitterionic form (deprotonated carboxyl group and protonated amino group). In the solid state, amino acids are usually in their zwitterionic form [40]. Previous studies, exploring the adsorption of amino acids with and without MAA on nickel crystals, are limited

only to the Ni{111} facet [40–47] and the polycrystalline nickel [48].

### **(S)-aspartic acid**

(S)-aspartic acid, at low coverages, forms oligosuccinimide clusters when it is adsorbed on the proximity of surface defects of the Ni{111}. Based on STM images, MAA at these coverages, is bound close to the modified area from the oligosuccinimide clusters, in step sites [41]. According to Ref.[41] the enantioselectivity of this particular system (aspartic acid) might be derived from the creation of these clusters from aspartic acid molecules, thus creating a docking position for MAA [41]. According to RAIRS results [41] at higher coverages, there is no indication of the construction of supramolecular assemblies, with the aspartic acid being in either in zwitterionic or anionic form. These coverages forbid the interaction of MAA on the nickel surface [41]. The pH of (S)-aspartic acid defines the protonation state of the molecule and in extension the tautomeric state of the co-adsorbed MAA on polycrystalline Ni [48] and on the Ni{111} surface [42]. Increase in the pH increases the deprotonation of the amino acid [42, 48]. At low pH, MAA is found in its diketo form since it can form hydrogen bonds as a proton acceptor with the protonated aspartic acid, while at higher pH, MAA is found in its enol form, acting as hydrogen bond donor in the hydrogen bond with the deprotonated aspartic acid [42, 48]. At optimum modification conditions (in terms of enantioselectivity) and upon washing the catalyst, the aspartic acid is untraceable spectroscopically in both polycrystalline nickel [48] and Ni{111} surface [42].

### **(S)-glutamic acid**

RAIRS and STM studies of (S)-glutamic acid on Ni{111} [43] suggest when the amino acid adsorbs on the nickel surface at 300 K in its zwitterionic form at low coverages, whereas at higher coverages (at 300 K) it converts to its anionic form. Adsorption at 350 K leads to the formation of anionic glutamic acid, which also causes corrosion of the steps of the surface [43]. According to Ref.[43] the presence of  $\text{NH}_3^+$  at 300 K adsorption temperature favours the interaction with the  $\beta$ -ketoester reactant via hydrogen bonding, which might favour the formation of the R-enantiomer product while the corrosion at 350 K might favour the production of the S-enantiomer [43]. Work by Jones et al. (2006) [40] on the co-adsorption of (S)-glutamic and MAA on Ni{111}, show that adsorption of MAA on Ni{111} pre-adsorbed with glutamic acid at 300 K, causes interaction between these two molecules through the  $\text{NH}_3^+$  group of the amino acid and most probably the ketone group of the MAA which is in its diketo form, in parallel geometry which favours the generation of the R-product. After co-adsorption of glutamic acid with MAA at 350 K, MAA is found in its enol form and most probably with its

plane perpendicular to the surface [40]. The authors of Ref.[40] suggested that this form will produce a racemic mixture of the product. The catalytic reaction at 350 K produces the S-enantiomer in excess, therefore, some other interaction with the modifier must be taking place [16, 40]. The co-adsorption of the amino acid in solution with MAA, studied by Jones et al. (2007) [44] confirmed the aforementioned results. The results suggested that the increase in the modification temperatures decreases the keto:enol ratio of MAA, whereas decrease in the pH (and by extension increase in the protonation of the amino acid) increases the keto-enol ratio, linking the structure of the MAA on the nickel surface pre-modified with glutamic acid with the enantioselectivity of the reaction: under modification conditions which favour the formation of the R-product, MAA is mainly in its diketo form, while enol MAA is found under conditions that generate the S-product in excess [44]. At 300 K and low pH, glutamic acid is predominantly in its cationic/zwitterionic form, while the increase in the pH extents the degree of the deprotonation of the amino acid [44]. At higher temperatures (350 K), the authors found substantiation of the production of nickel glutamate and mixture of nickel and sodium glutamate at low and high pH, respectively [44]. The dependence of the coverage of pre-adsorbed glutamic acid on the interaction of the amino acid with MAA on Ni{111} surface, was studied by Trant et al. (2011) [45]. Prior to the dosing of the MAA molecule, the Ni{111} surface modified with glutamic acid was exposed to 10 L of H<sub>2</sub> gas. The presence of the chiral modifier at low coverages boosts further the corrosion of step edges caused by the adsorption of MAA, thus producing, possibly leading to the generation of chiral facets on the nickel surface. Intermediate coverages of pre-adsorbed glutamic acid, lead to the creation of 2-D supramolecular domains. According to Ref. [45] the enantioselectivity of this system originates from the two possible pro-(R) or pro-(S) configuration of the MAA, which form hydrogen bonds with the glutamic acid molecule. Higher coverages of pre-adsorbed glutamic acid do not allow the interaction of MAA with the nickel surface [45].

### **(S)-alanine**

The adsorption of (S)-alanine on Ni{111} was studied by Nicklin et al. (2015) using XPS and NEXAFS [46]. On Ni{111}, alanine chemisorbs in both zwitterionic and anionic form supporting a bidentate and tridentate geometry, respectively with the latter species being in majority on the nickel surface. The molecule decomposes on Ni{111} at temperatures between 300 K and 450 K, following multistep processes [46]. Exposing the saturated (S)-alanine layer on Ni{111} (0.25 ML) to elevated pressures of H<sub>2</sub>, causes protonation of the amino group of (S)-alanine and reorientation to bidentate geometry, which under the

presence of elevated pressures of  $H_2$ , is the majority species on the nickel surface [47].

### 1.3.4 Possible models

There are several models that could explain the enantioselective behaviour of nickel catalysts following their chiral modification:

#### **One to one interaction/The active chiral site model**

The one to one model (or active chiral site model [14]) suggests 1:1 to interaction between the modifier and the reactant, in configuration, that during hydrogenation, will generate enantiopure product in excess. This kind of mechanism is at work in the enantioselective hydrogenation of  $\alpha$ -ketoesters using chirally modified Pt (Fig. 1.1) as a catalyst [15, 49]. In the Pt/ $\alpha$ -ketoesters system the modifiers are large enough, to stabilise a pro-chiral configuration of the reactant in 1:1 interaction (Fig. 1.1-1.2) [45]. In the Ni/ $\beta$ -ketoesters system the molecular size of the modifiers and the  $\beta$ -ketoester reactant are similar (Fig. 1.3-1.4). However, RAIRS data of Jones et al. (2006) [40] obtained upon adsorbing (S)-glutamic on Ni{111} at 300 K (this temperature favours the formation of the R-product during the catalytic reaction, using (S)-glutamic as a modifier [16]), and subsequent exposing the overlayer to MAA, showed evidence of 1:1 interaction of the amino acid with the diketo form of MAA mainly through the  $NH_3^+$  group of the amino acid and most probably the ketone group of the MAA, in a parallel geometry that will favour the generation of the R-product [40].

#### **Chiral surfaces defects/adsorbed induced chiral restructuring**

Metal surfaces can be chiral, if the step lengths on either side of the kink site are uneven [8]. These kind of chiral surfaces are present on polycrystalline metal catalysts or supported metal catalysts as defects, in an equal amount between the two chiral surfaces [40, 45, 50]. Previous studies [51, 52] have shown that two enantiomers of a chiral molecule present different adsorption energetics when they are adsorbed on a chiral surface [51], whereas a chiral surface itself is more reactive towards one enantiomer of a chiral molecule with respect to the other [52]. In addition, interaction of pure R and S propylene oxide on chiral Cu surfaces (Cu{643}) [53], show that the desorption of the enantiopure molecule depends on the chirality of the Cu{643} surface. This kind of different adsorption behaviour, should be expected also for the two pro-chiral configurations of the  $\beta$ -ketoester reactant on a chiral nickel substrate during the hydrogenation reaction [45]. In the case of the Pt/ $\alpha$ -ketoesters system (Fig. 1.1) evidence was found that the highest enantioselective sites for this reaction using Pt/graphite and Pt/silica as

a catalyst, are at or close to the step edges [54]. It is possible that a chiral modifier will interact with one of the two chiral surfaces leaving the other one for interacting with the  $\beta$ -ketoester reactant in a configuration which will lead to asymmetric hydrogenation [50, 52].

XPS [48] and RAIRS [42] studies of modified polycrystalline nickel and Ni{111}, respectively, with (S)-aspartic acid (upon washing the catalyst) showed that at optimum (in terms of enantioselectivity) conditions, the aspartic acid is untraceable spectroscopically. These studies [42, 48] provided evidence that asymmetric hydrogenation could occur at low or even in the absence of a chiral modifier, during the reaction. Previous studies have shown that chirality can be bestowed on an achiral metal surface via the adsorption of a chiral molecule [34, 35, 55–58]. Adsorption of L-lysine [55] and S-alanine [56–58] on Cu{100} caused the generation of {3 1 17} chiral facets. Adsorption of (R,R)-tartaric acid on Ni{110} in its bitartrate form [34], caused relaxation and reconstruction of the nickel surface, resulting in chiral footprint on the surface. Calculations propose that one chiral footprint is preferred energetically over the other suggesting that at room temperature the same mirror motif will be expected to dominate the surface by 90% ensuring the creation of an enantiospecific system [34]. Studies of the electronic structure of the (R,R) tartaric acid on Ni{110} system [35], showed that bitartrate tartaric acid in the gas phase presents an intrinsic chirality not only in terms of atomic arrangement but also in its electronic structure, due to the uneven charge distribution between the four oxygen atoms of the two carboxylate groups which is transferred to the Ni-O bonds and by extension to all the nickel surface through the bonds between the nickel atoms [35].

Chiral metal arrangements could be generated through etching of the crystal. Modification of Ni{111} with a solution of (R,R)- tartaric acid [38] show evidence of generation of nickel tartrate species on the Ni{111} surface at low modifying pH and nickel and sodium tartrate species at higher pH. The formation of these salt species points to a widespread etching of the nickel crystal. RAIRS data, obtained upon adsorbing (R,R) tartaric acid on oxidised Ni{111} as well as the decomposition temperature of R,R-tartaric acid on the NiO/Ni{111} substrate, suggest also the formation of species similar to nickel tartrate [39]. In addition, based on XPS results of modified Raney nickel catalyst with (R,R) tartaric acid [32], the stoichiometry of nickel, carbon and oxygen on the surface layer resembles the stoichiometry of nickel (II) tartrate complex. The high solubility of the nickel tartrate species in aqueous solution in combination with the strong electrostatic interaction between the charged tartrate species and the Ni<sup>2+</sup> substrate, could assist the etching of the nickel catalyst during modification [39], and generate chiral

surfaces/arrangements similar to those shown in Ref.[8]. The work of McFadden et al. (1996) [8], suggested, that a single crystal can produce intrinsically chiral surfaces if it is cut to expose high Miller indices planes. If at these high Miller indices, the step lengths on either side of the kink site are uneven, then the kink sites can be considered chiral [8]. Evidence of production of nickel glutamate and mixture of nickel and sodium glutamate was also found by Jones et al. (2007) [44], following modification of Ni{111} with (S)-glutamic acid from solution at 350 K, at low and high pH, respectively.

The enantioselectivity of a catalyst could be improved if any chiral recognition at the step sites is amplified into the terraces sites of the catalyst. This kind of amplification was observed upon adsorbing enantiopure propylene oxide on chiral Cu{643} surface from Horvath et al. (2001) [53]. Ref.[53] suggested enantiospecificity in the desorption of enantiopure propylene oxide adsorbed on the terraces of the chiral Cu{643} surface, suggesting transfer of the chiral environment of the steps to the molecules adsorbed on the terrace via the adjacent molecules adsorbed on the step edge of the Cu{643} surface.

### **Supramolecular assemblies/Ordered structures**

Adsorption of (R,R) tartaric acid in its bitartrate form causes generation of arrays of ordered layers and 2D supramolecular assemblies of tartaric acid on the on the Cu{110} surface, which break the symmetry of the crystal [59–61]. This structure is formed through intermolecular hydrogen bonds [59]. The induced chirality is mirrored upon adsorbing the other enantiomer ((S,S)-tartaric acid) [61] on the Cu{110} surface. According to Ref.[61], the MAA could be accommodated within this 2D structure. If these kind of structures are formed during chiral modification of nickel catalysts, they could act as a “chiral template” for the  $\alpha/\beta$ -ketoester reactant, stabilising a pro-chiral configuration of the reactant. Similar structures were observed upon adsorbing alanine on Cu{110} [62, 63]. Adsorption of (S)-alanine on Cu{110} causes the formation of chiral clusters of six or eight molecules (generated via intermolecular hydrogen bonding), interspersed with chiral channels of metals which assemble into a chiral array without creation of its mirror domain on the surface [62, 63]. This induced chirality is mirrored upon adsorption of R-alanine on the copper surface, which also generates similar chiral assemblies [62]. Mahapatra et al (2014) [64] have found evidence of formation of both zwitterionic and anionic alanine on Pd{111} surface, with the isolated anionic form of the molecule, based on DFT calculations, being significantly more stable. The molecule was found to construct dimers or tetramers on Pd{111}, which could potentially behave as chiral templates [64].

Adsorption of (R,R) tartaric acid Ni{111} caused also the formation of ordered

layers [36] however to a lesser extent in comparison with the Cu{110} surface. Co-adsorption of (R,R)-tartaric acid and MAA on Ni{111} , studied by Jones and Baddeley (2002) [37], produced two ordered arrays with 0.113 ML (one tartrate and one MAA molecules per unit cell) and 0.167 ML (one tartrate and two MAA molecule per unit cell) local coverage, stabilised via hydrogen bonding between the modifier and the  $\beta$ -ketoester reactant. In addition, according to Ref.[37], the presence of MAA on the Ni{111} surface, pre-adsorbed with tartaric acid, caused the coordination of the surrounded tartaric acid molecules, into a well-defined arrangement. Ref.[37], suggested that in the low coverage structure, the hydrogenation will be enantiospecific and generate the R-product in excess whereas the high coverage structure will produce a racemic mixture of products [37]. Adsorption of MAA onto intermediate coverages of pre-adsorbed (S)-glutamic acid on Ni{111}, performed by Trant et al. 2010 [45], lead to the creation of 2-D supramolecular domains [45]. Prior to the dosing of the MAA molecule, the Ni{111} surface modified with glutamic acid was exposed to 10 L of H<sub>2</sub> gas [45]. According to Ref.[45] the enantioselectivity of this system originates from the two possible pro-(R) or pro-(S) configuration of the MAA, which form hydrogen bonds with the glutamic acid molecule.

## 1.4 The pressure and complexity gap

The catalytic activity and selectivity of a surface is influenced by its composition, electronic properties and atomic structure. As it is described in section 1.3, several surface science techniques have been employed to determine not only the surfaces at atomic level, but also explain this particular catalytic system. These surface techniques, in most of the cases, are carried out in ultra high vacuum condition (UHV) using single crystals as model surfaces. Ultra high vacuum refers to pressures below  $10^{-9}$  mbar, and it is used to maintain a well defined condition of the surface and have a quantitative function of the electron based techniques [65–68]. Electrons emitted from a sample, are subject to elastic and inelastic collisions with other molecules, which causes decrease in their detected signal. The mean free path of electrons, the average distance that a particle travels between collisions, is inversely proportional to the pressure of the chamber [66, 68]. According to Ref.[66], the mean free path of electron at  $P_{N_2} \approx 1000$  mbar is 70 nm whereas at  $P_{N_2} \approx 1 \times 10^{-10}$  mbar the mean free path is over 500 km!

The aforementioned conditions are not realistic, since most of the reactions take place in ambient pressure conditions, using more complex surfaces such as

nanoparticles. These two disparities are called, pressure and complexity gap, respectively [65].

## 1.5 Aim of the project

This project is part of a bigger project in our group which is aiming to provide insights into the enantioselective sites of the chirally modified nickel catalyst which lead to the asymmetric hydrogenation of  $\beta$ -ketoesters. This is done by adsorbing typical modifiers and reactants on nickel single crystals of low Miller indices ( $\{111\}$ ,  $\{110\}$ ,  $\{100\}$ ) under ultra high vacuum conditions and study their thermal stability, chemical state, bond coordination and molecular orientation on the nickel surface, using surface science techniques such as X-ray photoelectron spectroscopy (XPS), near edge X-ray absorption fine structure (NEXAFS) spectroscopy, temperature programmed desorption (TPD) and low energy electron diffraction (LEED). Previous studies [46, 69–72] have shown that the combination of XPS and NEXAFS is a very powerful tool for characterising the adsorption complex in terms of chemical state and molecular orientation. The use of single crystals of low Miller indices is important since these terminations are found in the nanoparticles of fcc metals [73]. Izumi (1983) [16] showed that the enantioselective behaviour on Raney nickel depends on how the reactant MAA adsorbs on the Ni surface and how it interacts with the modifier rather than on the transition state of the hydrogenation reaction. Hence, by understanding the behaviour of the surface and the modifiers during chiral modification of the nickel surface and the effect of that on the adsorption geometry of  $\beta$ -ketoesters reactants (such as MAA) on the nickel surface, is key step to understand and optimize the enantioselectivity of the chirally modified nickel catalysts.

The main focus of this PhD will be the  $\{100\}$  termination, which its study for this reaction, is lacking from literature. Preliminary studies of our group have shown that amino acids present high thermal stability on Ni $\{100\}$  facet, with respect to the other nickel single crystals of low Miller indices (Ni $\{110\}$ , Ni $\{111\}$ ). Four systems are investigated in this PhD thesis:

1. Interaction of (R,R)-tartaric acid on clean and oxidised Ni $\{100\}$  under UHV and ambient pressure (AP) conditions (elevated H<sub>2</sub> and H<sub>2</sub>O pressures).
2. Interaction of (S)-alanine on clean Ni $\{100\}$  under UHV and elevated hydrogen pressures.
3. Co-adsorption of (S)-alanine and water on Ni $\{110\}$ .

## 4. Adsorption of methyl acetoacetate (MAA) on Ni{100}.

The interaction of the molecules under the presence of elevated pressures is performed using ambient pressure (XPS), so we could bridge the pressure gap, which is also lacking from literature at least for this reaction, and approach more realistic reaction condition. The elevated  $H_2$  pressures are used to mimic the reactions conditions and  $H_2O$  is one of the typical modifying solvents [17, 24]. The interaction of molecules on oxidised surfaces, also approaches the enantioselective catalysis conditions, since the modification occurs from aqueous solution and the catalyst itself is exposed to air before the modification [39].

# Chapter 2

## Experimental techniques

### 2.1 X-ray Sources

The conventional laboratory UV and X-ray sources consist of gas discharge lamps and X-ray anode sources, respectively. The most common gas discharge lamps include the He I and He II lamps. The aforementioned sources produce monochromatic radiation of 21.2 and 40.8 eV respectively [74]. In anodes, the X-rays are generated by electron-induced electron excitation in the anode, with subsequent emission of fluorescence radiation [73, 75]. Common anodes in the low photon energy region are the Mg  $K_{\alpha 1,2}$  and Al  $K_{\alpha 1,2}$ , which produce 1253.6 eV and 1486.7/1486.3 eV monochromatic radiation, respectively [74], with natural line widths of 0.6 eV and 0.8 eV, respectively [74]. The use of crystal monochromators allows to reduce the line width to approximately 0.2-0.3 eV [74]. X-ray anodes exist in the high photon energy region, as well with Cr  $K_{\beta 1,3}$  and Cu  $K_{\beta 1,3}$  generating monochromatic radiation of 5496.7 eV and 8905.3 eV, respectively [74].

Synchrotron radiation is generated when charged relativistic particles (such as electrons), in vacuum conditions, are compelled to pass onto a curved trajectory. An electron beam is created from a linear accelerator, which is further accelerated in a small synchrotron called a booster. Bunches of electrons are inserted into the main storage ring, where they reach about 2 GeV or higher energy. Bending magnets, placed in the storage ring are keeping the electrons in a circular orbit, causing the emission of radiation, since in bending magnets the electrons are subject to acceleration. The radiation is directed to the beamline, and a monochromator permits the selection of the desired photon energy for the X-ray based techniques [74–77]. Third generation synchrotron radiation is generated by insertion devices such as wigglers and undulators, which are arrays of small bending magnets, placed in the linear sections of the ring [74–77]. The insertion

Table 2.1: Specifications of the SuperESCA beamline (Elettra synchrotron, Trieste, Italy), HE-SGM beamline (BESSY II synchrotron, Berlin, Germany) and D1011 beamline (MAX-Lab synchrotron, Lund, Sweden) along with specifications of the lab source NAP-XPS facility in the University of Manchester.

	SuperESCA beamline [79]	HE-SGM beamline [80]	D1011 beamline [81]	Lab source (University of Manchester) [82]
<b>Source</b>	Lineal planar undulator	Bending magnet	Bending magnet	Al $K_{\alpha}$ anode
<b>Energy range (<math>h\nu</math>)</b>	90-1800 eV	100-750 eV	40-1500 eV	1486.7 eV
<b>Photon flux</b>	$\sim 10^{12}$ photons/s at $h\nu=400$ eV $^{\alpha}$	$5 \times 10^{11}$ photons/(s $\times$ 100 mA)	$\sim 10^{10}$ - $10^{12}$ photons/(s $\times$ 100 mA) at $h\nu=400$ eV and at $h\nu=650$ eV $^{\beta}$	No information
<b>Beamline resolution (<math>E/\Delta E</math>)</b>	$\sim 10000$ at $h\nu=400$ eV $\sim 5000$ at $h\nu=650$ eV	500-2500	$\sim 2700$ at $h\nu=400$ eV $^{\gamma}$ $\sim 2600$ at $h\nu=650$ eV $\sim 2600$ at $h\nu=900$ eV	$\Delta E \approx 0.5$ eV $^{\delta}$

$^{\alpha}$ Measured during the top-up mode of the Elettra storage ring (2 GeV with 300 mA ring current) [79].

$^{\beta}$  Depends on the slit width. The photon flux as a function of photon energy, was measured at 6 different slit widths: 6  $\mu\text{m}$ , 16  $\mu\text{m}$ , 44  $\mu\text{m}$ , 92  $\mu\text{m}$ , 190  $\mu\text{m}$  [81].

$^{\gamma}$  The values shown are at slit width of 16  $\mu\text{m}$ . The beamline resolution ( $E/\Delta E$ ) as a function of photon energy, was measured at 6 different slit widths: 6  $\mu\text{m}$ , 16  $\mu\text{m}$ , 44  $\mu\text{m}$ , 92  $\mu\text{m}$ , 190  $\mu\text{m}$  [81].

$^{\delta}$  Refers to  $\Delta E$  value (including also the electron analyser resolution) [82].

devices, generate spectra with narrow lines of high intensity [74]. Synchrotron radiation offers many advantages compared to conventional laboratory X-sources such as [78]:

- Choice of photon energy from a continuous spectrum and broad energy range.
- High intensity and brightness.
- Variable polarisation.
- Small photon spots.
- Time resolution.

Specifications (such as energy range, source and photon flux, and beamline resolution) of of the three synchrotron beamlines (SuperESCA, HE-SGM and D1011) and the lab source facility (NAP-XPS in the University of Manchester) that were used for experiments leading to this thesis, are shown in Tab. 2.1

## 2.2 X-ray photoelectron spectroscopy (XPS)

### 2.2.1 The XPS process

X-ray photoelectron spectroscopy (known as XPS) is based on the photoelectric effect. The XPS process is shown in Fig. 2.1. The irradiation of a sample with X-rays, causes the emission of photoelectrons from a core level with kinetic energy related to the binding energy of the electron, according to Eq. 2.1 [66, 78, 83, 84]:

$$E_b = h\nu - \phi - E_{kin} \quad (2.1)$$

Where  $E_b$  and  $E_{kin}$  are the photoelectron's binding and kinetic energy, respectively,  $h\nu$  is the energy of incident photon and  $\phi$  the work function of the sample, which is the energy separation between the  $E_f$  and the vacuum level ( $E_v$ ). The binding energy in solids is referred with respect to the Fermi level, and is equal to the difference between the final and initial state of the atom. Photoemission will only occur if the photon energy is higher than the sum of the  $E_b$  of the electron and the  $\phi$  of the sample [66, 67, 78, 83, 84].

An XPS peak will only be generated if the electrons reach the analyser. XPS is, generally, a surface sensitive technique, since the escape depth of electrons is only a few Å [66, 83]. Electrons emitted from a sample, are subject to elastic and inelastic collisions with other molecules, which causes decrease in their detected signal [66, 68]. The attenuation of the XPS peak due to inelastic collisions, can be calculated using the Beer-Lambert law which relates the attenuation of an XPS signal with the inelastic mean free path (IMFP) of electrons through a material ( $\lambda$ ) [67, 84]:

$$I = I_0 e^{-\frac{d}{\lambda}} \quad (2.2)$$

Where  $I_0$  and  $I$  is the intensity before and after the electron has travelled a distance  $d$  through the material. The IMFP is a measure of the distance that a particle (such as an electron) travels on average before it loses energy [84]. The IMFP depends on the kinetic energy of the electron [66]. By varying the energy of the incident photon, we can tune the surface sensitivity of the XPS technique. This fact highlights the importance of the use of synchrotron radiation as an X-ray source.

The XPS technique is a useful technique to identify the elements in a sample. Deep core electrons are not involved in chemical bonding, and therefore their energy is characteristic of the atom which they derive from. However small shifts

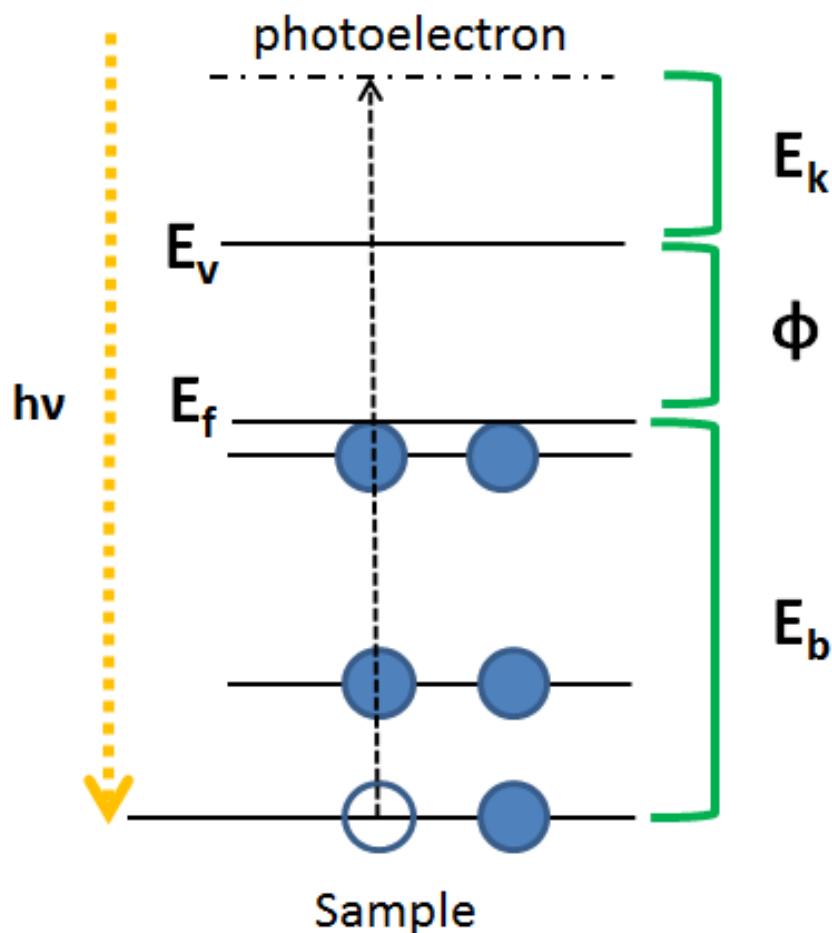


Figure 2.1: The XPS process in a solid [83].

can be observed, depending on the bonding environment of the atom. For example, a high oxidation state of an atom, causes shift to higher binding energies. Also, atoms binding to high electronegative substituents, present also higher binding energies. Chemical shifts are also observed between surface and bulk atoms [66, 78, 83].

These chemical shifts are often seen as initial state effects. According to the Koopmans' theorem, the binding energy of an electron is equal to the negative energy of its original orbital ( $E_b(k) = -\epsilon_k$ ) if the spectator electrons do not rearrange upon photoemission. However, electrons are not frozen and therefore the binding is equal to the difference between the final (photoemission and creation of a core hole) and initial state of the atom (before photoemission). When an electron is ejected from an atom, electrons from the atom and the neighbouring atoms (in solids) relax to screen the hole created by the ejected electron, reducing the final state energy and by extension the binding energy of the photoelectron. In conductors, the size of relaxation is higher than in insulators, since in the former

the valence electrons can move from one atom to a neighbour atom [66]. In states with orbital angular momentum greater than zero ( $l > 0$ ) photoemission will cause doublet splitting of the state, originated by spin-orbit coupling ( $j = l \pm 1/2$ ) and generation of two XPS peaks [66]. Multiplet splitting of a state could be caused by spin-spin interactions of the unpaired electron of the ionised orbital with any unpaired electrons in the outer shells [66].

Final state effects are the shake up and shake off events. In the shake up event the photoelectron, interacts with a valence electron, exciting the latter to an unoccupied state. The photoelectron loses some of its energy, thus a peak is observed at the high binding energy region. In the shake off event the photoelectron causes excitation of the valence electron to the vacuum. For the shake off event, as opposed to the shake up, the generated peak is not very distinct [66]. Vibrational transitions from the initial to final state (following the Franck-Condon principle) can cause the generation of vibrational side bands which typically contribute to the (often asymmetrical) broadening of the XPS peak, since these transitions are usually less than 1 eV [83, 85, 86].

Figure 2.2 shows XP-spectra after dosing  $\text{H}_2\text{O}$  onto  $\text{Ni}\{110\}$  at 180 K up to saturation. The XP-spectra, shows 2 peaks around 533.2 eV and 531.3 eV which correspond to the oxygen atom of the  $\text{H}_2\text{O}$  and  $-\text{OH}$  species, respectively. This assignment of the XPS peaks cannot be explained with the electrostatic model, presented in previous paragraphs, since the atom with the highest oxidation state, the oxygen of the OH species, presents the lowest binding energy. These chemical shifts can be explained with the equivalent core or  $(Z+1)$ -approximation [83, 85, 87]. In the  $(Z+1)$  approximation, the generation of a core hole via photoemission can be approximated by the addition of a proton in the nucleus [83, 85, 87]. This means that the core ionised atom is replaced by an atom which has  $(Z+1)$  nuclear charge and is lacking an electron in the valence orbitals [83]. In the case of core-ionised  $\text{H}_2\text{O}$  and  $-\text{OH}$ , the oxygen atom is replaced with a F atom with 6  $e^-$  in the outer shells ( $\text{H}_2\text{F}^6$  and  $-\text{HF}^6$ , respectively)[85]. The H-F bond in these molecules is increased with respect to the natural  $\text{H-F}^7$  bond, which destabilises the molecule and increases the final state (and by extension the binding energy of the O 1s electron). Since the  $\text{H}_2\text{F}^6$  contains two H-F, the core electron of the oxygen atom in  $\text{H}_2\text{O}$  molecule will have the larger binding energy with respect to the core electron of the oxygen atom in the OH species [85].

The intensity of an XPS peak depends on several factors such as concentration of the atoms in the material, the photoemission cross section, the IMFP of the photoelectron, the angle of incidence and instrumental factors (X-ray source/beamline and detector). However photoelectrons of similar binding have similar IMFP while

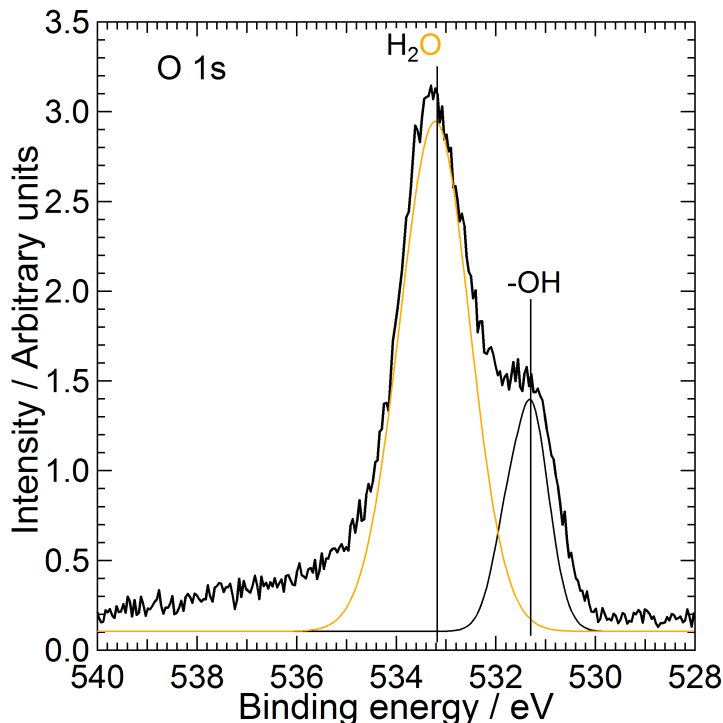


Figure 2.2: XP-spectra in the O 1s region ( $h\nu=650$  eV) after dosing H<sub>2</sub>O onto Ni{110} at 180 K up to saturation. The solid black thick lines are the raw data and the solid coloured curves are the individual peaks obtained upon fitting.

at the same time they present also similar response to the instrumental factors. In addition, the photoionisation cross section of core levels is independent of the chemical environment, therefore an XPS peak can provide useful quantitative information especially if the peak arises from photoelectrons of the same core level [66, 84]. The presence of an inhomogeneous sample (especially throughout the sampling depth) as well as photoelectron diffraction effects can cause variations in the intensity of the XPS peak [66, 84]. The latter is caused by the elastic scattering of the photoelectrons from the surrounding atoms and is observed for photoelectrons of kinetic energy of few hundred eV. Since the wavelength of the photoelectron is similar to the interatomic distance, the photoelectron diffraction can alter the intensities of the XPS peaks. The photoelectron diffraction effects on the intensity of the XPS signal, could be minimised by probing high kinetic energy electrons [75, 85, 88].

The use of high flux photon sources can significantly alter the XP-signal of an adsorbed molecule causing either reduction of its multilayer signal or decomposition of the molecule (beam damage, Fig. 2.3). This effect can be minimised by either recording or observing the change of the XP-signal after each sweep and/or moving the sample under the beam, between recordings of XP-spectra.

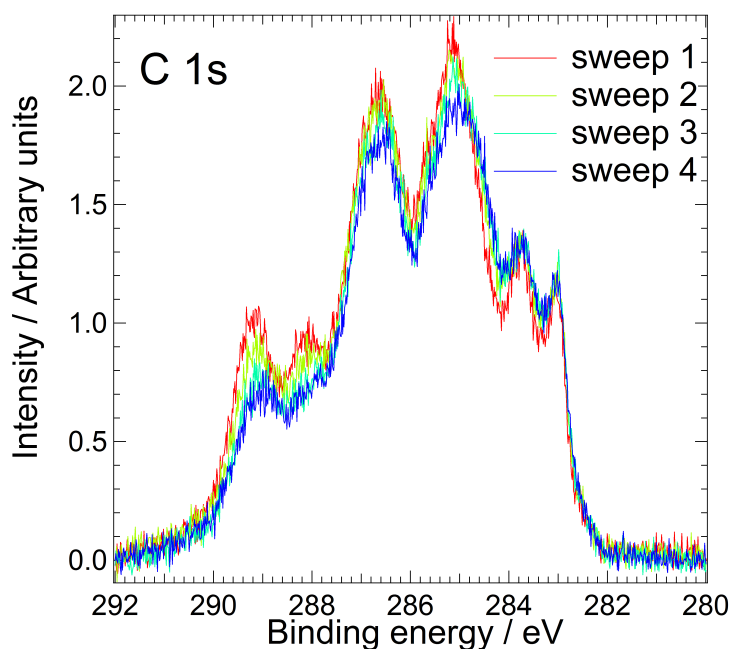


Figure 2.3: Example of beam damage in XP-spectra after several sweeps. The spectra were obtained in the C 1s region ( $h\nu=400$  eV) upon dosing methyl acetate (MAA) onto Ni{100} at  $T_{\text{sample}}=180$  K up to  $\Theta_{\text{MAA}}=0.23$  ML.

## 2.2.2 Experimental set-up

The experimental set-up of a typical XPS instrument is shown in Fig. 2.4. An X-ray radiation with particular energy  $h\nu$  and polarisation vector  $\vec{E}$  strikes the sample at an angle  $\theta$  with respect to the surface normal, generating electrons with particular kinetic energy. The electron analyser consists of two electrically isolated concentric hemispheres with a potential difference between them. The generation of XP-spectra (number of electrons vs kinetic/binding energy) is achieved by applying a retarding (negative) voltage to the electrons, before entering the analyser, using a negative electrode (retard plate). The applied retarding voltage is related to the actual kinetic energy of the electron, since the analyser allows only electrons with a certain energy (pass energy) to reach the detector. Electrons with kinetic energy less than the pass energy will be attracted by the positive potential of the inner hemisphere, whereas electrons with kinetic energy higher than the pass energy, will hit the outer hemisphere. [78, 84].

Ambient pressure XPS (AP-XPS), in pressure range of 1-10 mbar, can be performed by introducing 1 mm diameter or less entrance apertures between the sample (ambient pressure) and the electrostatic lens system (in UHV conditions), while differentially pumping within the analyser (Fig. 2.5) [74]. The short distance between the sample and the differentially pumped system allows improvement in the attenuation of the XPS signal from the molecules in the gas phase. In the

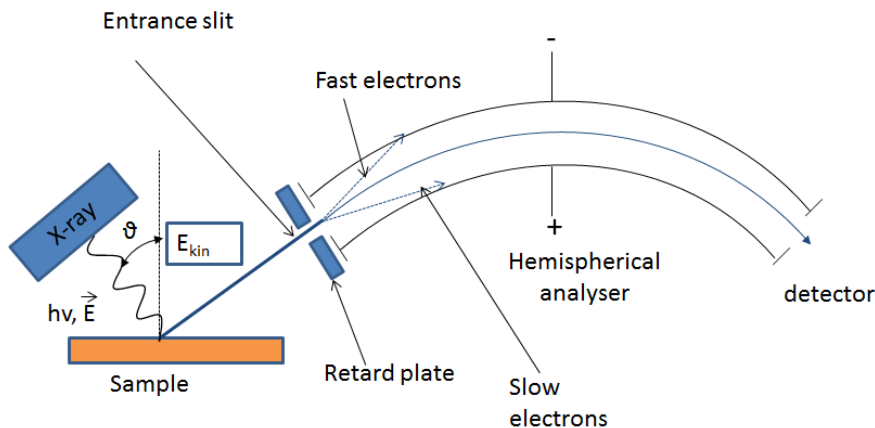


Figure 2.4: The XPS instrumentation [78, 84].

differentially pump system, the electron beam is focused through the use of an electron lens system [89].

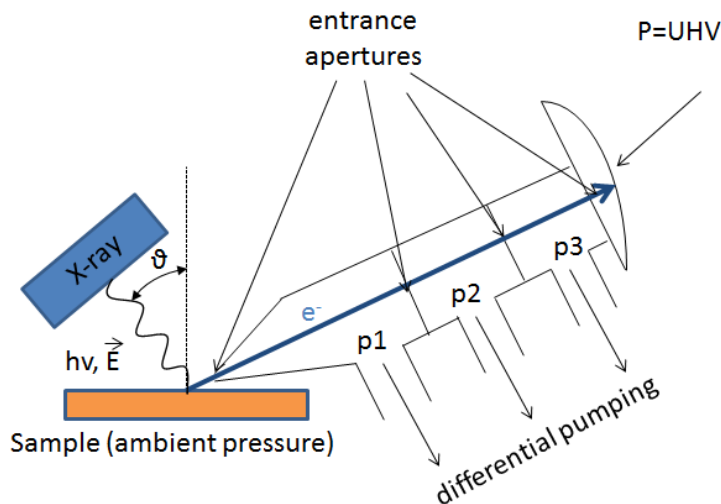


Figure 2.5: The AP-XPS instrumentation [74].

The instrumental resolution (beamline and analyser), as a function of photon energy, for each experiment of this study, was determined by measuring the  $\Delta_{\text{binding energy}}$  at the 12% and 88% of the intensity of the spectra of the Fermi edge and subtracting by  $4k_{\text{B}}T$ , where  $k_{\text{B}}$  is the Boltzmann constant ( $\sim 1.38 \times 10^{-23} \text{ m}^2\text{kg s}^{-2}\text{K}^{-1}$ ) and  $T$  is the temperature of the sample. In the cases where the exact temperature of the sample was not stable, during the acquisition of the spectra of the Fermi edge, because of the cooling of the sample, we have used as a temperature, the average between the annealing temperature (before the acquisition of the spectra) and the room temperature (300 K) [83].

### 2.2.3 XPS Data Analysis

Inelastically scattered electrons contribute to the formation of background in the high binding energy region. Initially all the XP-spectra are normalised with respect to the low binding region with simultaneously correcting of the offset of the binding energy axis. In this study the correction of the binding energy axis was performed either by using spectra of the Fermi edge, recorded every time the monochromator was moved (synchrotron experiments), or by using the position of the Ni 2p peak (BE=852.7 eV) at the experiments conducted using Al  $K_\alpha$  anode ( $h\nu=1486.7$  eV) as an X-ray source (NAP-XPS facility in the University of Manchester). The second step is the subtraction of the background in order to quantify the XPS data, from the area of the peaks. The subtracted background could be linear or Shirley. In Shirley background, the step of the background is directly related to the integral of the peak, as is shown in Fig. 2.6 [67, 90].

The final step of XPS data analysis is the fitting of the curves in order to determine the position and the intensity of the peaks that consist the XPS spectrum. The instrumental resolution produces a Gaussian lineshape (Eq. 2.3), while the core hole lifetime effect generates a Lorentzian lineshape (Eq. 2.4) [91]:

$$I_G = H e^{-\frac{(E-P)^2}{2W^2/c^2}} \quad (2.3)$$

$$I_L = H \left( \frac{(W/2)^2}{(E-P)^2 + (W/2)^2} \right) \quad (2.4)$$

Where H is the maximum value of the function, E is the energy (independent variable), P is the peak position, W is the the full width at half maximum

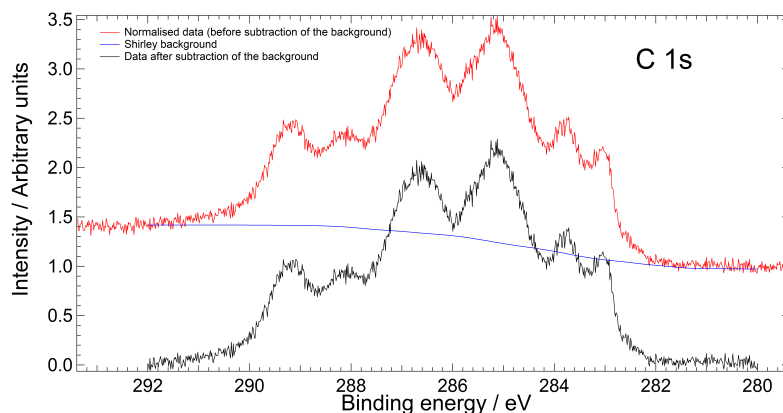


Figure 2.6: Shirley background subtraction. The data were recorded in the C 1s region ( $h\nu=400$  eV) upon dosing methyl acetoacetate (MAA) onto Ni{100} at  $T_{\text{sample}}=180$  K up to  $\Theta_{\text{MAA}}=0.23$  ML.

(FWHM) and  $c$  is a constant ( $c=2\sqrt{\ln 4}$ )[91].

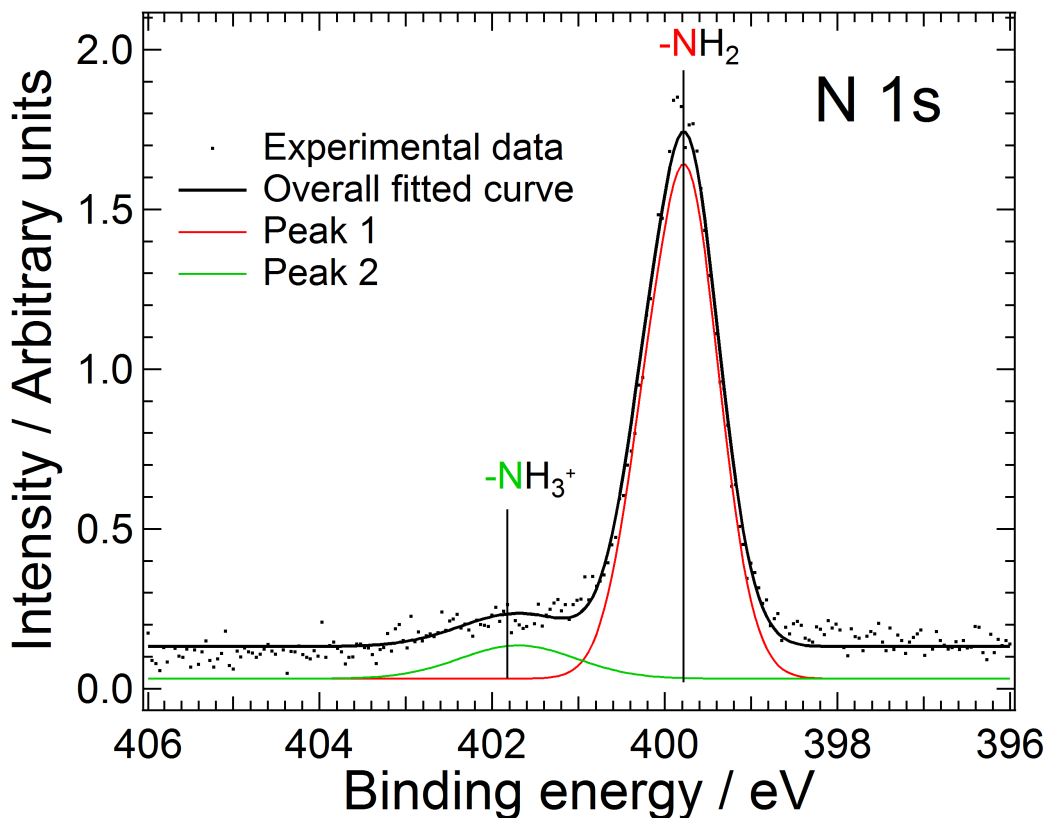


Figure 2.7: Example of peak fitting in XPS. The data were recorded in the N 1s region ( $h\nu=510$  eV) upon dosing (S)-alanine onto Ni{110} at  $T_{\text{sample}}=200$  K for 30 minutes ( $\Theta_{\text{Ala}}=80\%$  saturation). The black dots are the raw data and the solid black thick lines are the fitted curves. The solid coloured curves are the individual peaks obtained upon fitting.

Table 2.2: Fit parameters of the XP-spectra in Fig. 2.7.

Parameters	Values
Offset	0.03135
Peak 1 intensity	1.6107
Peak 1 position	399.8
Peak 1 FWHM	0.95803
Peak 1 mixture	0.14
Peak 1 asymmetry	0.68406
Peak 2 intensity	0.10388
Peak 2 position	401.7
Peak 2 FWHM	1.6074
Peak 2 mixture	0.08
Peak 2 asymmetry	0.01

The overall line profile which was used for fitting the spectra in the current

study is a pseudo Voigt function as shown Eq. 2.5 [92, 93]:

$$I_{G,L} = H[\exp[\frac{-c^2}{2}(1-m)\frac{(E-P)^2}{W^2}]][\frac{W^2}{4m(E-P)^2 + W^2}] \quad (2.5)$$

Where  $m$  is the Lorentzian fraction in the pseudo-Voigt function. An example of peak fitting of a spectra is shown in Fig. 2.7. An asymmetry parameter (Eq. 2.6),  $as$ , is introduced in order to account for the high binding energy region of the peak, where  $0$  accounts for a symmetric peak [85].

$$I_{G,L,as} = I_{G,L} * [I_{G,L} + (1 - I_{G,L})e^{\frac{as(E-P)}{w}}] \quad (2.6)$$

Typical values of asymmetry, in this study, were 0.01-1, whereas the  $m$  (the Lorentzian fraction) was set according to the lifetime width of the core hole of each atom [94]. Finally, an offset parameter is introduced, in case the intensity of the low binding energy of the XPS profile is not zero [67]. Example of peak fitting of XP-spectra with the corresponding fit parameters are shown in Fig. 2.7 and Tab. 2.2, respectively.

#### 2.2.4 Temperature programmed-X-ray photoelectron spectroscopy (TP-XPS)

During a TP-XPS experiment, the sample is heated at a constant rate while simultaneously obtaining XP-spectra. Normally, the sample is moved under the beam to minimise any potential beam damage. The spectra are combined to a 2D image, in which the x axis is the binding energy and y axis is the temperature (Fig. 2.8a). Change in the intensity of the XPS signal is depicted using a colour scale. This technique, in combination with TPD, allows the full determination of any changes that occur in the chemical nature of the surface and its adsorbed species as a function of the temperature, providing insights into the decomposition pathways of the adsorbed molecule.

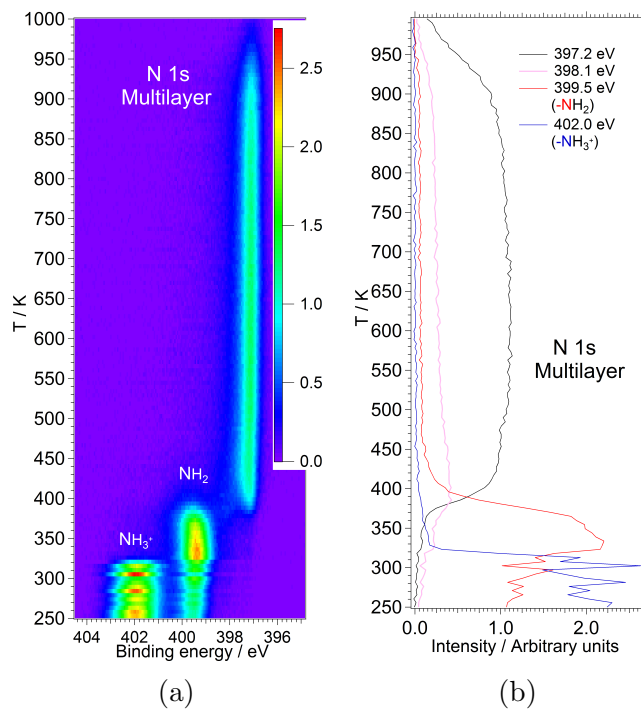


Figure 2.8: (a+b) TP-XP-spectra in the (a) N 1s region, obtained upon dosing (S)-alanine onto Ni{100} at  $T_{\text{sample}}=250$  K up to the multilayer regime. Heating rate:  $8 \text{ K min}^{-1}$ ,  $h\nu=510$  eV. (b) Intensity profiles (in 0.5 eV wide bands) as a function of temperature, obtained from the TP-XP-spectra in 4.4b for the the nitrogen peaks at 397.2 eV, 398.1 eV, 399.5 eV and 402.0 eV.

## 2.3 Near edge X-ray absorption fine structure (NEXAFS) spectroscopy

### 2.3.1 The NEXAFS-Process

Near edge X-ray absorption Fine Structure (NEXAFS) spectroscopy is a technique which allows the study and determination of the electronic structure and the orientation of adsorbed molecules on the surface. The NEXAFS process is shown in Fig. 2.9a. When monochromatic X-ray radiation is applied to the sample, an electron from a core level is ejected either into an unoccupied molecular orbital or into vacuum, creating a core hole [77, 91].

A NEXAFS spectrum can be obtained either by measuring the fluorescence or electron yield. The core hole, created as a result of the photoabsorption process, is filled from an electron from higher orbitals causing the emission of fluorescence radiation (Fig. 2.9b) or the emission of an Auger electron (Fig. 2.9c), in order to conserve the energy of the system. Both these processes are a direct measure of the presence of a core hole, created as a result of the photoabsorption process,

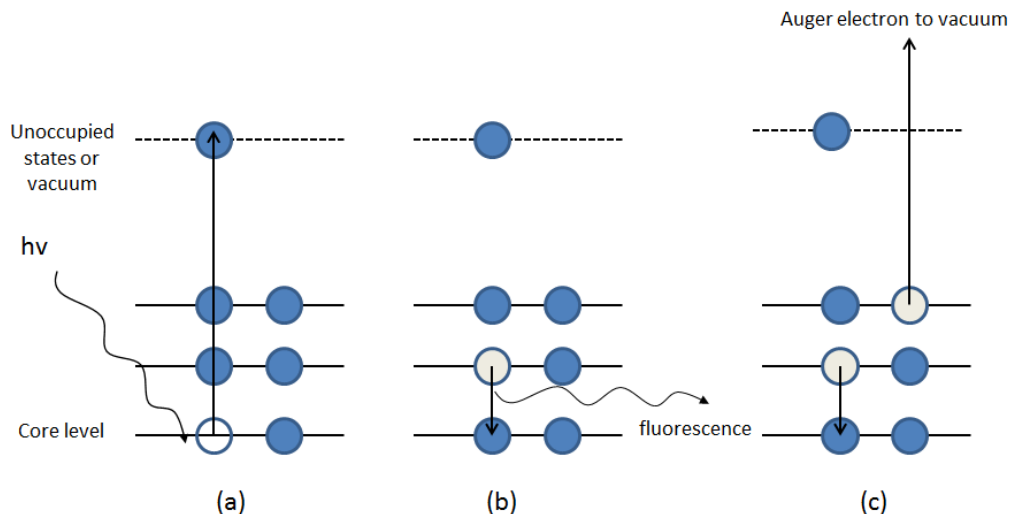


Figure 2.9: Schematic diagram of (a) the NEXAFS process (b) the fluorescence process and (c) the Auger process [77, 91].

therefore can be used as a measure of the X-ray absorption cross section [77, 91].

The kinetic energy of an emitted Auger electron is independent of the photon energy and is described in Eq. 2.7:

$$E_k = E_1 - E_2 - E_3 \quad (2.7)$$

Where  $E_1$  is the energy level of the core hole,  $E_2$  the energy of the level from which the core hole is filled and  $E_3$  is the energy level of the Auger electron. The nomenclature of an Auger process depends on these levels. For example a KLL Auger process refers to a process in which the core hole was created in the K-shell, filled up from an electron from the L-shell and finally generating the Auger electron from the L-shell as well [67]. The Auger process is the predominant one in low mass atoms such as carbon, nitrogen and oxygen [77].

An example of a NEXAFS spectrum (absorption probability or absorption cross section as a function of photon energy) of a diatomic molecule AB along with the origin of the peaks is shown in Fig. 2.10. The excitation of the electron occurs from the  $1s$  core level (K-edge). In this example, the lowest unoccupied molecular orbital has  $\pi^*$  symmetry, producing a sharp  $\pi^*$  resonance. The transition of  $1s$  electron to  $\pi^*$  orbitals, only occurs in the presence of  $\pi^*$  bonds in the probed molecules. The  $\pi^*$  orbital is followed by the Rydberg states. Above the ionisation potential, the orbitals of the AB molecule have  $\sigma^*$  symmetry. The  $\sigma^*$  resonances have broader shape, due to vibrational effects and due to their interaction with continuum which increases the decay probability of the electron and as a result the core lifetime. The absorption step in the spectra is originated from the excitation

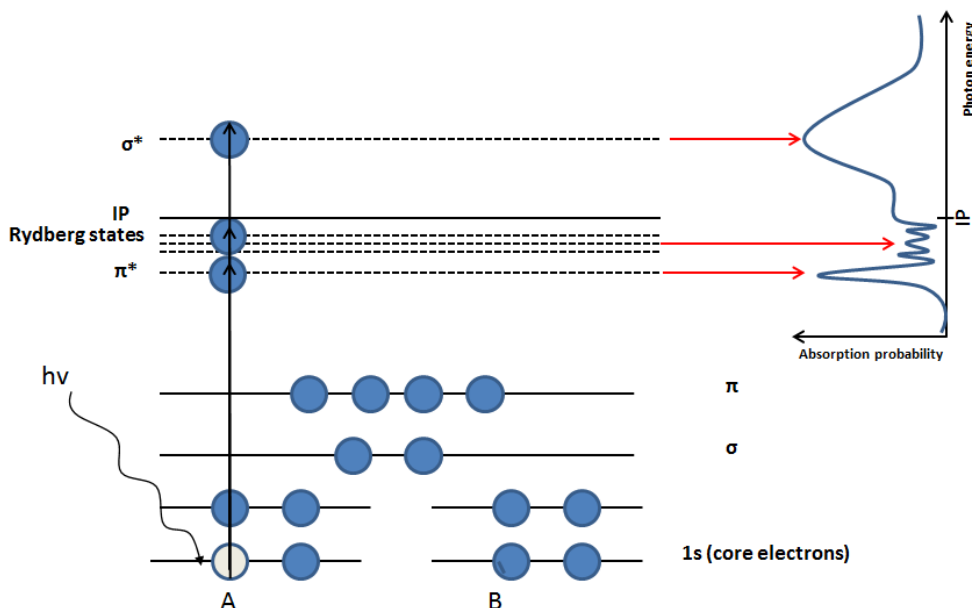


Figure 2.10: NEXAFS K-edge spectra of a diatomic molecule AB showing the the origin of the NEXAFS peaks [77, 91, 95].

of the electron to continuum states [77, 91, 95].

NEXAFS spectra can reveal information on the electronic structure of adsorbed species. Since the absorption is due to the excitation of core electrons, the technique can provide details on the elemental composition of a surface. The probing of the unoccupied molecular orbitals can give also information on the nature of chemical species of the adsorbed molecule [77, 91, 95]. NEXAFS can also provide information on the molecular orientation of adsorbed species. According to Eq. 2.8 (related to the Fermi's golden rule), there is a strong link between the intensity of a resonance in a NEXAFS spectrum ( $I$ ) and the direction of the final state orbital  $\vec{O}$  ( $\pi^*$  or  $\sigma^*$  orbital)[77, 96]:

$$I \propto |\vec{e} \langle \Psi_f | \vec{p} | \Psi_{1s} \rangle|^2 \propto |\vec{e} \vec{O}|^2 \propto \cos^2 \delta \quad (2.8)$$

Where  $\vec{e}$  is the unit electric field vector,  $\Psi_{1s}$  and  $\Psi_f$  initial and final state, respectively,  $\vec{p}$  the dipole transition operator and  $\delta$  the angle between the electric field vector and the direction of the final state orbital. Based on this equation, the intensity of a resonance is maximum when the electric vector is parallel to the direction of the final state orbital and in minimum when the electric vector is perpendicular to the direction of the orbital [77]. Information on the molecular orientation of adsorbed species, using NEXAFS, can be obtained by changing

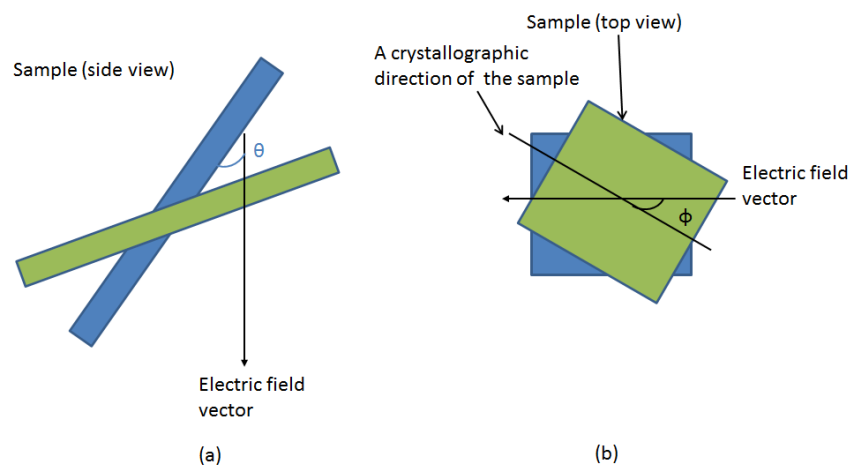


Figure 2.11: (a) The polar ( $\theta$ ) and (b) the azimuthal angle ( $\phi$ ) of the electric field vector with respect to the surface plane.

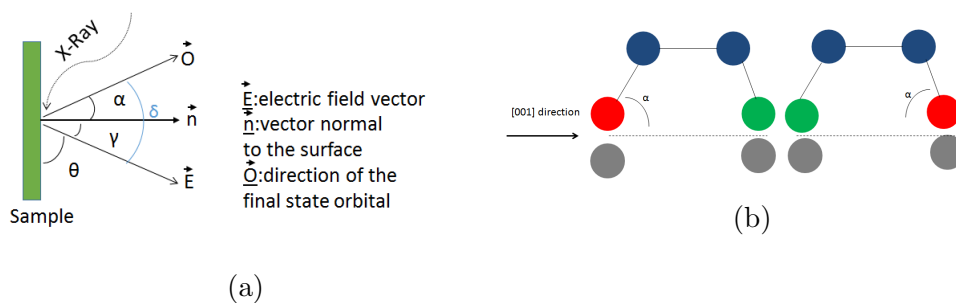


Figure 2.12: (a) Relationship of the angle of incidence  $\gamma$  (angle between the electric field vector and the surface normal), the angle  $\alpha$  (angle between the direction of the final state orbital of the adsorbed molecule and the surface normal) and the angle  $\delta$  (the angle between the electric field vector and the direction of the final state orbital). (b) Schematic view of the tilt angle  $\alpha$ , which is the angle between the C=O/COO<sup>-</sup> groups of the alanine molecule with respect to the Ni{110} surface plane (equivalent with the angle between the direction of the final state orbital of the C=O/COO<sup>-</sup> groups and the surface normal as shown in Fig. 2.12a), for the two possible adsorption orientations. The blue circles are carbon atoms, the red circles are oxygen atoms, the green circles are nitrogen atoms and grey circles are nickel atoms.

either the (out of plane) polar or (in plane) azimuthal angle of the electric field vector of the X-ray beam with respect to the surface (angle dependent NEXAFS) as shown in Fig. 2.11. In this study angle dependent NEXAFS were acquired by changing the out of plane angle of incidence  $\theta/\gamma$ . Angle  $\theta$  refers to the angle between the electric field vector and the surface plane (Fig. 2.11) whereas angle  $\gamma$  refers to the angle between the electric field vector and the surface normal (Fig. 2.12a). This allowed us to determine the tilt angle  $\alpha$  of chemical groups of adsorbed molecules, with respect to the surface as shown in Fig. 2.12, for the case of C=O/COO<sup>-</sup> groups of the alanine molecule with respect to the Ni{110} surface plane. As mentioned above the intensity of a resonance depends on the angle  $\delta$  (the angle between the electric field vector and the direction of the final state orbital), which depends on both  $\alpha$  and  $\gamma$  angles (Fig. 2.12).

### 2.3.2 Experimental set-up

For this work, the NEXAFS spectra were obtained by using electron yield as detection mode. Electron yield offers higher surface sensitivity with respect to the use of fluorescence radiation [77]. The electron yield can be measured in three ways: total electron yield (TEY), and partial electron yield (PEY) and Auger electron yield (AEY). The TEY is the easiest set-up in terms of experimental configuration. It detects the signal of all the photoelectrons and Auger electrons by just using an electron channeltron multiplier. This detection mode is more bulk sensitive. The PEY detects a part of the emitted electrons by applying a retarding voltage before the detector. The detector suppresses the low kinetic energy electrons coming from the bulk, however it can still detect photoelectrons and inelastic scattered electrons as long as their kinetic energy exceeds the cut-off energies due to bias voltage. Typical cut off energies for C, N, and O are  $\sim 180$ - $230$  eV,  $\sim 290$ - $340$  eV,  $\sim 430$ - $480$  eV, respectively. The AEY detects only Auger electrons of a specific transition [77, 91, 95]. In this work the Auger electrons were detected using a hemispherical analyser.

### 2.3.3 NEXAFS Data Analysis

In order to be able to analyse raw NEXAFS data of an adsorbate molecule on a metal surface, two additional spectra should be obtained: the spectra of the clean surface and  $I_0$ , which is the intensity of the beam as a function of energy. Initially, all the spectra should be normalised at low energies, just before the beginning of the resonances. The spectra are normalised with respect to  $I_0$  and background subtracted using the clean surface spectra. Finally for angle dependent NEXAFS

with the same coverage of adsorbate, the spectra are normalised at high photon energy, under the assumption that the step in the spectra depends only on the coverage of the adsorbate.

The spectra are fitted using an equation which consists of a linear background, a step function and several Gaussian functions depending on the number of resonances (Eq. 2.9):

$$I(E) = B_0 + B_S(E - S_P) + S_H \left[ \frac{1}{\pi} \arctan\left(\frac{E - S_P}{0.2 * S_W}\right) + \frac{1}{2} \right] + \sum_i G_{i,H} \exp\left[-4 \ln 2 \frac{(E - G_{i,P})^2}{G_{i,W}^2}\right] \quad (2.9)$$

Where  $B_0$  is the offset at the point of the absorption step,  $B_S$  is the slope of the linear background,  $S_P$  is the step position,  $S_H$  is the step height,  $S_W$  is the width of the step, and  $G_{i,H}$ ,  $G_{i,P}$  and  $G_{i,W}$  are the height, position and full width at half maximum of an  $i$ th resonance. An example of peak fitting of NEXAFS spectra with the corresponding fit parameters are shown in Fig. 2.13 and Tab. 2.3, respectively.

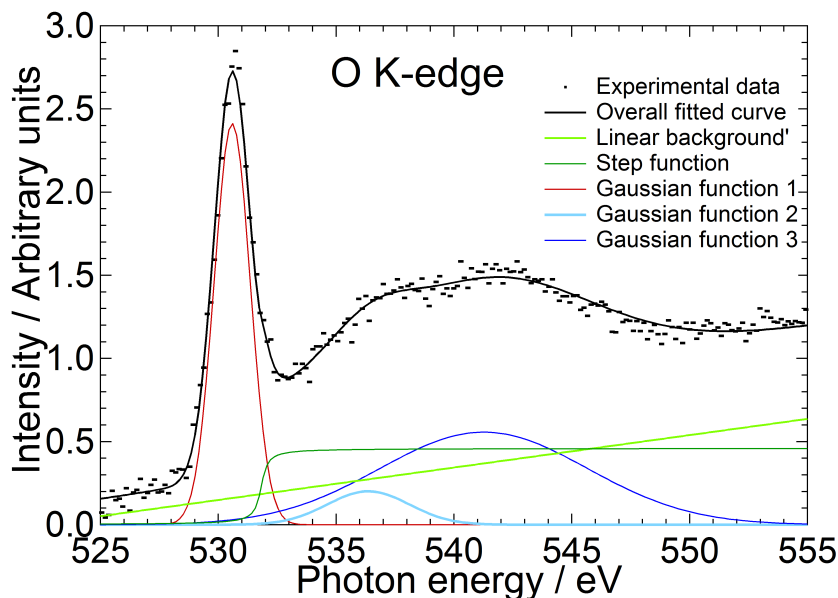


Figure 2.13: Example of fitting NEXAFS spectra. The data were obtained in the O K-edge region after dosing (S)-alanine onto Ni{110} at  $T_{\text{sample}}=200$  K up to multilayer regime ( $\Theta_{\text{Ala}}=390\%$  sat) and anneal the layer to 346 K. The data were recorded at  $\theta=35^\circ$ , where the  $\theta$  is the angle between the electric field vector and the surface plane. The dots represent the raw data and the solid thick lines the fitted curves. The curves below the spectra show the individual Gaussian peaks, the linear background and the the step function used during the fitting process.

Table 2.3: Fit parameters of the NEXAFS spectra in Fig. 2.13.

Parameters	Values
$B_0$	0.184192
$B_S$	0.0195004
$S_P$	531.823 eV
$S_H$	0.459025
$S_W$	1.01122 eV
$G_{1,H}$	2.41235
$G_{1,P}$	530.593 eV
$G_{1,W}$	1.80596 eV
$G_{2,H}$	0.201137
$G_{2,P}$	536.371 eV
$G_{2,W}$	4.0917 eV
$G_{3,H}$	0.556594
$G_{3,P}$	541.267 eV
$G_{3,W}$	10.3858 eV

## 2.4 Temperature programmed desorption (TPD)

Temperature programmed desorption (TPD) is a technique that among other things can provide information on [66, 84]:

1. The nature of the adsorbates on a surface.
2. The relative coverage of the adsorbates on the surface.
3. The activation energy for desorption.

When a surface, exposed to an adsorbate in the gas phase, is heated the adsorbed species can either desorb or decompose. The species that are removed from the surface are measured by recording the partial pressure of chosen mass fragments using a quadrupole mass spectrometer, thus generating different figures of partial pressure as a function of temperature for different molecular masses (Fig. 2.14). The peak in a TPD figure, represents the temperature where the desorption rate is at its maximum .

The heating is introduced by applying linear temperature ramp according to Eq. 2.10 [66, 84]:

$$T = T_0 + \beta * t \quad (2.10)$$

Where  $T$  is the sample temperature,  $T_0$  is the initial temperature,  $\beta$  the heating rate ( $\frac{dT}{dt}$ ) and  $t$  is the time. The Polanyi-Wigner equation express the rate of

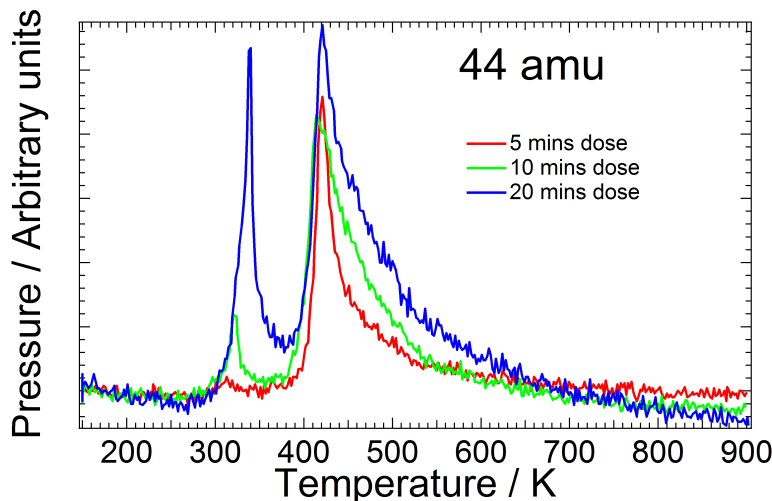


Figure 2.14: Example of TPD data for mass 44. The data were obtained after dosing (S)-alanine onto Ni{110} at  $T_{\text{sample}}=200$  K at three different dosing times. Heating rate  $1 \text{ K s}^{-1}$ .

desorption ( $\frac{d\Theta}{dt}$ ) [66, 84]:

$$r_{\text{des}} = -\frac{d\theta}{dt} = A * \theta^n * \exp\left(\frac{-E_{\text{des}}}{RT}\right) \quad (2.11)$$

Where A is the pre-exponential factor,  $\Theta$  is the number of surface atoms, n and  $E_{\text{des}}$  are the kinetic order and activation energy of the desorption process, respectively, and T is the sample temperature. Now [66, 84]:

$$\frac{d\theta}{dt} = \frac{d\theta}{dT} * \frac{dT}{dt} \quad (2.12)$$

Combination of Eq. 2.11 and Eq. 2.12 and substitution of  $\frac{dT}{dt}$  with  $\beta$ , leads to the following expression, W [66, 84]:

$$-\frac{d\theta}{dT} = \frac{A}{\beta} * \theta^n * \exp\left(\frac{-E_{\text{des}}}{RT}\right) \quad (2.13)$$

Differentiation of Eq. 2.13 with respect to temperature and equating to zero (when the desorption rate is at maximum,  $\frac{d^2\theta}{dT^2}=0$ ), leads to the following expression (Eq. 2.14), which relates the  $T_p$  (the temperature of the desorption peak),  $\Theta_p$  (the coverage at  $T_p$ ) and the activation energy for desorption  $E_{\text{des}}$  [66, 84]:

$$\frac{E_{\text{des}}}{RT_p^2} = \frac{A}{\beta} * n * \theta_p^{n-1} * \exp\left(\frac{-E_{\text{des}}}{RT_p}\right) \quad (2.14)$$

First order desorption ( $n=1$ ) leads to asymmetric peaks where the position of the desorption peak ( $T_p$ ) is independent of the initial surface coverage. Second order desorption peaks are symmetric, and their position shifts to lower tempera-

tures with increasing initial surface coverage (Eq. 2.14), whereas desorption peaks of  $0 \leq n < 1$  order shift to higher temperatures with increasing initial surface coverage. TPD peaks originating from multilayer desorption for different coverages, do not saturate with increasing coverage and are typically zero order. Zero order desorption peaks for different coverages have the same leading edge at the low temperature region [66, 84].

## 2.5 Low energy electron diffraction (LEED)

The principle and schematic diagram of a LEED system is shown in Fig. 2.15. An electron gun produces a monochromatic electron beam with energy  $E_{\text{beam}}$  between 30 and 500 eV. These electrons are back-scattered after interaction with the sample, pass through four grids and reach the fluorescent screen, where the kinetic energy of the electrons causes light emission. The screen is positive biased to force the acceleration of the electrons towards it. An example of LEED pattern is shown in Fig. 2.16 [66, 84].

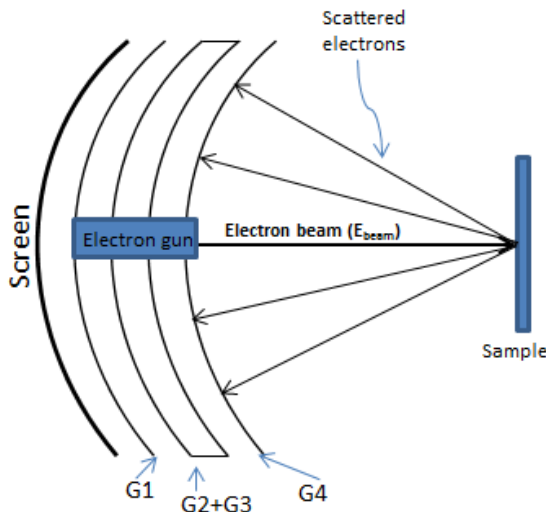


Figure 2.15: Schematic diagram of the LEED system [84].

The G2 and G3 grids act as electron energy filter by applying a retarding negative potential in them ( $-E_{\text{beam}} + \Delta V$ ,  $\Delta V$  is in the magnitude of 0 to 10V), in order to allow only the elastic scattered electrons to travel towards the screen. The inner and outer grid (G1 and G4 respectively) are grounded in order to permit the electrons to pass through a “field free” region. Incident electrons with energy between 20 and 500 eV can travel only 3 or 4 atomic layers below the surface, hence LEED is a surface sensitive technique. The penetration depth of the electrons influences only the intensity of the spots and not the position [66, 84].

The spot position of the diffracted beams allows to reveal information on the periodicity of the surface and to detect and identify superstructures after adsorption of a gas on the surface. The relationship between the real space and reciprocal vectors of the two dimensional (2D) unit cell are shown in Eq. 2.15-2.16 [66, 84]:

$$|\vec{a}_1| = \frac{2\pi}{|\vec{a}_1^*| * \cos\theta_1}; |\vec{a}_2| = \frac{2\pi}{|\vec{a}_2^*| * \cos\theta_2} \quad (2.15)$$

$$\vec{a}_1 \cdot \vec{a}_2^* = \vec{a}_2 \cdot \vec{a}_1^* = 0 \quad (2.16)$$

Where  $\vec{a}_1$  and  $\vec{a}_2$  are the real space lattice vectors of the 2D unit cell,  $\vec{a}_1^*$  and  $\vec{a}_2^*$  are the lattice vectors of the corresponding reciprocal unit cell and  $\theta_1$  and  $\theta_2$  are the  $\angle\vec{a}_1-\vec{a}_1^*$  and  $\angle\vec{a}_2-\vec{a}_2^*$  angles respectively. Eq. 2.15 suggests that small and large distances in real space become large and small, respectively, in the reciprocal space whereas Eq. 2.16 suggests, that the  $\vec{a}_1$  and  $\vec{a}_2$  vectors are perpendicular to the direction of the  $\vec{a}_2^*$  and  $\vec{a}_1^*$  vectors, respectively. The superstructures can be described either by Matrix or Wood notation. The overlayer structure in Wood notation is expressed in the form of:

$$\left( \frac{|\vec{b}_1|}{|\vec{a}_1|} \times \frac{|\vec{b}_2|}{|\vec{a}_2|} \right) R\theta^\circ - A \quad (2.17)$$

Where  $|\vec{a}_1|$  and  $|\vec{a}_2|$  are the magnitudes of the lattice vectors of the unit cell of the substrate,  $|\vec{b}_1|$  and  $|\vec{b}_2|$  are the magnitudes of the lattice vectors of the unit cell of the overlayer and  $\theta$  is the angle between the substrate and the overlayer

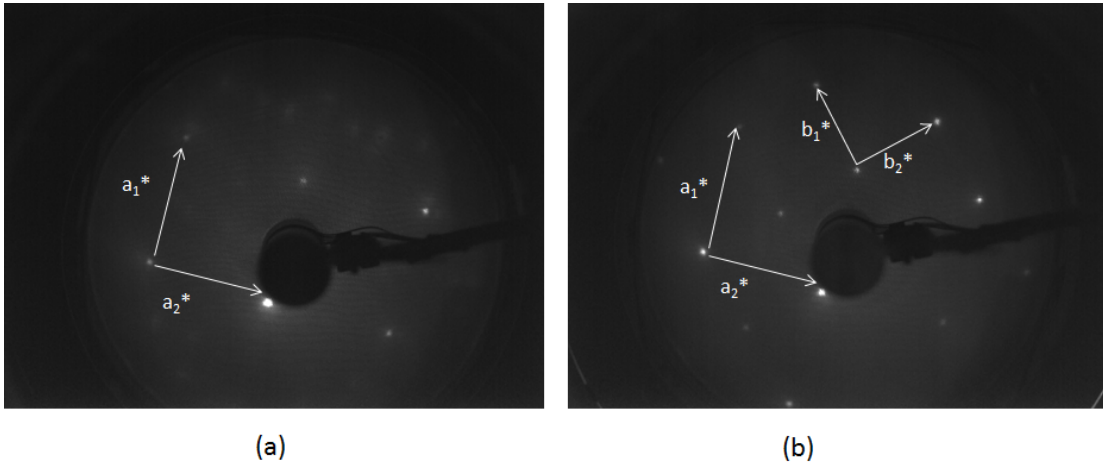


Figure 2.16: (a)1x1 LEED pattern of Ni{100}. (b) c(2 × 2) or  $(\sqrt{2} \times \sqrt{2})R45^\circ$  LEED pattern of an oxygen overlayer, generated upon step annealing the TA<sub>sat</sub>/NiO/Ni{100} layer to 750 K. The LEED patterns were recorded at E<sub>beam</sub>=90 eV.

meshes. If  $\theta=0$  the angle is omitted from the expression. A is the chemical symbol of the surface species and is omitted when expressing a clean substrate. The letter p or c are used to indicate whether the overlayer lattice a is primitive or centred unit cell (absence of symbol means a primitive unit cell). For example the oxygen superstructure on Ni{100}, shown in the LEED pattern in Fig. 2.16b can be either expressed simply as  $c(2 \times 2)$  or  $p(\sqrt{2} \times \sqrt{2})R45^\circ$  [66, 84].

LEED can also provide information on the surface geometry such as bond lengths and angles, by analysing the change in the spot intensity with the beam energy [66, 84].

# Chapter 3

## Interaction of (R,R)-tartaric acid (TA) on clean and oxidised Ni{100} under UHV and ambient pressure (AP) conditions

### Abstract

Enantioselectivity is a key aspect in the field of heterogeneous catalysis, since it can provide products with valuable biological activity. Hydroxy-dicarboxylic acids such as tartaric acid are the most effective chiral modifiers in the enantioselective hydrogenation of  $\beta$ -ketoesters. The present study explores the chemical state, thermal stability and molecular orientation of (R,R)-tartaric acid (TA) on clean and oxidised Ni{100} using X-ray photoelectron spectroscopy (XPS), angle resolved near edge X-ray absorption fine structure (NEXAFS) spectroscopy and low energy electron diffraction (LEED). In addition the chemical state of the molecule was also investigated under elevated pressures of H<sub>2</sub> (up to 6.4 mbar) and H<sub>2</sub>O (up to 10 mbar) using ambient pressure (AP)-XPS. This study provides evidence for the influence of the temperature of the crystal, the dosing rate of the TA molecule and its surface coverage on the formation of TA<sup>2-</sup> and HTA<sup>-</sup> species on the nickel surface. The formation of bitartrate phase of the TA molecule (TA<sup>2-</sup>) which supports an  $\mu_4$  adsorption geometry is favoured as we increase the temperature of the crystal away from room temperature. Cooling the crystal towards room temperature while having high coverages of TA molecule, causes the formation of HTA<sup>-</sup> species (which support an  $\mu_2/\mu_3$  adsorption geometry). High deposition rates (deposition time  $\leq$  24 min/saturated layer) at T < 400 K as

well as the presence of elevated pressures of H<sub>2</sub> and H<sub>2</sub>O also cause the formation of HTA<sup>-</sup> species. Under UHV conditions, TA fully decomposes on Ni{100} at T>440 K. Its thermal stability is further enhanced under the presence of hydrogen (P<sub>H<sub>2</sub></sub> = 6.4 mbar). Deposition of TA onto oxidised Ni{100}, causes the formation of tartrate species whose thermal stability resembles the thermal behaviour of the nickel (II) tartrate complex. Depending on the chemical state, adsorption configuration of the TA molecule, and the substrate (Ni{100} or NiO/Ni{100}), the C=O/COO<sup>-</sup> groups of the TA molecule are tilted by ~ 42-69° with respect to the surface plane of the nickel substrate. The contribution of this study into the understanding of the mechanism of the chiral modification of the nickel catalyst is discussed at the end of the chapter.

### 3.1 Introduction

The pharmaceutical and agrochemical industry has increasing interest in the synthesis of pure enantiopure chemical products since the chirality of a molecule affects the biological activity and response. Moreover, many of these compounds are also used as flavours and fragrances [1–5]. In the area of heterogeneous catalysis enantioselectivity is achieved in several ways, such as attaching a metal to a chiral support or adsorbing a chiral auxiliary to the metal [4]. The chiral modification of the metal can occur either before or during the reaction [4]. The merit of using heterogeneous catalysts in comparison with homogeneous is the fact that these catalysts can be easily separated and recycled, can reduce the presence of metal traces in the product and they can be easily controlled during their use [2, 6]. One great example of a enantioselective catalysed reaction is the hydrogenation of  $\beta$ -ketoesters (such as methyl acetoacetate MAA) using nickel as a catalyst. The reaction generates optically active products, if the catalyst is modified with chiral molecules. These molecules can be either  $\alpha$ -hydroxyacids (such as tartaric acid) or  $\alpha$ -amino acids (such as alanine) [2, 11, 12, 16]. The interaction of tartaric acid on different single crystals was investigated using various surface science techniques, in order to obtain insights into the mechanism of chiral modification and the active sites of the enantioselective reaction. Hydroxy-dicarboxylic acids such as tartaric acid (TA) have been proven to be the the most effective modifiers for hydrogenation of MAA (methyl acetoacetate) to MHB (methyl-3-hydroxybutyrate) [18]. Tartaric acid can exist in three different forms, according to the protonation or not of its two carboxyl groups: neutral biacid form, monotartrate form (one deprotonated carboxyl group) and bitartrate form (both carboxyl groups are

deprotonated) [33].

Lorenzo et al. (1999) [59] and (2002) [60] have investigated the interaction of (R,R)-tartaric acid on Cu{110} as a function of coverage, temperature and time. Adsorption at room temperature causes generation of monotartrate species of the molecule. Increase in temperature ( $T > 400$  K) at low coverages of tartaric acid favours the formation of bitartrate species. Bitartrate species are also formed from monotartrate species, at lower temperatures ( $T = 350$  K) if the system is allowed to relax [59, 60]. In the bitartrate phase, the molecule chemisorbs on the surface via the two carboxylate groups. The C2-C3 bond is found parallel with respect to the surface, with the two C-OH bonds be directed close to the surface normal [59]. According to Ref.[59–61], the bitartrate phase is important for enantioselective catalysis, since at this phase the molecule creates arrays of ordered layers and 2D supramolecular assemblies on the Cu{110} surface, which break the symmetry of the crystal. In addition, this phase is the only one that can accommodate spatially the pro-chiral reactant (MAA) [60]. The induced chirality is mirrored upon adsorbing the other enantiomer ((S,S)-tartaric acid) [61] on the Cu{110} surface. The chirality of the molecule and its rigid bitartrate adsorption geometry on the surface forbids the generation of any reflectional domains on the surface. In addition the C2 space group of the chiral unit mesh of the molecule (created by the supramolecular assembly of the adsorbed bitartrate units) which matches with the C2 rotational symmetry of the surface, ensures the transfer of a single, two dimensional, chirality to the whole range of the surface [59–61]. The interaction of tartaric acid on Cu{110} was compared with the achiral succinic acid. The molecular structure of succinic acid contains hydrogens attached to C2 and C3 carbon atom instead of hydroxyls [97, 98]. As in the case of tartaric acid, succinic acid forms a trimer chain structure with chiral motif which produces a 2D molecular assembly, originating either from molecular distortion or/and local chiral reconstruction. This implies that the generation of these structures are determined by the molecule-metal bonding and not the molecular structure of the adsorbate. The growth initiates by chiral nucleation points and not randomly. This nucleation point governs the chirality. In the case of succinic acid however, this chirality is expressed only locally, since its achiral nature will generate both chiral nucleation points with equal probability producing a racemic conglomerate on the surface [97, 98].

The adsorption of (R,R) tartaric acid on Ni{110} was studied using a combination of experimental techniques (RAIRS and STM), and theoretical calculations (DFT)[33–35]. Similar to Cu{110}, the chemical state of the TA molecule on the Ni{110} [33] changes as a function of temperature and coverage. According

to Ref.[33], tartaric acid is present, in the multilayer, in its biacid form regardless from the adsorption temperature. At 90-120 K, tartaric acid is in its biacid form at all coverages. Adsorption at higher temperatures (170-270 K) causes chemisorption of tartaric acid through the one deprotonated carboxyl group. At these temperatures, tartaric acid is presented in its monotartrate form. The other protonated carboxyl group is directed outside the surface plane, presenting also hydrogen bonding interactions. Above room temperature, tartaric acid exists in two forms up to the saturation coverage: at lower coverages it is found in its bitartrate form and at higher coverages tartaric acid is converted to its monotartrate form. The bitartrate phase does not present any ordered overlayers [33]. In the bitartrate form [34], tartaric acid is bound to 4 nickel atoms, with the oxygen atoms of the two corresponded carboxylate groups positioned above the Ni atoms, in a short bridge site. Based on DFT calculations, this geometrical orientation of the molecule, causes relaxation and reconstruction of the nickel surface, resulting in chiral footprint on the surface. Calculations propose that one chiral footprint is preferred energetically over the other suggesting that at room temperature the same mirror motif will be expected to dominate the surface by 90% ensuring the creation of an enantiospecific system [34]. Studies of the electronic structure of the (R,R) tartaric acid on Ni{110} system [35], showed that bitartrate tartaric acid in the gas phase presents an intrinsic chirality not only in terms of atomic arrangement but also in its electronic structure, due to the uneven charge distribution between the four oxygen atoms of the two carboxylate groups which is transferred to the Ni-O bonds and by extension to all the nickel surface through the bonds between the nickel atoms [35]. Temperature-dependent behaviour on the formation of either the monotartrate and bitartrate form was also observed upon adsorbing (R,R) tartaric acid on Ni{111} [36]. The former structure is more stable at 300 K, where the latter is favoured at 350 K. On this facet, tartaric acid forms ordered layers however to a lesser extent in comparison with the Cu{110} surface [36]. Co-adsorption of (R,R)-tartaric acid and MAA on Ni{111} produced two ordered arrays with 0.113 ML (one tartrate and one MAA molecules per unit cell) and 0.167 ML (one tartrate and two MAA molecule per unit cell) local coverage [37]. According to Ref.[37], in the low coverage structure, the hydrogenation will be enantiospecific and generate the R-product in excess whereas the high coverage structure will produce a racemic mixture of products [37]. Modification of Ni{111} with a solution of (R,R)-tartaric acid [38] show evidence of generation of nickel tartrate species on the Ni{111} surface at low modifying pH and nickel and sodium tartrate species at higher pH. The formation of these salt species points to a widespread etching of the nickel crystal. The etching of the surface is believed

to cause the chiral modification of the surface, since it creates step-kink sites. A large quantity of the adsorbed species is removed from the surface, after washing it with water [38]. The remaining coverage is important for the chiral modification of the surface, since as it was shown in previous studies [37], high coverages of modifiers forbid the interaction of MAA with the nickel surface, while absence of modifiers generates product without optical activity. Since this quantity depends on the pH and modification temperature, the pH of the tartaric acid solution controls the enantioselectivity of the surface by controlling the coverage of the modifier [38]. Modification of Ni{111} with (R,R)-tartaric acid from solution at 350 K (which according to Ref.[37, 38] is the optimum modification temperature for attaining the highest enantioselectivity using TA as modifier) following washing of the catalyst, caused generation of HTA<sup>-</sup> species on the nickel surface [38]. Subsequent immersion of the crystal in a MAA solution caused enhancement of the diketone/enol ratio of MAA substrate with respect to the modification at 300 K [38]. According to Ref.[38] the origin of the enantioselectivity of this system might be due to the formation of hydrogen bonds between the diketone and the HTA<sup>-</sup> species, in orientation that will preferably generate the R-enantiomer as a product during the hydrogenation reaction. Sodium bromide, on the other hand does not affect the RAIRS spectra of tartaric acid at 350 K modification temperature, whereas at 300 K, it enhances the diketo-enol form, thus increasing the enantioselectivity [38].

In this chapter we will explore the chemical state, molecular orientation and thermal stability of tartaric acid on clean and oxidised Ni{100} as a function of coverage and temperature using XPS and angle-dependent NEXAFS. Interaction of tartaric acid on oxidised Ni{111} [39], provided evidence of the formation of species similar to nickel tartrate, which might assist the etching and the generation of chiral surfaces. In addition, for approaching more realistic conditions, we have studied the interaction of tartaric on Ni{100} under elevated pressures of H<sub>2</sub> (up to 6.4 mbar) and H<sub>2</sub>O (up to 10 mbar) using AP-XPS. The elevated H<sub>2</sub> pressures are used to mimic the reactions conditions and H<sub>2</sub>O is one of the typical modifying solvents [24]. All the data were analysed by the author. The experimental data were collected by the author, by Dr. Chanan Euaruksakul (University of Reading), by Dr. Rachel Price (University of Reading), by Prof. Georg Held (University of Reading) and by Alex Large (University of Reading). The overall contribution of the author to this study is ~ 80% of the total work.

## 3.2 Experimental Methods

The experiments were performed in three different UHV chambers. The UHV experiments were performed in the BESSY II synchrotron in Berlin (Germany) and in the MAX-Lab synchrotron in Lund (Sweden) in the UHV endstations of the HE-SGM and D1011 beamlines, respectively. The X-rays were linear polarized with the  $\vec{E}$  vector in the horizontal plane. The ambient pressure experiments took place in the near-ambient pressure XPS (NAP-XPS) facility in the University of Manchester using Al  $K_\alpha$  anode ( $h\nu=1486.7$  eV) as an X-ray source. The base pressure of all three chambers was between  $10^{-10}$  and  $10^{-9}$  mbar. Sample cleaning was achieved by cycles of sputtering or oxygen treatment at room temperature with subsequent annealing, or by annealing and cooling in oxygen atmosphere followed by annealing. Sample cleaning was confirmed by XPS and LEED.

The dosing and the sputtering occurred in preparation chambers. The XPS and NEXAFS experiments were performed in an analysis chamber. The XPS experiments were performed using a Scienta analyser in the HE-SGM and D1011 endstations and a SPECS system in the NAP-XPS facility in the University of Manchester. During the NAP-XPS experiments the sample was mounted inside a NAP-cell which was docked into the analyser. With this configuration the pressure inside the analysis chamber did not change significantly during the exposure of the crystal to high pressures. The temperature was measured using a thermocouple fixed either on the sample (D1011 and NAP-XPS facility/elevated  $H_2$  pressures experiments) or on the sample holder (HE-SGM and NAP-XPS facility/elevated  $H_2O$  pressures experiments) and heated resistively or via an e-beam heater. (R,R)-tartaric acid (L-(+)-tartaric acid) was dosed from a home built evaporator which was mounted on the chamber through a gate valve. The evaporator consisted of a stainless steel crucible containing a glass tube filled with TA powder. Deposition of the TA molecule was performed by resistively heating the crucibles to 400-423 K and opening the gate valve to the chamber. The measurement of the temperature was achieved by K-type thermocouples spot-welded on the crucibles. This configuration led to deposition times of  $\sim 60$ -150 min/saturated layer for the clean substrate (Ni{100}) and  $\sim 130$ -145 min/saturated layer for the oxidised Ni{100}. Higher deposition rates of the molecule were achieved by moving the evaporator closer to the sample using a small diameter tube which was mounted in the base of the evaporator. This configuration was provided by the HE-SGM beamline and led to deposition times of  $<23$  min/saturated layer (referred in the text as “high deposition rate”).

The XP-spectra were obtained in the C 1s and O 1s region. In the synchrotron experiments the spectra were obtained using  $h\nu=400$  eV and  $h\nu=650$  eV as photon energies, respectively, and 50 eV as pass energy. In order to calibrate the the offset of the binding energy axis, we have also acquired spectra of the Fermi edge every time the monochromator was moved. For some C 1s spectra (obtained in the D1011 endstation), we have used the average value of the lowest and the largest offset observed during the beamtime, for calibrating the binding energy axis, since we did not have available spectra of the Fermi edge. In the ambient pressure experiments the spectra were acquired using 30 eV as pass energy. The offset of the binding energy was calibrated using the Ni 2p peak (BE=852.7 eV). For quantitative analysis the spectra were normalised at the low binding region followed by linear subtraction of the background. The instrumental resolution (beamline and analyser) was  $\sim 0.2-0.3$  eV ( $h\nu=400$  eV) and  $\sim 0.6-0.7$  eV ( $h\nu=650$  eV) in the HE-SGM beamline,  $\sim 0.2-0.3$  eV ( $h\nu=400$  eV) and  $\sim 0.4-0.5$  eV ( $h\nu=650$  eV) in D1011 beamline and  $\sim 0.4$  eV in the NAP-XPS facility.

The NEXAFS spectra were obtained in the C K-edge and O K-edge region using the partial electron yield mode by applying a retarding voltage in front of the electron detector. The O K-edge spectra were obtained by applying 0.4 kV (HE-SGM beamline) and 0.25 kV (D1011 beamline) as retarding voltage. The NEXAFS in the C K-edge region in both beamlines, were acquired using 0.15 kV as retarding voltage. For determining the molecular orientation of the tartaric acid on Ni{100} we have obtained angle dependent NEXAFS. Three angle of incidence were used in the HE-SGM beamline:  $\theta=0^\circ$  (normal incidence),  $\theta=35^\circ$  and  $\theta=60^\circ$ , and four angles in the D1011 beamline:  $\theta=0^\circ$  (normal incidence),  $\theta=20^\circ$ ,  $\theta=40^\circ$  and  $\theta=60^\circ$ , where  $\theta$  refers to the angle between the electric field vector and the surface plane. Spectra of the clean surface were also obtained for the purpose of background subtraction. Initially, all the spectra were normalised in the low photon energy region. After background subtraction the spectra were normalised with respect to the  $I_0$  spectra (transmission of the beamline as a function of energy). The latter spectra were acquired either by measuring the partial electron yield of a clean gold sample (HE-SGM beamline) or by measuring the drain current of a gold mesh in the back chamber of the D1011 beamline. Finally the spectra were also normalised with respect to the step height, at energies above all oxygen and carbon absorption resonances.

## 3.3 Results

### 3.3.1 Tartaric acid on clean Ni{100}/UHV

#### XPS Results

Figure 3.2 shows top-up XP-spectra of tartaric acid (TA) on Ni{100} in the C 1s and O 1s region at two different dosing temperatures: 303-304 K (Fig. 3.2a-3.2b) and 310-350 K (Fig. 3.2c-3.2d). The coverages were adjusted by varying the dosing time. In both cases the signal of tartaric acid was saturated. The coverages shown are based on the fitted XPS area of the saturated signal of tartaric acid in the O 1s region. Carbon and oxygen impurities were present on the surface before dosing. The XPS area (obtained upon fitting) of the oxygen impurities were  $\sim 6\%$  (Fig. 3.2b) and  $\sim 2\%$  (Fig. 3.2d) of the XPS area (obtained upon fitting) of the corresponded saturated signal of TA in the O 1s spectrum in Fig. 3.2b and Fig. 3.2d, respectively. The fitted XPS area of the carbon impurities were  $\sim 40\%$  (Fig. 3.2a) and  $\sim 14\%$  (Fig. 3.2c) of the fitted XPS area of the corresponded saturated signal of TA (excluding impurities) in the C 1s spectrum in Fig. 3.2a and Fig. 3.2c.

The O 1s spectrum in the submonolayer regime (79% sat) at 303-304 K (Fig. 3.2b) can be fitted by three peaks at 531.6 eV, 532.9 eV and 534.8 eV. The low binding energy peak is assigned to oxygen atoms of the carboxyl group chemisorbed on the nickel surface ( $\text{COO}^-/\text{COOH}$ , Fig. 3.1) [46, 69]. The peak at 532.9 eV is attributed to oxygen atoms dangling from the surface (either oxygen atoms from hydroxyl groups,  $\text{COH}$  or oxygen atoms belonging to the protonated carboxyl group,  $\text{COOH}/\text{COOH}$ ). The high binding energy peak accounts for approximately 5-6% of the XPS signal area in both coverages (Fig. 3.2b). This peak was also observed in the case of tartaric acid on Cu{531} [99] and it was assigned to either oxygen atoms of the carboxyl groups with high degree of protonation or to a satellite peak. The former effect could probably explain this feature, since work on the interaction of tartaric acid on Cu{110}[59], on Ni{110} [33] and Ni{111}[36], show that the molecule can form intermolecular hydrogen bonds between the non chemisorbed moieties of the molecule (hydroxyls or carboxyl groups), where sometimes these molecules can even form dimers and supramolecular assemblies. The ratio of the area of the low binding energy peak (corresponding to the chemisorbed oxygen atoms of the carboxyl group of the TA molecule) and the sum of the areas of the two high binding energy peaks, which correspond to the non chemisorbed oxygen atoms of the TA molecule ( $\frac{[\text{COO}^- + \text{COOH}(\text{ads})]}{[\text{COOH} + \text{COOH} + \text{COH}(\text{nonads})]}$ ) is  $\sim 1.8:1$  (O 1s

spectrum in Fig. 3.2b). With the error margin caused by photoelectron diffraction and attenuation effects, this would suggest, that in the submonolayer regime, the oxygen atoms of the carboxyl groups of the tartaric acid molecule are deprotonated ( $\text{TA}^{2-}$ ) and chemisorbed on the nickel surface in a bitartrate/ $\mu_4$  geometry (Fig. 3.1). Increasing the coverage to saturation (O 1s spectrum in Fig. 3.2b), causes decrease in the aforementioned ratio to 1.3:1. In the saturated layer, TA accommodates a geometry closer to tridentate (3-point adsorption geometry or  $\mu_3$ ), where one of the oxygen of one of the carboxyl groups is protonated and dangling from the surface ( $\text{HTA}^-$ , Fig. 3.1). There is a possibility that at this coverage we find coexistence of bitartrate ( $\mu_4$ ) and monotartrate ( $\mu_2$ ) phases, which spectroscopically will be equivalent to a molecule, with  $\mu_3$  adsorption geometry (Fig. 3.1). In the monotartrate phase, TA chemisorbs on the nickel surface through one of its deprotonated carboxyl groups whereas the other carboxyl group remains protonated and dangling from the surface (Fig. 3.1). In any case, increasing the

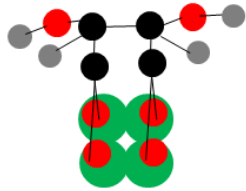
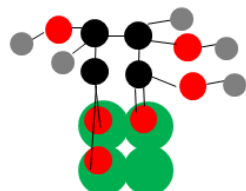
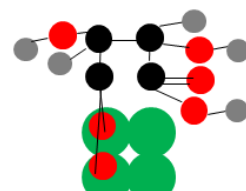
Adsorption geometry	Chemical state	Expected area ratio XPS (O 1s) $\frac{[\text{COO}^- + \text{COOH}(\text{ads})]}{[\text{COOH} + \text{COOH} + \text{COH}(\text{non ads})]}$
 <p><b>Tetradentate Bitartrate <math>\mu_4</math></b></p>	$\cdot\text{OOC-CH(OH)CH(OH)-COO}\cdot$ $\text{TA}^{2-}$	2:1
 <p><b>Tridentate <math>\mu_3</math></b></p>	$\cdot\text{OOC-CH(OH)CH(OH)-COOH}$ $\text{HTA}^-$	1:1
 <p><b>Bidentate Monotartrate <math>\mu_2</math></b></p>	$\cdot\text{OOC-CH(OH)CH(OH)-COOH}$ $\text{HTA}^-$	1:2

Figure 3.1: The three possible chemical states of the chemisorbed (R,R)-tartaric acid on Ni{100} surface with their corresponding adsorption geometries and the expected XPS area ratio in the O 1s region, of the low binding energy peak (corresponding to the chemisorbed oxygen atoms of the carboxyl group of the TA molecule) and the sum of the areas of the two high binding energy peaks, which correspond to the non chemisorbed oxygen atoms of the TA molecule ( $\frac{[\text{COO}^- + \text{COOH}(\text{ads})]}{[\text{COOH} + \text{COOH} + \text{COH}(\text{nonads})]}$ ). The black circles are carbon atoms, the red circles are oxygen atoms, the grey circles are hydrogen atoms and green circles are nickel atoms.

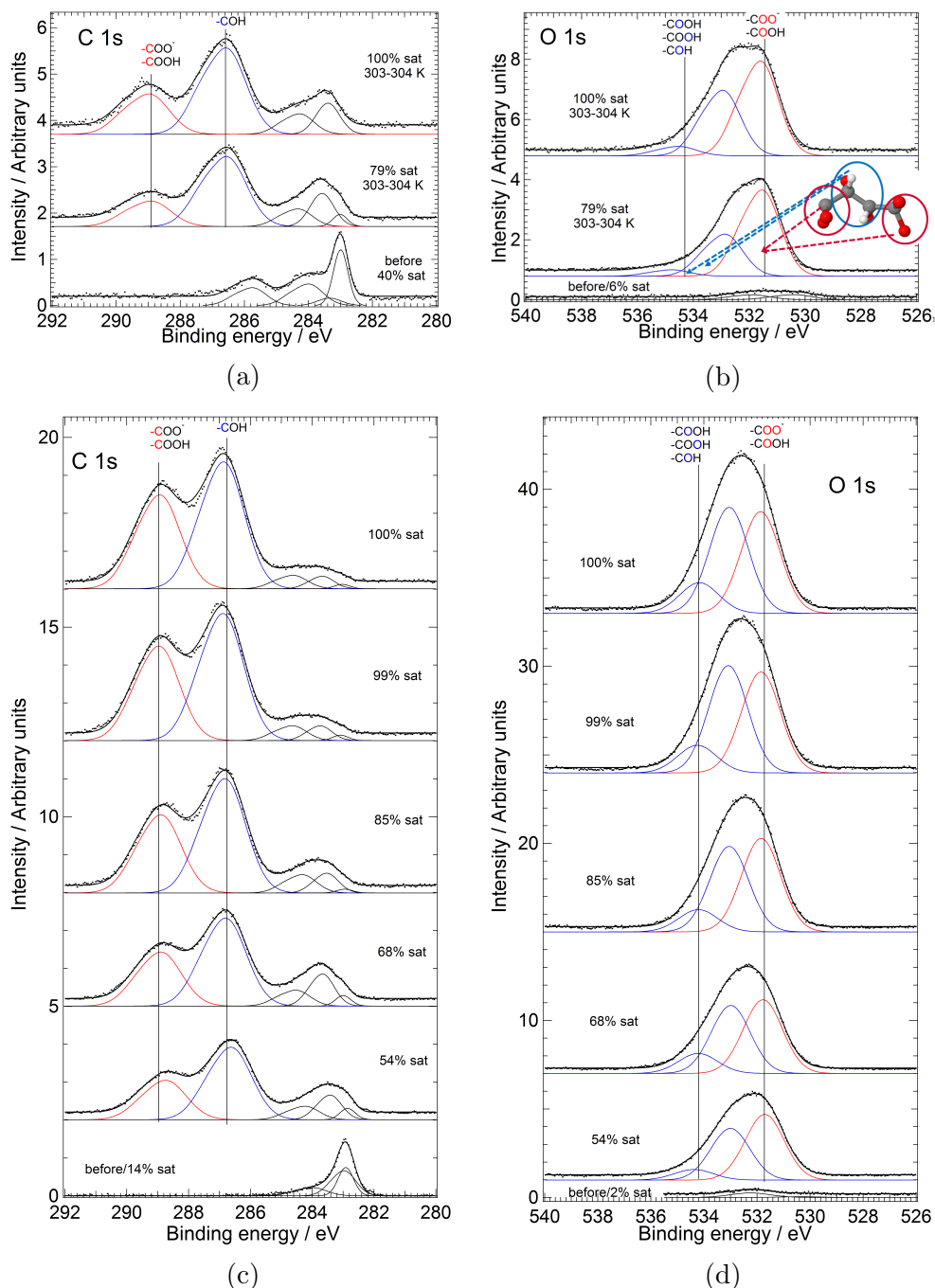


Figure 3.2: Top-up XP-spectra of (R,R)-tartaric acid (TA) on Ni{100} in (a+c) C 1s region ( $h\nu=400$  eV) and (b+d) O 1s region ( $h\nu=650$  eV). Top panel, dosing conditions (D1011 beamline):  $T_{\text{sample}} \approx 303\text{-}304$  K,  $T_{\text{evaporator}} \approx 403\text{-}404$  K,  $P_{\text{base}} \approx 2 \times 10^{-10}\text{-}1 \times 10^{-9}$  mbar,  $P_{\text{dosing}} \approx 5 \times 10^{-9}\text{-}1 \times 10^{-8}$  mbar, Deposition time  $\approx 60\text{-}150$  min/saturated layer. Bottom panel, dosing conditions (HE-SGM beamline, higher deposition rate):  $T_{\text{sample}} \approx 310\text{-}350$  K,  $T_{\text{evaporator}} \approx 402\text{-}403$  K,  $P_{\text{dosing}} \approx 1 \times 10^{-8}\text{-}7 \times 10^{-8}$  mbar, Deposition time  $\approx 23$  min/saturated layer. The black thick dots are the raw spectra and the black thick lines are the fitted curves. The solid coloured curves are the individual peaks.

coverage of the TA molecule on the nickel surface, increases the  $\text{HTA}^-:\text{TA}^{2-}$  ratio on the nickel surface. This is consistent with what was found in previous studies on Cu{110} [59] on Ni{110} [33], on Ni{111} [36] and on Pd{111} [100], where higher coverages trigger the formation of monotartrate species induced by the molecular crowding of the surface [100]. The high binding energy peak shifts towards lower binding energies (534.5 eV), suggesting weaker hydrogen bonding at this conformation of the molecule. In the C 1s region (Fig. 3.2a), (saturated layer) we can observe 4 peaks at 283.4 eV, 284.3 eV, 286.6 eV and 289.0 eV whereas in the submonolayer regime (79% sat) we can observe another peak at 283.0 eV. It is worth noting that the binding energy axis in the submonolayer regime (79% sat) is highly inaccurate since we did not have available spectra of the Fermi edge. Calibration of the binding energy axis was performed by using the average value of the lowest and the largest offset observed during the beamtime. The three low binding energy peaks are associated with decomposition products. The peak at 283.0 eV was previously assigned to carbidic/surface carbon [101, 102]. The peaks at 283.4 eV and 284.3 eV were observed upon adsorbing alanine on Ni{111} [46]. The peak at 283.4 eV is related to either atomic carbon/nickel carbide [46, 103] and/or allylic carbon [102] and the peak at 284.3 eV is associated with  $\text{sp}^2(-\text{C}=\text{C}-)$ /graphitic carbon [46, 103]. The peak at 286.6 eV is assigned to the carbon attached to hydroxyl group (COH) and the high binding energy peak to the convoluted signal of  $\text{COO}^-/\text{COOH}$  species. The ratio of the area of the low binding energy peak in the C 1s region (286.6 eV) and area of the high binding energy peak (289.0 eV) is close to 2.7:1 in the submonolayer regime, and decreases to 2.1:1 in the saturated coverage. Based on the atomic stoichiometry of the molecule, we should expect 1:1 area ratio between those peaks, however photoelectric diffraction and attenuation effects could influence the ratio of these peaks, especially in the submonolayer regime, where the tartaric acid adsorbs in a bitartrate geometry ( $\mu_4$ ).

Dosing TA at 310-350 K and higher deposition rate, causes a decrease (with respect to the spectra in Fig. 3.2a-3.2b) in the ratio of the area of the low binding energy peak and the sum of the areas of the two high binding energy peaks ( $\frac{[\text{COO}^-+\text{COOH}(\text{ads})]}{[\text{COOH}+\text{COOH}+\text{COH}(\text{nomads})]}$ ), O 1s spectra in Fig. 3.2d) especially close to the saturation coverage ( $\sim 1.1:1$  at 54% sat and  $\sim 0.7:1$  in the saturated layer). In the saturated layer, TA is found predominantly in its  $\text{HTA}^-$  form supporting an  $\mu_2$  (monotartrate)/ $\mu_3$  adsorption configuration (Fig. 3.1). We might also expect the presence on the surface (in minority) of some bitartrate phases (Fig. 3.1). The two low binding energy peaks (O 1s spectrum in Fig. 3.2d) are found at 531.7 eV and 533.0 eV at 54% saturation coverage. The low binding energy peak shifts

to 531.9 eV in the saturated layer. Similar feature is also observed in the C 1s region (Fig. 3.2c), where the peak associated with COH is found at 286.6 eV (54% sat) and shifts to 286.9 eV in the saturated layer, and the peak associated with COO<sup>-</sup>/COOH is found at 288.7 eV at 54% coverage and at 288.9 eV in the saturated layer. The area ratio of the aforementioned peaks ( $\frac{[COH]}{[COO^-/COOH]}$ ) is  $\sim 1.8:1$  at 54% sat and 1.3:1 at the saturation coverage. The latter ratio is very close to the expected ratio based on the atomic stoichiometry of the molecule. It is very likely that at this molecular configuration, the attenuation effects are less significant, since one of the carboxyl groups is dangling from the surface. The increased HTA<sup>-</sup>:TA<sup>2-</sup> ratio in the saturated layer in Fig. 3.2c-3.2d with respect to the saturated layer in Fig. 3.2a-3.2b can be explained by the higher deposition rate of the molecule, rather than the dosing temperature. For example, on Cu{110}, the generation of the bitartrate phase at 350 K [60] is only facile in the early stages of adsorption (only in the presence of small island of molecules) since it involves increase in the adsorption area. In addition this conversion is time dependent [60]. The high deposition rate of TA causes the creation of larger islands whose large adsorption area could not induce the formation of bitartate species (even at coverages below saturation) as in the case of the O 1s spectrum in Figure 3.2b (bottom panel). The high binding energy peak in the O 1s spectra in Fig. 3.2d (which accounts  $\sim 8-13\%$  of the XPS signal) is found at 534.4 eV at 54% sat coverage and shifts to 534.2 eV in the saturated layer in line with the O 1s spectra in Fig. 3.2b.

Figure 3.3 shows step annealed XP-spectra in the C 1s and O 1s region upon dosing TA at 303-304 K (Deposition time $\approx$ 75-90 min/saturated layer, Fig. 3.3a-3.3b) and 298 K (Deposition time $<$ 10 min/saturated layer, Fig. 3.3c-3.3d). In the former dosing conditions, the coverage of TA on Ni{100} is saturated, chemisorbing on the nickel surface in an average of a  $\mu_3$  adsorption geometry (O 1s spectrum in Fig. 3.2a and C 1s spectrum in Fig. 3.2b). The latter conditions (Fig. 3.3c-3.3d), triggered the formation of multilayers, so thick that they attenuate the signal of the Fermi edge (results not shown). Figures 3.4a and 3.4b show the temperature dependence on the area of the low binding energy peak (COO<sup>-</sup>/COOH) and the sum of two high binding energy peaks (COOH/COOH/COH) in the O 1s region obtained from the O 1s spectra in Fig. 3.3b and 3.3d, respectively. Figure 3.4c compares the temperature dependence on the area ratio of the aforementioned signals ( $\frac{[COO^-+COOH(ads)]}{[COOH+COOH+COH(nonads)]}$ ) between the areas shown in Fig. 3.4a and Fig. 3.4b. Carbon and oxygen impurities were present on the surface before dosing. The XPS area (obtained upon fitting) of the oxygen impurities were  $\sim 6\%$  (Fig. 3.3b) and  $\sim 11\%$  (Fig. 3.3d) of the XPS area (obtained upon fitting)

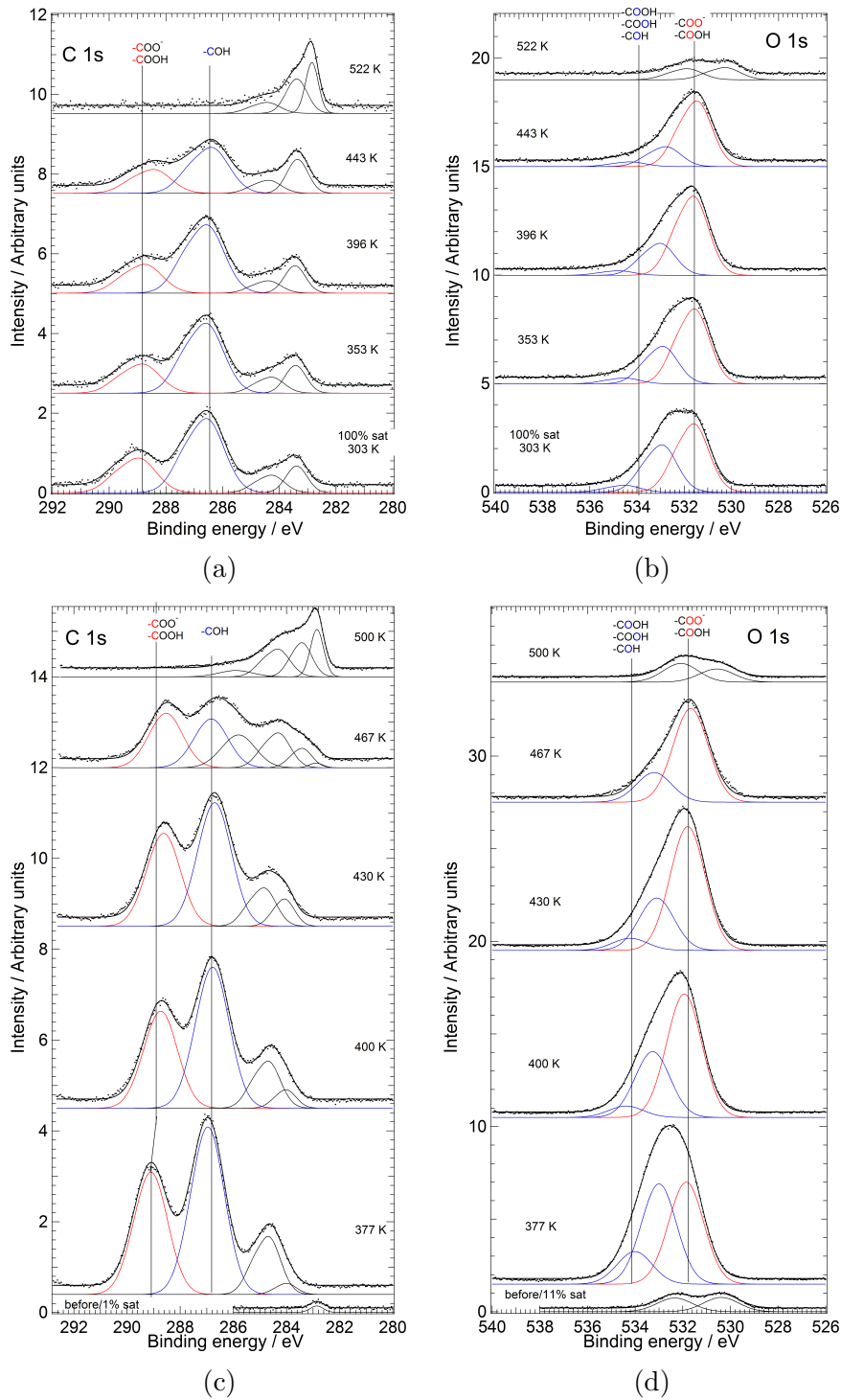


Figure 3.3: Step anneal XP-spectra of (R,R)-tartaric acid (TA) on Ni{100} in (a+c) C 1s region ( $h\nu=400$  eV) and (b+d) O 1s region ( $h\nu=650$  eV). Top panel, dosing conditions (D1011 beamline):  $T_{\text{sample}} \approx 303\text{-}304$  K,  $T_{\text{evaporator}} \approx 403\text{-}404$  K,  $P_{\text{base}} \approx 2 \times 10^{-10}\text{-}1 \times 10^{-9}$  mbar,  $P_{\text{dosing}} \approx 5 \times 10^{-9}\text{-}1 \times 10^{-8}$  mbar, Deposition time  $\approx 60\text{-}150$  min/saturated layer. Bottom panel, dosing conditions (HE-SGM beamline, higher arrival rate):  $T_{\text{sample}} \approx 298$  K,  $T_{\text{evaporator}} \approx 423$  K,  $P_{\text{dosing}} \approx 4 \times 10^{-8}$  mbar, Deposition time  $< 10$  min/saturated layer. The black thick dots are the raw spectra and the black thick lines are the fitted curves. The solid coloured curves are the individual peaks.

of the corresponded saturated signal of TA in the O 1s spectrum in Fig. 3.2b and Fig. 3.2d, respectively. The fitted XPS area of the carbon impurities were  $\sim 40\%$  (Fig. 3.3a) and  $\sim 1\%$  (Fig. 3.3c) of the fitted XPS area of the corresponded saturated signal of TA (excluding impurities) in the C 1s spectrum in Fig. 3.2a and Fig. 3.2c, respectively.

Heating the saturated layer (Fig. 3.3a-3.3b) to 353 K and 396 K caused increase in the area ratio ( $\frac{[COO^-+COOH(ads)]}{[COOH+COOH+COH(nonads)]}$ ) in the O 1s spectra in Fig. 3.3a from 1.3:1 to 1.7:1 and 2.2:1, respectively (Fig. 3.4a and Fig. 3.4c). The XPS total area in O 1s and C 1s region does not change, significantly (96% and 94% of the saturated signal, respectively). This effect suggests, that heating the sample at this temperature causes deprotonation of the HTA<sup>-</sup> species converting their configuration to a bitartrate ( $\mu_4$ , (Fig. 3.1)). According to previous work [59, 60], the conversion of the monotartrate phase to the bitartrate has a significant kinetic barrier, which in our study is probably overcome by the annealing. In addition, heating to 396 K causes a shift of the high binding energy peak in the O 1s region from 534.5 eV to 534.8 eV. This effect was also observed, reversibly by changing from the submonolayer to saturated regime in the O 1s spectra in Fig. 3.2b, and implies stronger hydrogen bonds when the molecule chemisorbs in its bitartrate ( $\mu_4$ ) conformation with respect HTA<sup>-</sup> chemical state of the molecule.

Heating the multilayer to 377 K causes desorption of most of the multilayer features. (Fig. 3.3c-3.3d). In the C 1s region (Fig. 3.3c) we can observe 4 peaks at 284.0 eV, 284.7 eV, 287.0 eV and 289.1 eV and 3 peaks in the O 1s region (Fig. 3.3d) at 531.9 eV, 533.0 eV and 534.0 eV. It is worth noting that the shape of the peaks associated with the intact TA molecule in the C 1s region in Fig. 3.3c differ from the C 1s spectra in Fig. 3.2c. The area ratio ( $\frac{[COO^-+COOH(ads)]}{[COOH+COOH+COH(nonads)]}$ ) in the O 1s spectrum in Fig. 3.3d is  $\sim 0.8:1$  (Fig. 3.4b-3.4c) suggesting the same conformation/chemical state of TA as it was found in the saturated layer in Figures 3.2c-3.2d (HTA<sup>-</sup> chemical state supporting an  $\mu_2$  (monotartrate)/ $\mu_3$  adsorption configuration, Fig. 3.1). The coverage at this temperature is 94% of the saturated layer in Figures 3.2c-3.2d. Further heating to 400 K (Fig. 3.3c-3.3d), causes increase in the area ratio ( $\frac{[COO^-+COOH(ads)]}{[COOH+COOH+COH(nonads)]}$ ) in the O 1s spectrum in Fig. 3.3d to 1.6:1 (Fig. 3.4b-3.4c), causing the transition of the molecule towards more  $\mu_4$  adsorption configuration (Fig. 3.1). The peak at 534 eV shifts to 534.4 eV in line with the O 1s spectra in Figure 3.3b. The area percentage of the aforementioned peak (with respect to to the total XPS area) drops from 14% to 6%. The coverage at this temperature is 81% of the saturated layer.

Heating the saturated layer to 443 K (Fig. 3.3a-3.3b) causes significant loss in the XPS signal in both regions ( $\Theta_{TA}=74\%$  sat). All the peaks associated with TA

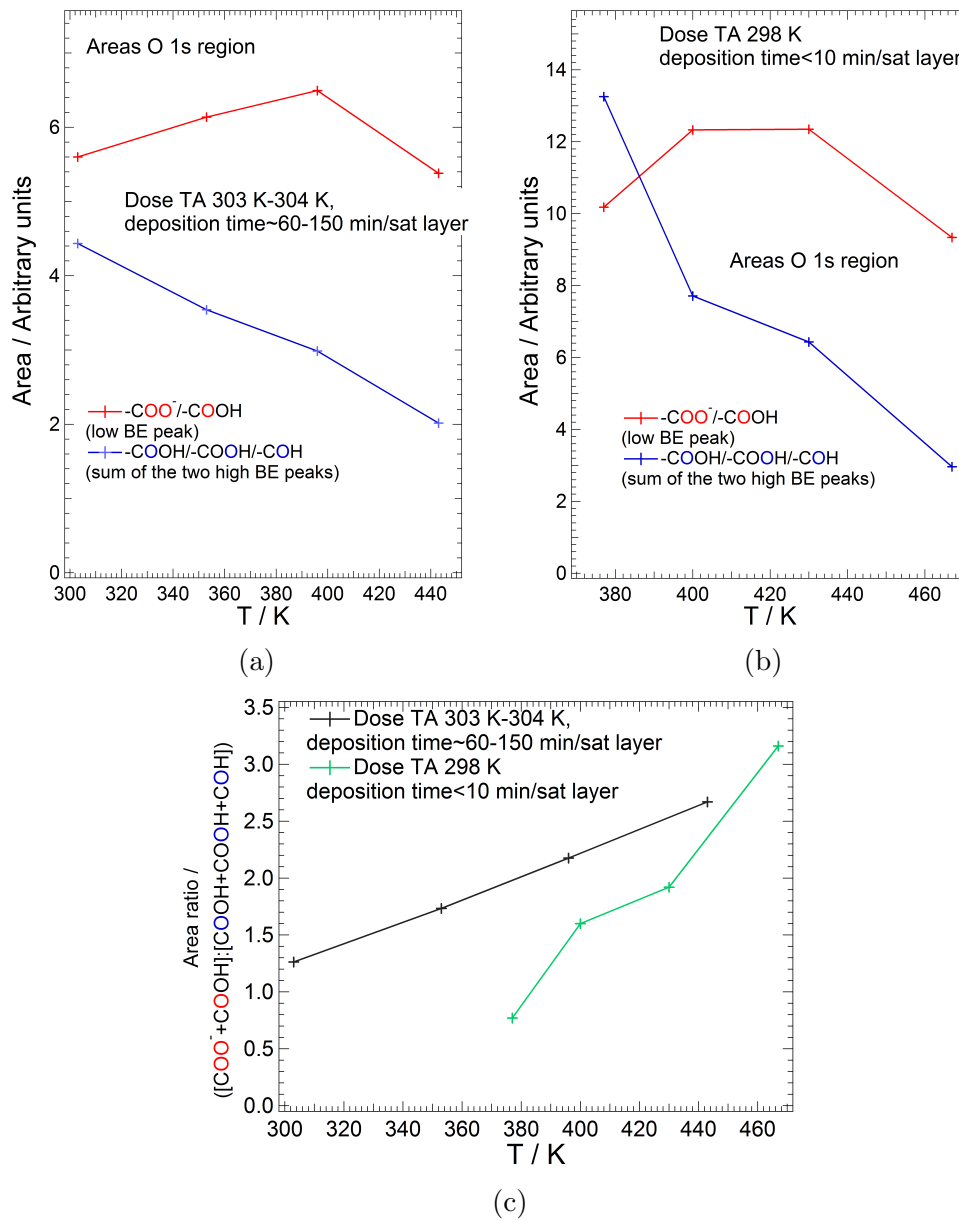


Figure 3.4: (a+b) Areas profiles as function of temperature obtained from the O 1s spectra in Figures (a) 3.3b and (b) 3.3d. (c) Area ratio of the peaks shown in Figures 3.4a and 3.4b as a function of temperature.

shift to lower binding energies, confirming the decrease in the coverage of tartaric molecules on the nickel surface. The area ratio ( $\frac{[COO^-+COOH(ads)]}{[COOH+COOH+COH(nonads)]}$ ) in the O 1s spectrum in Fig. 3.3b at this temperature increases to 2.7:1 (Fig. 3.4a and Fig. 3.4c). Heating the multilayer to 430 K (Fig. 3.3c-3.3d) causes a slight decrease in the XPS signal area with respect to the spectrum at T=400 K ( $\Theta_{TA}=76\%$  sat) but increase in the area ratio ( $\frac{[COO^-+COOH(ads)]}{[COOH+COOH+COH(nonads)]}$ ) in the O 1s spectrum in Fig. 3.3d to 1.9:1 (Fig. 3.4b-3.4c). Significant changes are observed upon annealing to 467 K. In particular we can observe the generation of decomposition species in the C 1s region (Fig. 3.3c) at 282.9 eV and 285.8 eV, the latter been assigned to CO species. The area ratio ( $\frac{[COO^-+COOH(ads)]}{[COOH+COOH+COH(nonads)]}$ ) in the O 1s spectrum in Fig. 3.3d at this temperature is close to 3.2:1 (Fig. 3.4b-3.4c), which might be explained by also the presence of decomposition species on the surface. Heating the saturated layer 522 K (Fig. 3.3a-3.3b) and the multilayer to 500 K (Fig. 3.3c-3.3d), triggers the full decomposition of the molecule leaving only dissociation products on the surface.

## NEXAFS Results

Figure 3.5 shows angle resolved NEXAFS in the C K-edge and O K-edge region obtained in the HE-SGM beamline upon dosing TA onto Ni{100} at 310-350 K to 85% saturation (Fig. 3.5a-3.5b) and upon dosing TA onto Ni{100} at 298 K to multilayer regime and anneal the layer to 377 K to 94% saturation (Fig. 3.5c-3.5d). According to the O 1s spectra in Fig. 3.2d and Fig. 3.3d (which present the corresponding O 1s XP-spectra of the two aforementioned layers) the area ratio ( $\frac{[COO^-+COOH(ads)]}{[COOH+COOH+COH(nonads)]}$ ) is 0.9:1 and 0.8:1, respectively, which suggest that TA is found predominantly in HTA<sup>-</sup> chemical state supporting an  $\mu_2$  (monotartrate)/ $\mu_3$  adsorption configuration (Fig. 3.1). The C K-edge NEXAFS consist of a sharp  $\pi^*$  resonance at 288.8 eV, three  $\sigma^*$  resonances at 292.1 eV, 295.6 eV and 301.7 eV and a step at 289-289.1 eV. The O K-edge NEXAFS consist of a sharp  $\pi^*$  resonance at 532.6-532.7 eV, two  $\sigma^*$  resonances at 539.2-539.3 eV and 544.0 eV and a step at 532.8-533 eV. It is difficult to determine the exact position of the  $\sigma^*$  resonances due to their large FWHM, however this does not influence the purpose of our NEXAFS data analysis which relies on the intensity of the  $\pi^*$  resonance.

The  $\sigma^*$  resonances in the C and O K-edge region regions are due to C-C and C-O bonds [46, 99, 104, 105]. We cannot exclude the presence in the NEXAFS spectra of features associated with decomposition products or contamination of the surface, especially in the C K-edge region (Fig. 3.5a and 3.5c), where we

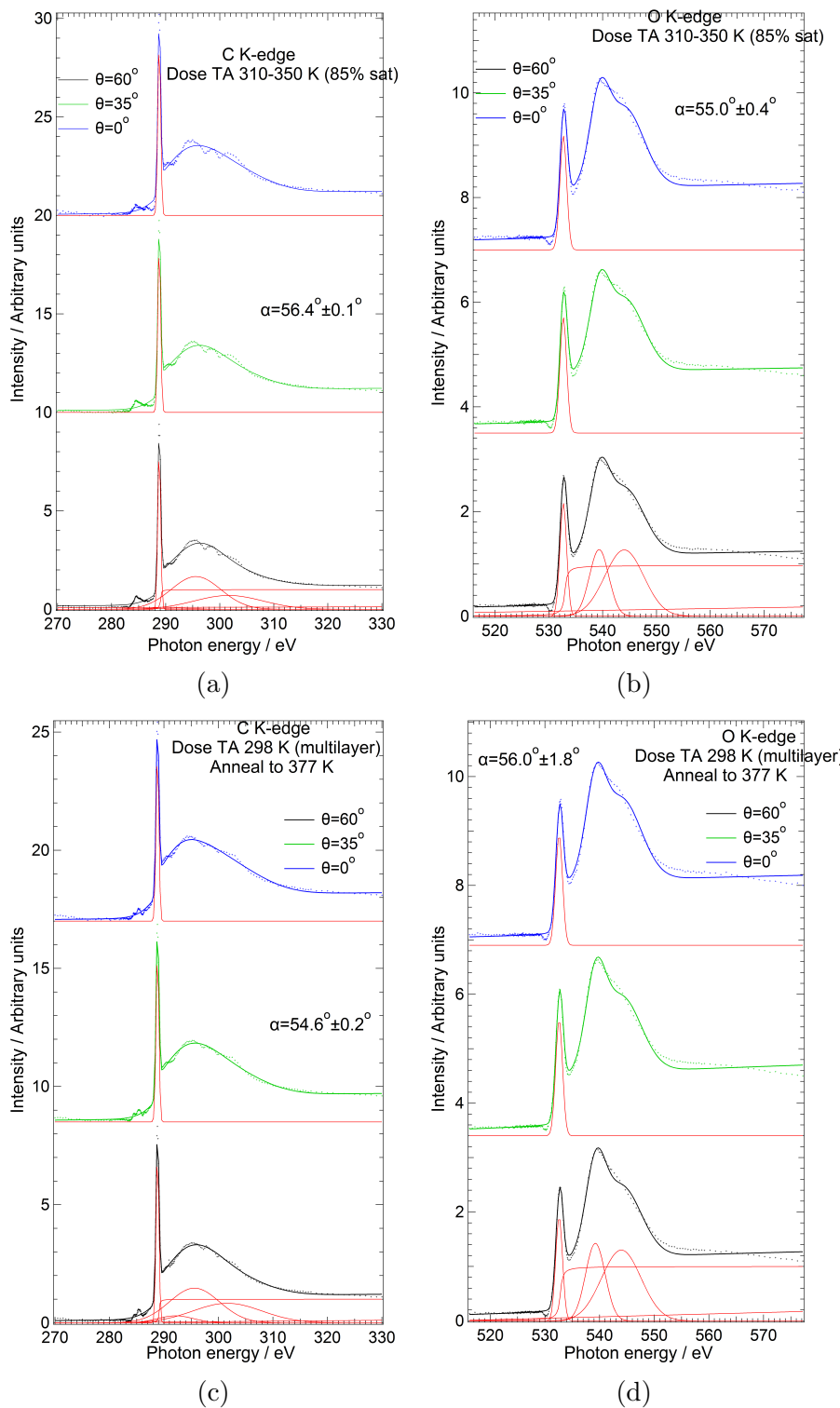


Figure 3.5: Angle resolved NEXAFS acquired at the HE-SGM beamline. Top panel: (a) C K-edge and (b) O K-edge NEXAFS spectra obtained after dosing (R,R)-tartaric acid onto Ni{100} at 310-350 K to 85% saturation (see Fig. 3.2c-3.2d for the corresponding XP-spectra). Bottom panel: (c) C K-edge and (d) O K-edge NEXAFS spectra obtained after dosing (R,R)-tartaric acid onto Ni{100} at 298 K to multilayer regime and anneal the layer to 377 K (see Fig. 3.3c-3.3d for the corresponding XP-spectra). The markers represent the raw data and the solid thick lines the fitted curves. The red curves below the spectra show the individual Gaussian peaks, the linear background and the the step function used for fitting.

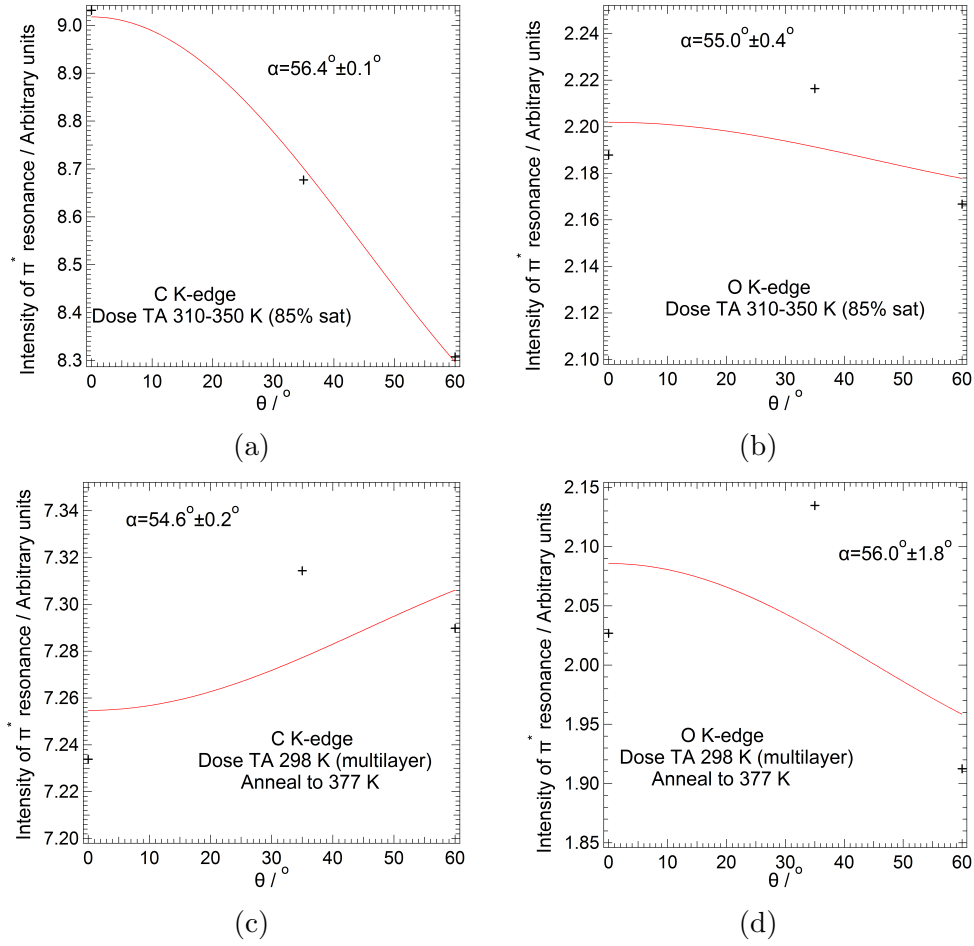


Figure 3.6: (a-d) Plots (black markers) showing the intensity of the oxygen and carbon  $\pi^*$  resonance in Fig. 3.5a-3.5a, respectively as a function of angle  $\theta$ , where  $\theta$  refers to the angle between the electric field vector and the surface plane. The solid red line shows the fitted curve calculated by the function in Eq. 3.1.

can clearly observe features between  $\sim 283.3$ - $287$  eV. These peaks are probably associated with  $sp^2(-C=C-)$ /graphitic carbon [106], or atomic carbon [105], which has been also observed in the C 1s XPS signal (Fig. 3.2c and 3.3c). Alternatively, these peaks could also be due to transitions related to the central carbons (C-OH) of the TA molecule [104, 107, 108].

The  $\pi^*$  resonance (Fig. 3.5) in the C and O K-edge region is associated with the  $COO^-$  group and C=O group of the protonated carboxyl group of the TA molecule [69, 99, 109, 110]. By plotting the intensity of these peaks, obtained upon fitting the NEXAFS figures, as a function of angle  $\theta$  (Fig. 3.6), where  $\theta$  refers to the angle between the electric field vector and the surface plane, we could determine the tilt angle  $\alpha$  of the C=O/ $COO^-$  groups of the TA molecule with respect to the Ni{100} surface plane, using the following equation for surfaces with 4-fold symmetry [96]:

$$I(\theta) = A[P(\sin\theta)^2 \cdot (1 - \frac{3}{2}\sin^2\alpha) + \frac{1}{2}\sin^2\alpha] \quad (3.1)$$

where P is the polarisation factor (0.91 for the HE-SGM beamline). The values of the tilt angle  $\alpha$  obtained upon fitting using Eq. 3.1 along with the fitting error are shown in the corresponding figures (Fig. 3.5-3.6). The values lie between  $\sim 55$ - $56^\circ$ , which are close to the “magic angle” ( $\alpha=54.7^\circ$ ), i.e the tilt angle in which the intensities of the resonance are independent of the angle of incidence [96], which is partially observed in our NEXAFS spectra (Fig. 3.6). Alternatively, the lack of polar angle anisotropy in the intensity of the  $\pi^*$  resonance might also reflect a lack of ordering of the TA overlayer on the Ni{100} surface.

Figures 3.7a and 3.8a show angle resolved NEXAFS in the C and O K-edge region, respectively, obtained in the D1011 beamline upon dosing TA at T=303-304 K to 79% saturation. According to the XP-spectrum in the O 1s region (Fig. 3.2b) the TA in this layer exists mainly in its bitartrate form, chemisorbing on the nickel surface through both of the deprotonated oxygen atoms of the carboxyl group in a 4-point adsorption geometry (Fig. 3.1). The C K-edge NEXAFS spectra (Fig. 3.7a) consist of a sharp  $\pi^*$  resonance at 287.9 eV, three  $\sigma^*$  resonances at 291.0 eV, 295.6 eV and 300.0 eV and a step at 288.2 eV. The O K-edge NEXAFS spectra (Fig. 3.7a) could only be reasonably fitted with two  $\pi^*$  resonances which are found at 530.0 eV and 531.2 eV. The O K-edge NEXAFS spectra (Fig. 3.7a) consist also of two  $\sigma^*$  resonances at 537.0 eV and 541.7 eV and a step at 531.7 eV. The small discrepancy on the energy positions with respect to C and O K-edge spectra in Fig. 3.5 is attributed to the difference in the energy calibration of the monochromator of the two beamlines. By using Eq. 3.1 ( $P \approx 1$  for

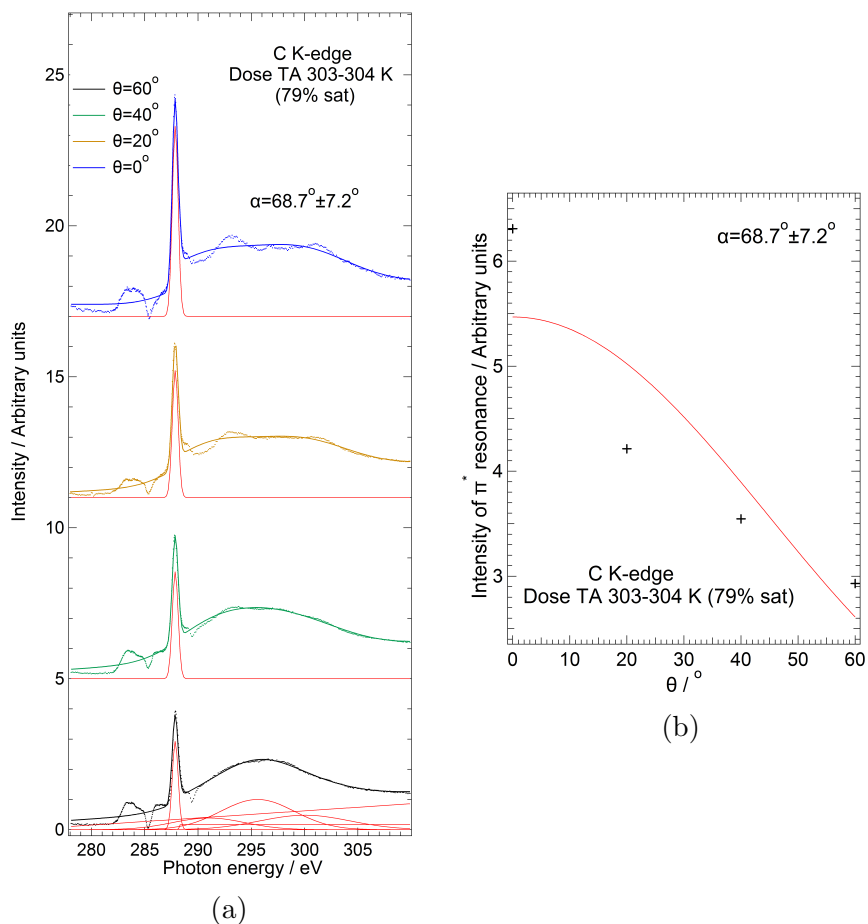


Figure 3.7: (a) Angle resolved C K-edge NEXAFS acquired at the D1011 beamline after dosing (R,R)-tartaric acid onto Ni{100} at 303-304 K to 79% saturation (see Fig. 3.2a-3.2b for the corresponding XP-spectra). The dots represent the raw data and the solid thick lines the fitted curves. The red curves below the spectra show the individual Gaussian peaks, the linear background and the the step function used for fitting. (b) Plots (black markers) showing the intensity of the carbon  $\pi^*$  resonance in Fig. 3.7a as a function of angle  $\theta$ , where  $\theta$  refers to the angle between the electric field vector and the surface plane. The solid red line shows the fitted curve calculated by the function in Eq. 3.1.

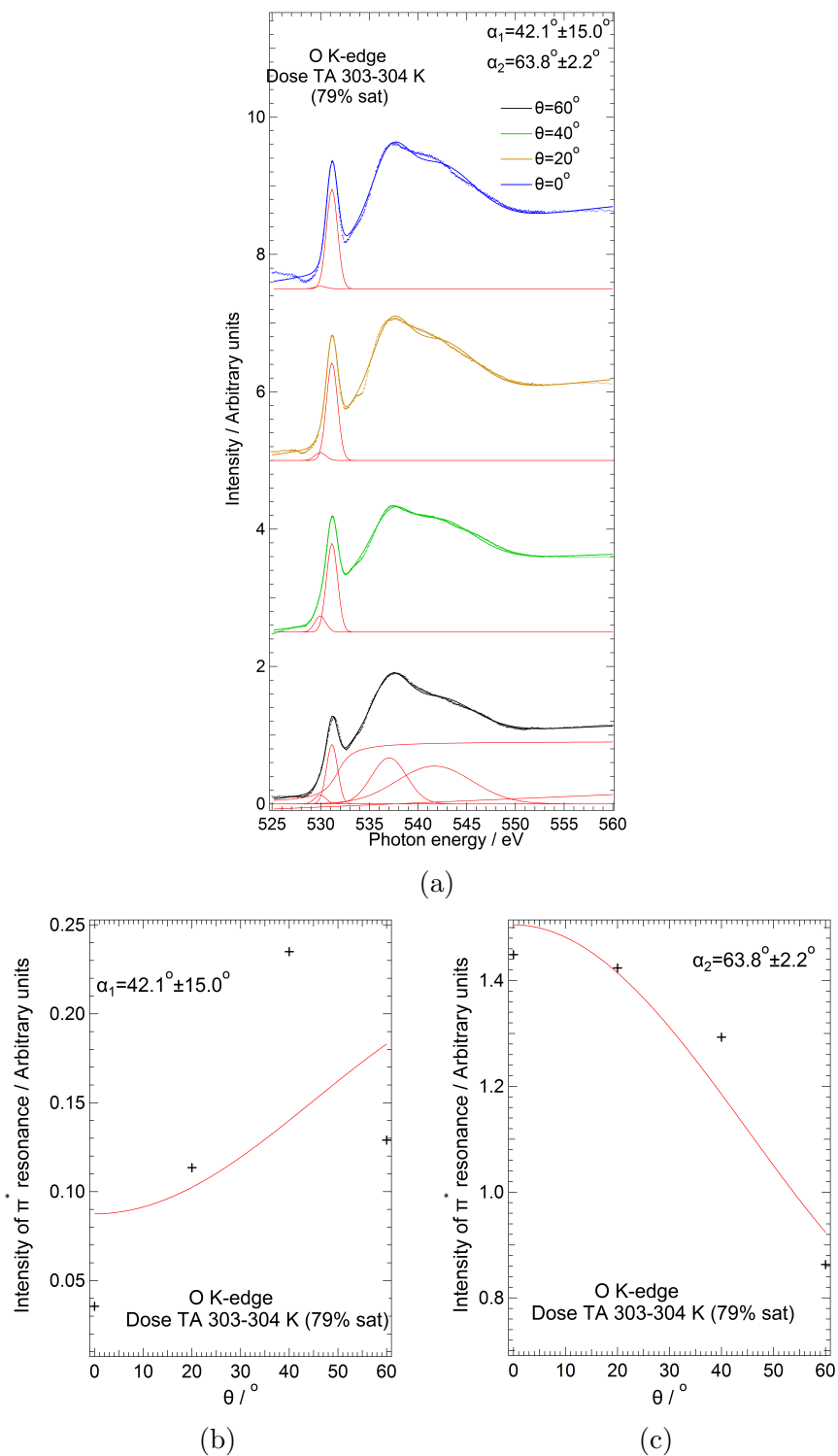


Figure 3.8: (a) Angle resolved O K-edge NEXAFS acquired at the D1011 beamline after dosing (R,R)-tartaric acid onto Ni{100} at 303-304 K to 79% saturation (see Fig. 3.2a-3.2b for the corresponding XP-spectra). The markers represent the raw data and the solid thick lines the fitted curves. The red curves below the spectra show the individual Gaussian peaks, the linear background and the the step function used for fitting (b+c) Plots (black markers) showing the intensity of the two oxygen  $\pi^*$  resonances in Fig. 3.8a as a function of angle  $\theta$ , where  $\theta$  refers to the angle between the electric field vector and the surface plane. The solid red line shows the fitted curve calculated by the function in Eq. 3.1.

the D1011 beamline) the angular dependency of the  $\pi^*$  resonance in the C K-edge region (Fig. 3.7b) returned tilt angle  $\alpha=68.7^\circ$  whereas the angular dependency of the two  $\pi^*$  resonances in the O K-edge region (Fig. 3.8b-3.8c) returned tilt angles  $\alpha_1=42.1^\circ$  and  $\alpha_2=63.8^\circ$  for the peaks at 530.0 eV and 531.2 eV, respectively. The presence of two  $\pi^*$  resonances in the O K-edge spectra (Fig. 3.8a) suggest that, in this layer, the carboxylate of the TA molecule exists in two different conformations with respect to the nickel surface. We cannot exclude the contribution to this signal from CO molecules, which were present before dosing, although investigation on the adsorption of CO on Ni{100}, [111] show that the molecule is upright, close to the surface normal of the nickel surface ( $\alpha=90^\circ$ ), something that is not consistent with the obtained tilt angles of this layer.

### 3.3.2 Tartaric acid on oxidised Ni{100}/UHV

#### Introduction

The oxidation of Ni{100} has been a subject of many studies [112–129]. According to Ref.[116] the oxidation of Ni{100} occurs in three reaction regions. The first two regions consist of rapid dissociative chemisorption followed by rapid generation of epitaxial NiO (2 layers thick) [116]. These regions depend on the oxygen exposure [116]. The last reaction is the slow thickening of the bulk NiO which according to Ref.[116] it only occurs at high oxygen pressures and low surface temperatures. The chemisorption of oxygen leads to the generation of  $p(2 \times 2)$  and  $c(2 \times 2)$  superstructures [114, 116, 119, 121, 123, 125, 126, 129], which correspond to 0.25 ML and 0.5 ML coverage, respectively [114].

Three structures of the NiO film on Ni{100} were observed in previous studies. One of the structures is referred to as NiO{111} and it is identified by a 12 spot ring pattern (Fig. 3.9), which was initially explained by two hexagonal unit meshes (twice the parameter of nickel atom), in two equivalent orientations [119]. In a later study [112], the 12 spot ring pattern was explained by the presence of four orientational domains with (111) stacking sequence, in four azimuthal orientations. The formation of this structure is favoured at temperatures close and/or below room temperature (it is formed under conditions of kinetic limitations) [112, 115, 128–130]. The surface of this structure is polar and is stabilized by the presence of OH groups [127, 129]. Heating this oxide layer causes dehydroxylation of the surface and reconstruction to the non-polar NiO(100) [115, 129]. The NiO(100) structure is the thermodynamically-favoured [115, 128, 129] and is formed at  $T>500$  K [112, 115, 125, 127, 128]. The third oxide structure, is

observed mainly between 300 K to 400 K and presents a O-(7x7) superstructure [115, 122, 128]. According to Ref.[122] this oxide grows mainly as NiO(001) in a strained superlattice which is expanded by  $\frac{1}{6}$  with respect to the metal substrate. This layer is thinner, more ordered and uniform than the NiO(100) structure, which is kinetically limited at these temperatures [128]. Kopatzki et al (1995) [113] have studied the temperature dependence on the rate oxide nucleation on Ni{100}. The nucleation proceeds mainly at steps and grows laterally forming 2D oxide islands. At 300 K the oxidation is facile even at low exposures, forming (7x7) and NiO(111) suboxide phases. At higher temperatures, the steps facet to {001} segments due to the interaction of chemisorbed oxygen and Ni atoms, suppressing the oxide nucleation [113].

### XPS/LEED Results

Figure 3.9 shows LEED patterns and the corresponding Ni 2p XP spectra of clean and oxidised Ni{100}. Fig. 3.10 shows top up XP-spectra of tartaric acid (TA) onto two different oxidised layers (top and bottom panel). In both cases the signal of tartaric acid was saturated. The coverages shown are based on the fitted XPS area of the saturated signal of tartaric acid (excluding impurities) in the C 1s region (Fig. 3.10a and 3.10c). It is worth mentioning the binding energy axis in the C 1s region (Fig. 3.10a and 3.10c) is highly inaccurate since we did not have available spectra of the Fermi edge. Calibration of the binding energy axis was performed by using the average value of the lowest and the largest offset observed during the beamtime. The first oxidised layer (top panel, Fig. 3.10a-3.10b) was generated by the following procedure :

1. Dose O<sub>2</sub> at  $P \approx 2 \times 10^{-8}$  mbar for 1 min at room temperature (room temperature).
2. Anneal the crystal to 850 K in O<sub>2</sub> atmosphere and switch off the gas and heating at the same time.
3. Heat in vacuum to 500 K.
4. Re-expose the crystal to O<sub>2</sub> at  $P \approx 1 \times 10^{-7}$  mbar for 1 min at  $T_{\text{sample}} \approx 318$  K, annealed to 900 K in O<sub>2</sub> atmosphere and cool to 373 K in the same atmosphere ( $P_{\text{O}_2} \approx 1 \times 10^{-7}$  mbar).

The second oxidised layer (bottom panel, Fig. 3.10c-3.10d) was created by the following procedure:

1. Dose O<sub>2</sub> at P<sub>≈</sub>1 × 10<sup>-7</sup> mbar at T<sub>sample</sub>≈357 K for 1 min, anneal to 900 K and cool to 373 K all in oxygen atmosphere (P<sub>O<sub>2</sub></sub>≈1 × 10<sup>-7</sup> mbar).
2. Dose O<sub>2</sub> at P<sub>≈</sub>1 × 10<sup>-7</sup>-2 × 10<sup>-7</sup> mbar at T<sub>sample</sub>≈311-317 K for 64 min.
3. Dose O<sub>2</sub> at P<sub>≈</sub>1 × 10<sup>-7</sup> mbar at T<sub>sample</sub>≈306 K for 1 min, anneal to 900 K and cool to 373 K all in oxygen atmosphere (P<sub>O<sub>2</sub></sub>≈1 × 10<sup>-7</sup> mbar).
4. Dose O<sub>2</sub> at P<sub>≈</sub>5.8 × 10<sup>-7</sup>-7.6 × 10<sup>-7</sup> mbar at T<sub>sample</sub>≈323 K for 60 min.

The aforementioned procedures were followed in order to create an oxide layer on the Ni{100} surface while at the the same time treat the carbon impurities by annealing in O<sub>2</sub> atmosphere. Cooling in O<sub>2</sub> atmosphere prevented also the contamination of the surface from adventitious carbon or CO present in the background pressure of the chamber. Carbon impurities were present on the surface before dosing tartaric acid. The XPS area (obtained upon fitting) of the carbon impurities were ~ 11% (Fig. 3.10a) and ~ 22% (Fig. 3.10c) of the XPS area (obtained upon fitting) of the corresponded saturated signal of TA (excluding impurities) in the C 1s spectra in Fig. 3.10a and Fig. 3.10c, respectively.

The LEED image of the NiO layer (Fig. 3.9, top panel) presents a 12-spot ring pattern which is characteristic for a NiO{111} film grown on the Ni{100} surface [112, 129, 130]. The formation of this structure under our experimental conditions is in disagreement with previous studies [112, 115, 129, 130], which suggested that the NiO{111} film on Ni{100} is formed only at T<sub>≤</sub>300 K . Figure 3.9 shows XP-spectra in the Ni 2p region of clean and oxidised Ni{100}. The spectrum corresponding to NiO shows 7 peaks at 852.6 eV, 854.0 eV, 855.9 eV, 860.8 eV, 869.9 eV, 872.2 eV and 879.9 eV. The peak positions are in close agreement with the work of Langell et al (1994, 1995) [129, 130] on NiO{111}/Ni{100}. The peaks at 852.6 eV and 869.9 eV are associated with doublet splitting of the 2p state of the Ni<sup>0</sup> substrate (2p<sub>3/2</sub> and 2p<sub>1/2</sub>, respectively) caused by spin orbit coupling [129]. The peaks at 854 eV/855.9 eV and 872.2 eV are linked to multiplet splitting of the 2p state of the Ni<sup>2+</sup> substrate (2p<sub>3/2</sub> and 2p<sub>1/2</sub> transitions, respectively). These transitions generate satellite peaks at 860.8 eV and 879.8 eV, respectively [129, 130]. The O 1s spectra of the oxide layer (Fig. 3.10b and 3.10d) show two peaks at 529.5-529.6 eV and 531.3 eV which are assigned to lattice oxide (O<sup>-2</sup>) and hydroxyls species (OH), respectively [129–132]. The hydroxyls are formed through interaction of the oxide layer with background pressure of H<sub>2</sub>O and/or H<sub>2</sub> [127, 129, 131]. The presence of the hydroxyls might explain the formation of NiO{111} structures at these temperatures, over the other structures observed in previous studies, because they are known to stabilize the NiO{111}

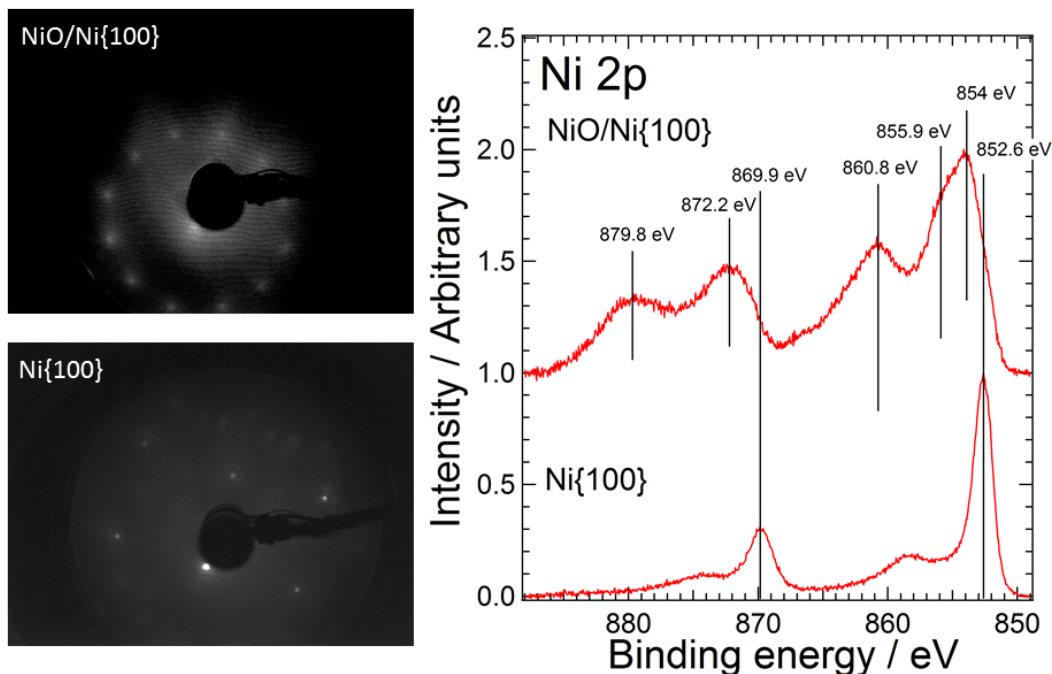


Figure 3.9: LEED patterns and the corresponding Ni 2p XP spectra for the clean (bottom panel) and oxidised Ni{100} (top panel) obtained in the MAX-Lab synchrotron in Lund (Sweden) in the UHV endstation of the D1011 beamline. The LEED patterns were recorded at  $E_{\text{beam}}=90$  eV. The XP-spectra were obtained at  $h\nu=1000$  eV and 50 eV pass energy. The data were normalised also to the peak for clarity.

polar surfaces, and their presence is essential for the formation of these structures [127, 129]. Based on the area of saturated TA (O 1s spectrum in Fig. 3.2b), the expected saturation coverage of TA on Ni{100} (0.25 ML, 1 TA molecule per 4 nickel atoms, see Fig. 3.1), correcting by factor of 6 (6 oxygen atoms per TA molecule) and without taking account any attenuation effects, the oxide concentration ( $\text{O}^{-2}$ ) in the layer in the O 1s spectrum in Fig. 3.10b is  $\sim 1.4$  ML and  $\sim 1.0$  ML in Fig. 3.10d. The corresponding hydroxyl concentration is 0.9 ML and 1.1 ML, respectively. The extent of oxidation is higher in the first layer (O 1s spectrum in Fig. 3.10b), even though we have used more oxidising conditions during the formation of the second oxide layer. This is probably related to the base pressure of the chamber during oxidation, which was approximately one magnitude higher during the second oxidation cycle (Fig. 3.10c-3.10d,  $P_{\text{base}} \approx 3 \times 10^{-9}$  mbar) in comparison with the first oxidation cycle (Fig. 3.10a-3.10b,  $P_{\text{base}} \approx 4 \times 10^{-10}$  mbar). This resulted in lower amount of impinged oxygen atoms on the nickel surface during the second oxidation cycle (Fig. 3.10c-3.10d) while at the same time increased the

hydroxyl concentration on the nickel surface due to the increased background pressure. In addition, during the second oxidation cycle (Fig. 3.10c-3.10d), the nickel surface was exposed for a longer period at lower temperatures in O<sub>2</sub> atmosphere, inducing even more the formation of hydroxyl species.

Dosing TA onto hydroxylated NiO{111}/Ni{100} film causes an increase in the XPS signal at the high binding energy end of the O 1s region (Fig. 3.10b and 3.10d), which is consistent with the presence of an organic molecule on the surface. The C 1s spectra in Fig. 3.10a show 4 peaks at 283.7-284.0 eV, 284.6-284.8 eV, 286.6-287.0 eV and 288.6-289.0 eV whereas the C 1s spectra in Fig. 3.10c show three peaks at 284.4-284.7 eV, 286.3-286.7 eV and 288.4-288.8 eV. The two high binding energy peaks are assigned in a similar fashion to the previous C 1s spectra in Fig. 3.2a of the TA/Ni{100} system, to the (COH and to the COO<sup>-</sup>/COOH of the adsorbed TA molecule, respectively). The area ratio of these two peaks ( $\frac{[COH]}{[COO^-+COOH]}$ ) is  $\sim 1.2-1.3:1$ . The other two peaks (283.7-284.0 eV and 284.4-284.8 eV) are associated with decomposition fragments. Comparing the saturated C 1s XPS signal of the two TA/NiO/Ni{100} systems, we observe that the TA overlayer area is higher in the least hydroxylated layer (C 1s spectrum in Fig. 3.10a), which is also higher than the corresponding C 1s XPS area of the saturated layer in the TA/Ni{100} system (Fig. 3.2a).

Langell et al (1994) [130] and Jones et al (2004) [39] have investigated the adsorption of acetic and tartaric acid respectively on hydroxylated NiO{111} films. Acetic acid was found to adsorb in a bridging acetate form on Ni<sup>2+</sup> ion through condensation reaction of the adsorbed hydroxyl and the hydrogen of the molecule, which releases H<sub>2</sub>O in the gas phase [130] (Fig. 3.11). Similar results were obtained by Jones et al. (2004) [39] upon interaction of TA on the hydroxylated NiO{111}/Ni{111} substrate. The author found evidence of the formation of species similar to nickel tartrate. In this system [39], TA is found in its bitartrate form, bridging two OH-Ni<sup>2+</sup>-OH surface sites and releasing two H<sub>2</sub>O molecules in the gas phase [39]. Fitting the O 1s spectra in our study (Fig. 3.10b and 3.10d) was particularly challenging because of the overlap of the signal corresponding to the deprotonated carboxyl group of TA (COO<sup>-</sup>) and the hydroxyls. Fitting was achieved by keeping the fitting parameters of the substrate NiO and adjusting the fitting signal corresponding to the TA molecule, so that the estimated TA coverage will be in close agreement to the coverage estimated using the XPS fitted area of the TA molecule in the C 1s region. The XPS signal corresponding to the TA molecule is fitted by three peaks at 531.4-531.75 eV, 532.8-532.9 eV and 533.9-534.2 eV. The peaks are assigned in a similar fashion to the previous O 1s spectra in Fig. 3.2b of the TA/Ni{100} system, to oxygen atoms of the de-

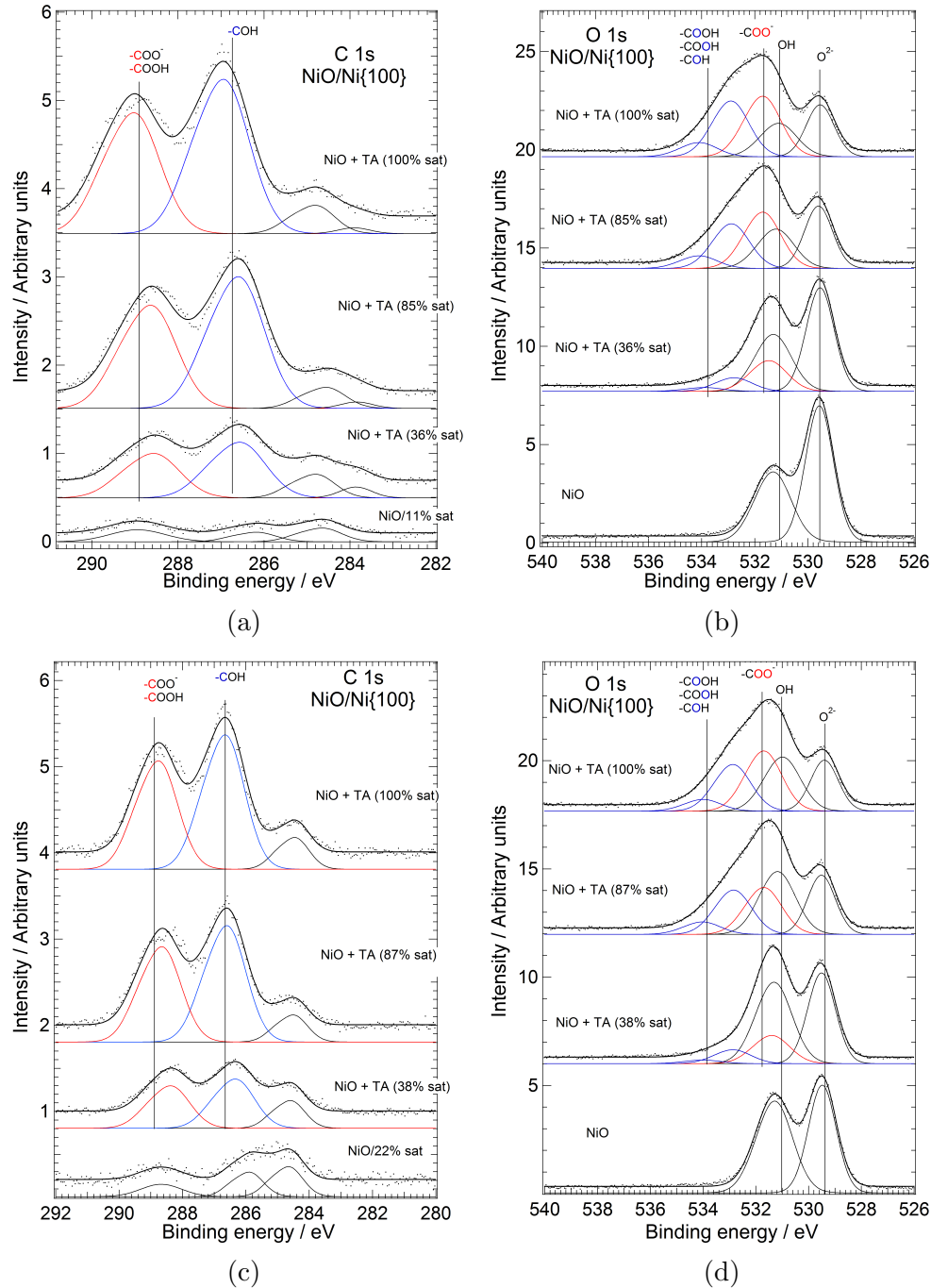


Figure 3.10: Top-up XP-spectra of (R,R)-tartaric acid (TA) onto two different NiO/Ni{100} layers (bottom and top panel) in (a+c) C 1s region ( $h\nu=400$  eV) and (b+d) O 1s region ( $h\nu=650$  eV). Top panel, dosing conditions of TA:  $T_{\text{sample}} \approx 302\text{--}304$  K,  $T_{\text{evaporator}} \approx 404\text{--}406$  K,  $P_{\text{base}} \approx 4 \times 10^{-10}\text{--}3 \times 10^{-9}$  mbar,  $P_{\text{dosing}} \approx 5 \times 10^{-9}\text{--}2 \times 10^{-8}$  mbar, Deposition time  $\approx 145$  min/saturated layer. Bottom panel, dosing conditions:  $T_{\text{sample}} \approx 301$  K,  $T_{\text{evaporator}} \approx 403\text{--}404$  K,  $P_{\text{base}} \approx 1 \times 10^{-9}\text{--}2 \times 10^{-9}$  mbar,  $P_{\text{dosing}} \approx 6 \times 10^{-9}\text{--}1 \times 10^{-8}$  mbar, Deposition time  $\approx 130$  min/saturated layer. The spectra were obtained in the MAX-Lab synchrotron in Lund (Sweden) in the UHV endstation of the D1011 beamline. The black thick dots are the raw spectra and the black thick lines are the fitted curves. The solid coloured curves are the individual peaks.

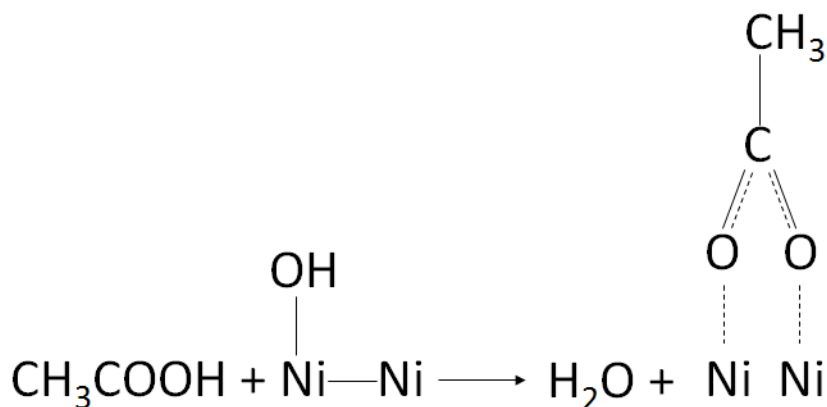


Figure 3.11: The adsorption mechanism of acetic acid on hydroxylated NiO{111} as it is proposed and shown in Ref.[130].

protonated carboxyl group of the TA molecule chemisorbed on the nickel surface ( $\text{COO}^-$ ), to oxygen atoms dangling from the surface ( $\text{COH}/\text{COOH}/\text{COOH}$ ) and to oxygen with high degree of protonation, respectively. The signal corresponding to hydroxyls decreases with increasing coverage of TA suggesting the Langell mechanism [130] of adsorption of acetic acid on hydroxylated NiO{111} (Fig. 3.11) is the most possible adsorption mechanism in our study [130]. For the purpose of elaborating this mechanism, we tried to correlate the amount of desorbed hydroxyls with the amount of deprotonated carboxyl groups. This mechanism suggests that for every hydroxyl desorbed from the surface we have a 2fold gain in the signal corresponding to the oxygen atoms of the deprotonated carboxyl group (peak at 531.4-531.75 eV). Comparing the value of desorbed hydroxyls with the signal of carboxylate species (peak at 531.4-531.75 eV), and correcting by factor of two, we observe that at low coverages (36% sat, O 1s spectrum in Fig. 3.10b) and 38% sat (O 1s spectrum in Fig. 3.10d), the amount of deprotonated carboxyl group is  $\sim 19\%$  and  $\sim 36\%$  higher than the desorbed -OH, respectively. It is possible that at low coverages, TA binds on empty sites of the  $\text{Ni}^{2+}$  substrate, without displacing any hydroxyls. In addition, it is probable, especially at low coverages, that the oxide surface will react with background pressure or the tartaric acid itself and generate more hydroxyls [39, 127, 129, 131]. At 100% saturation, the amount of desorbed hydroxyls is  $\sim 20\text{-}24\%$  higher than the amount of deprotonated carboxyl groups of the TA molecule (Fig. 3.10b and 3.10b). This is probably explained by attenuation of the carboxylate group from the rest of the TA molecule. It is also possible that a hydroxyl and a hydrogen (originating the background pressure of the chamber) or two hydroxyls, coalesce, releasing  $\text{H}_2\text{O}$  in the gas phase. It is

probable that the increased crowding of the surface from the TA molecules could have triggered this kind of behaviour. The presence of hydroxyls in the saturated overlayer of TA, suggest that some hydroxyls are unreactive to the presence of TA molecules, or even blocking the adsorption. The latter probably explains why the increased hydroxylation of the second oxide (O 1s spectrum in Fig. 3.10b) in comparison with the first (O 1s spectrum in Fig. 3.10b), decreased the amount of adsorbed TA. The peak associated with the deprotonated carboxyl group of the tartaric acid molecule (531.4-531.75 eV) shifts to higher binding energies with increasing coverage ( $\sim 0.2$ - $0.3$  eV) while at the same time the peak associated with the hydroxyl species shifts to lower binding energy by the same magnitude ( $\sim 0.2$ - $0.3$  eV). The species described in Ref.[39], generated upon deposition of TA onto hydroxylated NiO{111}/Ni{111}, imply that the carboxylate group of the TA molecule is co-bonded on the Ni<sup>2+</sup> substrate with the hydroxyls. It is very likely that there is a charge transfer between the co-bonded hydroxyl and deprotonated carboxyl group, which alters the binding energy of the two species. The ratio of the area of the low binding energy peak and the the sum of areas of the two high binding energy peaks ( $\frac{[COO^-(ads)]}{[COOH+COH(nonads)]}$ ) is  $\sim 1.8:1$  and  $\sim 1.6:1$  in the O 1s spectra in Fig. 3.10b (36% sat) and in Fig. 3.10d (38% sat), respectively, whereas at the saturated coverage the aforementioned ratio is  $\sim 0.9:1$  and  $\sim 1:1$ , respectively. The ratio implies that tartaric acid is mainly on its bitartrate form in the submonolayer regime, whereas in the saturated layer, we have coexistence of bitartrate (TA<sup>2-</sup>) and monotartrate (HTA<sup>-</sup>) phases. The strong electrostatic interaction between the negatively charged carboxylate groups and the Ni<sup>2+</sup> substrate [39] makes the presence of an  $\mu_3$  adsorption geometry (which involves adsorption of TA on the Ni<sup>2+</sup> substrate without deprotonation of one of its carboxyl groups, Fig. 3.1), highly unlikely. The increase in the HTA<sup>-</sup>:TA<sup>2-</sup> ratio with increasing coverages is consistent with what we have observed in the TA/Ni{100} system in Fig. 3.2 and is induced by the molecular crowding of the surface with increasing coverages [100]. A further insight into the chemical state of TA on NiO/Ni{100} substrate will be provided further on. The peak related to the oxide (529.4 eV) in the saturated layer decreases by  $\sim 62\%$  (O 1s spectrum in Fig. 3.10b) and  $53\%$  (O 1s spectrum in Fig. 3.10d) with respect to the pure oxide layer. This decrease is most likely related to attenuation effects of the oxide layer from the TA overlayer, even though it is also possible that the oxide layer is reduced from gases from the background pressure of the chamber or from the TA molecule itself [39, 127, 129, 131].

Figures 3.12a and 3.12b show step anneal XP-spectra of the TA saturated overlayer on NiO/Ni{100} shown in Fig. 3.10c and 3.10d. As in the case of the

C 1s spectra in Fig. 3.10a and 3.10c, the binding energy axis in the C 1s region is highly inaccurate since we did not have available spectra of the Fermi edge. Calibration of the binding energy axis was performed by using the average value of the lowest and the largest offset observed during the beamtime. Leaving the TA<sub>sat</sub>/NiO/Ni{100} layer for some period ( $\sim 8$  hours) in the chamber at room temperature, caused some decomposition of the TA overlayer (reduced to 84% of the saturated signal, Fig. 3.12a-3.12b). At 84% sat/room temperature (O 1s spectrum in Fig. 3.12b), we can observe a small increase in the signal of the peaks corresponding to the oxide (529.6 eV) and to the hydroxyl by  $\sim 15\%$  and  $\sim 20\%$ , respectively with respect to the saturated layer shown in the O 1s spectrum in Fig. 3.10d, while at the same time the peak corresponding to hydroxyls has been also shifted by 0.3 eV to the high binding energy region (peak position 531.3 eV). The area ratio ( $\frac{[COO^-(ads)]}{[COOH+COOH+COH(nonads)]}$ ) has been reduced to  $\sim 0.8:1$  (O 1s spectrum in Fig. 3.10d), indicating an increase in the HTA<sup>-</sup>/TA<sup>2-</sup> ratio in the TA overlayer. Heating to 400 K, causes some desorption and dissociation of TA (reduced to 75% of the saturated signal). At this temperature, we can observe also a slight increase in the signal corresponding to hydroxyls ( $\sim 531.2$  eV) and an increase in the area ratio ( $\frac{[COO^-(ads)]}{[COOH+COOH+COH(nonads)]}$ ) to  $\sim 1.2:1$  (O 1s spectrum in Fig. 3.12b). At 460 K (68% of the saturated signal), the bitartrate phase is the dominant geometry of the TA molecule ( $\frac{[COO^-(ads)]}{[COOH+COOH+COH(nonads)]} \approx 1.6:1$ ).

Major changes are observed upon annealing to 530 K ( $\Theta_{TA} = 47\%$  sat). At this temperature, more than half of the TA molecule is decomposed. The high binding energy peak in the O 1s region (Fig. 3.12b) has disappeared, indication of the deterioration of the intermolecular interaction between the TA molecules. The area ratio in the O 1s spectrum in Fig. 3.12b ( $\frac{[COO^-(ads)]}{[COOH+COOH+COH(nonads)]}$ ) has increased to  $\sim 5.5:1$ , however we can argue that the low binding energy peak has contribution from decomposition fragments of TA. The peak corresponding to hydroxyls shifts to high binding energies ( $\sim 531.6$  eV) while at the same time, the peak corresponding to the carboxylate group of TA shifts to low binding energies ( $\sim 531.45$  eV, O 1s spectrum in Fig. 3.12b). This feature is the opposite effect to what we have observed in the top up XP-spectra in the O 1s region (Fig. 3.10b and 3.10d) and is attributed to charge transfer between the co-bonded hydroxyls and carboxylate groups on the Ni<sup>2+</sup> substrate. The oxide peak (529.7 eV, O 1s spectrum in Fig. 3.12b) increases by  $\sim 69\%$  with respect to the saturated layer. At this temperature, the attenuation is weaker, since a significant amount of the TA molecules have desorbed from the surface. Heating to 650 K decreases the TA signal to 10% of the saturated layer, while at the same time the peak corresponding to the carboxylate group of the TA molecule (COO<sup>-</sup>, O 1s spectrum in Fig. 3.12b)

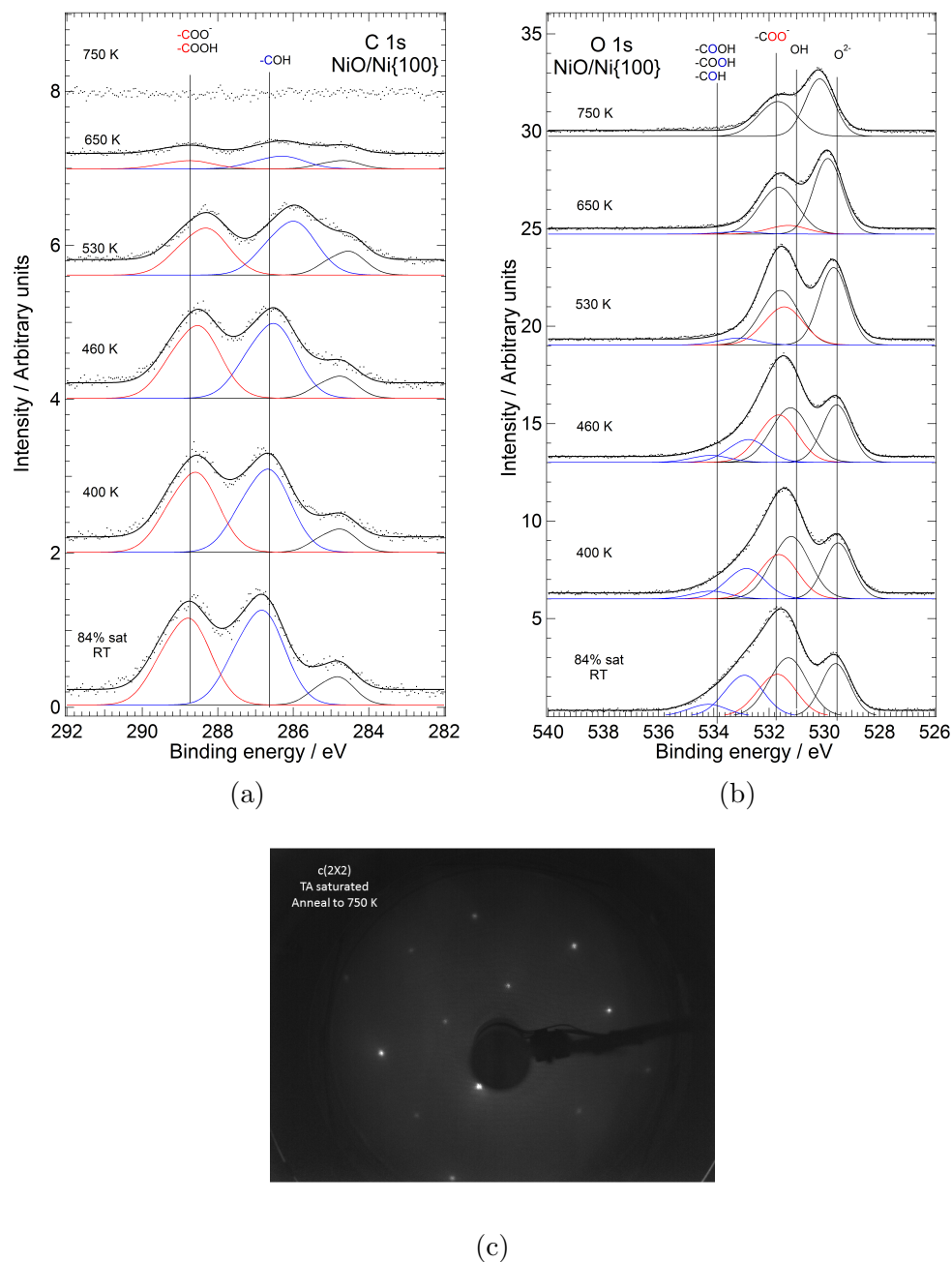


Figure 3.12: (a+b) Step anneal XP-spectra of saturated (R,R)-tartaric acid (TA) overlayer layer on NiO/Ni{100} (Fig. 3.10c-3.10d) (a) C 1s region ( $h\nu=400$  eV) and (b) O 1s region ( $h\nu=650$  eV). The black thick dots are the raw spectra and the black thick lines are the fitted curves. The solid coloured curves are the individual peaks (c) LEED pattern of the oxygen overlayer generated upon step annealing the TA<sub>sat</sub>/ NiO/Ni{100} layer to 750 K. The LEED was recorded at  $E_{\text{beam}}=90$  eV. The spectra and the LEED pattern were obtained in the MAX-Lab synchrotron in Lund (Sweden) in the UHV endstation of the D1011 beamline

shifts even more to low binding energies (531.3 eV).

Heating to 750 K causes the complete disappearance of the signal corresponding to TA with no traces of decomposition fragments in the C 1s region (Fig. 3.12a). At no time during the step anneal process, we have observed any significant signal of decomposition species in the C 1s region (Fig. 3.12a) like we have observed in the TA/Ni{100} system (Fig. 3.3a and 3.3c). It is likely that the surface carbon ( $BE \leq 283$  eV) is diffused and buried under the oxygen layer or desorbs as CO/CO<sub>2</sub>. Upon heating this layer to 1000 K (results not shown) and subsequent desorption of the oxygen layer we have observed a rise of signal at  $\sim 283$  eV, which could be either carbon originated from the TA molecule or from the background gases of the chamber. The peak corresponding to hydroxyls in the O 1s region (Fig. 3.12b) was reduced only by  $\sim 29\%$  with respect to the saturated layer. Step anneal XP-spectra of the NiO/Ni{100} [129], show that heating to  $T > 600$  K causes full desorption of hydroxyls from the nickel surface. The nature of our step anneal procedure (anneal and cool), could hydroxylate the surface through adsorption from the background gases, even though according to Langell et al. 1995 [129], the cooling of the crystal does not cause re-hydroxylation of the surface. It is also possible that the hydroxylation of the surface occurred from decomposition products of TA molecule (mainly hydrogen) from the COH and COOH group. At 750 K, the peak corresponding to the oxide in the O 1s region (Fig. 3.12b) has shifted to 530.2 eV. Based on the total area of the O 1s spectrum (Fig. 3.12b) the coverage of the oxygen layer is  $\sim 1.0$  ML. The LEED pattern (Fig. 3.12c) presents a  $c(2 \times 2)$  superstructure, in line with work of Langell et al 1995 [129]. At this temperature the oxide characteristics have almost vanished, and only chemisorbed oxygen is present on the surface.

Tartaric acid on NiO/Ni{100} decomposed fully  $T > 650$  K which is about 200 degrees higher than on clean Ni{100} (Fig. 3.3). A similar decomposition temperature was observed for the TA/NiO/Ni{111} system [39]. The higher decomposition temperature of the TA overlayer on NiO/Ni{111} substrate with respect to the TA/Ni{111} system was explained by the strong electrostatic interaction between the Ni<sup>2+</sup> substrate and the negatively charged bitartrate species [39]. Jones et al (2004) [39] argued that the TA/NiO/Ni{111} layer closely resembles the nickel (II) tartrate complex which also decomposes at  $\sim 650$  K [32]. In the light of this argument the monotartrate and bitartrate phase in this study, correspond actually to nickel monotartrate and nickel bitartrate phases, respectively. The positive charge of this adsorption complexes is compensated by the presence of -OH, co-bonded on the Ni<sup>2+</sup> substrate. Our data suggest that it is likely that the nickel monotartrate and bitartrate phases present 1 and 2 point adsorption

geometries, respectively. A two and four adsorption geometry for the monotartrate and bitartrate phase will require 3 hydroxyls atoms for every carboxylate adsorbed on the surface for full compensation of the positive charge, something that is not consistent with our data.

### NEXAFS Results

Figure 3.13 shows angle dependent O K-edge NEXAFS of the oxide layer on Ni{100}, corresponding to the O 1s spectrum in Fig. 3.10d. The NEXAFS spectra show 6 peaks at 528.5 eV, 530.0 eV, 530.9 eV, 534.4 eV, 538.4 eV and 543.7 and a step at 534.9 eV. It is in close resemblance with NEXAFS spectra of NiO in previous studies [133–136].

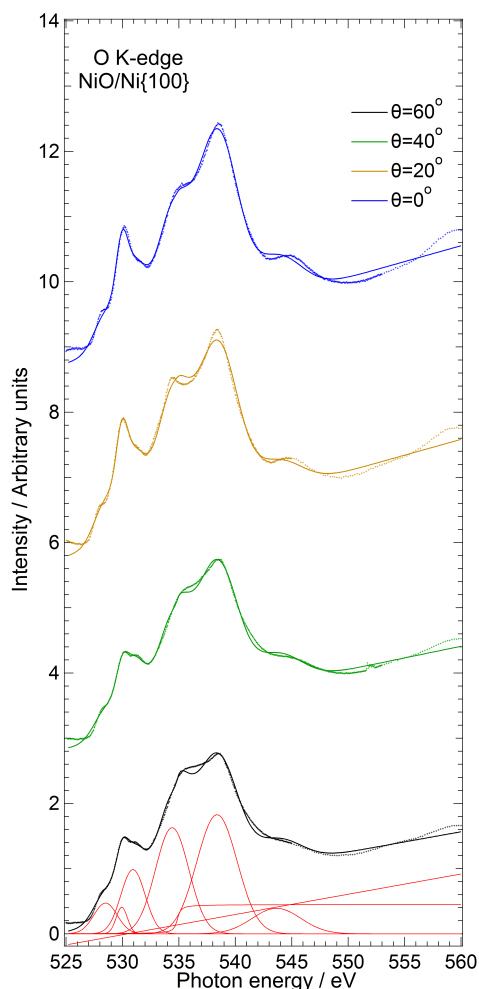


Figure 3.13: Angle resolved O K-edge NEXAFS acquired at the D1011 beamline of the oxide layer shown in the O 1s spectrum in Fig. 3.10d. The markers represent the raw data and the solid thick lines the fitted curves. The red curves below the spectra show the individual Gaussian peaks, the linear background and the step function used for fitting.

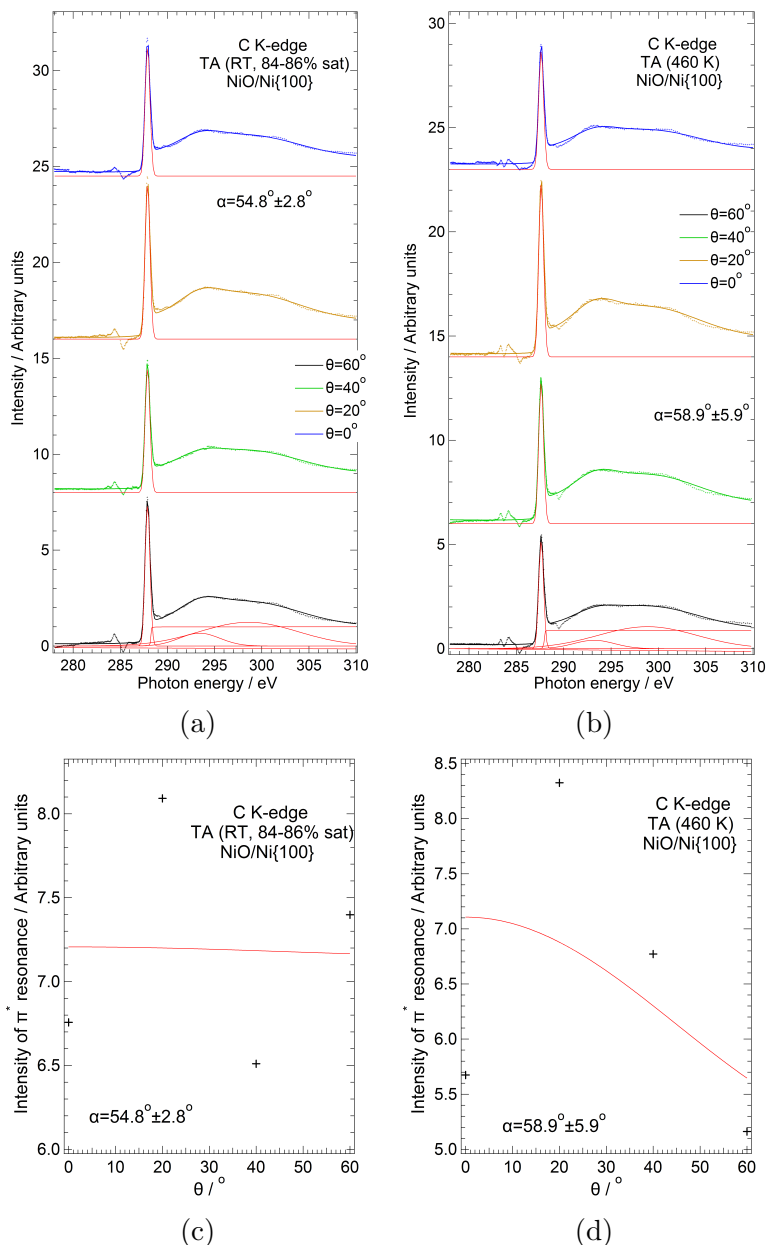


Figure 3.14: (a+b) Angle resolved NEXAFS in the C K-edge region obtained (a) upon dosing (R,R)-tartaric acid (TA) onto NiO/Ni{100} layer up to saturation (using the layer in the O 1s spectrum in Fig. 3.10d as precursor) and leaving the layer for some period ( $\sim 6$ -8 hours) in the chamber at room temperature, which decreased the coverage to  $\Theta_{\text{TA}}=84$ -86% (b) and upon step anneal the TA/NiO/Ni{100} saturated layer to 460 K (see Fig. 3.12a-3.12b for XPS reference). The markers represent the raw data and the solid thick lines the fitted curves. The red curves below the spectra show the individual Gaussian peaks, the linear background and the step function used for fitting. The spectra were obtained in the MAX-Lab synchrotron in Lund (Sweden) in the UHV endstation of the D1011 beamline. (c+d) Plots (black markers) showing the intensity of the carbon  $\pi^*$  resonance in Fig. 3.14a and 3.14b as a function of angle  $\theta$ , where  $\theta$  refers to the angle between the electric field vector and the surface plane. The solid red line shows the fitted curve calculated by the function in Eq. 3.1.

Figures 3.14a and 3.14b show angle dependent NEXAFS in the C K-edge region upon dosing TA on top of a NiO/Ni{100} layer to saturation using the layer in the O 1s spectrum in Fig. 3.10d as substrate and leaving the layer for some period ( $\sim 6-8$  hours) in the chamber at room temperature, which decreased the coverage to  $\Theta_{TA}=84-86\%$  (Fig. 3.14a) and upon step anneal the aforementioned layer to 460 K (Fig. 3.14b). At  $\Theta_{TA}=84-86\%$  (Fig. 3.14a) the O 1s spectrum (Fig. 3.12b/ $\Theta_{TA}=84\%$ , the spectrum shown was obtained upon completion of acquisition of the NEXAFS in Fig. 3.14a) suggest the coexistence of nickel bitartrate and monotartrate phases. At T=460 K (Fig. 3.14b), the O 1s spectrum (Fig. 3.12b/460 K) suggest the nickel bitartrate phase as the predominant species in the TA/NiO/Ni{100} overlayer ( $\frac{[COO^-(ads)]}{[COOH+COOH+COH(nonads)]} \approx 1.6:1$ ). The NEXAFS spectra show a sharp  $\pi^*$  resonance at 287.6-287.9 eV, two  $\sigma^*$  resonances at 293.2-293.4 eV and 298.6-298.9 eV and a step at 287.9-288.2 eV, assigned in a similar fashion to the C K-edge NEXAFS spectra in Fig. 3.5a and 3.5c of the TA/Ni{100} system. By using Eq. 3.1 ( $P \approx 1$  for the D1011 beamline) the angular dependency of the two  $\pi^*$  resonances in the C K-edge region (Fig. 3.14c-3.14d), returned tilt angles  $\alpha=54.8^\circ$  (Fig. 3.14a and 3.14c) and  $\alpha=58.9^\circ$  (Fig. 3.14b and 3.14d). As in the case with the NEXAFS spectra in Fig 3.5 the values of the tilt angle are close to the value of the “magic angle” ( $\alpha=54.7^\circ$ ), i.e the tilt angle in which the intensities of the resonance are independent of the angle of incidence [96], which might reflect a lack of ordering of the TA overlayer on the NiO/Ni{100} substrate.

### 3.3.3 Tartaric acid on clean Ni{100}/Elevated H<sub>2</sub> pressures

#### XPS Results

Figure 3.15 shows ambient pressure (AP) XP-spectra of the TA overlayer on Ni{100}. The spectra were obtained upon dosing TA onto Ni{100} and then exposing the TA overlayer to increasing hydrogen pressures, as shown in Fig. 3.15. Figure 3.16 compares step anneal XP-spectra of the TA layer under the presence of  $P_{H_2}= 6.4$  mbar (top panel) and under UHV conditions (bottom panel). The XP-spectra have detected no presence of oxygen before dosing dosing TA (O 1s spectra in Fig. 3.15b and Fig. 3.16d). The XPS area (obtained upon fitting) of the carbon impurities (present before dosing) were  $\sim 26\%$  (Fig. 3.15a) and  $\sim 29\%$  (Fig. 3.16c) of the XPS area (obtained upon fitting) of the corresponded TA signal (excluding impurities) in the C 1s spectra in Fig. 3.15a (UHV before)

and Fig. 3.16c (room temperature), respectively.

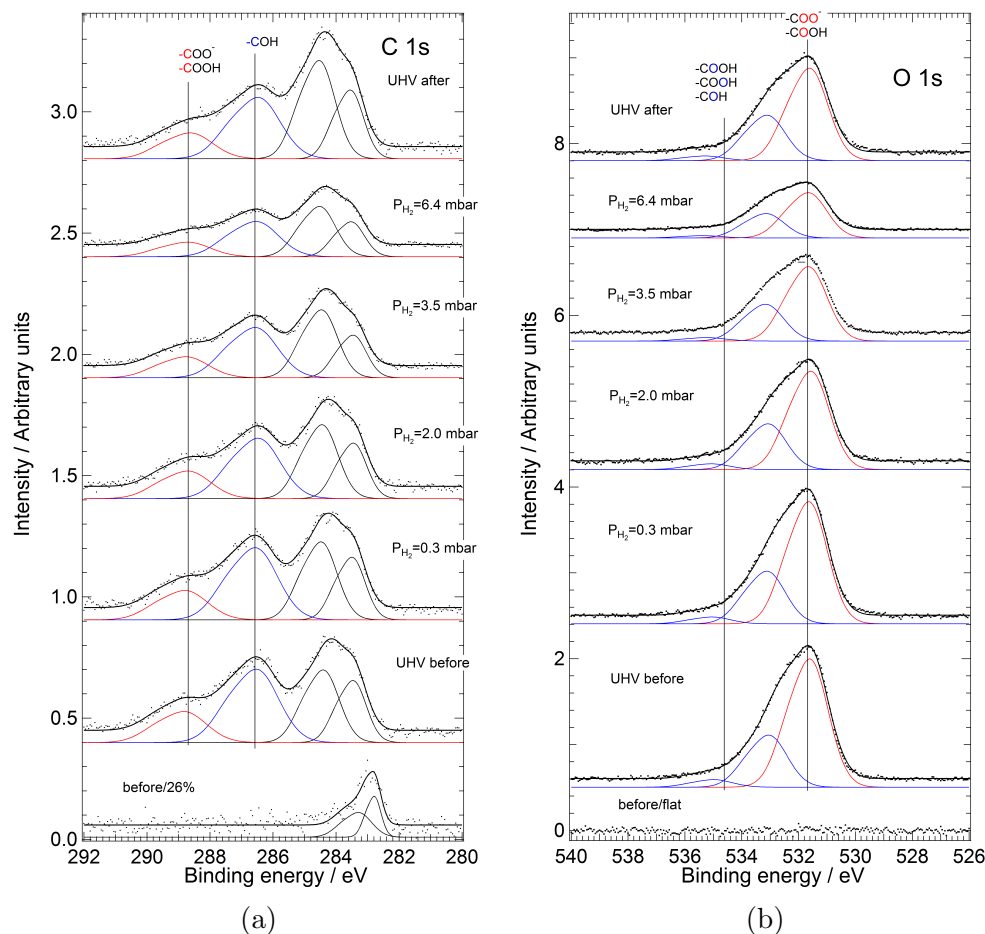


Figure 3.15: Ambient pressure (AP) XP-spectra of (R,R)-tartaric acid layer on Ni{100} at elevated hydrogen pressures in the (a) C 1s region and (b) O 1s region. The spectra were recorded in the near-ambient pressure XPS (NAP-XPS) facility in the University of Manchester using Al  $K_{\alpha}$  anode ( $h\nu=1486.7$  eV) as an X-ray source. The black thick dots are the raw spectra and the black thick lines are the fitted curves. The solid coloured curves are the individual peaks. Dosing conditions of TA:  $T_{\text{sample}} \approx 352\text{-}315$  K,  $T_{\text{evaporator}} \approx 412\text{-}417$  K,  $P_{\text{base}} \approx 1 \times 10^{-9}$  mbar,  $P_{\text{dosing}} \approx 8 \times 10^{-9}\text{-}1 \times 10^{-8}$  mbar, Deposition time  $\approx 90$  min/saturated layer.

The XP-spectra of the TA layer under UHV conditions (Fig. 3.15/UHV before and Fig. 3.16c-3.16d/room temperature) show three peaks in the O 1s region at 531.6-531.7 eV, at 533.1 eV and at 535.0-535.2 eV and four peaks in the C 1s region at 283.5 eV, 284.4-284.5 eV, 286.5-286.6 eV and 288.8-288.9 eV. The peaks are assigned in a similar fashion to the TA top-up XP-spectra on Ni{100} at  $T \approx 303\text{-}304$  K (Fig. 3.2a-3.2b). The area ratio ( $\frac{[COO^- + COOH(ads)]}{[COOH + COOH + COH(nonads)]}$ ) in the O 1s spectra in Fig. 3.15b/UHV before and 3.16d/room temperature is  $\sim 2.2:1$  and  $\sim 2:1$ , respectively, which suggest that TA in this layer chemisorbs on the nickel surface in a bitartrate geometry ( $\mu_4$ , Fig. 3.1). There is a discrepancy with the saturated layer in the O 1s spectrum in Fig. 3.2b where the area ratio of

the same peaks was  $\sim 1.3:1$ . This can be explained by two effects: the dosing temperature in these conditions is above room temperature ( $\sim 352-315$  K, it is worth mentioning that the referred dosing temperature is the temperature of the thermocouple on the UHV manipulator, since there was no thermocouple on the sample holder in the UHV manipulator). A preference for forming bitartrate phases at higher temperatures was found on Cu{110} [59, 60], Ni{110} [33] and Ni{111} [36]. In addition, step anneal O 1s XP-spectra of the saturated layer (Fig. 3.3b) show conversion of  $\text{HTA}^-$  species to  $\text{TA}^{2-}$  upon heating to 353 K, and it was related to the bridging of the kinetic barrier related to this conversion. Furthermore, at this temperature, the conversion to  $\text{HTA}^-$  phase might hindered by the lower amount of adsorbed hydrogen which will cause reprotonation of one of the carboxylate groups [36, 137, 138]. The ratio of the area of the peak at 286.5-286.6 eV and the area of the peak at 288.8-288.9 eV ( $\frac{[\text{COH}]}{[\text{COO}^-/\text{COOH}]}$ ) in the C 1s spectra in Fig. 3.15a/UHV before and Fig. 3.16c)/room temperature is  $\sim 2.4:1$ .

Exposing the TA overlayer to elevated hydrogen pressures (Fig. 3.15) causes a decrease in the area ratio ( $\frac{[\text{COO}^- + \text{COOH}(\text{ads})]}{[\text{COOH} + \text{COOH} + \text{COH}(\text{nonads})]}$ ) in the O 1s spectra in Fig. 3.15b, from 2.2:1 (UHV before) to 1.7:1 at  $P_{\text{H}_2} = 6.4$  mbar, implying the protonation of one of the carboxylate groups by the infinite source of hydrogen from the gas phase. The peak at 535.0 eV (O 1s spectra in Fig. 3.15b) shifts to 535.4 eV at  $P_{\text{H}_2} = 6.4$  mbar, suggesting stronger hydrogen bonds in this layer. Upon evacuation of the hydrogen gas from the NAP-cell (UHV after), the area ratio ( $\frac{[\text{COO}^- + \text{COOH}(\text{ads})]}{[\text{COOH} + \text{COOH} + \text{COH}(\text{nonads})]}$ ) in the O 1s spectrum in Fig. 3.15b increases to 1.8:1. In the C 1s region (Fig. 3.15a), we cannot observe any significant changes in binding energy and area ratio ( $\frac{[\text{COH}]}{[\text{COO}^-/\text{COOH}]}$ ), upon exposing the TA layer to elevated hydrogen pressures. The interesting feature is the increase in the area of the peaks at 283.4-283.6 eV and 284.4-284.5 eV with respect to the XPS fitted area of the TA molecule, as a function of hydrogen pressure. These peaks are associated with decomposition fragments and the increase of the signal occurs even upon evacuation of the hydrogen gas from the NAP-cell (UHV after). This feature can be either related to decomposition of TA, induced by the presence of elevated hydrogen pressures or adsorption of adventitious carbon from the background pressure of the NAP-cell.

Heating the TA layer under the presence of  $P_{\text{H}_2} = 6.4$  mbar (Fig. 3.16a-3.16b) to 372 K and 418 K does not change significantly the signal nor the chemical state of the molecule, apart from some increase in the signal at 284.3-284.5 eV. On the other hand, heating the TA layer under UHV conditions (Fig. 3.16c-3.16d) to 380 K and 394 K causes reduction in the TA C 1s XPS signal by  $\sim 14\%$  and  $\sim 28\%$ , respectively (Fig. 3.16c), with respect to the TA signal at room temper-

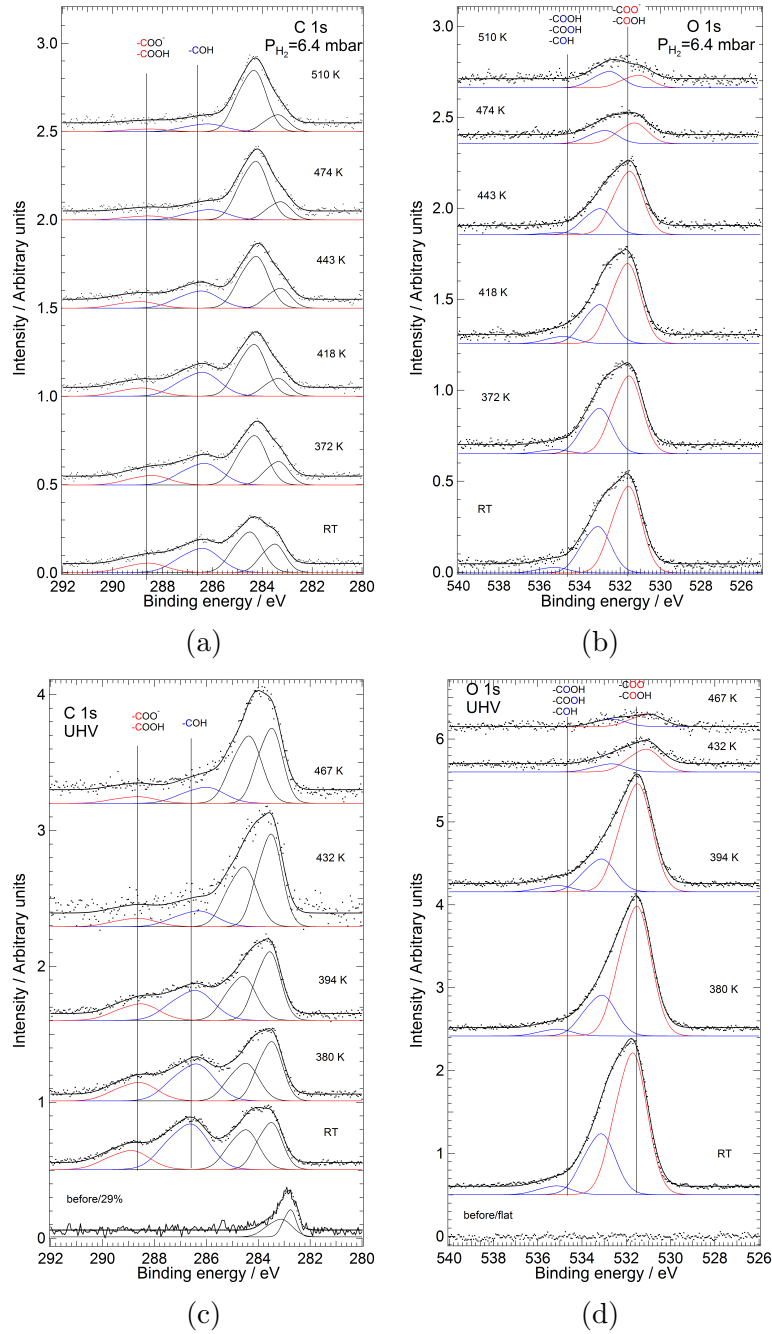


Figure 3.16: Comparison of step anneal XP-spectra of the TA layer on Ni{100} under the presence of  $P_{H_2} = 6.4$  mbar (top panel) and under UHV conditions (bottom panel). The spectra were recorded in the C 1s region (a+c) and O 1s region (b+d). The spectra were recorded in the near-ambient pressure XPS (NAP-XPS) facility in the University of Manchester using Al  $K_{\alpha}$  anode ( $h\nu = 1486.7$  eV) as an X-ray source. The black thick dots are the raw spectra and the black thick lines are the fitted curves. The solid coloured curves are the individual peaks. Dosing conditions (top panel):  $T_{\text{sample}} \approx 352\text{--}315$  K,  $T_{\text{evaporator}} \approx 412\text{--}417$  K,  $P_{\text{base}} \approx 1 \times 10^{-9}$  mbar,  $P_{\text{dosing}} \approx 8 \times 10^{-9}\text{--}1 \times 10^{-8}$  mbar, Deposition time  $\approx 90$  min/saturated layer. Dosing conditions (bottom panel):  $T_{\text{sample}} \approx 340\text{--}319$  K,  $T_{\text{evaporator}} \approx 415\text{--}416$  K,  $P_{\text{dosing}} 1 \times 10^{-8}$  mbar, Deposition time  $\approx 91$  min.

ature, whereas the O 1s XPS signal was reduced by  $\sim 16\%$  and  $\sim 30\%$ , respectively. In addition the area ratio ( $\frac{[COO^-+COOH(ads)]}{[COOH+COOH+COH(nonads)]}$ ) in the O 1s spectra in Fig. 3.16d increases from 2:1 to 2.7:1 and 2.8:1, respectively. In the C 1s region (Fig. 3.16c) we can observe a significant increase in the signal corresponding to decomposition products (peaks at 283.5-283.6 eV and 284.5-284.6 eV). Further heating to 432 K causes further reduction in the TA XPS signal in both regions ( $\sim 63\%$ /C 1s/ Fig. 3.16c,  $\sim 85\%$ /O 1s/ Fig. 3.16d, always with respect to the TA signal at room temperature) with simultaneously increase in the signal corresponding to decomposition products in the C 1s region (Fig. 3.16c) suggesting almost full decomposition of the TA molecule. On the other hand, at 443 K under the presence of  $P_{H_2} = 6.4$  mbar (Fig. 3.16a-3.16b), the XPS signal of the TA molecule in the C 1s and O 1s region decreases by  $\sim 29\%$  and  $34\%$ , respectively. The area ratio ( $\frac{[COO^-+COOH(ads)]}{[COOH+COOH+COH(nonads)]}$ ) in the O 1s spectrum in Fig. 3.16b increases to 2.3:1. The onset of decomposition under these conditions occurs by heating to 474 K, when the signal of the TA molecule drops by  $\sim 58\%$  (C 1s spectrum in Fig. 3.16a) and  $\sim 76\%$  (O 1s spectrum in Fig. 3.16b), always with respect to the layer at room temperature (Fig. 3.16a-3.16b). Small traces of TA molecule may be present even at  $T \geq 500$  K, under both conditions (Fig. 3.16). From the step anneal XP-spectra, it is obvious that the presence of hydrogen stabilises thermally the TA molecule on the Ni{100} surface which might be related to unavailability of adsorption sites for decomposition products as a result of the increased hydrogen concentration on the nickel surface. TPD results upon adsorption of TA on Ni{111} surface [39] show desorption of masses corresponding to  $CO_2$ , CO,  $H_2O$  and  $H_2$ . This decomposition mechanism suggest that the metal-molecule bond is stronger than the intermolecular bonds, which, according to Lorenzo et al (2002) [60], accounted partially for the lower thermal stability of the bitartrate phase with respect to the monotartrate, since the former has the highest heat of adsorption [60]. The presence of hydrogen in our study, increases the level of protonation of the TA molecule, increasing the  $HTA^-:TA^{2-}$  ratio, increasing the thermal stability of the molecule. The increased amount  $HTA^-$  species observed in the O 1s spectra in Fig. 3.3b with respect to the O 1s spectra in Fig. 3.16d might explain the increased thermal stability of the former system, however we have to treat this comparison cautiously, since we are comparing two different UHV chambers, with different sample configurations.

### 3.3.4 Tartaric acid on clean Ni{100}/Elevated H<sub>2</sub>O pressures

#### XPS Results

Figure 3.17 show AP XP-spectra of the TA layer on Ni{100}. The spectra were obtained upon dosing TA onto nickel surface and then exposing the TA layer to increasing water pressures. The XP spectra have detected no presence of oxygen before dosing TA (O 1s spectrum in Fig. 3.17b). The XPS area (obtained upon fitting) of the carbon impurities (present before dosing) were  $\sim 35\%$  (Fig. 3.17a) of the XPS area (obtained upon fitting) of the TA signal (excluding impurities) in the C 1s spectrum in Fig. 3.17a (UHV before).

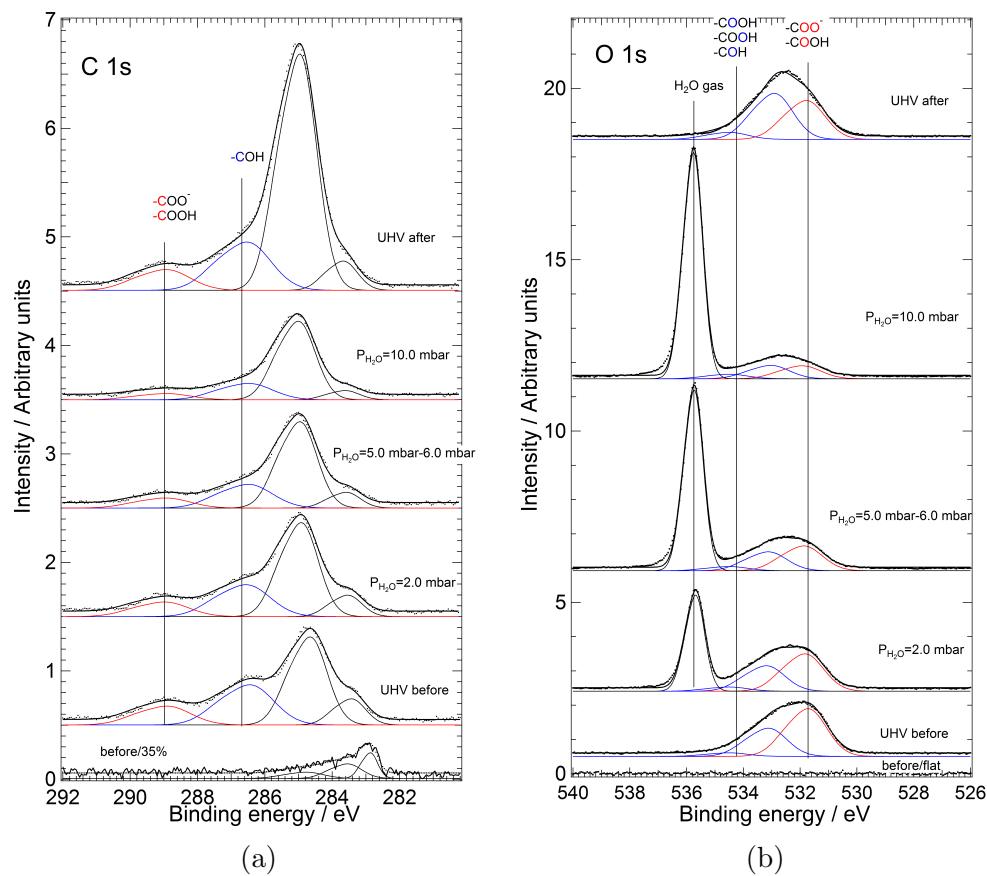


Figure 3.17: Ambient pressure (AP) XP-spectra of (R,R)-tartaric acid layer on Ni{100} at elevated water pressures in the (a) C 1s region and (b) O 1s region. The spectra were recorded in the near-ambient pressure XPS (NAP-XPS) facility in the University of Manchester using Al K $\alpha$  anode ( $h\nu=1486.7$  eV) as an X-ray source. The black thick dots are the raw spectra and the black thick lines are the fitted curves. The solid coloured curves are the individual peaks. Dosing conditions of TA:  $T_{\text{sample}} \approx 332\text{-}314$  K,  $T_{\text{evaporator}} \approx 417\text{-}418$  K,  $P_{\text{base}} \approx 2 \times 10^{-9}$  mbar,  $P_{\text{dosing}} \approx 1 \times 10^{-7}\text{-}5 \times 10^{-8}$  mbar, Deposition time  $\approx 82$  min.

The XP-spectra under UHV conditions show four resolved peaks in the C 1s

region at 283.4 eV, 284.7 eV, 286.5 eV and 288.9 eV (Fig. 3.17a) and three peaks at 531.7 eV, 533.1 eV, 534.5 eV in the O 1s region (Fig. 3.17b), assigned in a similar fashion to the TA top-up XP-spectra on Ni{100} at 303 K (Fig. 3.2a-3.2b). The area ratio ( $\frac{[COO^-+COOH(ads)]}{[COOH+COOH+COH(nonads)]}$ ) in the O 1s spectrum in Fig. 3.17b is  $\sim 1.5:1$ . The reduced ratio with respect to the O 1s spectra in Fig. 3.15b and Fig. 3.16d can be explained by the higher deposition rate of the molecule during dosing conditions (as a result of the increased pressure of the molecule during deposition), especially during the early stages of deposition ( $P_{dosing}$  was  $\sim 1 \times 10^{-7}$  mbar when the gate valve was opened and drop to  $\sim 5 \times 10^{-8}$  mbar when the deposition of the TA molecule was finished) and the lower sample temperature (332-314 K) both with respect to the dosing conditions in Fig. 3.15 and 3.16. Again, the referred dosing temperature is the temperature of the thermocouple on the UHV manipulator, since there was no thermocouple on the sample holder in the UHV manipulator. Both features increased the extent of protonation of one of the carboxylate groups and induce generation of some HTA<sup>-</sup> species along with the predominant TA<sup>2-</sup> ( $\mu_4$ ) phase. Introducing H<sub>2</sub>O gas in the NAP-cell increased even more the extent of protonation of the TA molecule. At  $P_{H_2O}=10$  mbar the area ratio ( $\frac{[COO^-+COOH(ads)]}{[COOH+COOH+COH(nonads)]}$ ) in the O 1s spectrum in Fig. 3.17b is  $\sim 0.7:1$ , implying the predominant presence of the HTA<sup>-</sup> form of the TA molecule, which supports an  $\mu_2$  (monotartrate)/ $\mu_3$  adsorption configuration (Fig. 3.1). This change in configuration due to the presence of H<sub>2</sub>O molecules in the gas phase was also observed under the presence of elevated H<sub>2</sub> pressures (O 1s spectra in Fig. 3.15b). The peak at 531.7 eV in the O 1s region (Fig. 3.17b) shifts to 531.9 eV at  $P_{H_2O}=10$  mbar. The XPS area of the peak at 534.5 (which is associated with TA groups with a high degree of protonation) increases from 4% of the total XPS area to 15% at  $P_{H_2O}=10$  mbar and drops to 8% upon evacuation of the water vapour from the NAP-cell (UHV after). This increase is related to the formation of hydrogen bonds between the non-chemisorbed moieties of the TA molecule and the H<sub>2</sub>O molecules. The chemical configuration of TA molecule does not change upon evacuation of the water vapour from the NAP-cell, suggesting that the change in the adsorption configuration of the TA molecule upon interaction with  $P_{H_2O}=10$  mbar is non-reversible. In the C 1s region (Fig. 3.17a), we can observe an increase in the signal at 284.7 eV (associated with decomposition fragments) with respect to the XPS fitted area of the TA molecule, as a function of increased water pressure and presence of the sample in the NAP-cell with subsequent shift of the peak peak position towards high binding energies (BE=285.0 eV at  $P_{H_2O}=10$  mbar). This feature can be related either to adsorption of impurities from the background pressure of the NAP-cell (adventitious

carbon or CO) or decomposition of TA, induced by the presence of elevated water pressures. The latter hypothesis is rejected by the XP-spectra upon evacuation of the water vapour from the NAP-cell (UHV after), which in fact show a 27% (C 1s region) and 16% (O 1s region) increase in the fitted XPS area corresponding to the TA molecule with respect to the area before the exposure of the sample to elevated H<sub>2</sub>O pressures (UHV before). This is most likely explained by the change in the configuration of the TA molecule upon exposures to elevated water pressures (from  $\mu_4$  to  $\mu_2/\mu_3$  adsorption geometry), since in the  $\mu_2/\mu_3$  adsorption geometry, one of the carboxyl groups is dangling from the surface (Fig. 3.1) and its signal is not attenuated from the rest of the molecule.

### 3.4 Discussion

This study provides evidence of the influence of the temperature of the Ni{100} surface, the deposition rate of the TA molecule and its surface coverage on the chemical state and adsorption geometry of (R,R)-tartaric acid (TA) on clean Ni{100}. The formation of bitartrate phase of the TA molecule (TA<sup>2-</sup>) which supports an  $\mu_4$  adsorption geometry is favoured as we increase the temperature of the crystal away from room temperature. Cooling the crystal towards room temperature while having high coverages of TA molecule, causes the formation of HTA<sup>-</sup> species (which support an  $\mu_2/\mu_3$  adsorption geometry). High deposition rates (deposition time  $\leq$  24 min/saturated layer) at T<400 K as well as the presence of elevated pressures of H<sub>2</sub> and H<sub>2</sub>O also cause the formation of HTA<sup>-</sup> species. Depending on the chemical state, adsorption configuration of the TA molecule, and the substrate (Ni{100} or NiO/Ni{100}), the C=O/COO<sup>-</sup> groups of the TA molecule are tilted by  $\sim$  42-69° with respect to surface plane of the nickel substrate. Under UHV conditions, TA fully decomposes on Ni{100} at T>440 K. Its thermal stability is enhanced under the presence of P<sub>H<sub>2</sub></sub>=6.4 mbar. TPD of the (R,R)TA/Ni{111} system [36], show that at high coverages, the molecule decomposes at T>400 K. The merit of TA (and other hydroxy-dicarboxylic acids), being the most effective modifier for the enantioselective hydrogenation of MAA, in comparison with other chiral modifiers [18], might be originated from its thermal stability under modification and reaction conditions [12, 16, 24]. According to Ref.[37, 38], the optimum modification temperature for attaining the highest enantioselectivity using TA as modifier is 350 K. Kukula et al (2001) [25] suggested that increasing the temperature during modification of TA on Raney nickel, increases the optical yield. In this study, at 350 K under UHV conditions, at lower deposi-

tion rate (Fig. 3.3, top panel and Fig. 3.16, bottom panel) the TA chemisorbs on the nickel surface, mainly in a bitartrate geometry ( $\mu_4$ ) whereas at high dosing rate at the same temperature and pressure (Fig. 3.2, bottom panel and Fig. 3.3, bottom panel), the XP-spectra suggest the predominant presence of HTA<sup>-</sup> species on the nickel surface. The conversion to the bitartate phase under these dosing conditions was facile at  $T \geq 400$  K (Fig. 3.3, bottom panel). The dosing rate of the molecule can model the concentration of the modified under reaction conditions. Modification of Raney nickel [25] and Ni/SiO<sub>2</sub> catalyst [24] with TA show that the enantioselectivity of the catalyst as a function of TA concentration goes through a maximum. The presence of elevated pressures of H<sub>2</sub>O (Fig. 3.17) favoured the formation of HTA<sup>-</sup> species. According to Keane (1997)[24], the use of water as modification medium decreases the amount of adsorbed TA molecules on Ni/SiO<sub>2</sub> catalyst and increases the amount of leached nickel with respect to the use alcoholic solvents as modification medium (methanol, ethanol and 1-butanol), while at the same time decreases the selectivity and activity of the chirally modified Ni/SiO<sub>2</sub> catalyst.

The interaction of TA on oxidised/hydroxylated Ni{100} created species which its decomposition temperature resembles the decomposition temperature of the nickel (II) tartrate complex [32], as it was also observed in the TA/NiO{111}/Ni{111} system [39]. This work approach more the enantioselective catalysis conditions, since the modification occurs from aqueous solution and the catalyst itself is exposed to air before the modification [39]. The decomposition temperature of the TA molecule on oxidised/hydroxylated Ni{100} points to the formation of nickel tartrate species. Based on XPS results of modified Raney nickel catalyst with (R,R) tartaric acid [32], the stoichiometry of nickel, carbon and oxygen on the surface layer resembles the stoichiometry of nickel (II) tartrate complex. Nickel tartrate species were generated upon adsorption of TA from solution (at low pH) on Ni{111} single crystal [38]. The high solubility of the nickel tartrate species in aqueous solution in combination with the strong electrostatic interaction between the charged tartrate species and the Ni<sup>2+</sup> substrate, could assist the etching of the nickel catalyst during modification [39], and generate chiral surfaces/arrangements similar to those shown in Ref.[8]. The work of McFadden et al. (1996) [8], suggested, that a single crystal can produce intrinsically chiral surfaces if it is cut to expose high Miller indices planes. If at these high Miller indices, the step lengths on either side of the kink site are uneven, then the kink sites can be considered chiral [8]. It is worth mentioning that chiral films have been grown on achiral Au surface, by electrodepositing copper oxide films in the presence of tartrate anions [139]. Adsorption of L-lysine [55] and S-alanine [56–58]

on Cu{100} caused the generation of {3 1 17} chiral facets whereas adsorption of (R,R)-tartaric acid on Ni{110} in its bitartrate form [34], caused relaxation and reconstruction of the nickel surface, resulting in chiral footprint on the surface. Previous studies [51, 52] have shown that two enantiomers of a chiral molecule present different adsorption energetics when they are adsorbed on a chiral surface [51], whereas a chiral surface itself is more reactive towards one enantiomer of a chiral molecule with respect to the other [52]. In addition, interaction of pure R and S propylene oxide on chiral Cu surfaces (Cu{643}) [53], show that the desorption of the enantiopure molecule depends on the chirality of the Cu{643} surface. This kind of different adsorption behaviour, should be expected also for the two pro-chiral configurations of the  $\beta$ -ketoester reactant on a chiral nickel substrate during the hydrogenation reaction [45].

During the actual modification procedure at 350 K using TA as modifier, depending on the concentration of the modifier and the modification medium we will have either  $\text{TA}^{2-}$  or  $\text{HTA}^-$  as predominant chemical species of tartaric acid on the Ni{100} facet. The former is favoured at low modifier concentration and the latter at high modifier concentrations and/or by using water as modification medium. Kukula et al (2002) [26] have suggested that the highest enantioselectivity of Raney nickel catalyst modified with (R,R) tartaric acid is achieved at  $T_{\text{reaction}}=333$  K with THF or no solvent as reaction medium, at  $P_{\text{H}_2}\approx 100$  bar. In Ref.[18] it is reported that aprotic solvents such as THF or methyl propionate are the most suitable solvents and highest enantioselectivity using (R,R)-tartaric acid as modifier is attained at  $T_{\text{reaction}}=313$  K. Izumi (1983) [16] have present data upon modification of Raney nickel with (R,R) tartaric acid, in which the reaction temperature as a function of optical yield, goes through a maximum between  $\sim 313$ -333 K. Under the aforementioned hydrogenation conditions we will expect the predominant presence of  $\text{HTA}^-$  species on the Ni{100} surface (O 1s spectra in Fig. 3.15b and Fig. 3.16b). Under modification and reaction conditions using NiO/Ni{100} as a catalyst (in the absence of elevated hydrogen pressure) the XP-spectra of our study suggest the coexistence of nickel monotartrate and nickel bitartrate species on the NiO/Ni{100} substrate (O 1s spectra in Fig. 3.12b), with most likely 1 and 2 point adsorption geometries, respectively. These adsorption geometries could not imprint a chiral environment on the nickel substrate. Only species with at least  $\mu_3$  or  $\mu_4$  adsorption geometries could create such an environment and generate chiral surfaces through etching of the crystal. The strong electrostatic interaction between the negatively charged carboxylate groups and the  $\text{Ni}^{2+}$  substrate [39] makes the presence of an  $\mu_3$  adsorption geometry (which involves adsorption of TA on the  $\text{Ni}^{2+}$  substrate without deprotonation of ones

of its carboxyl groups, Fig. 3.1), highly unlikely. Based on the XP-spectra of our study, an  $\mu_4$  (bitartrate) geometry in TA/NiO{111}/Ni{100} overlayer, suggests an excess of positive charge on the nickel surface.

The concentration of modifier on the nickel surface upon the washing procedure depends on the modification temperature and pH of the tartaric acid solution [38]), with increase in the pH, causing reduction in the concentration of the modifier on the Ni{111} surface [38]. The optimum pH in terms of enantioselectivity is 5 [38]. According to Ref.[37] high coverages of pre-adsorbed TA molecules on Ni{111}, forbade the interaction of the MAA with the nickel surface. XPS [48] and RAIRS [42] studies of modified polycrystalline nickel and Ni{111}, respectively, with (S)-aspartic acid (upon washing the catalyst) showed that at optimum (in terms of enantioselectivity) conditions, the aspartic acid is untraceable spectroscopically. These studies [42, 48] provided evidence that asymmetric hydrogenation could occur at low or even in the absence of a chiral modifier, during the reaction. If the coverage of the modifier is low (after washing) it is most likely that the chiral modification will occur by generation of chiral surfaces from the  $\mu_4$  nickel bitartrate species, as described above. The presence of  $\text{HTA}^-$  species, especially at higher TA concentration on the Ni{100} surface, could induce the interaction of the molecule with the  $\beta$ -ketoester reactant via hydrogen bonding and assisting its enantioselective hydrogenation through stabilising a pro-chiral configuration over the other. Modification of Ni{111} with (R,R)-tartaric acid from solution at 350 K following washing of the catalyst, caused also generation of  $\text{HTA}^-$  species on the nickel surface [38]. According to the aforementioned study [38], under these modification conditions and upon immersion of the crystal in an MAA solution, there was an enhancement of the diketone:enol ratio of the MAA molecule on Ni{111} surface with respect to the modification at 300 K [38]. According to Ref.[38] the origin of the enantioselectivity of this system might be due to the formation of hydrogen bonds between the diketone and the  $\text{HTA}^-$  species in orientation that will preferably generate the R-enantiomer as a product during the hydrogenation reaction.

### 3.5 Conclusions

This study characterises the influence of the temperature of the crystal, the dosing rate of the TA molecule and its surface coverage on the chemical state and adsorption geometry of TA on clean Ni{100}. The bitartrate phase in which both carboxyl groups of the TA molecule are deprotonated ( $\text{TA}^{2-}$ ) and chemisorbed on

the nickel surface in an  $\mu_4$  adsorption geometry is favoured as we increase the temperature of the crystal away from room temperature. Cooling the crystal towards room temperature while having high coverages of TA molecule, causes the formation of HTA<sup>-</sup> species (which support an  $\mu_2/\mu_3$  adsorption geometry). High deposition rates (deposition time  $\leq 24$  min/saturated layer) at  $T < 400$  K as well as the presence of elevated pressures of H<sub>2</sub> and H<sub>2</sub>O also cause the formation of HTA<sup>-</sup> species. Under UHV conditions, TA fully decomposes on Ni{100} at  $T > 440$  K. Its thermal stability is further enhanced under the presence of  $P_{H_2} = 6.4$  mbar. Deposition of TA on oxidised Ni{100}, causes the generation of tartrate species whose thermal stability resembles the thermal behaviour of the nickel (II) tartrate complex, since they decomposed fully on NiO/Ni{100} substrate at  $T > 650$  K. Their presence under modification conditions could assist the etching of the nickel surface and induce the generation of chiral surfaces/arrangements. On the other hand, the presence of HTA<sup>-</sup> species on Ni{100} under optimum modification and reaction conditions could potentially create an enantiospecific system through interaction of the substrate and the modifier via hydrogen bonding. Depending on the chemical state, adsorption configuration of the TA molecule, and the substrate (Ni{100} or NiO/Ni{100}), the C=O/COO<sup>-</sup> groups of the TA molecule are tilted by  $\sim 42$ - $69^\circ$  with respect to the surface plane of the nickel substrate.

# Chapter 4

## Interaction of (S)-alanine on clean Ni{100} under UHV and elevated hydrogen pressures

### Abstract

Enantioselectivity is a key aspect in the field of heterogeneous catalysis, since it can provide products with valuable biological activity. Alanine acts as a chiral modifier in the enantioselective hydrogenation of  $\beta$ -ketoesters. The present study explores the chemical state and thermal stability of (S)-alanine on clean Ni{100} upon depositing the molecule onto the nickel surface at  $T_{\text{sample}}=250$  K, using X-ray photoelectron spectroscopy (XPS) and temperature programmed-XPS (TP-XPS). Alanine at  $\Theta_{\text{Ala}} \leq 0.10$  ML chemisorbs on Ni{100} in both its anionic and neutral form, whereas at  $\Theta_{\text{Ala}} > 0.10$  M some zwitterionic species are formed, which coexist with the anionic and neutral forms of alanine. It is not fully conclusive whether these zwitterionic species belong to the first chemisorbed layer or they are found in a second layer deposited on top of the chemisorbed layer. In the multilayer, alanine is almost exclusively in its zwitterionic form. The multilayer desorbs at  $T \approx 320$  K whereas according to the TP-XP-spectra, alanine decomposes on Ni{100} at  $T \approx 330$ -390 K, depending on the molecule's initial surface coverage. According to angle dependent NEXAFS, the C=O/COO<sup>-</sup> groups of the alanine molecule are tilted by  $\sim 48.5^\circ$  with respect to the plane of the nickel surface.

The chemical state and thermal stability of (S)-alanine on clean Ni{100}, upon depositing the molecule onto the nickel surface at  $T_{\text{sample}}=\text{room temperature}$  ( $T \leq 330$  K), was investigated under the presence of elevated hydrogen pressure conditions using ambient pressure (AP)-XPS. Dosing alanine at room tempera-

ture ( $T \leq 330$  K), causes saturation of the XPS signal without formation of any multilayers. At  $\Theta_{\text{Ala}} \geq 78\%$  sat alanine chemisorbs on Ni{100} in both its anionic and neutral form. AP-XPS has shown that the presence of elevated hydrogen pressures causes increase in the amount of neutral species of alanine on Ni{100} and perhaps the generation of zwitterionic species. Step anneal XP-spectra of the alanine overlayers formed on Ni{100} at room temperature, show that the molecule fully decomposes on Ni{100} at  $T > 460$  K and  $T \geq 400$  K under UHV and elevated hydrogen pressure conditions ( $P_{\text{H}_2} = 6.3$  mbar), respectively. The contribution of this study into the understanding of the mechanism of the chiral modification of the nickel catalyst is discussed at the end of the chapter.

## 4.1 Introduction

The pharmaceutical and agrochemical industry is in demand of more enantiopure chemical compounds since the chirality of the molecule affects their biological activity and response. In addition many enantiopure products are also used as flavours and fragrances [1–5]. In the area of heterogeneous catalysis enantioselectivity could be achieved in several ways, such as attaching a metal to a chiral support or adsorbing a chiral auxiliary to the metal [4]. The merit of using heterogeneous catalysts in comparison with homogeneous is the fact that these catalysts can be easily separated and recycled, can reduce the presence of metal traces in the product, and they can be easily controlled during their use [2, 6]. One great example of an enantioselective catalysed reaction is the hydrogenation of  $\beta$ -ketoesters (such as methyl acetoacetate MAA) using nickel as a catalyst. The reaction generates optically active products, if the catalyst is modified with  $\alpha$ -hydroxyacids (such as tartaric acid) or  $\alpha$ -amino acids (such as alanine) [2, 11, 12, 16]. According to the work of Keane (1994) on silica-supported nickel catalysts [17], alanine is a promising chiral modifier since it not only enhances the enantioselectivity but also improves the reaction rates. The authors suggested that in aqueous solution, alanine presents higher affinity than tartaric acid, for the adsorption on the supported nickel metal [17].

Different studies attempted to understand the mechanism behind the chiral modification of the nickel surface. Adsorption of (R,R)-tartaric acid (TA) on Ni{110} [34] caused the creation of a chiral footprint on the nickel surface, breaking its symmetry. Depositing (R,R)-tartaric acid onto oxidised Ni{111} [39] caused the generation of species similar to nickel tartrate, which could assist the etching of the crystal and generation of chiral defects. Co-adsorption of (R,R)-

tartaric acid [37] and (S)-glutamic acid [40] with MAA on Ni{111} show evidence of interaction between the substrate (MAA) and the chiral modifier in a configuration that will generate the R-product during the hydrogenation reaction. On the other hand, work, on the adsorption of aspartic acid on Ni{111} [41] show evidence of formation of oligosuccinimide clusters which could create a docking position for the substrate.

The adsorption of alanine on different surfaces has been studied extensively, for obtaining spectroscopic and fundamental insights on the interaction of the amino acid on different metals. Of our main interest is the interaction of alanine on Cu{100} and Pd surfaces, since these two elements are the closest ones with nickel, in the periodic table. On Ni{111}, alanine chemisorbs in both zwitterionic and anionic form supporting a bidentate and tridentate geometry, respectively with the latter species being in majority on the nickel surface. The molecule decomposes on Ni{111} at temperatures between 300 K and 450 K, following multistep processes [46]. Exposing the saturated (S)-alanine layer on Ni{111} (0.25 ML) to elevated pressures of H<sub>2</sub>, causes protonation of the amino group of (S)-alanine and reorientation to bidentate geometry, which under the presence of elevated pressures of H<sub>2</sub>, is the majority species on the nickel surface [47].

The interaction of enantiopure and racemic alanine on Cu{100} was studied using STM, RAIRS, LEED and theoretical calculations [56, 57, 140–142]. According to Ref. [56, 140, 142], alanine chemisorbs on Cu{100} in its anionic form in an  $\mu_3$  adsorption geometry, through the two oxygen atoms of the carboxylate group and the nitrogen of the neutral amino group. Alanine forms  $c(2 \times 4)$  superstructures on the Cu{100} surface [56, 140, 142], driven by the presence of intermolecular hydrogen bonds between the hydrogen of the amino group and the oxygen atoms from the carboxylate group. According to STM, LEED and RAIRS studies upon exposing the Cu{100} to racemic alanine (DL-alanine) [56, 140, 142], D and L alanine segregate, creating their own  $c(2 \times 4)$  domains, in disagreement with theoretical calculations from Rankin et al. (2005) [141]. The authors of Ref.[141] suggested that an ordered racemic structure of both enantiomers of alanine on Cu{100} is favoured over the segregation of D and L- alanine. STM study upon adsorbing (S)-alanine on on Cu{100} [56], show that the molecule causes step faceting to  $\langle 310 \rangle$  directions and bunching of these  $\langle 310 \rangle$  steps to generate  $\{3 \ 1 \ 17\}$  facets. The faceting and the bunching is enhanced upon annealing the crystal [56]. According to Ref.[57, 58], adsorption of S-alanine on Cu{100} and subsequent annealing of the surface, will cause the generation of both  $\text{Cu}\{3 \ 1 \ 17\}^{\text{R}}$  and  $\text{Cu}\{3 \ 1 \ 17\}^{\text{S}}$  facets, with the latter being in slightly greater abundance.

The adsorption of alanine on Pd{111} was investigated by Gao et al (2007)

[143] and Mahapatra et al (2014) [64]. Gao et al (2007) [143] proposed that alanine adsorbs in its zwitterionic form on Pd{111} in the first layer whereas in the multilayer regime alanine exists both in its zwitterionic and neutral form. The multilayer desorbs at temperatures between 350 K and 380 K [143]. The dissociation of alanine on Pd{111} occurs via C-C cleaving, which leads to desorption of CO<sub>2</sub> and CO desorption from the COO<sup>-</sup> moiety, and desorption of ethylamine or HCN from the CH<sub>3</sub>-CH-NH<sub>3</sub><sup>+</sup> [143]. Mahapatra et al (2014) [64] have found evidence of formation of both zwitterionic and anionic alanine on Pd{111} surface, with the isolated anionic form of the molecule, based on DFT calculations, being significantly more stable. The molecule was found to construct dimers or tetramers on Pd{111}, which could potentially behave as chiral templates [64].

In this study we will explore the chemical state, molecular orientation and thermal stability of (S)-alanine on clean Ni{100} using XPS, TP-XPS and angle-dependent NEXAFS. In addition, we have investigated the influence of elevated pressures of H<sub>2</sub> (up to 6.3 mbar) on the chemical state and the thermal stability of alanine on Ni{100}, using AP-XPS. The elevated pressures of H<sub>2</sub> were used to approach more realistic (reaction) conditions. All the data were analysed by the author. The synchrotron (UHV) data, obtained in the Elettra synchrotron in Trieste (Italy) in the UHV endstation of the SuperESCA beamline, were collected by Jacopo Ardini (University of Reading), by Dr. Silvia Baldanza (University of Reading), by Dr. Chanan Euaruksakul (University of Reading), by Dr. Rachel Price (University of Reading) and by Prof. Georg Held (University of Reading). The AP-XPS data, obtained in the NAP-XPS facility in the University of Manchester, were collected by the author and by Tom Statham. The overall contribution of the author to this study is  $\sim 70\%$  of the total work.

## 4.2 Experimental methods

The XPS and NEXAFS experiments were performed in two different UHV chambers. The UHV experiments were performed in the Elettra synchrotron in Trieste (Italy) in the UHV endstation of the SuperESCA beamline, which provides a horizontally polarized X-ray beam. The high pressure experiments took place in the near-ambient pressure XPS (NAP-XPS) facility in the University of Manchester using a Al K<sub>α</sub> anode ( $h\nu=1486.7$  eV) as an X-ray source. The dosing and the sputtering occurred in the preparation chambers. The XPS and NEXAFS experiments were performed in an analysis chamber. The XPS experiments were performed using a 150 mm hemispherical electron analyser in the SuperESCA

beamline and a SPECS system in the NAP-XPS facility in the University of Manchester. The base pressure of both chambers in the SuperESCA endstation was in the  $10^{-10}$  mbar range whereas in the NAP-XPS facility was in the  $10^{-9}$  mbar range. Sample cleaning in the SuperESCA endstation, was achieved by cycles of sputtering at 170 K ( $P=3 \times 10^{-6}$  mbar) with subsequent annealing to 443 K, followed by cycles of oxygen treatment (dose  $O_2$  at  $P=1 \times 10^{-8}$  mbar at 170 K for 1-3 minutes and subsequent anneal to  $\sim 1100$  K). In the NAP-XPS facility, cleaning was achieved by sputtering at  $\sim 400$  K ( $P=2 \times 10^{-7}$  mbar/1.5 kV) followed by oxygen treatment (dose  $O_2$  at  $P=1 \times 10^{-7}$  mbar at  $T \approx 400$  K for 4 minutes and subsequent anneal to  $\sim 706$  K). Sample cleaning was confirmed by XPS. In the SuperESCA beamline, the nickel crystal was mounted at the base of a liquid nitrogen-cooled coldfinger. The sample was heated resistively and its temperature was adjusted using a programmable temperature controller and measured using a spot welded thermocouple fixed on the sample. In the NAP-XPS facility the sample was mounted on a sample holder and again its temperature was measured using a spot welded thermocouple fixed on the sample. The sample was heated both resistively and via an e-beam heater. For the purpose of NAP-XPS experiments, the sample was mounted inside a NAP-cell which was docked into the analyser. With this configuration the pressure inside the analysis chamber did not change significantly during the exposure of the crystal to high pressures.

(S)-alanine (L-alanine) was dosed from a home built evaporator which was mounted on the chamber through a gate valve. The evaporator consisted of a stainless steel crucible containing a glass tube filled with alanine powder. Deposition of the alanine molecule was performed by resistively heating the crucibles to  $\sim 418$ - $428$  K and opening the gate valve to the chamber. The measurement of the temperature was achieved by K-type thermocouples spot-welded on the crucibles. A pressure rise to  $\sim 4 \times 10^{-10}$ - $3 \times 10^{-9}$  mbar was observed during dosing of the molecule in the preparation chamber of the SuperESCA endstation, and to  $\sim 2 \times 10^{-9}$ - $2 \times 10^{-7}$  mbar in the NAP-XPS facility. Due to differences in pumping speed, there was no good correlation between dosing time and coverage, therefore the coverage was determined using XPS (see Results section).

The synchrotron XPS data were obtained in the C 1s ( $h\nu=400$  eV), N 1s ( $h\nu=510$  eV) and O 1s region ( $h\nu=650$  eV) using pass energies of 10 eV, 10 eV and 15 eV, respectively. Spectra of the Fermi edge were also obtained, every time the monochromator was moved, to calibrate the offset of the binding energy axis. The ambient pressure (AP)-XPS data were also acquired in C 1s, N 1s and O 1s, using an Al  $K_{\alpha}$  anode ( $h\nu=1486.7$  eV) as an X-ray source and 30 eV as pass energy. The offset of the binding energy was calibrated using the position of the Ni

2p peak (BE=852.7 eV). For quantitative analysis, all the spectra were normalised at the low binding region followed by linear subtraction of the background. In order to study the temperature dependence of alanine on Ni{100}, temperature-programmed XP-spectra were acquired at a rate of  $\sim 20$  s/spectrum, by heating the sample at a constant rate ( $8 \text{ K min}^{-1}$ ) in front of the analyser while recording alternating N 1s and C 1s or O 1s and C 1s spectra. During the TP-XPS experiments the sample was moved under the beam to minimise any potential beam damage.

The NEXAFS spectra were obtained in the O K-edge region, by detecting O KLL Auger electrons with kinetic energies of 505 eV. In order to determine the molecular orientation of alanine on Ni{100}, angle dependent NEXAFS spectra were obtained using three different angles of incidence:  $\theta = 0^\circ$  (normal incidence),  $\theta = 35^\circ$  and  $\theta = 70^\circ$  (normal emission), where  $\theta$  is the angle between the electric field vector and the surface plane. All the spectra were normalised in the low photon energy region and corrected for the transmission of the beamline through dividing by the photon flux ( $I_0$ ). The  $I_0$  was collected using the drain current of the last refocusing mirror. Spectra of the clean surface, corrected in the same way, were subtracted as background. Finally the spectra were also normalised with respect to the step height, at energies above all oxygen resonances.

## 4.3 Results

### 4.3.1 Alanine on clean Ni{100}/UHV

#### XPS Results

Figure 4.1 shows C 1s, N 1s and O 1s XP-spectra, as a function of surface coverage obtained upon dosing (S)-alanine onto Ni{100} at  $T_{\text{sample}}=250 \text{ K}$ . The coverage (in ML) was calibrated by comparison of O 1s spectra acquired at  $h\nu=1000 \text{ eV}$  with those of adsorbed CO to saturation at room temperature (293 K). According to Ref.[144] the saturation coverage of adsorbed CO on Ni{100} at room temperature is  $\Theta=0.5 \text{ ML}$

Five peaks are observed in the N 1s region at 397.3 eV, 398.0-398.1 eV, 399.4-399.7 eV, 400.3-401 eV and at 401.8-402.2 eV (Fig. 4.1b). The peak at 397.3 eV is associated with atomic nitrogen whereas the peak at 398.0-398.1 eV is related to decomposition fragments/surface impurities such HCN or  $\text{NH}_2\text{CHCH}_3$  species. The peak at 399.4-399.7 eV has been previously assigned to the nitrogen of the neutral amino group ( $\text{NH}_2$ ) of glycine whereas the peak at 401.8-402.2 eV was

assigned to the nitrogen of the protonated amino group ( $\text{NH}_3^+$ ) [69, 145]. The peak associated with the protonated amino group of alanine (401.8-402.2 eV) is present at  $\Theta_{\text{Ala}} > 0.10$  ML and grows with increasing coverage whereas the peak related to the amino group attenuates in the multilayer regime ( $\Theta_{\text{Ala}} \geq 0.33$  ML). The peak at 400.3-401 eV is present at  $\Theta_{\text{Ala}} > 0.06$  ML and its area accounts for approximately 6-11% of the XPS area of intact alanine (excluding impurities) at all coverages. This peak could be related either to the neutral amino group ( $\text{NH}_2$ ) chemisorbed on the nickel surface in a different adsorption site or to the amino group forming hydrogen bonds with other groups of the alanine molecule.

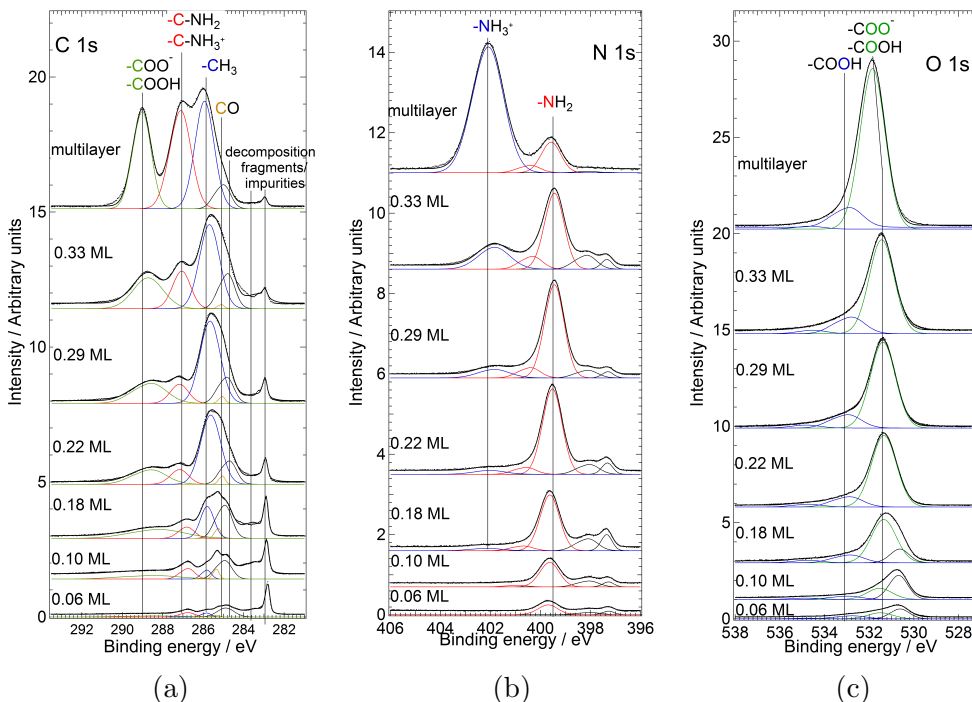


Figure 4.1: XP-spectra as a function of surface coverage (a) in the C 1s region ( $h\nu=400$  eV), (b) in the N 1s region ( $h\nu=510$  eV) and (c) in the O 1s region ( $h\nu=650$  eV) obtained upon dosing (S)-alanine onto Ni{100} at  $T_{\text{sample}}=250$  K. The spectra were obtained in the Elettra synchrotron in Trieste (Italy) in the UHV endstation of the SuperESCA beamline. The black dots are the raw data and the solid black thick lines are the fitted curves. The solid coloured curves are the individual peaks obtained upon fitting.

The O 1s spectra (Fig. 4.1c) consist of four peaks at 530.6-530.7 eV, 531.3-531.5 eV, 532.7-533.0 eV and 534.5-534.8 eV. The lower binding energy peak (530.6-530.7 eV) is only present at low coverages  $\Theta_{\text{Ala}} \leq 0.18$  and is probably related to CO or chemisorbed O. O 1s XP-spectrum, of saturated CO on Ni{100} (Fig. 4.2b) at  $T_{\text{sample}}=293$  K, obtained during this study, shows two peaks at  $\sim 531.0$  eV and  $\sim 532.0$  eV in close agreement with Ref.[146]. This kind of shift in the binding energy of the O 1s core electron was also observed

upon co-adsorption of CO with benzene on Ni{111} (from 531.0 eV/pure CO to 530.8 eV/CO+benzene)[147]. The peak at 531.3-531.5 eV is a combination of signal originating from the overlap contribution from the  $\text{COO}^-$  and  $\text{COOH}$  oxygen [69]. In the deprotonated form ( $\text{COO}^-$ ), the two oxygen atoms are in an equivalent chemical environment, hence the signal does not split [104]. The position of this peak shifts to 531.8 eV in the multilayer regime. In the multilayer the core hole experiences less screening from the metal substrate, thus increasing the binding energy of the O 1s core electron [69]. According to Ref.[109], both the peaks at 531.3-531.5 eV (O 1s spectra in Fig. 4.1c) and 399.5-399.8 eV (N 1s spectra in Fig. 4.1b) are indicators of alanine chemisorbed via the oxygen atoms of  $\text{COO}^-$  group and nitrogen atom of the amino group. The two high binding energy peaks (532.7-533 eV and 534.5-534.8 eV) are related to the carboxyl group of the alanine molecule with a high degree of protonation. The peak at 532.7-533 eV was previously attributed to the -OH group of the neutral carboxyl group ( $-\text{COOH}$ ) in glycine [69, 148], whereas the peak at 534.5-534.8 eV was previously assigned to satellite peak or oxygen atoms of the carboxyl group of tartaric acid with high degree of protonation (hydrogen bonds)[99]. In our study, these hydrogen bonds could be either between the protonated carboxyl groups of the alanine molecule or between the protonated carboxyl group and the neutral amino group (peak at 400.3-401 eV, N 1s spectra in Fig. 4.1b). The sum of the area of the peaks related to protonated carboxylic species (532.7-533 eV and 534.5-534.8 eV) accounts for approximately 33-43% of the XPS area of intact alanine (excluding impurities) at  $\Theta_{\text{Ala}} \leq 0.1$ ,  $\sim 18\text{-}24\%$  at  $0.1 \text{ ML} < \Theta_{\text{Ala}} \leq 0.33 \text{ ML}$ , and  $\sim 14\%$  in multilayer. We cannot exclude contribution to the XPS signal of alanine in the O 1s region (especially at low coverages) from co-adsorbed CO, oxygen, water and hydroxyls.

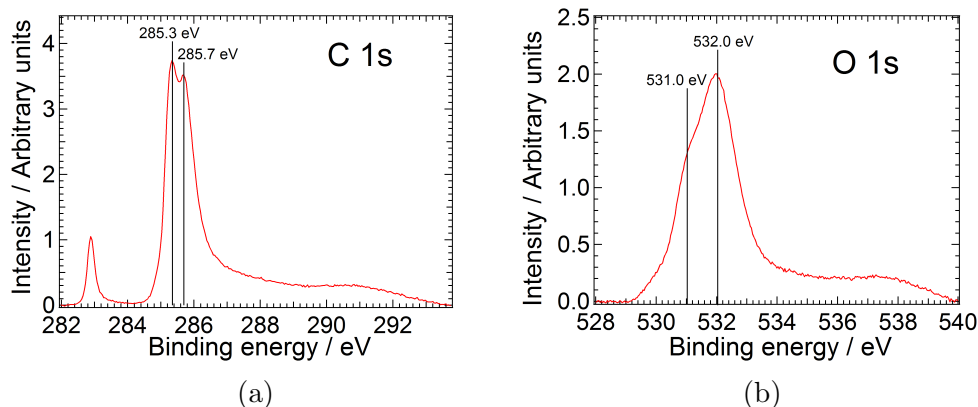


Figure 4.2: XP-spectra in the (a) in the C 1s region ( $h\nu=400$  eV) and (b) in the O 1s region ( $h\nu=650$  eV) obtained upon dosing CO onto Ni{100} to saturation at  $T_{\text{sample}}=293$  K. The spectra were obtained in the Elettra synchrotron in Trieste (Italy) in the UHV endstation of the SuperESCA beamline.

The C 1s spectra consist (Fig. 4.1a) of seven peaks. The three low binding energy peaks (282.8-283.0 eV, 283.3-283.6 eV, 284.7-285.0 eV), which represent a really intense signal (in comparison to the signal of intact alanine) at low coverages ( $\Theta_{\text{Ala}} \leq 0.18$  ML), are associated with decomposition fragments and surface impurities. The peak at 282.8-283.0 eV was previously assigned to carbidic/surface carbon [101, 102]. The peak at 283.3-283.6 eV was also observed upon adsorbing alanine on Ni{111} [46] and it can be assigned to atomic carbon/nickel carbide [46, 103], allylic carbon [102] and/or HCN species [46]. The peak at 284.7-285.0 eV could be associated with  $sp^2(-C=C-)$ /graphitic carbon [46, 103] and/or decomposition fragments of alanine such as  $\text{NH}_2\text{CHCH}_3$  species. C 1s XP-spectrum of saturated CO on Ni{100} (Fig. 4.2a) at  $T_{\text{sample}}=293$  K, obtained during this study, shows two peaks at  $\sim 285.3$  and  $\sim 285.7$  eV, in close agreement with Ref.[146], therefore the peak at 285.3 eV (C 1s spectra in Fig. 4.1a) is assigned to CO. This peak shifts to low binding energies (285.1 eV) with increasing coverage. Similar behaviour was observed upon co-adsorption of CO with alanine [46] and benzene [147] on Ni{111} surface. The peaks at 285.6-285.9 eV, 286.7-287.2 eV and 288.2-289.0 eV are assigned to the carbon of the methyl group of alanine ( $-\text{CH}_3$ ), to the  $\alpha$ -carbon of alanine ( $\text{C-NH}_2/\text{C-NH}_3^+$ ), and to the carbon of the carboxyl group of alanine ( $\text{COO}^-/\text{COOH}$ ). The XPS signal of the peak associated with the methyl carbon of alanine (285.6-285.9 eV), has most likely contribution from CO as well. This contribution will also explain the variation of the peak shape with coverage. The peak assigned to the carbon of the carboxyl group of alanine (288.2-289.0 eV) presents a large FWHM ( $\sim 3$  eV) at low coverages ( $\Theta_{\text{Ala}} \leq 0.18$  ML), suggesting also the contribution to this signal from surface impurities/decomposition fragments.

According to the XP-spectra in Fig. 4.1, alanine chemisorbs on Ni{100} in its anionic and neutral form at  $\Theta_{\text{Ala}} \leq 0.1$ . In its anionic form, the carboxyl group of alanine is deprotonated, and alanine forms three surface bonds with the nickel substrate (the two oxygen atoms of  $\text{COO}^-$  group and nitrogen atom of the amino group) whereas in its neutral form, one of the two oxygen atoms of the carboxyl group is protonated and dangled from the surface, which results in an  $\mu_2$  adsorption geometry (Fig. 4.3). Increasing the coverage of alanine on the nickel surface ( $\Theta_{\text{Ala}} > 0.1$  ML) causes the generation of zwitterionic species, which also support an  $\mu_2$  adsorption geometry (Fig. 4.3). The zwitterionic species coexist on the anionic and neutral forms of alanine. One might speculate that these zwitterionic species are found in a second layer deposited on top of the chemisorbed layer. According to Fig. 4.3, the estimated saturation coverage of alanine on Ni{100} is  $\sim 0.33$  ML (1 molecule per 3 nickel atoms). We need to be

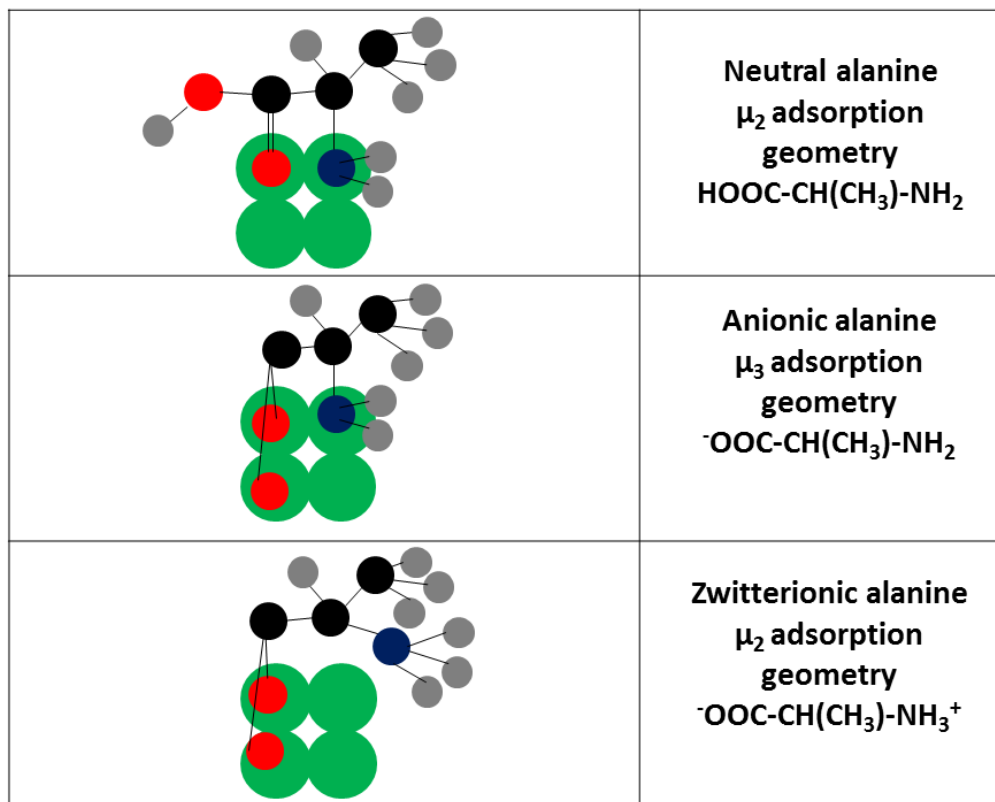


Figure 4.3: The three possible chemical states of the chemisorbed (S)-alanine on Ni{100} surface with their corresponding adsorption geometries. The black circles are carbon atoms, the red circles are oxygen atoms, the blue circles are nitrogen atoms, the grey circles are hydrogen atoms and green circles are nickel atoms.

cautious about the estimation of absolute coverage of alanine on Ni{100} using XPS, especially at low coverages, since the O 1s spectra contains features which do not correspond to intact alanine, such as water, hydroxyls and CO. In the multilayer, alanine is almost exclusively in its zwitterionic form.

The thermal behaviour of (S)-alanine on Ni{100} was evaluated using Temperature Programmed-XP-spectra (TP-XPS). Figures 4.4-4.6 show C 1s and N 1s TP-XP-spectra for three different coverages of (S)-alanine on Ni{100} surface (multilayer,  $\Theta=0.22$  ML,  $\Theta=0.10$  ML), whereas Fig. 4.7 shows C 1s and O 1s TP-XP-spectra obtained upon dosing (S)-alanine onto Ni{100} up to  $\Theta_{\text{Ala}}=0.18$  ML  $\Theta_{\text{Ala}}=0.18$  ML.

The XPS signal does not change significantly upon heating the alanine overlayers from 250 K to 300 K (Fig. 4.4-4.7). In this temperature range ( $\sim 250$ -300 K) there is some oscillating behaviour in the intensity of the XPS signal of the multilayer alanine, as a function of temperature, in both C 1s and N 1s region (Fig. 4.4), which is probably related to beam damage and/or the fact that the sample was moved during the TP-XPS experiments. Heating the multilayer to

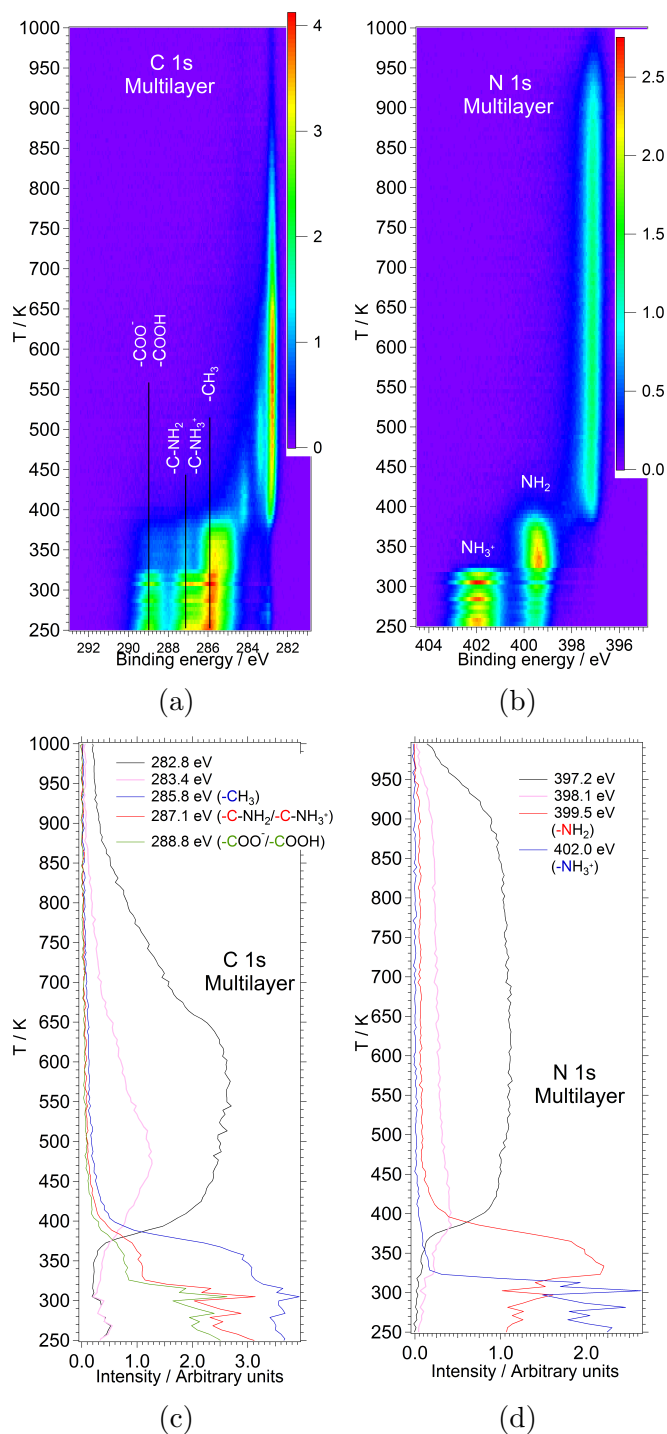


Figure 4.4: (a+b) TP-XP-spectra in the (a) C 1s region and (b) N 1s region, obtained upon dosing (S)-alanine onto Ni{100} at  $T_{\text{sample}}=250$  K up to the multilayer regime. Heating rate:  $8 \text{ K min}^{-1}$ ,  $h\nu=510$  eV. The spectra were obtained in the Elettra synchrotron in Trieste (Italy) in the UHV endstation of the SuperESCA beamline. (c+d) Intensity profiles (in 0.5 eV wide bands) as a function of temperature, obtained from the TP-XP-spectra in Fig. 4.4a and 4.4b, respectively for the (c) carbon peaks at 282.8 eV, 283.4 eV, 285.8 eV, 287.1 eV and 288.8 eV and (d) for the nitrogen peaks at 397.2 eV, 398.1 eV, 399.5 eV and 402.0 eV.

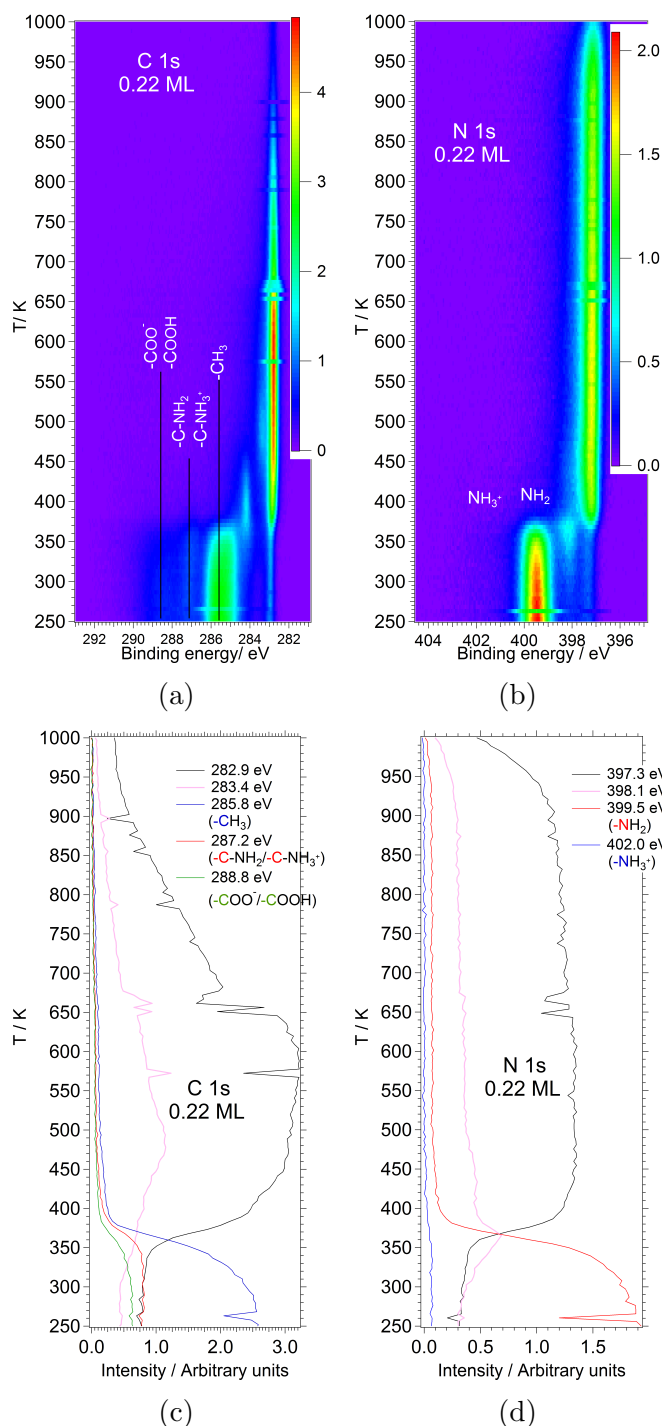


Figure 4.5: (a+b) TP-XP-spectra in the (a) C 1s region and (b) N 1s region, obtained upon dosing (S)-alanine onto Ni{100} at  $T_{\text{sample}}=250$  K up to  $\Theta_{\text{Ala}}=0.22$  ML. Heating rate:  $8$  K  $\text{min}^{-1}$ ,  $h\nu=510$  eV. The spectra were obtained in the Elettra synchrotron in Trieste (Italy) in the UHV endstation of the SuperESCA beamline. (c+d) Intensity profiles (in  $0.5$  eV wide bands) as a function of temperature, obtained from the TP-XP-spectra in Fig. 4.5a and 4.5b, respectively for the (c) carbon peaks at  $282.9$  eV,  $283.4$  eV,  $285.8$  eV,  $287.2$  eV and  $288.8$  eV and (d) for the nitrogen peaks at  $397.3$  eV,  $398.1$  eV,  $399.5$  eV and  $402.0$  eV.

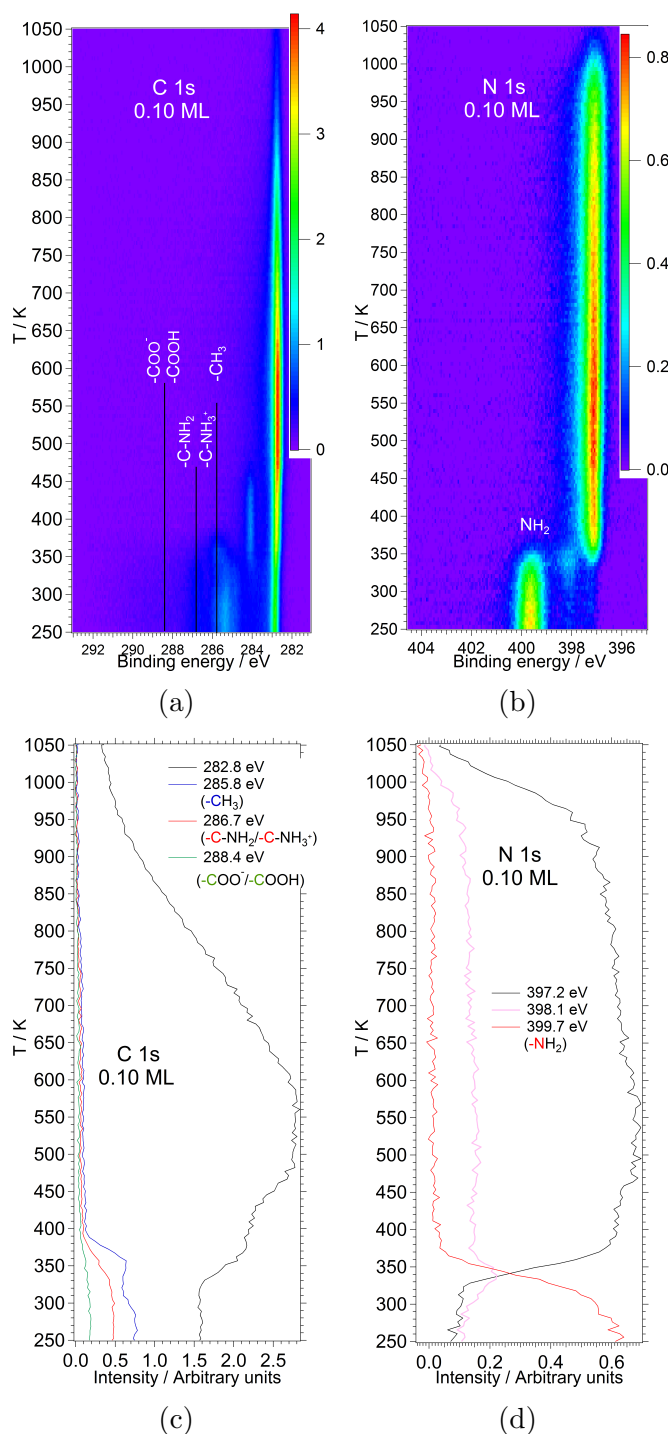


Figure 4.6: (a+b) TP-XP-spectra in the (a) C 1s region and (b) N 1s region, obtained upon dosing (S)-alanine onto Ni{100} at  $T_{\text{sample}}=250$  K up to  $\Theta_{\text{Ala}}=0.10$  ML. Heating rate:  $8 \text{ K min}^{-1}$ ,  $h\nu=510$  eV. The spectra were obtained in the Elettra synchrotron in Trieste (Italy) in the UHV endstation of the SuperESCA beamline. (c+d) Intensity profiles (in 0.5 eV wide bands) as a function of temperature, obtained from the TP-XP-spectra in Fig. 4.6a and 4.6b, respectively for the (c) carbon peaks at 282.8 eV, 285.8 eV, 286.7 eV and 288.4 eV and (d) for the nitrogen peaks at 397.2 eV, 398.1 eV, 399.7 eV.

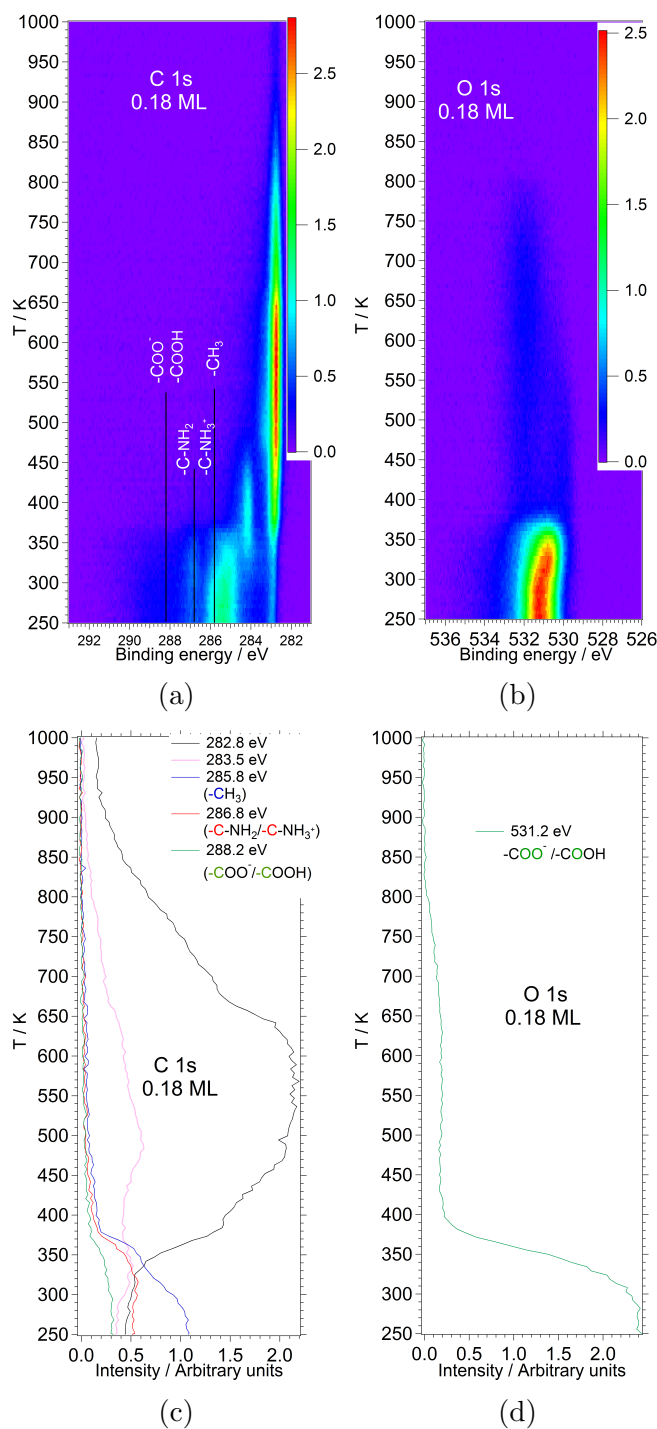


Figure 4.7: (a+b) TP-XP-spectra in the (a) C 1s region and (b) O 1s region, obtained upon dosing (S)-alanine onto Ni{100} at  $T_{\text{sample}}=250$  K up to  $\Theta_{\text{Ala}}=0.18$  ML. Heating rate:  $8$  K  $\text{min}^{-1}$ ,  $h\nu=650$  eV. The spectra were obtained in the Elettra synchrotron in Trieste (Italy) in the UHV endstation of the SuperESCA beamline. (c+d) Intensity profiles (in  $0.5$  eV wide bands) as a function of temperature, obtained from the TP-XP-spectra in Fig. 4.7a and 4.7b, respectively for the (c) carbon peaks at  $282.8$  eV,  $283.5$  eV,  $285.8$  eV,  $286.8$  eV and  $288.2$  eV and (d) for the oxygen peak at  $531.2$  eV.

$\sim 320$  K (Fig. 4.4) causes reduction in the signal corresponding to the protonated group ( $\text{NH}_3^+$ ) of alanine in the N 1s region (Fig. 4.4b and 4.4d) while at the same time there is a rise in the signal corresponding to the neutral amino group ( $\text{NH}_2$ ). In the C 1s region (Fig. 4.4a and 4.4a) at  $\sim 320$  K we can observe a significant reduction in the XPS signal of the alanine overlayer, suggesting desorption of the multilayer alanine. The full decomposition temperature of (S)-alanine on Ni{100} decreases with decreased initial surface coverage of the alanine overlayer. The full decomposition occurs at  $T \approx 370\text{-}390$  K for multilayer alanine (Fig. 4.4), at  $T \approx 350\text{-}370$  K for  $\Theta_{\text{Ala}}=0.22$  ML (Fig. 4.5), at  $T \approx 340\text{-}360$  K for  $\Theta_{\text{Ala}}=0.18$  ML (Fig. 4.7) and  $T \approx 330\text{-}350$  K for  $\Theta_{\text{Ala}}=0.10$  ML (Fig. 4.6). During decomposition, we can observe almost full disappearance of the XPS signal in the O 1s region (Fig. 4.7b) accompanied by rise in the signal associated with decomposition species in the C 1s region ( $\text{BE} < 285$  eV, Fig. 4.4a, 4.4c, 4.5a, 4.5c, 4.6a, 4.6c, 4.7a and 4.7c) and in the N 1s region ( $\text{BE} < 399$  eV, Fig. 4.4b, 4.4d, 4.5b, 4.5d, 4.6b and 4.6d). The peak associated with carbidic/surface carbon ( $\sim 282.8$  eV, C 1s spectra in Fig. 4.4-4.7) and the peak associated with the atomic nitrogen ( $\sim 397.2$  eV, N 1s spectra in Fig. 4.4-4.6) are still present in the XPS signal even upon heating to  $\sim 1050$  K, with the atomic nitrogen being thermally more stable than the carbidic/surface carbon.

## NEXAFS Results

Figure 4.8a shows angle resolved NEXAFS in the O K-edge region after dosing (S)-alanine onto Ni{100} at  $T_{\text{sample}}=250$  K up to  $\Theta_{\text{Ala}}=0.22$  ML. The O K-edge NEXAFS spectra consist of a sharp  $\pi^*$  resonance at 532.0 eV, two  $\sigma^*$  resonances at 539.3 eV and 542.3 eV and a step at 532.6 eV. It is difficult to determine the exact position of the  $\sigma^*$  resonances due to their large FWHM, however this does not influence the purpose of our NEXAFS data analysis which relies on the intensity of the  $\pi^*$  resonance. The  $\sigma^*$  resonances are due to C-C(539.3 eV) and C-O(542.3 eV) bonds [46, 104, 105].

The  $\pi^*$  resonance (532.0 eV, Fig. 4.8a) in the O K-edge region is associated with the  $\text{COO}^-$  group and C=O group of the protonated carboxyl group of the alanine molecule. The intensity of the  $\pi^*$  resonance shows angular dependency (Fig. 4.8b), therefore it was used to determine the tilt angle  $\alpha$  of the C=O/ $\text{COO}^-$  groups of alanine with respect to the Ni{100} surface, according to the following equation for surfaces with 4-fold symmetry [96]:

$$I(\theta) = A[P(\sin\theta)^2 \cdot (1 - \frac{3}{2}\sin^2\alpha) + \frac{1}{2}\sin^2\alpha] \quad (4.1)$$

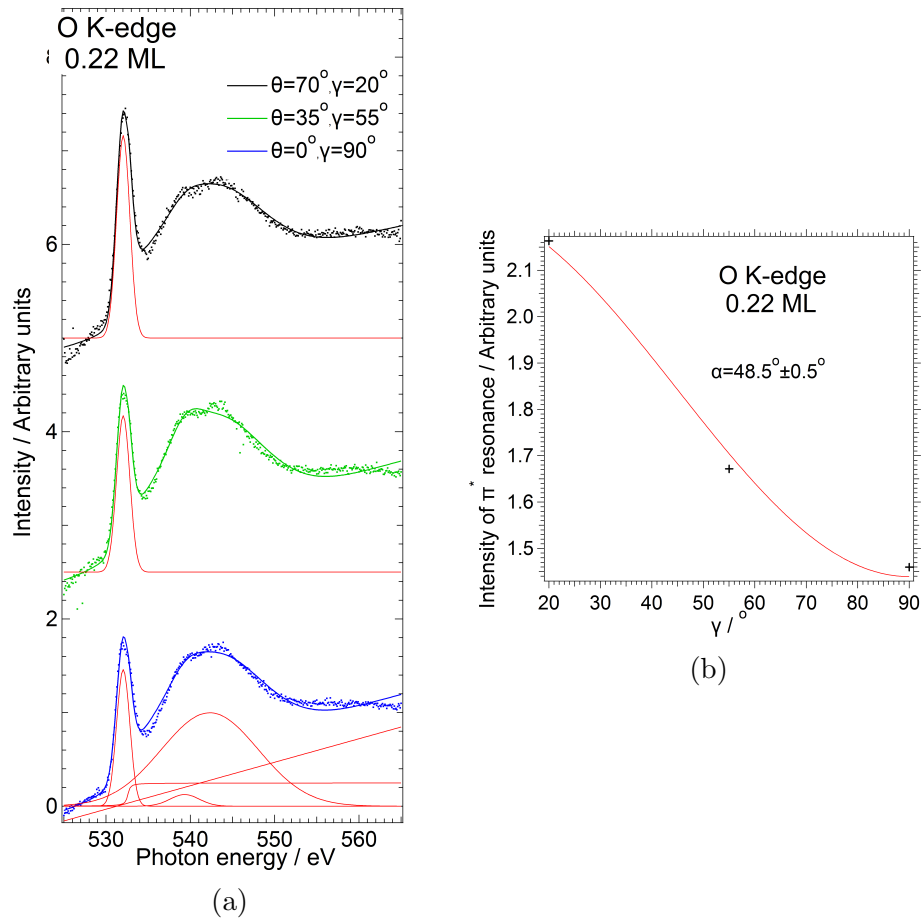


Figure 4.8: (a) Angle resolved O K-edge NEXAFS spectra after dosing (S)-alanine onto Ni{100} at  $T_{\text{sample}}=250$  K up to  $\Theta_{\text{Ala}}=0.22$  ML. The spectra were obtained in the Elettra synchrotron in Trieste (Italy) in the UHV endstation of the SuperESCA beamline. The dots represent the raw data and the solid thick lines the fitted curves. The red curves below the spectra show the individual Gaussian peaks, the linear background and the the step function used during the fitting process (b) Plots (black markers) showing the intensity of the oxygen  $\pi^*$  resonance in Fig. 4.8a as a function of angle  $\gamma$ , where  $\gamma$  is related to the angle of incidence  $\theta$  ( $\gamma=90^\circ-\theta$ ). The solid red line shows the fitted curve calculated by the cos function in Eq. 4.2.

Where  $\theta$  is the angle between the electric field vector and the surface plane and P is the polarisation factor. Assuming P=1 for the SuperESCA beamline, the Eq. 4.1, is transformed to Eq. 4.2:

$$I(\gamma) = \frac{A}{3} \left[ 1 + \frac{1}{2} (3\cos^2\gamma - 1)(3\cos^2\alpha - 1) \right] \quad (4.2)$$

Where  $\gamma=90^\circ-\theta$ . The angular dependency of the  $\pi^*$  resonance (Fig. 4.8b) returned tilt angle  $\alpha \approx 48.5^\circ$  (Fig. 4.8b). The error margin stated in Fig. 4.8b refers to the fitting error. Angle dependent NEXAFS of (S)-alanine on Ni{111} in the O K-edge region [46] showed two  $\pi^*$  resonances which were assigned to the carboxylate group in the tridentate (anionic alanine) and bidentate (zwitterionic alanine) adsorption mode of the alanine molecule on the Ni{111} substrate. The angular dependency of these two  $\pi^*$  resonances returned tilt angles  $\alpha=56^\circ$  and  $\alpha=64^\circ$  [46]. These values correspond to the tilt of the carboxylate group with respect to the Ni{111} surface plane in the anionic and zwitterionic alanine, respectively [46]. The XP-spectra of (S)-alanine on Ni{100} for  $\Theta_{\text{Ala}}=0.22$  ML (Fig. 4.1) suggest the coexistence of anionic, neutral and zwitterionic alanine on the Ni{100} surface which support an  $\mu_3$ ,  $\mu_2$  and  $\mu_2$  adsorption geometry, respectively (Fig. 4.3), with the signal of zwitterionic alanine being  $\sim 6\%$  (N 1s XP-spectrum in Fig. 4.1b) of the total N 1s XPS area (excluding impurities). The tilt angle of the C=O/COO- groups of alanine with respect to the Ni{100} surface plane ( $\sim 48.5^\circ$ ), obtained in our study is close to the tilt angle of carboxylate group of the anionic alanine with respect to the Ni{111} surface plane ( $56^\circ$ , [46]). It is possible that our NEXAFS data could not resolve the zwitterionic conformation of the alanine molecule because of its low concentration on the nickel surface. In a later study from Nicklin et al. (2018) [47], the tilt angle of the carboxylate group of (S)-alanine with respect to the Ni{111} surface plane was determined  $63^\circ$  and  $34^\circ$ , by using angle dependent NEXAFS in the O K-edge region under UHV conditions and under the presence of elevated pressures of  $\text{H}_2$  ( $P=4 \times 10^{-1}$  Torr), respectively. The two different tilt angles were associated with the tridentate and the bidentate conformation of the alanine molecule on the Ni{111} surface, respectively, since the presence of elevated pressures of hydrogen caused the protonation of the neutral amino group of anionic alanine, and generation of zwitterionic species of the molecule [47].

### 4.3.2 Alanine on clean Ni{100}/Elevated H<sub>2</sub> pressures

#### XPS Results

Figure 4.9 shows ambient pressure (AP) XP-spectra of the (S)-alanine layer on Ni{100}. The spectra were obtained upon dosing (S)-alanine onto Ni{100} to saturation (at room temperature,  $T \leq 330$  K) and then exposing the alanine layer to increasing hydrogen pressures as shown in Fig. 4.9. Dosing at room temperature ( $T \leq 330$  K) does not cause creation of multilayers, as expected from the the TP-XP-spectra of multilayer alanine in Fig. 4.4. Upon evacuation of the hydrogen gas from the NAP-cell (UHV after), the alanine layer was re-exposed to  $P_{\text{H}_2} = 6.3$  mbar (Fig. 4.9). Figure 4.10 compares step anneal XP-spectra of two (S)-alanine overlayers on Ni{100} under the presence of  $P_{\text{H}_2} = 6.3$  mbar (top panel) and under UHV conditions (bottom panel). The coverage of (S)-alanine on Ni{100} was calibrated based on the XPS area of the saturated signal of alanine in the O 1s region. It was difficult to determine the coverage in ML because of the the high amount of surface impurities and decomposition fragments present upon deposition of the molecule on the nickel surface. Surface impurities were present on the nickel surface before deposition of the molecule. The fitted XPS area of the carbon impurities present before dosing alanine in Fig. 4.10d were  $\sim 14\%$  of the fitted XPS area of the saturated alanine (excluding impurities) in the C 1s region, whereas the fitted XPS area of the nitrogen impurities (Fig. 4.10e) were  $\sim 23\%$  the fitted XPS area of the saturated alanine in the N 1s region (excluding impurities).

The XPS signal of the saturated (S)-alanine layer (at room temperature,  $T \leq 330$  K) in the C 1s region (Fig. 4.9a, UHV before), consists of five peaks at 283.4 eV, 284.8 eV, 285.9 eV, 286.9 eV and 288.3 eV. The peak at 283.4 eV is assigned to atomic carbon/nickel carbide [46, 103], allylic carbon [102] and/or HCN species [46] whereas the peak at 284.8 eV could be associated with  $sp^2$ /graphitic carbon [46, 103], co-adsorbed CO and/or decomposition fragments of alanine such as  $\text{NH}_2\text{CHCH}_3$  species. The peaks at 285.9 eV, 286.9 eV and 288.3 eV are assigned in a similar fashion to the (S)-alanine top-up XP-spectra on Ni{100} at 250 K (C 1s spectra in Fig. 4.1a), to the carbon of the methyl group of alanine ( $-\text{CH}_3$ ), to the  $\alpha$ -carbon of alanine ( $\text{C}-\text{NH}_2/\text{C}-\text{NH}_3^+$ ), and to the carbon of the carboxyl group of alanine ( $\text{COO}^-/\text{COOH}$ ). The intense signal of the peaks associated with decomposition fragments/surface impurities in the C 1s spectra in Fig. 4.9a (283.4 eV and 284.8 eV) with respect to the peaks associated with the intact alanine molecule (285.9 eV, 286.9 eV and 288.3 eV) is a result of the

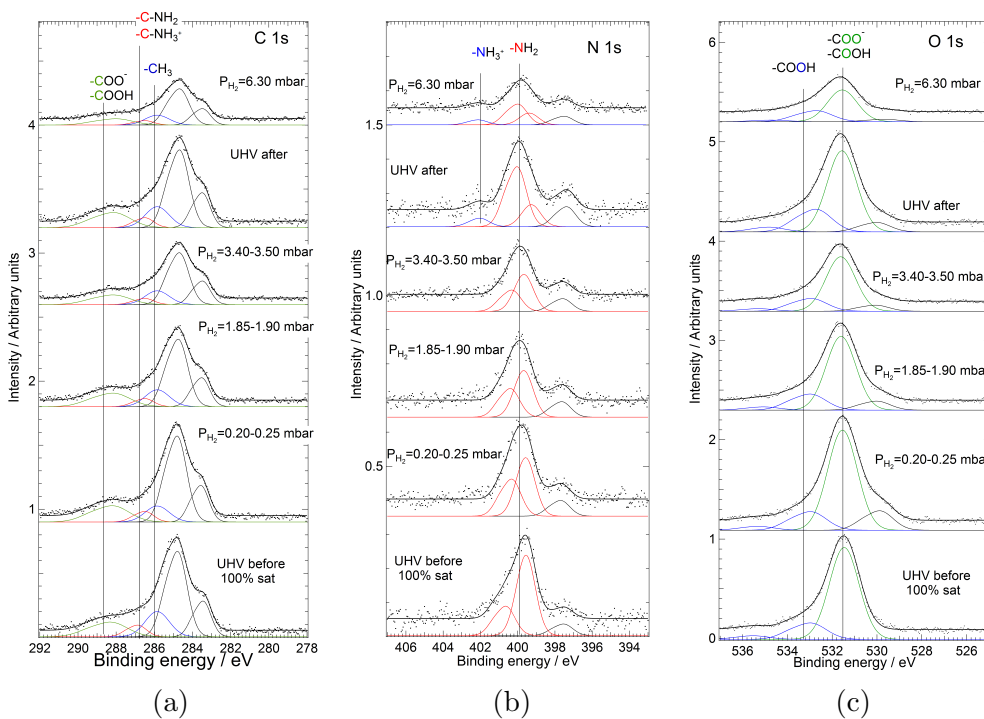


Figure 4.9: Ambient pressure (AP) XPS-spectra of 100% saturated (S)-alanine layer on Ni{100} at elevated hydrogen pressures (a) in the C 1s region, (b) in the N 1s region and (c) in the O 1s region. The black dots are the raw data and the solid black thick lines are the fitted curves. The solid coloured curves are the individual peaks obtained upon fitting. The spectra were recorded in the near-ambient pressure XPS (NAP-XPS) facility in the University of Manchester using Al  $K_{\alpha}$  anode ( $h\nu=1486.7$  eV) as an X-ray source. Dosing conditions of L-alanine:  $T_{\text{sample}}=\text{room temperature}(T\leq 330$  K),  $T_{\text{evaporator}}\approx 418\text{-}428$  K,  $P_{\text{base}}\approx 1 \times 10^{-9}\text{-}2 \times 10^{-9}$  mbar,  $P_{\text{dosing}}\approx 4 \times 10^{-9}\text{-}2 \times 10^{-7}$  mbar.

sample temperature during deposition of the alanine molecule onto the nickel surface (room temperature,  $T\leq 330$  K), which according to the the TP-XPS-spectra of alanine on Ni{100} in Fig. 4.4-4.7 is close to the decomposition temperature of alanine on Ni{100} surface (330-390 K). The N 1s spectrum of the same alanine layer (Fig. 4.9b, UHV before) consists of three peaks at 397.5 eV, 399.5 eV, and 400.6 eV whereas the O 1s spectrum (Fig. 4.9c, UHV before), shows also three peaks at 531.5 eV, 533.0 eV and 535.5 eV. The peak at 397.5 eV is related to atomic nitrogen and/or decomposition fragments/surface impurities such as HCN or  $\text{NH}_2\text{CHCH}_3$  species, whereas the peak 399.5 eV is related to the nitrogen of the neutral amino group ( $\text{NH}_2$ ) of alanine [69, 145]. The peak at 400.6 eV accounts for approximately 29% of the XPS area of intact alanine (excluding impurities) and it has been assigned, either to the neutral amino group ( $\text{NH}_2$ ) chemisorbed on the nickel surface in a different adsorption site or to the amino group forming hydrogen bonds with other groups of the alanine molecule. The peak at 531.5 eV in the O 1s spectrum in Fig. 4.9b, is a combination of signal originating from the

overlap contribution from the  $\text{COO}^-$  and  $\text{COOH}$  oxygen atoms [69]. The peak at 533.0 eV was previously attributed to the -OH group of the neutral carboxyl group (-COOH) in glycine [69, 148], whereas the peak at 535.5 eV could be assigned to satellite peak or to oxygen atoms of the carboxyl groups with high degree of protonation (hydrogen bonds) [99]. The sum of the area of the peaks related to carboxyl groups with high degree of protonation (533.0 eV and 535.5 eV, O 1s spectrum in Fig. 4.9c, UHV before) accounts for approximately 21% of the XPS area of intact alanine. In the light of this argument (Fig. 4.9, UHV before), in the saturated layer (room temperature,  $T \leq 330$  K) under UHV conditions, alanine chemisorbs on Ni{100} in both its anionic and neutral form (almost 1:1 ratio species), supporting an  $\mu_3$  and  $\mu_2$  adsorption geometry, respectively (Fig. 4.3).

Exposing the saturated layer to  $P_{\text{H}_2} = 0.20\text{-}0.25$  mbar causes generation of a peak in the O 1s region at 529.9 eV (Fig. 4.9c). This peak is probably related to atomic oxygen which originates either from the background pressure of the NAP-cell or decomposition fragments of alanine, even though we do not observe any significant increase in the signal of decomposition fragments/surface impurities in the C 1s (283.4-283.6 eV and 284.7-284.8 eV in Fig. 4.9a) and N 1s region (397.4-397.7 eV in Fig. 4.9b) with respect to the XPS signal of intact alanine. The signal of the peak at 529.9 eV (with respect to the signal of intact alanine) is reduced with increasing hydrogen pressure and presence of the sample in the NAP-cell, suggesting that the hydrogen gas is reacting with these species causing their desorption from the nickel surface. Increasing the hydrogen pressure in the NAP-cell causes an increase in the area of the peaks related to the protonated carboxylic species (532.7-533 eV and 534.7-535.5 eV, O 1s spectra in Fig. 4.9c). This increase is with respect to the total XPS area of intact alanine (excluding impurities). The extent of protonation of the carboxyl groups of alanine is caused by the infinite source of hydrogen from the gas phase. At  $P_{\text{H}_2} = 6.30$  mbar, the sum of the area of the peaks related to carboxyl groups with high degree of protonation (532.7 eV and 534.7 eV, O 1s spectrum in Fig. 4.9c) accounts for approximately 32% of the XPS area of intact alanine. Upon evacuation of the hydrogen gas from the NAP-cell (UHV after), we can observe an additional N 1s signal at 402.1 eV (N 1s spectrum in Fig. 4.9b). The low intensity of the signal makes it difficult to determine whether it is an actual peak or it is related to the noise of the background. The signal at 402.1 eV implies the protonation of the amino group of alanine ( $\text{NH}_3^+$ ) [69, 145] and generation of zwitterionic species of alanine (Fig. 4.3). The signal is further increased (with respect to the the total XPS area of intact alanine, excluding impurities) at  $P_{\text{H}_2} = 6.30$  mbar.

Heating the alanine overlayer to 352 K and 375 K under the presence of  $P_{\text{H}_2} =$

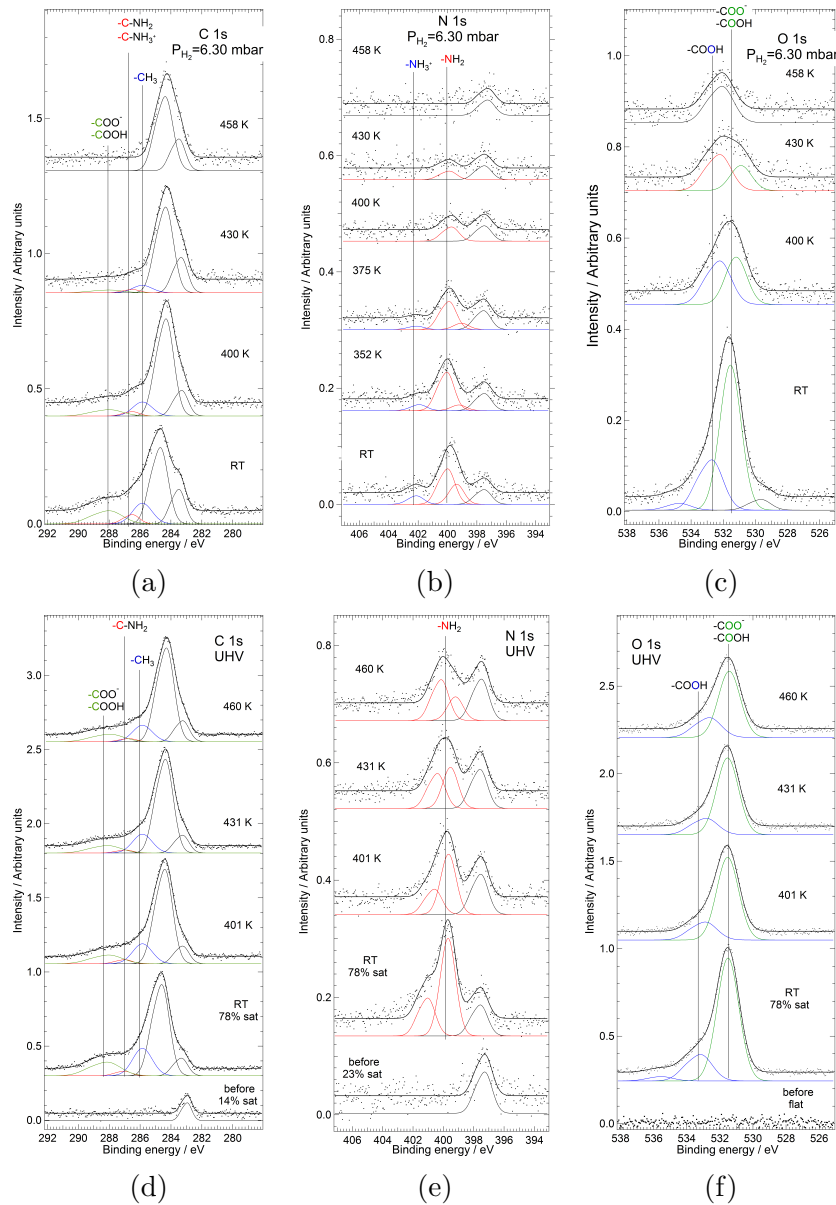


Figure 4.10: Comparison of step anneal XP-spectra of two (S)-alanine overlayers on Ni{100} under the presence of  $P_{H_2} = 6.3$  mbar (top panel) and under UHV conditions (bottom panel). The spectra were recorded in the C 1s region (a+d), in the N 1s region (b+e) and in the O 1s region (c+f). The black dots are the raw data and the solid black thick lines are the fitted curves. The solid coloured curves are the individual peaks obtained upon fitting. The spectra were recorded in the near-ambient pressure XPS (NAP-XPS) facility in the University of Manchester using Al  $K_{\alpha}$  anode ( $h\nu = 1486.7$  eV) as an X-ray source. Dosing conditions (top panel):  $T_{\text{sample}} = \text{room temperature}$  ( $T \leq 330$  K),  $T_{\text{evaporator}} \approx 418\text{--}428$  K,  $P_{\text{base}} \approx 1 \times 10^{-9}\text{--}2 \times 10^{-9}$  mbar,  $P_{\text{dosing}} \approx 4 \times 10^{-9}\text{--}2 \times 10^{-7}$  mbar. Initial surface coverage of (S)-alanine (before exposure to elevated hydrogen pressures): 100% sat. Dosing conditions (bottom panel):  $T_{\text{sample}} = \text{room temperature}$  ( $T \leq 320$  K),  $T_{\text{evaporator}} \approx 423\text{--}424$  K,  $P_{\text{dosing}} \approx 2 \times 10^{-9}\text{--}1 \times 10^{-8}$  mbar. Initial surface coverage of (S)-alanine (before step anneal process): 78% sat.

6.3 mbar (N 1s spectra in Fig. 4.10b) causes reduction in the XPS signal of alanine by  $\sim 21\%$  and  $\sim 40\%$ , (with respect to the layer at room temperature) respectively, but does not cause any significant change in the chemical state of the molecule. Heating to 400 K, under the presence of  $P_{H_2} = 6.3$  mbar (Fig. 4.10, top panel), causes the onset of full decomposition of the alanine molecule on the Ni{100} surface which is completed by  $T = 458$  K. At this temperature we can observe only decomposition fragments/surface impurities in all the three regions (Fig. 4.10, top panel). The decomposition of the alanine molecule on the Ni{100} surface under the presence of  $P_{H_2} = 6.3$  mbar did not cause any significant increase in the signal of the decomposition species in the C 1s region (Fig. 4.10a) and N 1s region (Fig. 4.10b), as we have observed in the TP-XP-spectra of alanine on Ni{100} in Fig. 4.4-4.7. It is likely that the hydrogen gas is reacting with the decomposition fragments of alanine causing their desorption or the presence of hydrogen gas alters the decomposition mechanism of alanine on Ni{100}.

Heating the alanine overlayer to 401 K under UHV conditions (Fig. 4.10, bottom panel) causes reduction in the XPS signal of alanine by  $\sim 30\text{-}37\%$  (with respect to the layer at room temperature), but does not change, significantly, the chemical state of the molecule on the Ni{100} surface. Heating to 460 K (again under UHV conditions) causes even further reduction in the XPS signal of alanine ( $\sim 42\text{-}51\%$ , always with respect to the layer at room temperature), but still does not cause full decomposition of the alanine molecule, as we have observed under the presence of  $P_{H_2} = 6.3$  mbar. In the light of this observation we can suggest that the presence of  $P_{H_2} = 6.3$  mbar destabilises thermally the alanine molecule on the Ni{100} surface. The TP-XP-spectra in Fig. 4.4-4.7 suggest that the decomposition temperature of alanine on Ni{100} is  $\sim 330\text{-}390$  K whereas the step anneal XP-spectra (under UHV conditions) in Fig. 4.10 (bottom panel) suggest that at 460 K approximately half of the alanine layer is still intact on the Ni{100} surface. This discrepancy is most likely originated from the nature of those experiments. In the TP-XPS experiments, the sample is heated at a constant rate whereas in the step anneal experiments the sample was heated to a constant temperature and then cooled while taking XP-spectra. In addition the two alanine overlayers were generated at different sample temperatures: in Fig. 4.4-4.7 the alanine layers were generated at  $T_{\text{sample}} = 250$  K whereas in Fig. 4.10 (bottom panel) was generated at  $T_{\text{sample}} =$  room temperature ( $T \leq 320$  K). Finally this discrepancy might be caused by the difference between sample configuration in the UHV endstation of the SuperESCA beamline and the sample configuration in the near-ambient pressure XPS (NAP-XPS) facility in the University of Manchester.

## 4.4 Discussion

Dosing (S)-alanine onto Ni{100} at room temperature ( $T \leq 330$  K, Fig. 4.9) causes saturation of the XPS signal. No multilayers are formed at this temperature (room temperature,  $T \leq 330$  K), whereas the XP-spectra in the C 1s region (Fig. 4.9a), suggest strong presence of decomposition fragments/surface impurities. In the saturated layer (formed at room temperature,  $T \leq 330$  K, Fig. 4.9) alanine chemisorbs on Ni{100} in both its anionic and neutral form. These chemical states support an  $\mu_3$  and  $\mu_2$  adsorption geometry, respectively (Fig. 4.3). Deposition of alanine onto Ni{100} at  $T_{\text{sample}}=250$  K (Fig. 4.1) causes also generation of anionic and neutral species. At  $\Theta_{\text{Ala}} > 0.10$  ML we can observe generation of zwitterionic species of alanine which also support an  $\mu_2$  adsorption geometry (Fig. 4.3), which coexist with the anionic and neutral forms of alanine. It is not fully conclusive whether these zwitterionic species belong to the first chemisorbed layer or they are found in a second layer deposited on top of the chemisorbed layer. Deposition of (S)-alanine onto Ni{100} at  $T_{\text{sample}}=250$  K, causes generation of zwitterionic multilayer alanine, which desorbs at  $T \approx 320$  K (TP-XP-spectra in Fig. 4.4). TP-XP-spectra of (S)-alanine layers on Ni{100} formed at  $T_{\text{sample}}=250$  K (Fig. 4.4-4.7), suggest that the molecule decomposes on the nickel surface at  $T \approx 330-390$  K, depending on the initial coverage of alanine (the decomposition temperature of alanine decreases with decreased initial surface coverage of the alanine overlayer). On the other hand step-anneal XP-spectra of 78% sat (S)-alanine layer on Ni{100} formed at room temperature ( $T \leq 320$  K, Fig. 4.10, bottom panel), suggest that at  $T=460$  K, approximately half of the alanine layer is still intact on the Ni{100} surface. Exposing the 100% sat alanine layer, grown on Ni{100} at room temperature ( $T \leq 330$  K, Fig. 4.10, top panel), to  $P_{\text{H}_2} = 6.3$  mbar, destabilises thermally the molecule, which decomposes at  $T \geq 400$  K. According to previous work [16, 17], the temperature range used for modification of Raney nickel [16] and silica-supported nickel catalysts [17] using alanine as chiral modifier, as well as the temperatures used for the enantioselective hydrogenation of MAA using the aforementioned catalysts lies between 273 K and 373 K [16, 17]. This temperature range is close to some of the decomposition temperatures of (S)-alanine on Ni{100}, observed in this study, therefore we cannot fully conclude whether the molecule remains intact on the Ni{100} in the range of temperatures typically used in enantioselective catalysis. A further study, which will exploit the interaction of the molecule on the Ni{100} surface under elevated solvent pressures is essential, to obtain full conclusions about the thermal stability of the molecule on the Ni{100} facet

under modification and reaction conditions.

Exposing the saturated layer (formed at room temperature,  $T \leq 330$  K, Fig. 4.9) to elevated hydrogen pressures, causes an increase in the amount of neutral species of alanine on Ni{100} and perhaps generation of zwitterionic species. It is clear that elevated pressures of hydrogen cause some loss of “chiral environment” on the nickel surface, resulting from the  $\mu_3$  adsorption geometry of the molecule and transition to an  $\mu_2$  adsorption geometry. Transition to an  $\mu_2$  adsorption geometry (from  $\mu_3$ ) was also observed upon exposing the saturated (0.25 ML) (S)-alanine layer on Ni{111} to elevated hydrogen pressures) [47]. These geometries may facilitate an interaction of the modifier with the  $\beta$ -ketoester reactant. Work on the interaction of (S)-glutamic acid and MAA on Ni{111} [40, 43, 44] provided evidence for a strong correlation between the increase of the keto:enol ratio of MAA, the protonation of the amino group of the modifier ((S)-glutamic acid) and the conditions that favour the generation of the R-product in excess. Under these conditions, it is possible, that the protonated amino group of the modifier ((S)-glutamic) can support an interaction with the  $\beta$ -ketoester reactant via hydrogen bonding in a configuration that will preferably produce the R-product during the hydrogenation reaction [40, 43, 44], as it was observed by Jones et al. (2006) [40] using RAIRS. In addition, modification of Ni{111} with (R,R)-tartaric acid from solution at 350 K (which according to Ref.[37, 38] is the optimum modification temperature for attaining the highest enantioselectivity using TA as modifier) following washing of the catalyst, caused generation of HTA<sup>-</sup> species on the nickel surface [38]. Subsequent immersion of the crystal in a MAA solution caused enhancement of the diketone/enol ratio of MAA substrate with respect to the modification at 300 K [38]. According to Ref.[38] the origin of the enantioselectivity of this system might be due to the formation of hydrogen bonds between the diketone and the HTA<sup>-</sup> species (maybe through the protonated carboxyl group of tartaric acid), in orientation that will preferably generate the R-enantiomer as a product during the hydrogenation reaction.

## 4.5 Conclusions

Alanine at  $T_{\text{sample}}=250$  K/ $\Theta_{\text{Ala}} \leq 0.10$  ML and  $T=\text{room temperature}$  ( $\Theta_{\text{Ala}} \geq 78\%$  sat) chemisorbs on Ni{100} in both its anionic and neutral form. Dosing alanine at room temperature ( $T \leq 330$  K) causes saturation of the XPS signal without formation of any multilayers. At  $T_{\text{sample}}=250$  K and  $\Theta_{\text{Ala}} > 0.10$  ML, some zwitterionic species are formed, which coexist with the anionic and neutral forms

of alanine. It is not fully conclusive whether these zwitterionic species belong to the first chemisorbed layer or they are found in a second layer deposited on top of the chemisorbed layer. In the multilayer alanine is almost exclusively in its zwitterionic form. The multilayer desorbs at  $\sim 320$  K. According to TP-XP-spectra, the alanine overlayers formed at  $T_{\text{sample}}=250$  K, decompose at  $T\approx 330$ - $390$  K depending on the initial coverage of alanine, whereas step anneal XP-spectra of alanine overlayers formed on Ni{100} at room temperature, show that the molecule fully decomposes on Ni{100} at  $T>460$  K and  $T\geq 400$  K under UHV and elevated hydrogen pressure conditions ( $P_{\text{H}_2}= 6.3$  mbar), respectively. According to angle dependent NEXAFS, the C=O/COO<sup>-</sup> groups of the alanine molecule are tilted by  $\sim 48.5^\circ$  with respect to the Ni{100} surface plane. AP-XPS has shown that the presence of elevated hydrogen pressures causes increase in the amount of neutral species of alanine on Ni{100} and perhaps generation of zwitterionic species, which both might be important for enantioselective catalysis since in both forms, alanine can interact with the reactant creating an enantiospecific environment for asymmetric hydrogenation.

# Chapter 5

## Co-adsorption of (S)-alanine and water on Ni{110}

### Abstract

Enantioselectivity is a key aspect in the field of heterogeneous catalysis, since it can provide products with valuable biological activity. Alanine acts as a chiral modifier in the enantioselective hydrogenation of  $\beta$ -ketoesters. The present study explores the chemical state and thermal stability of alanine and H<sub>2</sub>O on clean Ni{110} using temperature programmed desorption, (TPD), X-ray photoelectron spectroscopy (XPS) and Temperature Programmed-XPS (TP-XPS). In addition the thermal stability and chemical state of alanine was investigated under co-adsorption of the amino acid with pre-covered water on Ni{110}. In both cases, the tilt angle of alanine with respect to the surface plane was determined using angle resolved NEXAFS. The interaction of H<sub>2</sub>O with surfaces is of high importance since is the most abundant solvent of our planet. XPS results of alanine on clean Ni{110} under different coverages provide evidence that the amino acid is present in the chemisorbed layer mainly in its anionic and neutral form supporting an  $\mu_3$  and  $\mu_2$  adsorption geometry, respectively. The XPS signal in the submonolayer regime, suggests also the presence of zwitterionic alanine, however it is not fully conclusive whether these zwitterionic species belong to the first chemisorbed layer or they are found in a second layer deposited on top of the chemisorbed layer. In the multilayer, alanine is mainly in its zwitterionic form. TP-XPS and TPD results suggest that the multilayer desorbs around 300-340 K whereas the chemisorbed alanine dissociates around 400-420 K. The temperature is well above the temperature typically used in enantioselective catalysis and is the highest observed on any nickel surface. The presence of multilayer H<sub>2</sub>O

changes the chemical state of alanine, whereas at low coverages of H<sub>2</sub>O, alanine displaces the H<sub>2</sub>O molecules. In both cases water does not alter the decomposition temperature of alanine. The tilt angle of the C=O/COO<sup>-</sup> groups of the alanine molecule with respect to the surface plane was found to be  $\sim 42.1^\circ$  and did not change significantly upon co-adsorption of (S)-alanine with submonolayer H<sub>2</sub>O ( $\alpha \approx 42.0^\circ$ )

## 5.1 Introduction

The pharmaceutical and agrochemical industry is in demand of more enantiopure chemical compounds since the chirality of the molecule affects their biological activity and response. In addition many enantiopure products are also used as flavours and fragrances [1–5]. In the area of heterogeneous catalysis enantioselectivity could be achieved in several ways, such as attaching a metal to a chiral support or adsorbing a chiral auxiliary to the metal [4]. The merit of using heterogeneous catalysts in comparison with homogeneous is the fact that these catalysts can be easily separated and recycled, can reduce the presence of metal traces in the product, and they can be easily controlled during their use [2, 6]. One great example of an enantioselective catalysed reaction is the hydrogenation of  $\beta$ -ketoesters (such as methyl acetoacetate MAA) using nickel as a catalyst. The reaction generates optically active products, if the catalyst is modified with  $\alpha$ -hydroxyacids (such as tartaric acid) or  $\alpha$ -amino acids (such as alanine) [2, 11, 12, 16]. According to the work of Keane (1994) on silica-supported nickel catalysts [17], alanine is a promising chiral modifier since it not only enhances the enantioselectivity but also improves the reaction rates. The authors suggested that in aqueous solution, alanine presents higher affinity than tartaric acid, for the adsorption on the supported nickel metal [17].

Different studies attempted to understand the mechanism behind the chiral modification of the nickel surface. Adsorption of (R,R)-tartaric acid (TA) on Ni{110} [34] caused the creation of a chiral footprint on the nickel surface, breaking its symmetry. Depositing (R,R)-tartaric acid onto oxidised Ni{111} [39] caused the generation of species similar to nickel tartrate, which could assist the etching of the crystal and generation of chiral defects. Co-adsorption of (R,R)-tartaric acid [37] and (S)-glutamic acid [40] with MAA on Ni{111} show evidence of interaction between the substrate (MAA) and the chiral modifier in a configuration that will generate the R-product during the hydrogenation reaction. On the other hand, work, on the adsorption of aspartic acid on Ni{111} [41] show

evidence of formation of oligosuccinimide clusters which could create a docking position for the substrate.

The adsorption of alanine on different surfaces has been studied extensively, for obtaining spectroscopic and fundamental insights on the interaction of the amino acid on different metals. Of our main interest is the interaction of alanine on Cu{110} and Pd surfaces, since these two elements are the closest ones with nickel, in the periodic table. On Ni{111}, alanine chemisorbs in both zwitterionic and anionic form supporting a bidentate and tridentate geometry, respectively with the latter species being in majority on the nickel surface. The molecule decomposes on Ni{111} at temperatures between 300 K and 450 K, following multistep processes [46]. Exposing the saturated (S)-alanine layer on Ni{111} (0.25 ML) to elevated pressures of H<sub>2</sub>, causes protonation of the amino group of (S)-alanine and reorientation to bidentate geometry, which under the presence of elevated pressures of H<sub>2</sub>, is the majority species on the nickel surface [47].

The adsorption of alanine on Cu{110} was studied using different techniques such as RAIRS, LEED, STM, circular dichroism in the angular dependence (CDAD), XPS, NEXAFS, photoelectron diffraction (PhD) and theoretical calculations [62, 63, 104, 109, 141, 149–152]. According to Ref.[62, 63, 109, 149] alanine chemisorbs on Cu{110} in its anionic form. At low coverages (in the 300-520 K temperature range), (S)-alanine chemisorbs on Cu{110} in an  $\mu_3$  adsorption geometry, via both oxygen atoms of the carboxylate group and the nitrogen atom of the amino group [63]. This geometry causes generation of a chiral footprint on the copper surface [63]. High coverages of (S)-alanine (up to saturation), grown at room temperature, cause the generation of anionic  $\mu_2$  species which interact with the copper surface via the nitrogen of the amino group and only one of the oxygen atoms of the carboxylate group along with presence of  $\mu_3$  species. At room temperature, these species start to form single and double chains in a non symmetrical direction. Annealing the high coverage layer up to 430 K does not change the orientation and bonding of the molecule with respect to the copper surface (the alaninate molecules still chemisorb on the copper surface in both  $\mu_2$  and  $\mu_3$  adsorption configurations) [63], but causes the formation of chiral clusters (from the chiral chains formed at room temperature) of six or eight molecules, interspersed with chiral channels of metals which assemble into a chiral array without creation of its mirror domain on the surface [62, 63]. This induced chirality is mirrored upon adsorption of R-alanine on the copper surface, which also generates similar chiral assemblies [62]. Finally annealing the high coverage (S)-alanine/Cu{110} layer to 470 K, causes the generation of achiral (3×2) structure, in which all the alaninate molecules interact with the copper surface in an  $\mu_3$  adsorption geometry

[63]. This structure was also characterised by Rankin and Sholl [141, 152] using theoretical calculations, by Sayago et al. (2005) [151] using photoelectron diffraction and by Jones et al (2006) [104] using XPS, angle dependent NEXAFS and DFT. Finally, Shavorskiy et al. (2011) [109] have studied the interaction of alanine on Cu{110} under the presence of ambient pressure water. According to the results of Ref.[109], the presence of ambient pressure water destabilises thermally the molecule on the Cu{110} surface with respect to UHV conditions.

The adsorption of alanine on Pd{111} was investigated by Gao et al (2007) [143] and Mahapatra et al (2014) [64]. Gao et al (2007) [143] proposed that alanine adsorbs in its zwitterionic form on Pd{111} in the first layer whereas in the multilayer regime alanine exists both in its zwitterionic and neutral form. The multilayer desorbs at temperatures between 350 K and 380 K [143]. The dissociation of alanine on Pd{111} occurs via C-C cleaving, which leads to desorption of CO<sub>2</sub> and CO desorption from the COO<sup>-</sup> moiety, and desorption of ethylamine or HCN from the CH<sub>3</sub>-CH-NH<sub>3</sub><sup>+</sup> [143]. Mahapatra et al (2014) [64] have found evidence of formation of both zwitterionic and anionic alanine on Pd{111} surface, with the isolated anionic form of the molecule, based on DFT calculations, being significantly more stable. The molecule was found to construct dimers or tetramers on Pd{111}, which could potentially behave as chiral templates [64].

There are several models proposed for explaining the adsorption of water on Ni{110} surfaces. Benndorf and Madey (1988) [153] found four desorption peaks after obtaining thermal desorption spectra (TDS) of H<sub>2</sub>O on Ni{110} : peak C (T=155K), peak A<sub>2</sub> (T=210 K), peak A<sub>1</sub> (T=245K) and peak B (T=350-360 K). The authors assigned these four peaks to recombination of surface OH to generate desorbed H<sub>2</sub>O (T=350-360 K), desorption of H<sub>2</sub>O dimers probably stabilised by OH (T=245K), desorption of H<sub>2</sub>O from bilayer clusters (T=210) and multilayer desorption (C, ice layers)[153]. Based on their structural model, the authors have defined the saturation of A<sub>2</sub>, A<sub>1</sub> and B peaks to  $\Theta_{\text{H}_2\text{O}}=1$  [153]. For  $\Theta_{\text{H}_2\text{O}} < 0.5$  a four spot ESDIAD pattern was observed, which suggested the presence of H<sub>2</sub>O dimers, whereas at higher coverages ( $\Theta_{\text{H}_2\text{O}}=0.5-1$ ) the ESDIAD show normal emission of H<sup>+</sup> (suggesting that the OH groups are located perpendicular to the surface) while at the same time LEED showed a c(2x2) pattern [153]. Benndorf and Madey (1988) [153] suggested a distorted hexagonal bilayer form for  $\Theta_{\text{H}_2\text{O}}=0.5-1$ , where the water molecules form hydrogen bonded clusters in a c(2x2) arrangement. On the other hand, Callen et al. (1990) [154] recommended, based on nuclear reaction analysis, that the saturation coverage of the A<sub>1</sub>, A<sub>2</sub> and B desorption states is equalled to 0.48 ML, which represents the first chemisorbed layer that can be selectively populated at 180 K. This layer shows

a sharp  $c(2 \times 2)$  LEED pattern. Furthermore adding a second layer of water (total coverage 1 ML) by cooling to 130 K, produced also a  $c(2 \times 2)$  LEED pattern, but less sharp compared to the first chemisorbed layer. The second layer is part of the ice layer but it was distinguished from the rest of multilayer by specific work function change. Callen et al. (1990) [154] argued that the dosing method of Benndorf and Madey (1988) [153] could not clearly separate the chemisorbed layer from the ice layers. According to infrared spectroscopy measurements [155], the water on the first chemisorbed layer, does not present intermolecular hydrogen bonding since it was IR inactive, whereas the second layer (or first ice layer) forms a clustering structure, originating from strong hydrogen bonding interactions. The addition of the second layer, converted the initial plane of the water which was initially parallel to the surface, to be positioned normal to the surface. According to Callen et al. (1992) [156] the big distance between water molecules in the first chemisorbed layer forbades the formation of hydrogen bonds [156]. In addition, according to Ref.[156], the lowest temperature that the partial dissociation of water occurs is  $205 \pm 2$  K, whereas all the water is removed by 293K, leaving OH and H on the surface. Based on ESDIAD and FTIR-RAS measurements, the authors of Ref.[156] suggested that at low coverages of water (0.06-0.5 ML) and under their reported experimental conditions there is no evidence of formation of dimers of water [156], in contrast with Benndorf and Madey (1988) [153] findings, while at the same time they have not observed any FTIR activity at 80 K until the formation of multilayers [156]. The authors of Ref.[156] argued that the four spot ESDIAD pattern observed in previous report was detecting minority species [156]. The authors of Ref.[156] also suggested that  $H_2O$  molecules are forming hydrogen bonds with OH groups (generated by partial dissociation of  $H_2O$ ), increasing their binding energy, which results to the rise of the  $A_1$  thermal desorption state [156]. Based on Callen et al. (1992) [156] and Pangher et al. (1994) [157] work, the water, in the first chemisorbed  $c(2 \times 2)$  layer, is adsorbed on atop sites [157] and its molecular plane presents high inclination to the surface normal [156, 157]. Finally Pirug et al. (1994)[158], proposed a different model for the  $c(2 \times 2)$   $H_2O$  saturated layer formed at 180 K. This layer has total coverage 1 ML and contains water and hydroxyls in the ratio 1:1. The water and hydroxyls are forming a compressed bilayer with the hydroxyls groups located in the first layer forming hydrogen bonds with the molecular water in the second layer [158]. Moreover Pirug et al. (1994) [158] suggested that the water dissociation occurs even at temperatures below 163 K. A review by Hodgson et al. (2009), on the adsorption of water on metal surfaces [159], pointed out that the lack of OH stretching modes in vibrational spectroscopy suggests the presence of a planar OH/ $H_2O$  overlayer

and not necessary the absence of hydrogen bonds. The authors of Ref.[159] interpreted the results described in Ref.[156], at temperatures above the multilayer desorption ( $\sim 140$  K), with the presence of flat dissociated structure [159]. The model proposed by Pirug et al. (1994) [158] could explain the enhanced thermal stability of H<sub>2</sub>O on the Ni{110} surface with respect to intact water films, which typically desorb at  $\sim 160$ -170 K [159]. The model described in Ref.[158], suggests that the water and hydroxyls are forming a compressed bilayer with the hydroxyls groups located in the first layer forming hydrogen bonds with the molecular water in the second layer, with a small vertical displacement between the two layers [158, 159]. Further studies are essential to determine the chemical structure of the  $c(2 \times 2)$  H<sub>2</sub>O/Ni{110} chemisorbed layer.

The aim of this study was to study the interaction of alanine on Ni {110} using XPS, NEXAFS and TPD and the effect of pre-adsorbed water on the chemical state, thermal stability and molecular orientation of the amino acid on the nickel surface. The interaction of water on nickel surfaces is important for enantioselective catalysis since and is one of the typical modifying solvents [17] and it could be co-adsorbed in surfaces especially under realistic ambient pressure conditions [75]. The synchrotron data were collected by Dr. Alix Cornish (University of Reading), by Dr. Ed Nicklin (University of Reading), by Prof. Georg Held (University of Reading) and by Dr. David Watson (University of Surrey), whereas the TPD data were collected by Dr. Alix Cornish (University of Reading). The data were co-analysed by the author and by Dr. Alix Cornish [67]. The overall contribution of the author to this study is  $\sim 50\%$  of the total work.

## 5.2 Experimental methods

The XPS and the NEXAFS experiments were performed at the SuperESCA beamline in the synchrotron of Elettra in Trieste (Italy) which provides a horizontally polarized beam, whereas the TPD data were obtained at Reading University. The endstation in Elettra consisted of a preparation and analysis chamber (both under UHV conditions) connected through a gate valve. The dosing and the sputtering occurred in the preparation chamber. The XPS and NEXAFS experiments were performed in the analysis chamber which also contained a LEED system. The base pressure of both chambers in the SuperESCA beamline was in the  $10^{-10}$  mbar range. Sample cleaning was achieved by cycles of sputtering (1 kV,  $P=3 \times 10^{-6}$  mbar) and subsequent annealing to  $\sim 1100$  K, and it was verified by the XPS spectra. In the SuperESCA beamline, the nickel crystal was mounted

at the base of a liquid nitrogen-cooled coldfinger in an orientation such that the polarisation vector was parallel to the [001] direction of the nickel surface, perpendicular to the close-packed rows [67]. The sample was heated resistively and its temperature was adjusted using a programmable temperature controller and measured using a spot welded thermocouple fixed on the sample.

(S)-alanine (L-alanine) was dosed from a home built evaporator which was mounted on the chamber through a gate valve. The evaporator consisted of a stainless steel crucible containing a glass tube filled with alanine powder. Deposition of the alanine molecule was performed by resistively heating the crucibles to  $\sim 423$ - $436$  K and opening the gate valve to the chamber. The measurement of the temperature was achieved by K-type thermocouples spot-welded on the crucibles. A pressure rise to  $\sim 4 \times 10^{-10}$ - $1 \times 10^{-9}$  mbar was observed during dosing of the molecule in the preparation chamber of the SuperESCA endstation. The crystal temperature was kept at  $T=200$  K during deposition of the molecule, unless otherwise stated. Due to differences in pumping speed, there was no good correlation between dosing time and coverage, therefore the coverage was determined using XPS (see Results section). Water was dosed via a leak valve. Prior to dosing the liquid was purified by means of freeze thaw cycles. A pressure rise to  $\sim 10^{-9}$  range was observed during dosing of the water in the analysis chamber.

The XP-spectra were acquired in the C 1s region ( $h\nu=400$  eV), in the N 1s region ( $h\nu=510$  eV) and O 1s region ( $h\nu=650$  eV) using pass energies of 10, 20 and 20 eV respectively, which resulted in combined resolution of beamline and analyser of  $\sim 0.1$ - $0.2$  eV for all the aforementioned photon energies. Spectra of the Fermi edge were obtained, every time the monochromator was moved, to calibrate the offset of the binding energy axis. For quantitative analysis, all the spectra were normalised at the low binding region followed by linear subtraction of the background. In order to study the temperature dependence of alanine on Ni{110}, temperature-programmed XP-spectra were acquired by heating the sample at a constant rate in front of the analyser while recording XP-spectra of one region at a time. During the TP-XPS experiments the sample was moved under the beam to minimise any potential beam damage.

The NEXAFS spectra were obtained in the O K-edge and N K-edge region, by detecting O KLL and N KLL Auger electrons with kinetic energies of 505 eV and 380 eV, respectively. In order to determine the molecular orientation of alanine on Ni{110}, angle dependent NEXAFS spectra were obtained using three different angles of incidence:  $\theta=0^\circ$  (normal incidence),  $\theta=35^\circ$  and  $\theta=70^\circ$  (normal emission), where  $\theta$  is the angle between the electric field vector and the surface plane. All the spectra were normalised in the low photon energy region and

corrected for the transmission of the beamline through dividing by the photon flux ( $I_0$ ). The  $I_0$  was collected using the drain current of the last refocusing mirror. Spectra of the clean surface, corrected in the same way, were subtracted as background. The spectra were also normalised with respect to the step height, at energies above all resonances.

For the experiments in Reading, the sample was mounted at the base of the manipulator, and its temperature was measured via a spot welded thermocouple. Sample cleaning was achieved by cycles of sputtering ( $P=1 \times 10^{-5}$  mbar/ $I_{\text{drain}}=3.6-4.1 \mu\text{A}/t=30$  min) and subsequent annealing to  $\sim 900$  K for 1 min, and it was verified by LEED [67]. The sample was resistively heated and the manipulator was cooled through a liquid nitrogen coldfinger. Alanine was dosed as explained above, by heating the crucibles to 423 K. The crystal temperature was kept at  $T=150$  K during deposition of the molecule. A pressure rise to  $\sim 5 \times 10^{-9}-9 \times 10^{-9}$  mbar from  $\sim 1 \times 10^{-9}-2 \times 10^{-9}$  mbar was observed during deposition of the molecule. TPD data were obtained by heating the sample at 1 K/s from 150 K to  $\sim 900$  K while recording the partial pressure of the following masses: 2( $\text{H}_2$ ) 15(cracking pattern of alanine), 18( $\text{H}_2\text{O}$ ), 28( $\text{CO}$ ) and 44( $\text{CO}_2$ ). During the TPD experiments, the sample was 15 mm away in a direct sight from the quadrupole mass spectrometer ion source [67].

## 5.3 Results

### 5.3.1 TPD Results

Figure 5.1 shows TPD data of (S)-alanine adsorbed on Ni{110}, for masses 2( $\text{H}_2$ ), 15, 18 ( $\text{H}_2\text{O}$ ), 28 ( $\text{CO}$ ,  $\text{N}_2$ ,  $\text{HN}=\text{CH}$ ) and 44 ( $\text{CO}_2$ ), at three different initial coverages of the molecule on the nickel surface. Mass 15 was recorded as a signal for intact alanine, since it was observed in the cracking pattern of the amino acid and the same time does not correspond to any decomposition fragment. The TPD raw data had their background subtracted.

Two key temperatures can be identified from the TPD data:  $T=320-340$  K and  $T \approx 420$  K. The peaks in the lower temperature region are observed for masses 2, 15, 18, 44 amu and small traces for 28 amu for 10 and 20 minutes. These peaks grow upon increasing the dosing time of alanine and shift to high temperatures with increasing dosing time (initial surface coverage), therefore they can be assigned to multilayer desorption [66, 84]. At 420 K, peaks are observed for masses 2, 15, 28, 44 for all coverages and their position and size are almost independent of the initial surface coverage and they are associated to the decomposition of

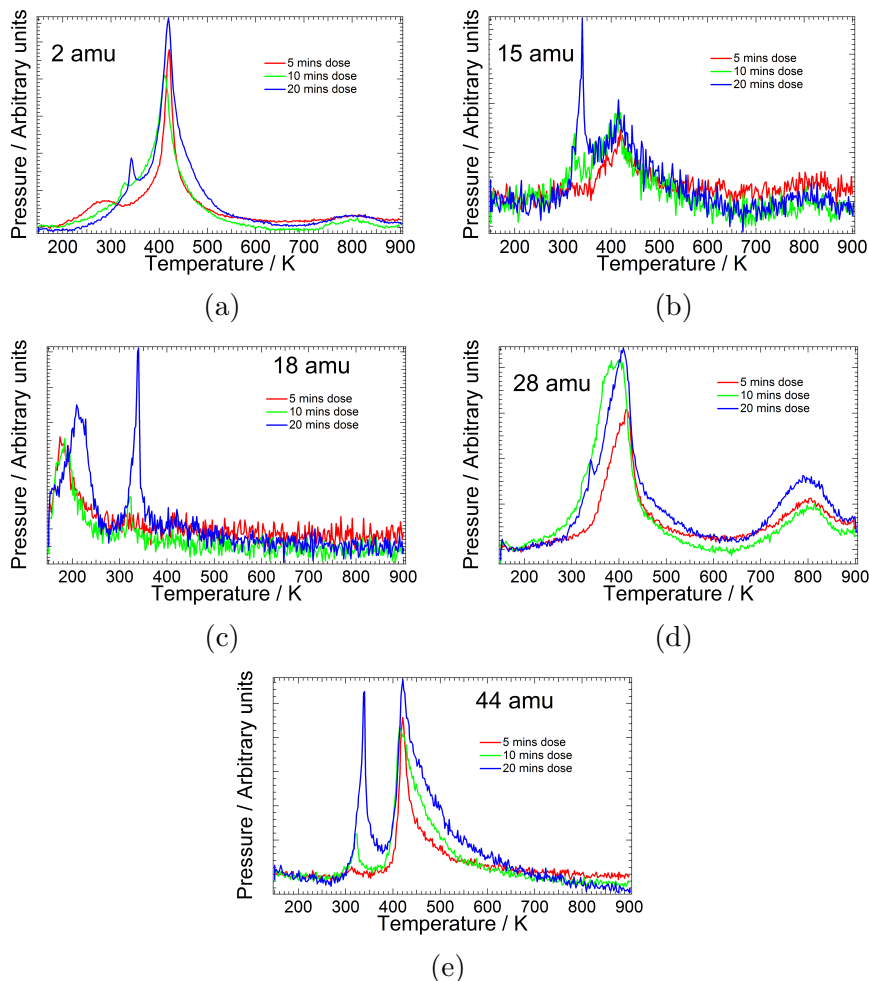


Figure 5.1: TPD data of (S)-alanine on Ni{110} for masses (a) 2 amu, (b) 15 amu, (c) 18 amu, (d) 28 amu and (e) 44 amu obtained at three different initial coverages of the molecule on the nickel surface. Heating rate  $1 \text{ K s}^{-1}$ .

chemisorbed alanine. Peaks are also visible at temperatures between 170 K and 210 K for mass 18, related to the desorption of intact  $\text{H}_2\text{O}$  from the sample or the heating wires. Finally two peaks are observed at 800 K for mass 2 and 28 which correspond to desorption of decomposition fragments of alanine. Their size is also independent of the initial surface coverage [67].

### 5.3.2 XPS Results

#### Adsorption of alanine on clean Ni{110}

Figure 5.2 shows XPS-spectra of (S)-alanine on clean Ni{110} as a function of different dosing time, in the three regions: N 1s, O 1s and C 1s.

Two peaks are observed in the N 1s region, which are centred approximately at 399.5-399.8 eV and 401.6-402.2 eV (Fig. 5.2b). These peaks have been previously assigned to  $\text{NH}_2$  and  $\text{NH}_3^+$  species, respectively [69, 145, 160]. The signal

of the first peak starts to attenuate at higher exposures ( $t > 10$  min) whereas the signal of  $\text{NH}_3^+$  species grows with coverages, indicating that at high coverages the amino group of alanine is predominantly present in its cationic form. It is worth noting that the high binding energy peak in the N 1s spectra (401.6-402.2 eV, Fig. 5.2b) is present at all coverages. The shift of this peak to low binding energies at  $t < 10$  min and its subsequent shift to high binding energies at higher exposures ( $t > 10$  min) indicates multilayer formation at exposures higher than 10 min. This shift coincides also with the saturation of the low binding energy peak (399.6 eV, N 1s spectrum in Fig. 5.2b). In the multilayer the core hole experiences less screening from the metal substrate, thus increasing the binding energy of the N 1s core electron [69]. The peak at 399.6 eV ( $t = 10$  min), also shifts by 0.2 eV towards high binding energies at  $t = 170$  min. The area of the low binding energy peak (399.6 eV, N 1s spectrum in Fig. 5.2b) at the onset of multilayer formation ( $t = 10$  min) was used to calibrate the coverage by defining it as  $\Theta_{\text{Ala}} = 100\%$  saturation. The coverage in the multilayer regime ( $\Theta_{\text{Ala}} \geq 240\%$  sat) was estimated by the attenuation of the low binding energy peak in N 1s region (Fig. 5.2b) using the Beer-Lambert Law which relates the attenuation of an XPS peak signal with the inelastic mean free path (IMFP) of electrons through a material ( $\lambda$ ) [67, 84]:

$$I = I_0 e^{-\frac{d}{\lambda}} \quad (5.1)$$

Where  $I_0$  and  $I$  is the intensity before and after the electron has travelled a distance  $d$  through the material. To the best of our knowledge, there is no information on the inelastic mean free path of electrons travelling through alanine, hence we will consider the guanine which contains the same chemical elements (H, C, N, O). The peak at 399.5-399.8 eV (N 1s spectra in Fig. 5.2b) is generated from electrons with  $\sim 110$  eV kinetic energy ( $h\nu = 510$  eV). The IMFP of electrons with 100 eV kinetic energy travelling in guanine is 6.2 Å [161] and the thickness of one layer of alanine is 2.8 Å [67]. The relative coverage of alanine after different exposures of the amino acid on Ni{110}, along with the exposure times is shown on the right hand side of the XP-spectra (Fig. 5.2). For instance, the ratio of the area of the peak at 399.8 eV at  $t = 170$  min to the area of the same peak at  $t = 10$  min (at the onset of multilayer formation) is  $\sim 0.33$ . According to Eq. 5.1 this ratio corresponds to 7.0 Å thickness of the multilayer alanine, which corresponds to 2.5 layers of molecules on top of the saturated layer (350% sat).

In the O 1s spectra (Fig. 5.2c), the signal consists of an asymmetric wide feature which could only be fitted by two peaks. The low binding energy peak is observed initially at 531.5 eV binding energy and shifts towards higher bind-

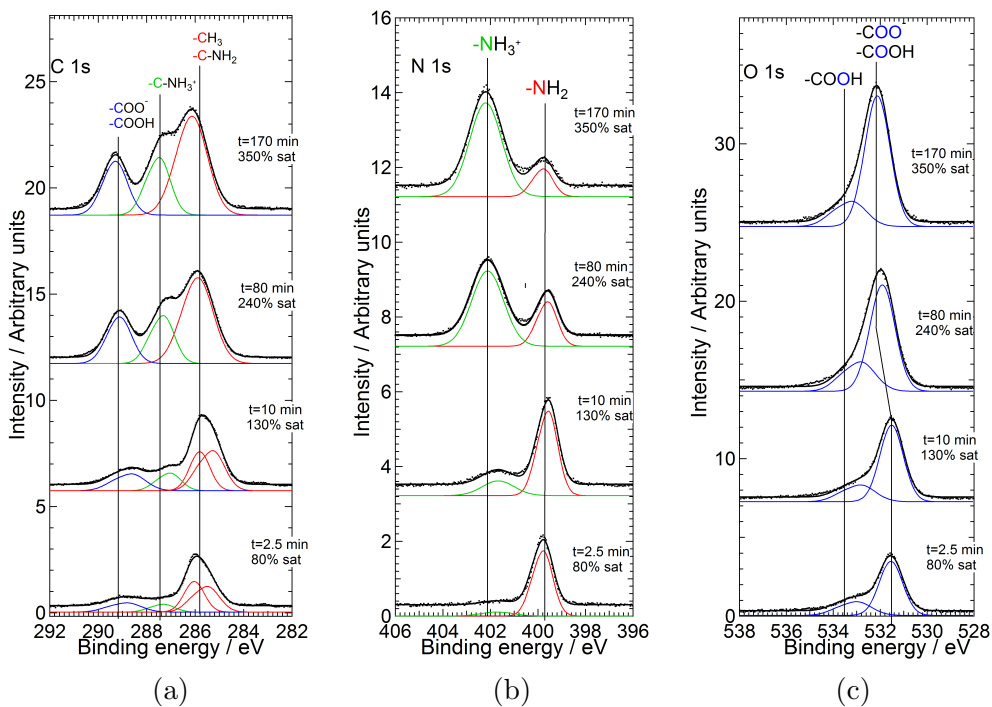


Figure 5.2: Top up XP-spectra of (S)-alanine on Ni{110} (a) in the C 1s region ( $h\nu=400$  eV), (b) in the N 1s region ( $h\nu=510$  eV) and (c) in the O 1s region ( $h\nu=650$  eV). The black dots are the raw data and the solid black thick lines are the fitted curves. The solid coloured curves are the individual peaks obtained upon fitting.

ing energies (532.1 eV) at  $t > 10$  min (130% sat). The latter is again evidence of multilayer formation, which is confirmed also by the change in the shape of the peak. The peak is a combination of signal originating from the overlap contribution from the  $\text{COO}^-$  and  $\text{COOH}$  oxygen atoms [69]. In the deprotonated form of alanine ( $\text{COO}^-$ ), the two oxygen atoms are in an equivalent chemical environment, hence the signal does not split [104]. According to Ref.[109], both the peaks at 531.5 eV (O 1s spectra in Fig. 5.2c) and 399.5-399.8 eV (N 1s spectra in Fig. 5.2b) are indicators of chemisorbed alanine via the oxygen atoms of  $\text{COO}^-$  group and nitrogen atom of the amino group. A smaller peak was found at 532.6-533.2 eV. This peak was previously attributed to the -OH group of the neutral carboxyl group ( $-\text{COOH}$ ) in glycine [69, 148]. The area of the peak, accounts for approximately 20-30% of the total XPS area for all coverages. We cannot exclude the contribution to the signal of this peak from oxygen atoms with a high degree of protonation due to intermolecular hydrogen bonding. The presence of the peak at 532.6-533.2 eV suggests the presence of neutral alanine as well, in the alanine overlayer, which supports an  $\mu_2$  adsorption geometry with the Ni{110} surface (Fig. 4.3).

According to Fig. 5.2a, three peaks are observed in the C 1s region at  $\Theta_{\text{Ala}}=80\%$  sat:

around 285-286 eV, 287.3 eV and 288.8 eV. Previous reports have assigned the peaks at 285-286 eV and 288.8 eV to an overlap of the C-NH<sub>2</sub>/-CH<sub>3</sub> and the overlap of the signals COO<sup>-</sup>/COOH), respectively [104, 105]. The first signal between 285-286 eV, at low coverages, was fitted by two peaks, with energy separation around 0.5-0.6 eV. Work of Powis et al. (2003) [162] on gaseous alanine proposes that the methyl carbon signal is found at lower binding energy region than the  $\alpha$ -carbon signal. In the multilayer regime, the signal of these two peaks merge into one peak since the low binding energy peak (285.3-285.5 eV), corresponding to the methyl carbon signal, moves to high binding energies. The peak at 288.8 eV shifts to high binding energies in the multilayer and changes its shape. Finally the peak at 287.3 eV shows a similar trend with the peak at 401.6-402.2 eV in the N 1s spectra in Fig. 5.2b, showing low signal at coverages  $\Theta < 130\%$  sat and increasing rapidly at higher coverages, hence this peak was assigned to the  $\alpha$ -carbon binding to the cationic amino group (C-NH<sub>3</sub><sup>+</sup>) found in the multilayer. This peak also shift to higher binding energies in the multilayer regime.

In order to determine the thermal stability of (S)-alanine on Ni{110}, TP-XPS-spectra were obtained in the submonolayer and multilayer regime. Figure 5.3 shows TP-XPS spectra in the N 1s and C 1s region after dosing alanine for 30 min. In this layer, the amino group is present in its neutral state, suggesting that the coverage of alanine is in the submonolayer regime ( $\Theta_{\text{Ala}}=80\%$  sat). No change in the signal is observed in both region upon heating to 350 K. Between 350 K and 420 K, a rise of a signal in the low binding region is observed in both spectra (more pronounced in the C 1s region), which can be associated with decomposition products (the nature of these products will be discussed below). At 420 K, all alanine is dissociated, leaving decomposition fragments on the surface.

Figures 5.4a-c and d-e show TP-XPS-spectra and image line profiles, respectively, upon exposing Ni{110} to higher amounts of alanine ( $\Theta_{\text{Ala}}=330-390\%$  sat). The predominant signal corresponding to the protonated amino group (402.1 eV and 287.4 eV in Fig. 5.4b and 5.4a, respectively), suggests that the coverage is in the multilayer regime. No change in the signal is observed upon heating to  $\sim 240$  K. Between  $\sim 240-280$  K an interesting oscillating behaviour is detected between the signals corresponding to NH<sub>3</sub><sup>+</sup> and NH<sub>2</sub> (N 1s spectra in Fig. 5.4b and 5.4e). This behaviour will be discussed below. At  $\sim 310$  K the signal corresponding to the protonated group almost disappears while at the same time there is a rise in the signal corresponding to the neutral amino group. The C 1s and N 1s TP-XPS data above this temperature resemble the spectra in the submonolayer coverage of alanine (Fig. 5.3), suggesting the desorption of the multilayer. At approximately 410-420 K the signal in the O 1s region (Fig. 5.4c) disappears

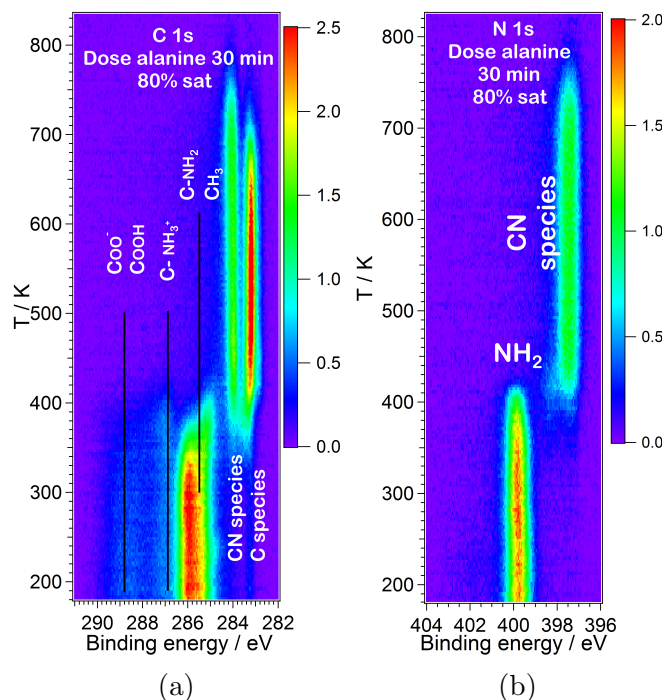


Figure 5.3: Submonolayer TP-XP-spectra of (S)-alanine on Ni{110} in the: (a) C 1s region ( $h\nu=400$  eV) and (b) N 1s region ( $h\nu=510$  eV) (Heating rate= $9$  K  $\text{min}^{-1}$ ).

coinciding with the generation of decomposition fragments in the C 1s (Fig. 5.4a) and N 1s (Fig. 5.4b) region. Based on these results, alanine is decomposing by C-COO<sup>-</sup> cleaving, which generates a desorbed CO<sub>2</sub> and leaves carbon and nitrogen fragments on the surface. High resolution XP-spectra (Fig. 5.4f-5.4h) were obtained between the TP-XP-spectra in the O 1s region (Fig. 5.4c) at 274 K and 346 K. Upon annealing to 274 K, all peaks in all the regions have shifted to the low binding energy region (Fig. 5.4f-5.4h). In the N 1s region (Fig. 5.4g), a small loss in the signal of multilayer alanine is observed together with a small increase in the signal corresponding to NH<sub>2</sub>. In the O 1s region, the low binding energy peak increases in intensity whereas the signal of the high binding energy peak decreases, suggesting a re-arrangement of the COO<sup>-</sup>/COOH<sub>(ads)</sub> groups upon heating. Heating to 346 K, causes fading in the signal of the zwitterionic alanine and the shift of all peaks to the low binding region, confirming that the molecule has almost lost all its multilayer characteristics.

The thermal behaviour of (S)-alanine on Ni{110} was also studied at lower coverage of alanine (N 1s TP-XP-spectra in Fig. 5.5a,  $\Theta_{\text{Ala}}=190\%$  sat) and by using two different ramping rates (N 1s TP-XP-spectra in Fig. 5.5b,  $12$  K  $\text{min}^{-1}$  and N 1s TP-XP-spectra in Fig. 5.5c,  $6$  K  $\text{min}^{-1}$ ). The coverage and the ramping rate did not influence the multilayer desorption and decomposition temperature of

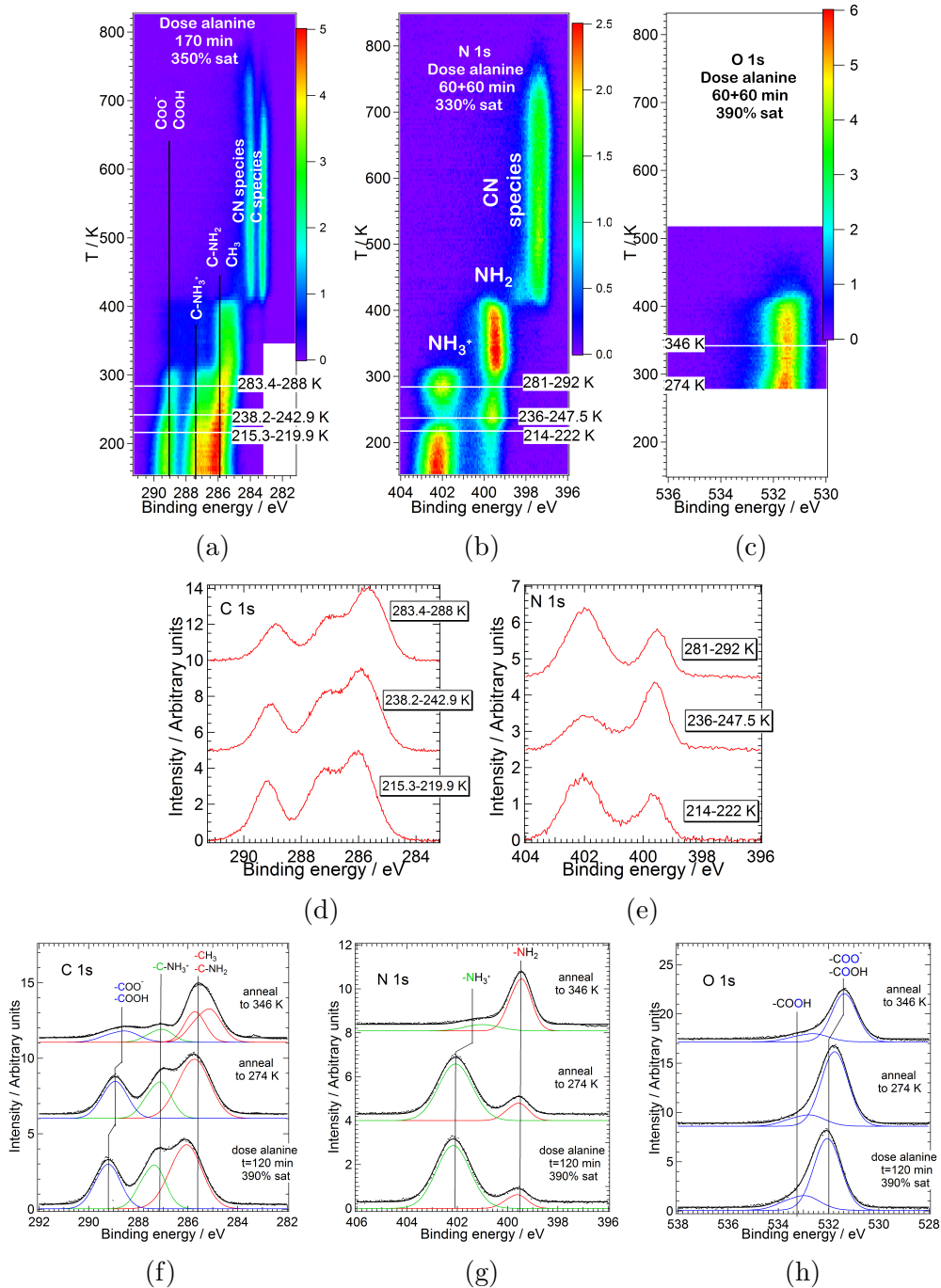


Figure 5.4: Temperature dependence of (S)-alanine on Ni{110} in multilayer region: (a-c) TP-XP-spectra in the (a) C 1s region ( $h\nu=400$  eV) (b) N 1s region ( $h\nu=510$  eV) and (c) O 1s region ( $h\nu=650$  eV) (Heating rate= $9$  K  $\text{min}^{-1}$ ). (d-e) Image line profiles from the corresponded TP-XP-spectra in the (d) C 1s region ( $h\nu=400$  eV) and (e) N 1s region ( $h\nu=510$  eV) (f-h) XP-spectra in the: (f) C 1s region ( $h\nu=400$  eV) (g) N 1s region ( $h\nu=510$  eV) and (h) O 1s region ( $h\nu=650$  eV). The black dots are the raw data and the solid black thick lines are the fitted curves. The solid coloured curves are the individual peaks obtained upon fitting.

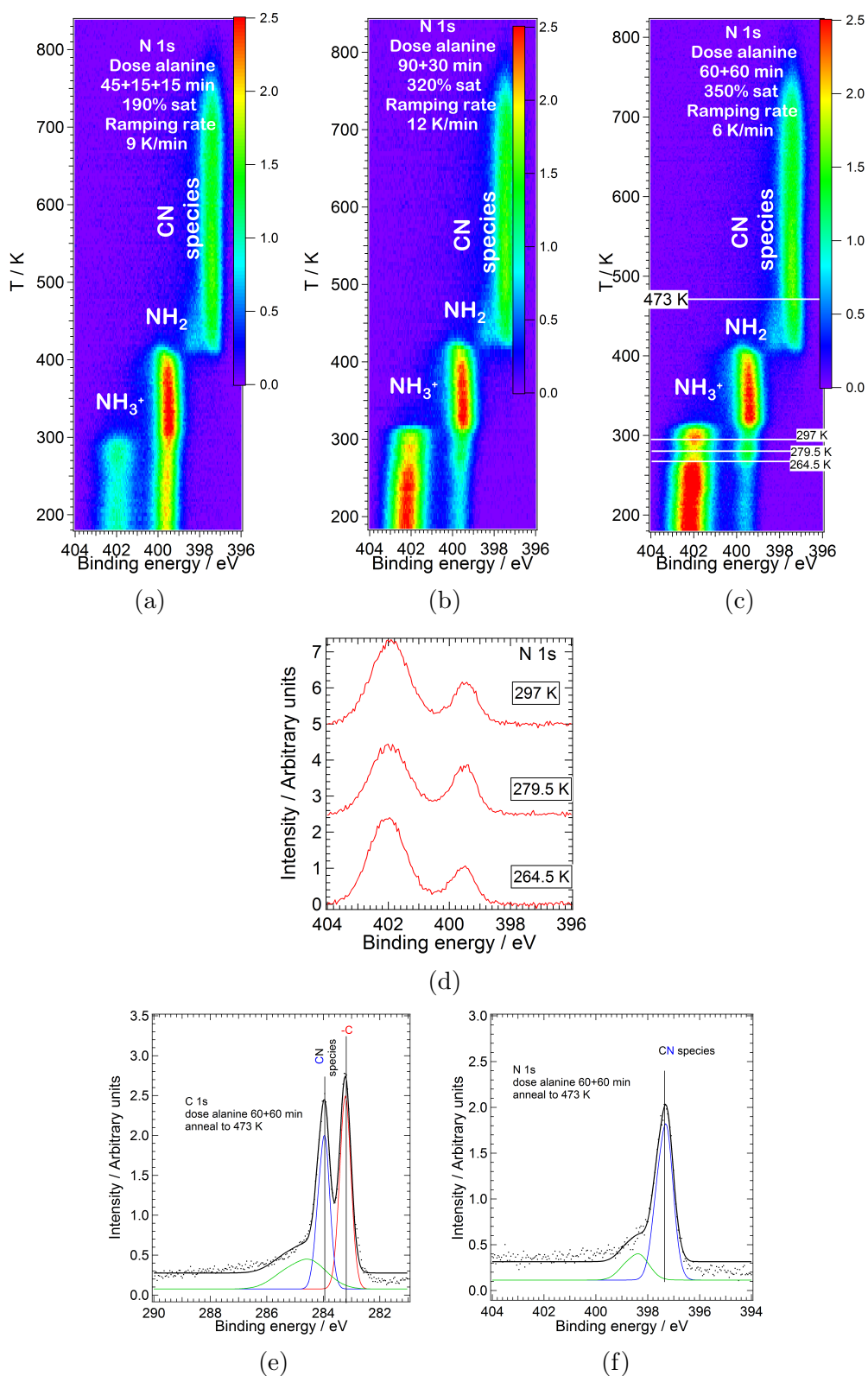


Figure 5.5: Temperature dependence of (S)-alanine on Ni{110}. (a-c) TP-XP-spectra of (S)-alanine on Ni{110} in the N 1s region ( $h\nu=510$  eV). (d) Image line profiles from the N 1s TP-XP-spectra in Fig. 5.5c ( $h\nu=510$  eV). (e-f) XP-spectra in the: (e) C 1s region ( $h\nu=400$  eV) and (f) N 1s region ( $h\nu=510$  eV). The black dots are the raw data and the solid black thick lines are the fitted curves. The solid coloured curves are the individual peaks obtained upon fitting.

alanine. No significant oscillating behaviour is observed for  $\Theta_{\text{Ala}}=190\%$  sat (N 1s TP-XP-spectra in Fig. 5.5a) and for  $\Theta_{\text{Ala}}=320\%$  sat/heating rate=12 K min<sup>-1</sup> (N 1s TP-XP-spectra in Fig. 5.5b). At 6 K min<sup>-1</sup> heating rate and  $\Theta_{\text{Ala}}=350\%$  (N 1s XP-spectra in Fig. 5.5c and 5.5d) the onset of the oscillation took place at a slightly higher temperature ( $\sim 280$  K) compared to the N 1s TP-XP-spectra in Fig. 5.4b. High resolution XP-spectra were obtained in the C 1s and N 1s region (Fig. 5.5e-5.5f, the signal of oxygen was flat) at T=473 K. The spectra were obtained between the N 1s TP-XP-spectra in Fig. 5.5c. Two peaks are observed in the N 1s region at 397.3 eV and 398.4 eV and three peaks in the C 1s region: 283.2 eV, 284 eV and 284.6 eV. The peak at 284 eV disappears along with peak at 397.3 eV at T $\approx$ 770-800 K and can be associated with CN species. The exact chemical nature of this peak will be discussed in the NEXAFS part. The peaks at 398.4 eV and 284.6 eV disappear at T>500 K. These peaks are probably fragments of NH<sub>2</sub>CHCH<sub>3</sub>, kept on the surface, before the full dissociation of alanine. Finally the low binding energy peak in the C 1s region is atomic carbon generated upon further decomposition of alanine and is thermally less stable than the CN species. All fragments of alanine have disappeared from the surface at T>800 K.

### Adsorption of H<sub>2</sub>O on clean Ni{110}

Figures 5.6a and 5.6e show TP-XP-spectra and XP-spectra in the O 1s region after dosing H<sub>2</sub>O onto Ni{110} at 120 K and 180 K, respectively. Figure 5.6b-5.6c show vertical image line profiles obtained from Fig. 5.6a for the two main peaks (533.6 eV and 530.85 eV). Figure 5.6d shows horizontal image line profiles for several temperatures also obtained from TP-XP-spectra. The high binding energy peak is assigned to molecular water whereas the low binding energy peak is associated with hydroxyl groups [158]. Dosing H<sub>2</sub>O at 120 K creates ice multilayers on Ni{110} (Fig. 5.6a). The multilayer desorption occurs around 150 K, in line with Benndorf and Madey (1988) [153]. The multilayer desorption is indicated by the significant decrease in the H<sub>2</sub>O signal and its shift to the lower binding region (from 534 eV to 533.3 eV, Fig. 5.6a-b). An increase in the signal of the peak corresponding to hydroxyls (530.85 eV) is also observed (Fig. 5.6c), which suggests that at this temperature, the H<sub>2</sub>O is not only desorbed, but also partially dissociates to hydroxyls. Increase from 150 K to 220 K, causes significant reduction in the signal corresponding to water while at the same time the signal of the hydroxyls stays almost the same (Fig. 5.6a-d). Heating to 250-260 K induces almost full dissociation and desorption of water, while at the same time the peak corresponding to hydroxyls moves to lower binding energies (around 530.7 eV, Fig. 5.6a and

5.6d). The two latter effects are consistent with the  $A_2$  and  $A_1$  thermal desorption peaks in the work of Callen et al (1992) [156], observed at 220 K and 260 K, respectively. The authors of Ref.[156] proposed that the aforementioned desorption peaks originate from the desorption of  $H_2O$  bonded to nickel in the chemisorbed layer and desorption of  $H_2O$  stabilised by adsorbed OH, respectively. Annealing above 350 K causes almost total removal of the hydroxyls from the nickel surface (Fig. 5.6a, 5.6c and 5.6d).

Dosing  $H_2O$  at 180 K (O 1s spectrum in Fig. 5.6e) causes saturation of the XPS signal. The XP-spectra show 2 peaks around 533.2 eV and 531.3 eV in 3.7:1 ratio, which correspond to  $H_2O$  and -OH species, respectively [158]. The total coverage ( $H_2O$  and -OH species) of the saturated layer was estimated  $\sim 0.61$  ML, whereas the coverage of  $H_2O$  species is  $\sim 0.48$  ML. The coverage was calculated based on area of the signal of alanine in the N 1s and O 1s region at  $\Theta_{Ala}=80\%$  sat (Fig. 5.2b-5.2c) and the area of the low binding energy peak (399.6 eV) in the N 1s spectrum in Fig. 5.2b at the onset of multilayer formation ( $t=10$  min,  $\Theta_{Ala}=130\%$  sat) which corresponds to  $\Theta_{Ala}=100\%$  sat or 0.33 ML absolute coverage (3 bonds on 3 nickel atoms). The estimated value was corrected by factor of 2 (2 oxygen atoms per alanine molecule). This estimated coverage of  $H_2O$  species ( $\sim 0.48$  ML) in the saturated layer (O 1s spectrum in Fig. 5.6e) is in agreement with the work of Callen et al (1990) [154] on the adsorption of  $H_2O$  on Ni{110}. The authors of Ref.[154] suggested that saturation coverage of the  $A_1$ ,  $A_2$  and B desorption states of water is equalled to 0.48 ML, which represents the first chemisorbed layer that can be selectively populated at 180 K. However the presence of the peak associated with hydroxyls (531.3 eV), implies partial dissociation of water at 180 K (in a later study Callen et al. (1992) [156] suggested that the partial dissociation of water occurs at  $205\pm 2$ K). Both peaks shift to low binding energies ( $\sim 0.1$  eV) upon annealing to 190 K. At this temperature the  $H_2O$  signal is reduced by 22% with respect to the saturated layer, implying desorption of  $H_2O$  species from the chemisorbed layer, and also partial dissociation which is reflected in increase of the signal corresponding to the hydroxyl species. Further annealing to 215 K induces further dissociation and desorption of both water (58% reduction with respect to the saturated layer) and hydroxyl species (25% reduction with respect to the layer at 190 K). The ratio of the peaks at this temperature is 1.8:1. At 240 K, the low binding energy peak becomes broader while at the same time the ratio of the peaks is reduced to 0.9:1. The hydroxyl signal does not change significantly with respect to 215 K while at the same time the water signal drops by 77% with respect to the saturated layer. At this temperature the  $A_2$  state has been fully desorbed, leaving only  $H_2O$ -OH species in a hydrogen bonding complex

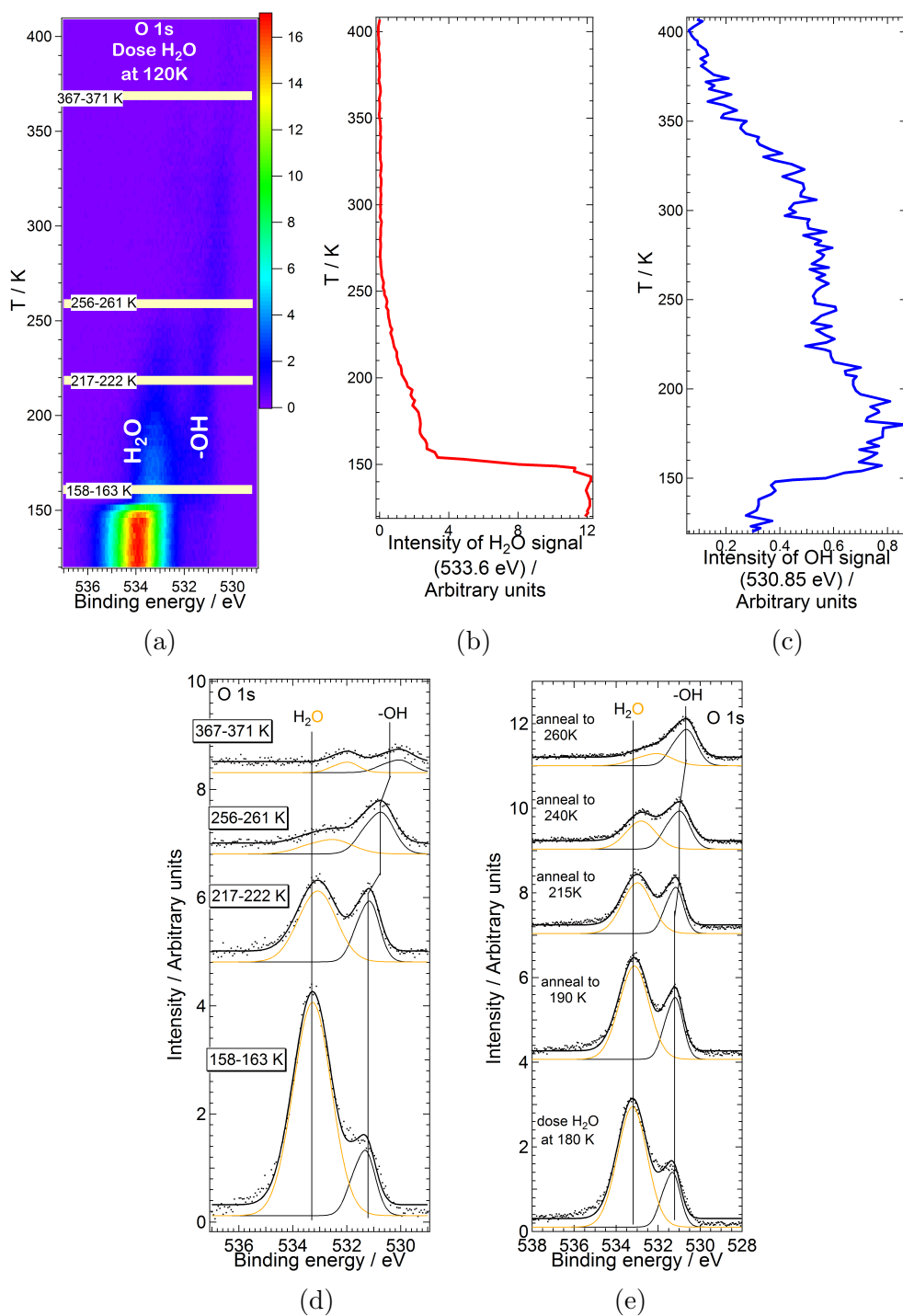


Figure 5.6: (a) TP-XP-spectra in the O 1s region ( $h\nu=650$  eV) after dosing H<sub>2</sub>O onto Ni{110} at 120 K (Heating rate= 6 K min<sup>-1</sup>), (b-c) the corresponded vertical image line profiles for the two main peaks (in 2 eV wide bands) and (d) the corresponded horizontal image line as shown in Fig. 5.6a. (e) XPS-spectra in the O 1s region ( $h\nu=650$  eV) after dosing H<sub>2</sub>O onto Ni{110} at 180 K up to saturation and subsequent annealing to different temperatures. The black dots are the raw data and the solid black thick lines are the fitted curves. The solid coloured curves are the individual peaks obtained upon fitting.

[156]. The coverage of water-hydroxyls at this temperature is  $\sim 0.23$  ML. Both peaks have been shifted to low binding energies by 0.3-0.4 eV with respect to the saturated layer. At 260 K, only small traces of water are present on the surface (reduced by 88% with respect to the saturated layer) while at the same time we can argue that the signal of both peaks contains CO species co-adsorbed on the nickel surface, since both peaks are broader with respect to the spectrum of the chemisorbed layer at 180 K. The signal of the peak corresponding to the hydroxyls species does not change significantly and its position is shifted by  $\sim 0.6$ - $0.7$  eV to the low binding energy region (530.65 eV) with respect to the spectrum of the saturated layer at 180 K. This shift, which was also spotted in the TP-XP-spectra at 120 K (Fig. 5.6a and 5.6d) at 250-250 K, coincides with the  $A_1$  desorption state [156]. The  $H_2O$  and -OH species interact through hydrogen bonding, therefore the presence of  $H_2O$  shifts the binding energy of the -OH to 531.2-531.3 eV, an effect that deteriorates following desorption and dissociation of  $H_2O$ , restoring the peak position at 530.7-530.6 eV [158]. According to Ref.[158] this effect is reversible after re-adsorption of  $H_2O$  at lower temperatures. This effect might also explain the broadening of the peak corresponding to OH (at 240 K) and the  $H_2O$  (at 260 K) with respect to the spectrum of the saturated layer. The presence of hydrogen bonds causes elongation and weakening of OH bond of water, causing decrease in the vibrational frequency of the bond [159], which makes the XPS peak less broader with respect to the XP-spectra without the presence of hydrogen bonds. It is worth noting that the present study provides evidence of dissociation of  $H_2O$  even at temperatures  $T < 163$  K, as proposed by Ref.[158].

### Co-Adsorption of alanine and multilayer $H_2O$ on Ni{110}

Figure 5.7 shows XP-spectra after co-adsorbing alanine and  $H_2O$  on Ni{110}. The layer was prepared by dosing  $H_2O$  at 141 K for 400 s and subsequently dosing alanine for 30 min at  $T=140$  K. XP-spectra of alanine deposited on clean surface at  $T_{\text{sample}}=200$  K ( $t=30$  min,  $\Theta_{\text{Ala}} = 80\%$  sat) are shown for the purpose of comparison.

The O 1s spectrum upon dosing  $H_2O$  at 141 K (Fig. 5.7c, top panel) shows three resolved peaks at 531.1 eV, 533.3 eV and 534.4 eV. The two low binding energy peaks are assigned in similar fashion to the O 1s  $H_2O$  step anneal XP-spectra in Fig. 5.6e to -OH and molecular  $H_2O$  species, respectively [158]. The high binding energy peak (534.4 eV) is linked with ice water multilayer species, as expected at this dosing temperature ( $T=141$  K). Based on the area of the peak at 533.3 eV the coverage of  $H_2O$  species found under the ice multilayer species is

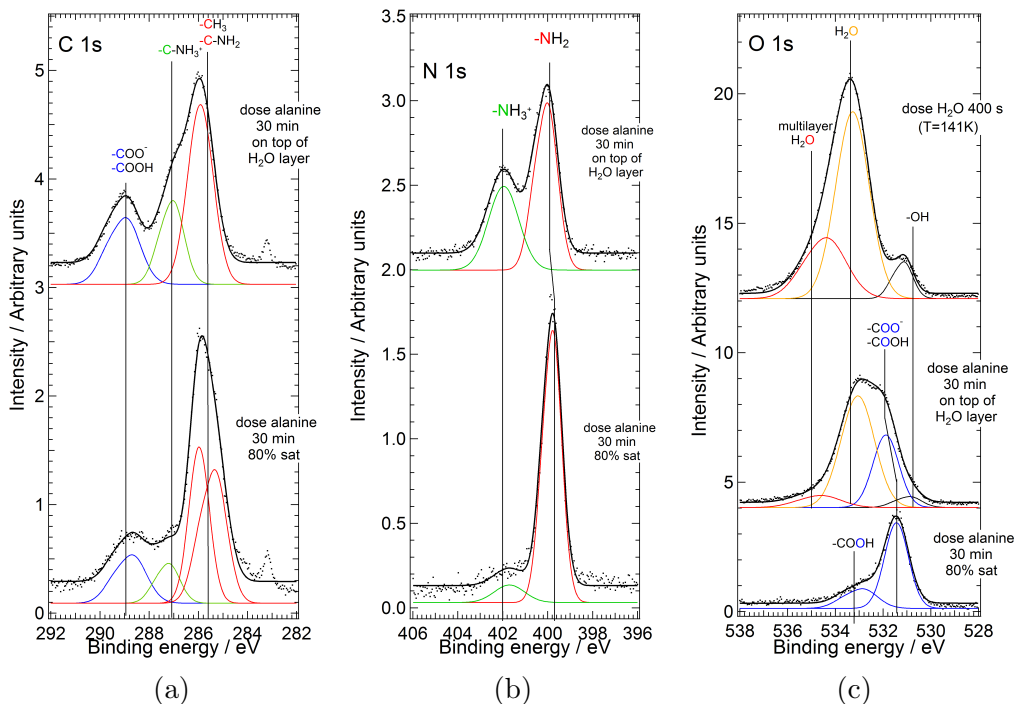


Figure 5.7: Comparison of XP-spectra obtained after dosing (S)-alanine for 30 minutes onto Ni{110} at 140 K which was previously dosed with H<sub>2</sub>O for 400s at 141K (multilayer H<sub>2</sub>O), with spectra with the same alanine dosing time without pre-adsorption of water and with the O 1s spectrum of the pure H<sub>2</sub>O/OH overlayer, present before dosing alanine in the (a) C 1s region ( $h\nu=400$  eV), (b) N 1s region ( $h\nu=510$  eV) and (c) O 1s region ( $h\nu=650$  eV).

$\sim 1.2$  ML, which is in close agreement with the bilayer model of water on Ni{110} (1 ML total coverage) described in Ref.[154]. It is possible, however, that the formation of the multilayer takes place before the completion of this layer, which will lead to underestimating the calculated coverage of the non multilayer water. It is worth pointing that the XP-spectrum in Fig. 5.7c (top panel) suggests the presence of hydroxyls even at this low adsorption temperature ( $T=141$  K).

Dosing alanine onto Ni{110} covered with multilayer H<sub>2</sub>O, causes an increase in the level of protonation of the amino group with respect to the spectra of pure alanine overlayer, indicated by the increase in the intensity of the peak at 401.9 eV (N 1s spectrum in Fig. 5.7b) and 287.0 eV, (C 1s spectra in Fig. 5.7a) corresponding to the nitrogen and the carbon of the C-NH<sub>3</sub><sup>+</sup> group, respectively) and the decrease in the signal of the peak corresponding to the NH<sub>2</sub> group found at 400.0 eV (N 1s spectrum in Fig. 5.7b). The presence of H<sub>2</sub>O does not influence significantly the amount of adsorbed alanine (Fig. 5.7b). The XP-spectrum in the O 1s region (Fig. 5.7c) upon depositing alanine on top of multilayer H<sub>2</sub>O, contains one extra peak in comparison with the spectrum of pure H<sub>2</sub>O/OH overlayer, found at 531.9 eV, which is associated with COO<sup>-</sup>/COOH species. The peaks associated

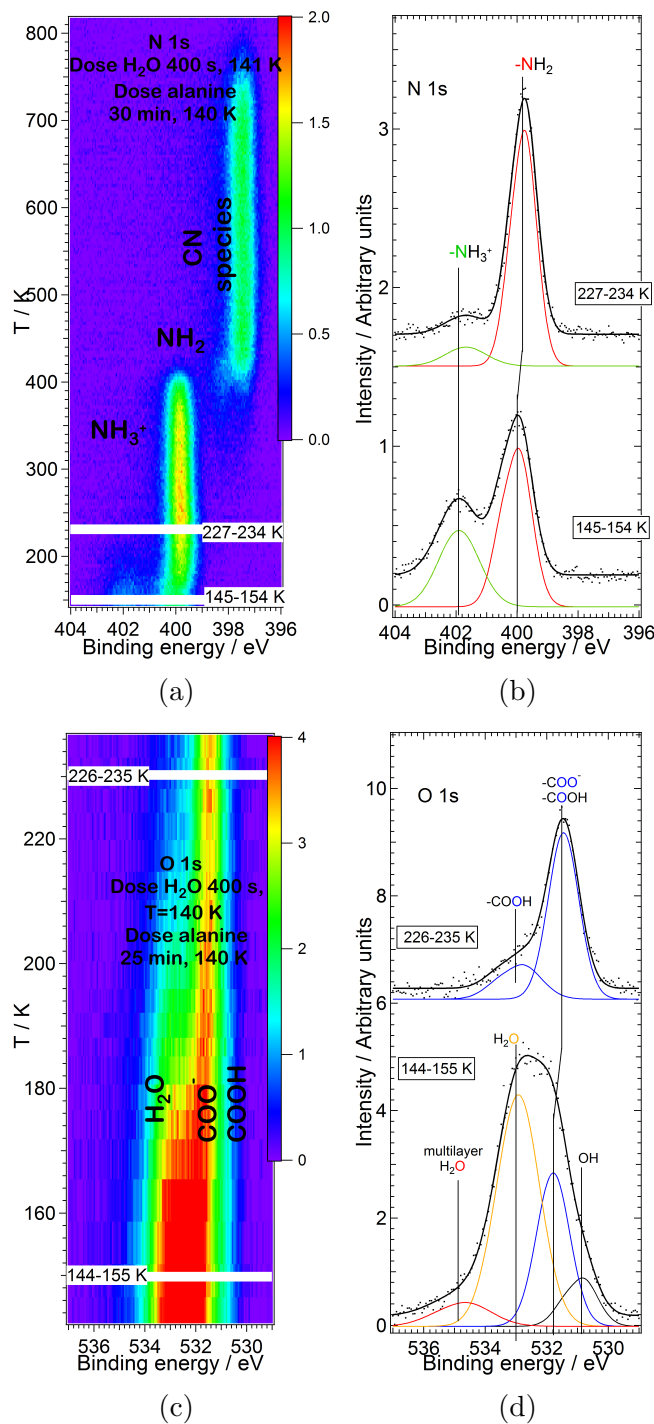


Figure 5.8: TP-XP-spectra and the corresponded image line profiles, obtained upon dosing H<sub>2</sub>O onto Ni{110} up to the multilayer regime and subsequently dosing (S)-alanine. The spectra were obtained in the (a-b) N 1s region ( $h\nu=510$  eV) (Heating rate= $9$  K min<sup>-1</sup>) and (c-d) in the O 1s region ( $h\nu=650$  eV) (Heating rate= $12$  K min<sup>-1</sup>). The black dots are the raw data and the solid black thick lines are the fitted curves. The solid coloured curves are the individual peaks obtained upon fitting.

with the  $\text{COO}^-/\text{COOH}$  (O 1s spectrum in Fig. 5.7c) and  $\text{NH}_2$  groups (N 1s spectrum in Fig. 5.7a) shift to high binding energies with respect to the spectrum of alanine deposited on clean nickel (from 531.4 eV to 531.9 eV and from 399.8 eV to 400.0 eV, respectively), implying that these species are not chemisorbed on the nickel surface. The peak linked to molecular  $\text{H}_2\text{O}$  (533.3 eV) decreases by  $\sim 40\%$  with respect to the spectrum of the pure  $\text{H}_2\text{O}/\text{OH}$  overlayer. According to Eq. 5.1, and considering  $\lambda=6.2 \text{ \AA}$  [161] and  $d=2.24\text{\AA}$  ( $80\% \text{ sat} \times 2.8\text{\AA}$ ,  $2.8\text{\AA}$  being the thickness of one layer alanine [67]), the expected attenuation of the  $\text{H}_2\text{O}$  signal from the alanine overlayer ( $1-I/I_0$ ) is  $\sim 30\%$ , therefore a partial destruction of the  $\text{H}_2\text{O}$  “bilayer” from the alanine molecule, must have taken place. It is worth noting that the XPS signal of molecular  $\text{H}_2\text{O}$  (533.3 eV) might have contribution from the signal of  $\text{COOH}$  groups, which might be present in the alanine overlayer. The peak of multilayer water is reduced by  $\sim 80\%$  with respect to the spectrum of the pure  $\text{H}_2\text{O}/\text{OH}$  overlayer and its position shifts to 534.6 eV, suggesting that the alanine layer almost destroys the water multilayer while at the same time some of the remaining  $\text{H}_2\text{O}$  layer is interacting with the molecule. It is possible also that some of this effect is caused by attenuation effects. Finally the significant reduction of the peak associated to hydroxyls ( $\sim 61\%$ ) with respect to the spectrum of the  $\text{H}_2\text{O}/\text{OH}$  overlayer, might be due to condensation reaction between the hydrogen of the molecule and the hydroxyl group, as it was proposed by Langell et al. (1994) [130], for describing the adsorption of acetic acid on hydroxylated  $\text{NiO}\{111\}$  (see Fig. 3.11). The reduction can be also related to attenuation effects. The shift of this peak from 531.1 eV to 530.9 eV suggests that the presence of the alanine layer distorts the hydrogen bonding between the  $\text{H}_2\text{O}$  and  $-\text{OH}$  molecules.

The temperature dependence of alanine upon depositing the molecule onto  $\text{Ni}\{110\}$  covered with multilayer  $\text{H}_2\text{O}$  is shown in Figure 5.8. Heating the sample to 200 K causes significant reduction in the signal corresponding to  $\text{H}_2\text{O}$  layer whereas the signal corresponding to the  $\text{COO}^-/\text{COOH}$  groups of the alanine molecule (531.8 eV) does not alter significantly (Fig. 5.8c). At  $\sim 225\text{-}235 \text{ K}$ , the water signal is untraceable with XPS (O 1s spectra in Fig. 5.8c-5.8d) while at the same time spectra in the O 1s and N 1s region (Fig. 5.8b+d) resemble the spectra of the chemisorbed alanine (almost all the amino group has deprotonated) maintaining the same thermal stability (decomposition at  $\sim 420 \text{ K}$ , Fig. 5.8a) with the pure alanine overlayer. The thermal destabilisation of  $\text{H}_2\text{O}$  upon co-adsorption with alanine molecules with respect to the pure water overlayer is explained by the suppression of the hydrogen bonding between  $\text{H}_2\text{O}$  and  $-\text{OH}$  molecules by the alanine molecules, which normally will stabilise the former, and cause the desorp-

tion of  $A_1$  desorption state at  $T \approx 250$ - $260$  K [153, 156]. Tzvetkov et al 2005 [163], have also observed thermal destabilisation of  $H_2O$  upon co-adsorbed with glycine on single crystalline of  $Al_2O_3$ . This effect was explained by the suppression in the transition between the amorphous to crystalline phase at 140-160 K from the glycine molecules [163].

### Co-Adsorption of alanine and submonolayer $H_2O$ on Ni{110}

Figure 5.9 shows TP-XP-spectra upon depositing (S)-alanine onto Ni{110}, covered with submonolayer  $H_2O$ . The layer of  $H_2O$  was prepared by dosing  $H_2O$  at 213 K to saturation. Two peaks are observed at 533.1 eV and 531.1 eV (in  $\sim 1.7:1$  ratio) which are unambiguously assigned to molecular  $H_2O$  and OH species, respectively. The coverage of  $H_2O$  at 213 K ( $\Theta \approx 0.27$  ML, O 1s spectrum in Fig. 5.9b) are below the saturation coverage of  $H_2O$  at 180 K ( $\Theta \approx 0.48$  ML, O 1s spectrum in Fig. 5.6e). The XP-spectra in all the regions, upon dosing alanine on top of submonolayer  $H_2O$  (O 1s spectrum in Fig. 5.9b carbon and nitrogen are not shown), almost resemble the spectra of alanine on clean Ni{110} (Fig. 5.7), therefore it is assumed that either  $H_2O$  species are suppressed by the alanine molecules or were displaced from the surface. Work of Langell et al (1994) [130] on the adsorption of acetic acid on hydroxylated NiO(111), has proposed that the acetic acid displaces the hydroxyls from the surface, through condensation reaction between the hydroxyl on the surface and the hydrogen of the molecule, releasing  $H_2O$  in the gas phase (see Fig. 3.11). Heating the layer to 365-375 K (Fig. 5.9) causes a shift of both peaks ( $\sim 531.4$  eV and  $\sim 532.8$  eV) to 531.1 eV and 532.4 eV, respectively. The O 1s signal disappears at 420 K in agreement with the previous TP-XP-spectra.

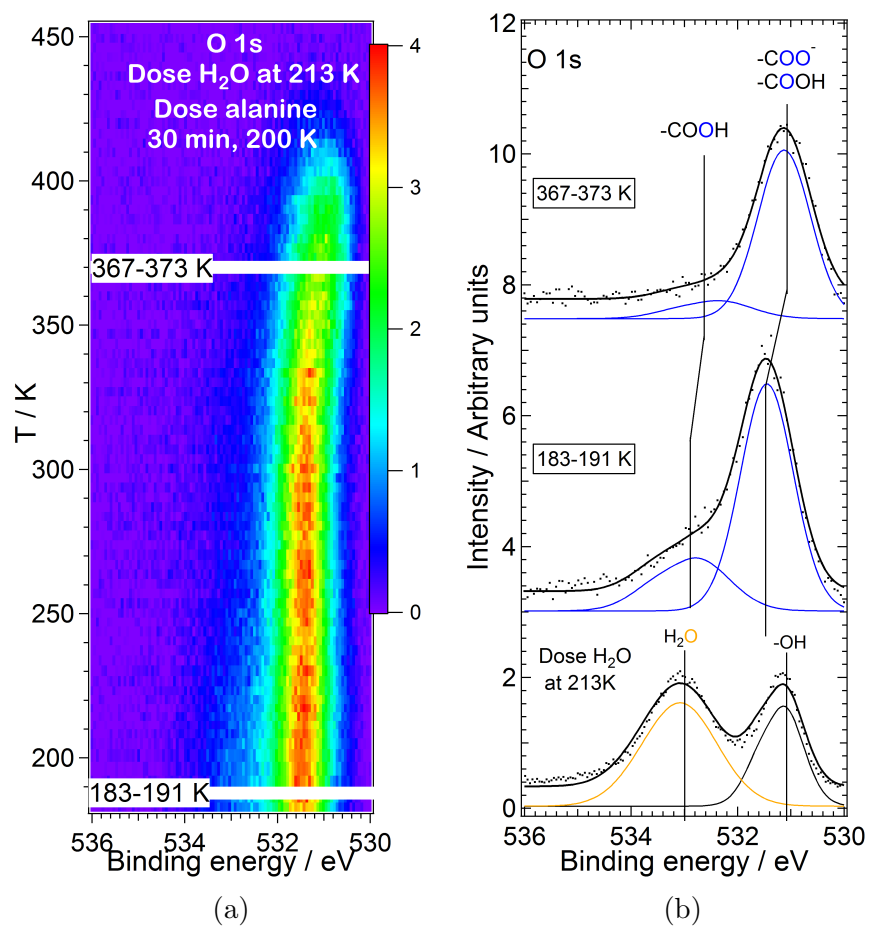


Figure 5.9: TP-XP-spectra of in the O 1s region ( $h\nu=650$  eV) (Heating rate= $9$  K  $\text{min}^{-1}$ ) and the corresponded image line profiles upon dosing H<sub>2</sub>O onto Ni{110} at  $T_{\text{sample}}=213$  K and subsequently dosing (S)-alanine for 30 min at  $T_{\text{sample}}=200$  K. The black dots are the raw data and the solid black thick lines are the fitted curves. The solid coloured curves are the individual peaks obtained upon fitting.

### 5.3.3 NEXAFS Results

Figures 5.10a and 5.11a show angle resolved NEXAFS in the O K-edge region upon depositing (S)-alanine onto clean Ni{110} up to multilayer regime ( $\Theta_{\text{Ala}}=390\%$  sat) and anneal the layer to 346 K (Fig. 5.10a) and upon dosing H<sub>2</sub>O onto Ni{110} at  $T_{\text{sample}}=213$  K and subsequently dosing (S)-alanine for 30 min at  $T_{\text{sample}}=200$  K (Fig. 5.11a). The XP-spectra of these two layers are shown in Fig. 5.4f-5.4h and Fig. 5.9b, respectively. In both layers the coverage of (S)-alanine on Ni{110} is close to the saturation ( $\Theta_{\text{Ala}}=130\%$  sat and  $\Theta_{\text{Ala}}=80\%$  sat, respectively), existing predominantly in its anionic and neutral form, with traces of zwitterionic alanine (16% and 8% of the total XPS area, respectively). The O K-edge NEXAFS spec-

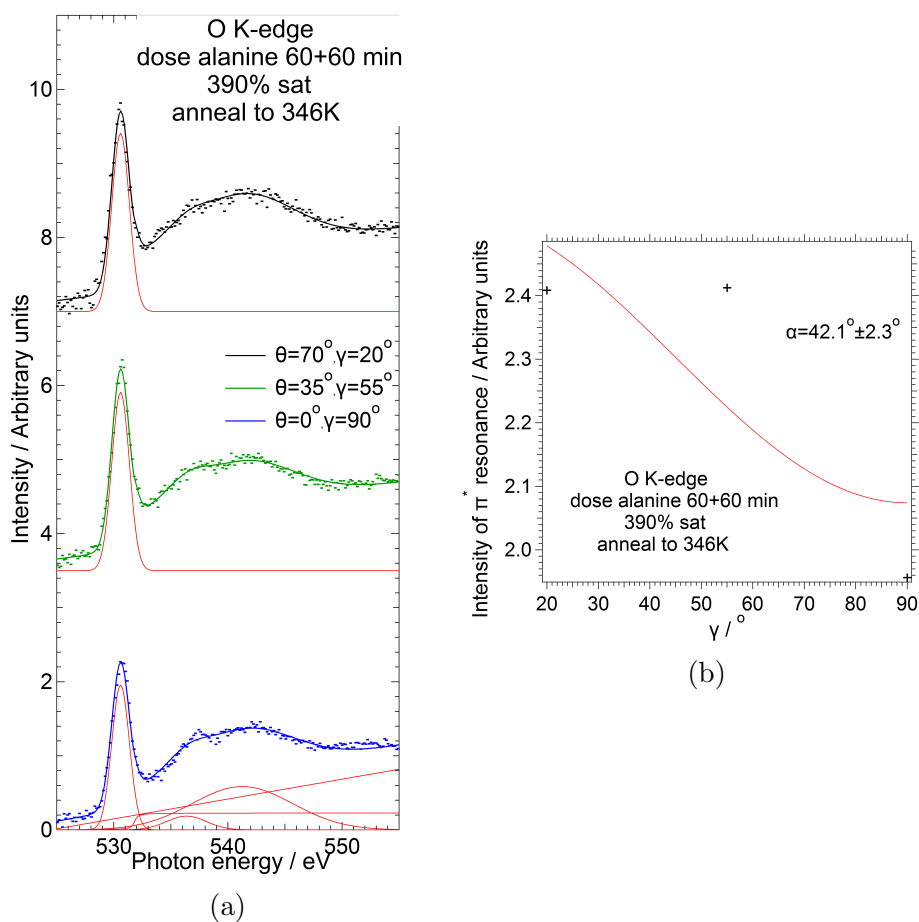


Figure 5.10: (a) Angle resolved O K-edge NEXAFS spectra obtained upon dosing (S)-alanine onto Ni{110} for 60+60 min ( $\Theta_{\text{Ala}}=390\%$  sat) and anneal the layer to 346 K. The dots represent the raw data and the solid thick lines the fitted curves. The red curves below the spectra show the individual Gaussian peaks, the linear background and the the step function used during the fitting process. (b) Plots (black markers) showing the intensity of the oxygen  $\pi^*$  resonance in Fig. 5.10a as a function of angle  $\gamma$ , where  $\gamma$  is related to the angle of incidence  $\theta$  ( $\gamma=90^\circ-\theta$ ). The solid red line shows the fitted curve calculated by the cos function in Eq. 5.3.

tra (Fig. 5.10a and 5.11a) consist of a sharp  $\pi^*$  resonance at 530.6 eV, two  $\sigma^*$  resonances at 535.3-536.3 eV and 541.2-541.3 eV and a step at 531.8 eV. It is difficult to determine the exact position of the  $\sigma^*$  resonances due to their large FWHM, however this does not influence the purpose of our NEXAFS data analysis which relies on the intensity of the  $\pi^*$  resonance. The  $\sigma^*$  resonances are due to C-C (535.3-536.3 eV) and C-O (541.2-541.3 eV) bonds [46, 104, 105].

The  $\pi^*$  resonance (530.6 eV, (Fig. 5.10a and 5.11a) in the O K-edge region is associated with the the  $\text{COO}^-$  group and C=O group of the protonated carboxyl group of the alanine molecule. The intensity of the  $\pi^*$  resonance shows angular dependency (Fig. 5.10b and 5.11b), therefore it was used to determine the tilt angle  $\alpha$  of the C=O/ $\text{COO}^-$  groups of the alanine molecule (Fig. 5.12) with respect

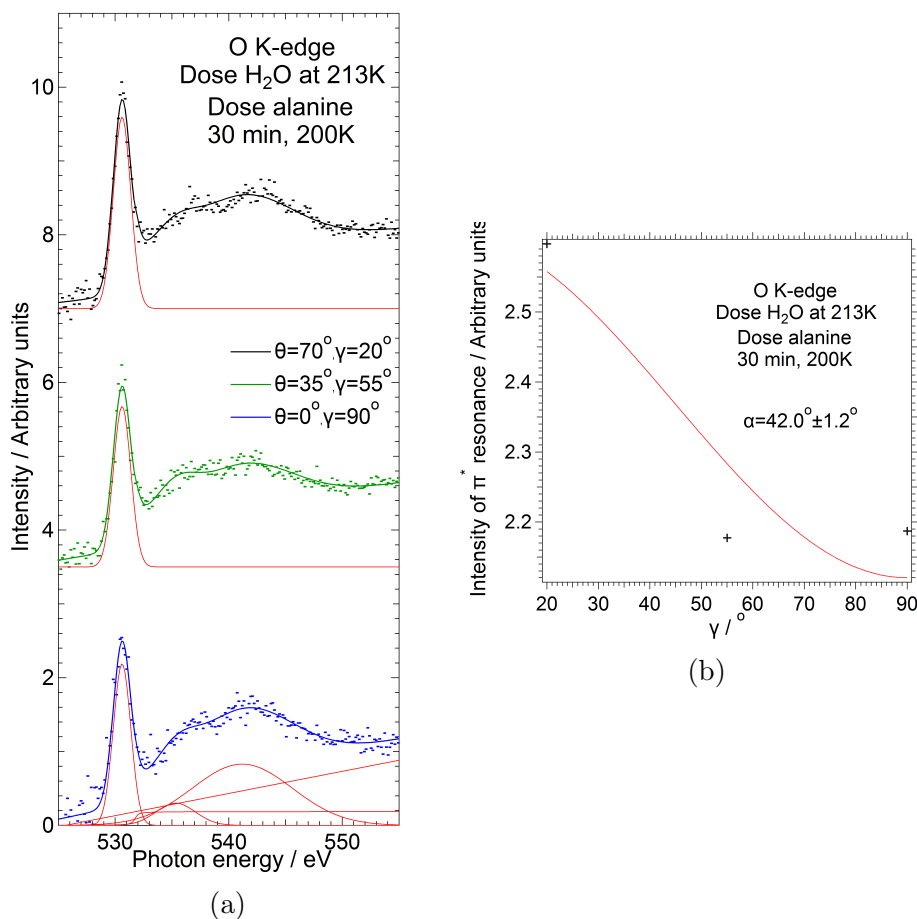


Figure 5.11: (a) Angle resolved O K-edge NEXAFS spectra obtained upon dosing  $\text{H}_2\text{O}$  onto Ni{110} at  $T_{\text{sample}}=213$  K and subsequently dosing (S)-alanine for 30 min at  $T_{\text{sample}}=200$  K. The red curves below the spectra show the individual Gaussian peaks, the linear background and the the step function used during the fitting process. (b) Plots (black markers) showing the intensity of the oxygen  $\pi^*$  resonance in Fig. 5.11a as a function of angle  $\gamma$ , where  $\gamma$  is related to the angle of incidence  $\theta$  ( $\gamma=90^\circ-\theta$ ). The solid red line shows the fitted curve calculated by the cos function in Eq. 5.3.

to the Ni{110} surface according to Eq. 5.2[96]:

$$I(\theta) = A[P(\sin^2\theta * \cos^2\alpha + \cos^2\theta * \sin^2\alpha * \cos^2\phi - \sin^2\alpha * \sin^2\phi) + \sin^2\alpha * \sin^2\phi] \quad (5.2)$$

Where  $\theta$  is the angle between the electric field vector and the surface plane,  $\phi$  the azimuthal angle of the vector of the final state orbital and P is the polarisation factor. Assuming  $\phi=0$  and P=1 for the SuperESCA beamline, the Eq. 5.2, is transformed to Eq. 5.3:

$$I(\gamma) = B[(\cos^2(\gamma + \alpha)) + (\cos^2(\gamma - \alpha))] \quad (5.3)$$

Where  $\gamma=90^\circ-\theta$ . The angular dependency of the  $\pi^*$  resonance (Fig. 5.10b and 5.11b) returned tilt angle  $\alpha \approx 42.1^\circ$  (Fig. 5.10b) and  $\alpha \approx 42.0^\circ$  (Fig. 5.11b) for the NEXAFS spectra in Fig. 5.10a and Fig. 5.11a, respectively. The error margins stated in Fig. 5.10b and 5.11b refer to the fitting error. Both angles are in close agreement with the corresponding tilt angle of the carboxylate group of alanine on Cu{110} ( $45^\circ$ ) [104]. Angle dependent NEXAFS of (S)-alanine on Ni{111} in the O K-edge region [46] showed two  $\pi^*$  resonances which were assigned to the carboxylate group in the tridentate (anionic alanine) and bidentate (zwitterionic alanine) adsorption mode of the alanine molecule on the Ni{111} substrate. The angular dependency of these two  $\pi^*$  resonances returned tilt angles  $\alpha=56^\circ$  and  $\alpha=64^\circ$  [46]. These values correspond to the tilt of the carboxylate group with respect to the Ni{111} surface plane in the anionic and zwitterionic alanine, respectively [46]. The tilt angles of the C=O/COO<sup>-</sup> groups of alanine with respect to the Ni{110} surface plane ( $\sim 42^\circ$ ), obtained in our study are close to the tilt angle of carboxylate group of the anionic alanine on the Ni{111} surface plane ( $56^\circ$ , [46]). It is possible that our NEXAFS data could not resolve the zwitterionic conformation of the alanine molecule because of their low concentration on the nickel surface. In a later study from Nicklin et al. (2018) [47], the tilt angle of the carboxylate group of (S)-alanine with respect to the Ni{111} surface plane was determined to be  $63^\circ$  and  $34^\circ$ , by using angle dependent NEXAFS in the O K-edge region under UHV conditions and under the presence of elevated pressures of H<sub>2</sub> (P= $4 \times 10^{-1}$  Torr), respectively. The two different tilt angles were associated with the tridentate and the bidentate conformation of the alanine molecule on the Ni{111} surface, respectively, since the presence of elevated pressures of hydrogen caused the protonation of the neutral amino group of anionic alanine, and generation of zwitterionic species of the molecule [47].

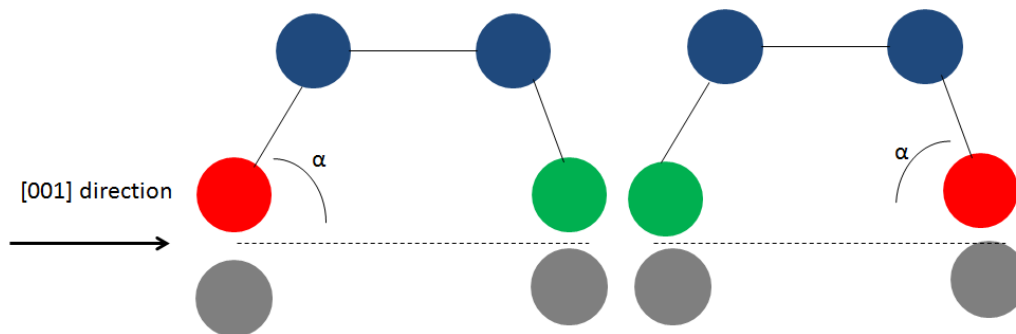


Figure 5.12: Schematic view of the tilt angle  $\alpha$ , which is the angle between the C=O/COO<sup>-</sup> groups of the alanine molecule with respect to the Ni{110} surface plane, for the two possible adsorption orientations. The blue circles are carbon atoms, the red circles are oxygen atoms, the green circles are nitrogen atoms and grey circles are nickel atoms.

N K-edge NEXAFS spectra were recorded (Fig. 5.13a) in order to define the nature of the decomposition products of alanine on Ni{110} at 473 K (N 1s spectrum in Fig. 5.5f). The N K-edge NEXAFS spectra (Fig. 5.13a) consist of two  $\pi^*$  resonances at 396.7 eV and 398.5 eV, a  $\sigma^*$  resonance at 411.6 eV and a step at 399.0 eV. The presence of two  $\pi^*$  resonances in the N K-edge region suggest that the decomposition species contain multiple bonds between the C and N atoms. The TPD data of mass 2 in Fig. 5.1a show a peak at 800 K which suggests desorption of molecular hydrogen from the decomposition species, therefore we propose that the decomposition fragments are H,C,N species with general chemical formula H<sub>x</sub>CN. Zubavichus et al. (2004) [164] have also observed generation of peaks in the N K-edge region in the the range of 399-403 eV, upon irradiating pristine with soft X-rays. The authors have attributed these peaks to  $\pi^*$  transitions due to N=C and N≡C bonds [164]. By using Eq. 5.3, the angular dependency of the two  $\pi^*$  resonances (Fig. 5.13b-5.13c), returned tilt angles  $\alpha_1 \approx 26.7^\circ$  and  $\alpha_1 \approx 25.4^\circ$  for the peaks at 396.7 eV (Fig. 5.13b) and 398.5 eV (Fig. 5.13c), respectively. The error margins stated in Fig. 5.13b and 5.13c refer to the fitting error.

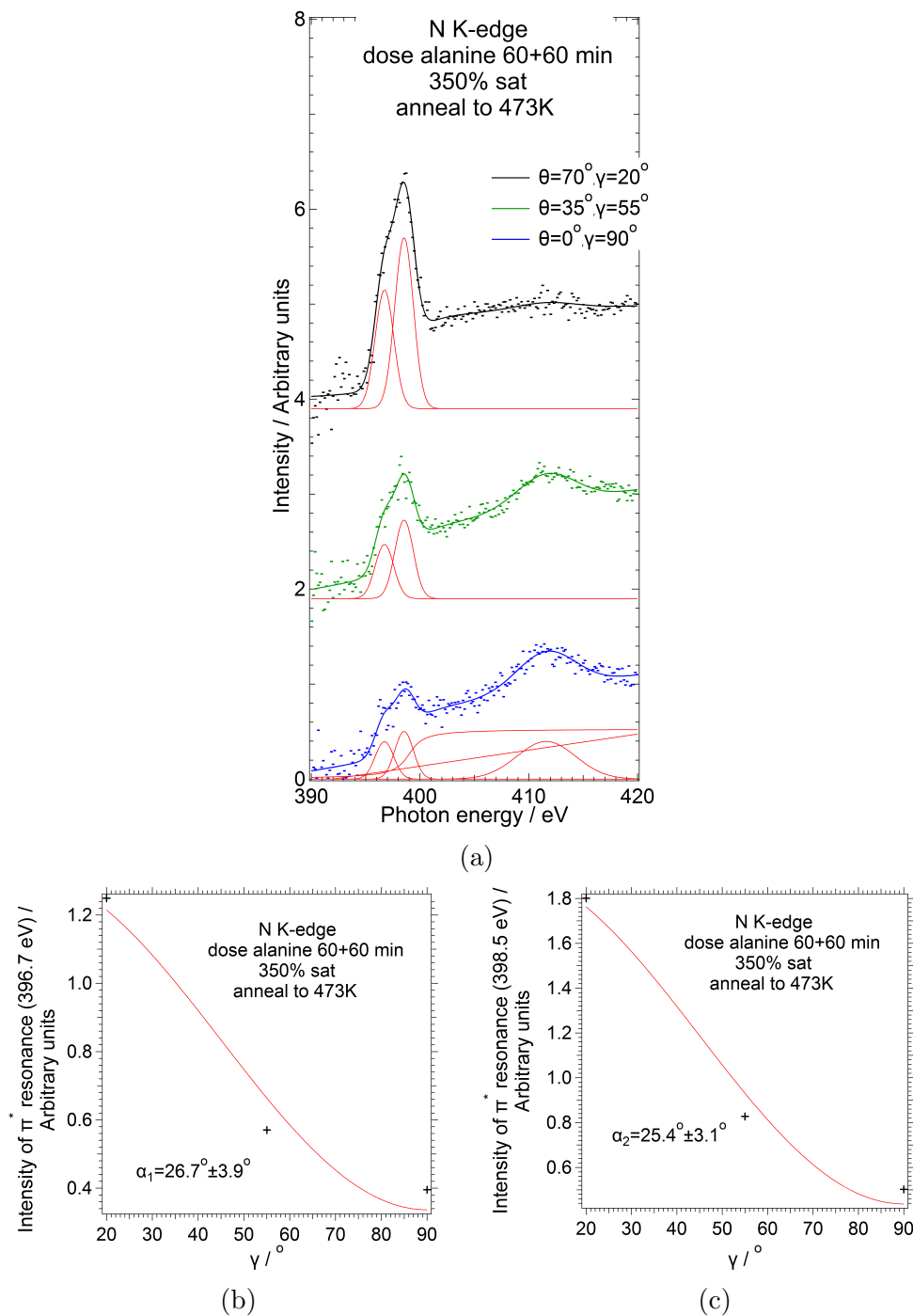


Figure 5.13: (a) Angle resolved N K-edge NEXAFS spectra obtained upon dosing (S)-alanine onto Ni{110} for 60+60 min ( $\Theta_{\text{Ala}}=350\%$  sat) and heating to 473 K. The dots represent the raw data and the solid thick lines the fitted curves. The red curves below the spectra show the individual Gaussian peaks, the linear background and the the step function used during the fitting process. (b-c) Plots (black markers) showing the intensity of the two nitrogen  $\pi^*$  resonances in Fig. 5.13a as a function of angle  $\gamma$ , where  $\gamma$  is related to the angle of incidence  $\theta$  ( $\gamma=90^\circ-\theta$ ). The solid red line shows the fitted curve calculated by the cos function in Eq. 5.3.

## 5.4 Discussion

Alanine chemisorbs on Ni{110} mainly in its anionic and neutral form. These chemical states support an  $\mu_3$  and  $\mu_2$  adsorption geometry, respectively (Fig. 4.3). Traces of protonated amino group ( $\sim 8$ -21% of the total signal), are also present in the submonolayer regime. These species point to the existence of zwitterionic alanine in the submonolayer regime (which supports also an  $\mu_2$  adsorption geometry, Fig. 4.3), however it is not fully conclusive whether this species belong to the first chemisorbed layer or they are found in a second layer deposited on top of the chemisorbed layer. The tilt angle of the C=O/COO<sup>-</sup> groups of the alanine molecule with respect to the surface plane was found to be  $\alpha \approx 42.1^\circ$  and did not change significantly upon co-adsorption of (S)-alanine with submonolayer H<sub>2</sub>O ( $\alpha \approx 42.0^\circ$ ). In the multilayer, alanine exists in its zwitterionic form, with the XP-spectra in the O 1s region showing a peak at 532.6-533.2 eV (the signal of this peak accounts for  $\sim 20$ -27% of the total XPS signal). This signal could be due to the signal of the -OH group of the neutral carboxyl group found in the chemisorbed layer of alanine or from oxygen atoms with a high degree of protonation due to intermolecular hydrogen bonding. TP-XP-spectra suggest that the multilayer desorbs around 300-310 K whereas TPD data suggest that the desorption of multilayer occurs at 320-340 K. This discrepancy is related to the heating rate between the two experiments. According to Eq. 2.14, higher heating rates cause a positive shift in the position of the desorption peak ( $T_P$ ). In the TP-XPS experiments the heating rate was 6-12 K min<sup>-1</sup> and in the TPD experiments was 1 K s<sup>-1</sup> or 60 K min<sup>-1</sup>, with the latter experiments, presenting the highest desorption temperature of the multilayer alanine.

There is an interesting oscillating behaviour in intensity in the N 1s TP-XP spectra in Fig. 5.4b ( $\Theta_{\text{Ala}}=330\%$  sat/heating rate=9 K min<sup>-1</sup>) at temperatures between  $\sim 240$  K and  $\sim 280$  K. In particular there is a rise in the signal of anionic alanine at  $\sim 240$  K with sudden decrease in the signal at  $\sim 402$  eV, a feature that disappears at  $\sim 280$  K, when the signal of zwitterionic alanine upsurges again. This behaviour (in less extent) is also observed in the N 1s TP-XP spectra in Fig. 5.5c ( $\Theta_{\text{Ala}}=350\%$  sat/heating rate=6 K min<sup>-1</sup>) at slightly higher temperatures (onset of oscillation took place at  $\sim 280$  K). In both cases the XPS signal in the N 1s region does not change significantly after the oscillation ( $T \approx 281$ -292 K in Fig. 5.4b and  $T \approx 297$  K in Fig. 5.5c) with respect to the signal before the oscillation ( $T \approx 214$ -222 K in Fig. 5.4b and  $T \approx 264.5$  K in Fig. 5.5c). Some decrease in the N 1s XPS area (with respect to the XPS area before the oscillation) is

observed during this oscillation ( $\sim 17\%$  in Fig. 5.4b/ $T \approx 236-247.5$  K and  $\sim 10\%$  in Fig. 5.5c/ $T \approx 279.5$  K). This behaviour is most likely due to diffusion of anionic/neutral alanine from the chemisorbed layer to the bulk multilayer. This will cause attenuation of the zwitterionic alanine from the anionic/neutral alanine and cause rise in the signal of the peak corresponding to the neutral amino group in the N 1s region ( $\sim 400$  eV) with simultaneous decrease in the signal corresponding to the protonated amino group ( $\sim 402$  eV). This behaviour is triggered by the constant heating in the TP-XPS experiments, which explains why it is not observed in the high resolution XP-spectra obtained between the O 1s TP-XP-spectra in Fig. 5.4c (Fig. 5.4f-5.4g) and it is reversible with further heating (hence the oscillation). This oscillation depends on the initial coverage of (S)-alanine on the Ni{110} surface (was not observed at  $\Theta_{\text{Ala}}=190\%$  sat, N 1s TP-XP-spectra in Fig. 5.5a) and on the heating rate (was not observed for heating rate= $12$  K  $\text{min}^{-1}$ , N 1s TP-XP-spectra in Fig. 5.5b, whereas the onset of oscillation was found at different temperatures at  $9$  K  $\text{min}^{-1}$  and  $6$  K  $\text{min}^{-1}$  heating rate). This behaviour is not observed in the C 1s TP-XP-spectra in Fig. 5.4a. It is possible that the XPS signal associated with the  $\alpha$ -carbon of the anionic/neutral alanine in the multilayer ( $\text{C-NH}_2$ ), overlaps with the signal of the  $\alpha$ -carbon of zwitterionic alanine ( $\text{C-NH}_3^+$ ).

Figure 5.14 provides a possible decomposition mechanism for alanine on clean Ni{110} based on the TPD and TP-XPS results. The full decomposition of alanine occurs between  $400-420$  K, even though an appearance of decomposition fragments was observed at  $T=350$  K in submonolayer coverages (Fig. 5.3). The first step of the decomposition of alanine on clean Ni{110} is the cleavage of  $\text{C}_\alpha\text{-COO}$  bond, which releases  $\text{CO}_2$  (Fig. 5.14), as was indicated by TPD peaks for masses 28 and 44 and the loss of the TP-XPS signal in the O 1s at the decomposition temperature. This decomposition, results with  $\text{NH}_2\text{CHCH}_3$  species on the surface, detected as a small signal in the XPS spectra at  $473\text{K}$  (Fig. 5.5d-e), vanishing upon heating to  $500$  K. Apart from the aforementioned peak, one peak in the N 1s region and two peaks in the C 1s are detected in the XP-spectra, stable up to  $700-800$  K. The TPD results show a desorption peak for mass 2 at the decomposition temperature, therefore a successive decomposition of the  $\text{NH}_2\text{CHCH}_3$  fragment must take place. This could involve a  $\text{C}_\alpha\text{-CH}_3$  backbone cleavage with simultaneously desorption of  $\text{H}_2$  leaving  $\text{H}_x\text{CN}$  species and atomic carbon on the surface (Fig. 5.14). The former species are validated by the NEXAFS results (Fig. 5.13a) which suggest the presence of multiple bonds in the nitrogen contained decomposition fragments. At  $800$  K a thermal desorption peak is observed for mass 2 and 28, which probably originates from thermal decomposition of the

amino species. A study on the interaction of methylamine and ethylamine [165] proposed that the final thermal dissociation stage of these two amines is atomic carbon and nitrogen. It is likely that the TPD peak at 800 K for mass 2 and 28 originates from recombinant desorption of atomic hydrogen and nitrogen, respectively. At this temperature the atomic carbon diffuses into the bulk leaving no fragments of alanine on the nickel surface. The decomposition temperature of alanine on Ni{110} is much higher than Ni{111}[46]. On Ni{111} the onset of the decomposition occurs at  $T \sim 300$  K following a different multistep process which includes first dehydrogenation and then breaking of the  $C_\alpha$ -COO bond [46].

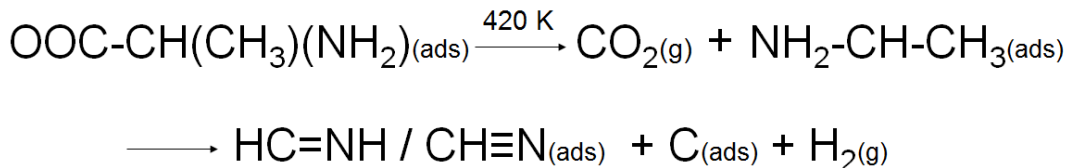


Figure 5.14: Proposed decomposition mechanism of (S)-alanine on Ni{110}.

The presence of multilayer water enhances the partial formation to zwitterionic alanine but does not influence the decomposition temperature of the amino acid whereas submonolayer water is displaced from the surface by the alanine molecules. Adsorption of glycine on Pt{111} pre-covered with chemisorbed or amorphous solid water (ASW) studied by Shavorskiy et al. (2013) [69], favours also the conversion to zwitterionic alanine, a state which was also observed in the multilayer regime as is the case with study. The authors of Ref.[69] suggested that glycine is adsorbed on top of the ice layer, since at this adsorption sequence, and at  $T_{\text{sample}} < 170$  K, the interlayer diffusion is kinetically hindered. Upon desorption of water, the layer of glycine resembles spectroscopically the pure glycine overlayer deposited at 200 K [69], as we also observed in our experiments. Exposure of the low covered adsorbed glycine on Pt{111} to ambient pressure water (up to 0.2 Torr) does not influence the chemical state at  $T > 300$  K nor its decomposition temperature, but it does stabilise the decomposition products of the molecule [69]. Similar results were obtained by Tzvetkov et al. (2005) [163], who found that glycine is predominantly in its zwitterionic form, when it is deposited on top of low density amorphous ice phase which was condensed on single crystalline of  $\text{Al}_2\text{O}_3$  [163]. The authors recommended that upon desorption of  $\text{H}_2\text{O}$ , glycine lands on the  $\text{Al}_2\text{O}_3$  surface [163]. Work of Shavorskiy et al. (2011) [109] on the interaction of alanine and glycine on Cu{110} after exposed to near-ambient pressure water, did not show any significant change in the chemical state of the

amino acids, which maintain their anionic form. The presence of ambient pressure water, decreases the decomposition temperature of alanine and glycine on Cu{110} (in the magnitude of 75-80 K) and changes the decomposition path of the amino acids, due to interaction of the decomposition products of H<sub>2</sub>O with the adsorbed amino acid [109]. In the present study, even though an amount of alanine was converted to its zwitterionic form, alanine is still predominantly in its anionic form. Theoretical work from Campo et al. (2006) [166] on the interaction of glycine with water, provided evidence that zwitterionic glycine forms six hydrogen bonds with water molecules at infinite dilution. Ab initio molecular dynamics from Leung et al. [167], show the zwitterionic glycine is surrounded by 8 water molecules in an aqueous solution. Computational work on the interaction of alanine with water [168], revealed that increase of the number of water molecules, makes the hydrated zwitterionic alanine more thermodynamically stable. Six or seven surrounding water molecules can favour the coexistence of the neutral and zwitterionic alanine, whereas 8 surrounding water molecules assure the dominance of the zwitterionic alanine. It is possible that the limiting factor of the low amount of zwitterionic alanine is the low concentration of the adsorbed H<sub>2</sub>O on Ni{110} surface. DFT calculations on the interaction of solvated alanine on Ni{111} [169], showed that in bulk water, alanine is favoured in its zwitterionic form, since the charged groups can form hydrogen bonds. The amino acid is bonded on the nickel surface through the one oxygen of the carboxylate group and one water molecule forms a hydrogen bond with the protonated amino group. We propose that dosing alanine onto pre-covered multilayer H<sub>2</sub>O on Ni{110}, causes almost total destruction of the water multilayer while the alanine molecule sits on top of the H<sub>2</sub>O bilayer. The latter explains the change in the shape of the peak at 531.9 eV (O 1s spectrum in Fig. 5.7c), which is the same with the corresponding peak of multilayer alanine, and the change in the shape of the peak corresponding to the neutral amino group (N 1s spectrum in Fig. 5.7b) and their shift to high binding energies with respect to the spectra of alanine deposited on clean Ni{110}. In addition, according to Ref.[69], at this adsorption temperature ( $\sim 140$  K), we should not expect any interlayer diffusion of the alanine molecule within the water layer. The presence of the water also causes protonation of the amino group, which probably forms hydrogen bonds with the remaining H<sub>2</sub>O molecules of the multilayer. Upon desorption of H<sub>2</sub>O ( $T \sim 220-220$  K), alanine sits on the nickel surface as and behaves thermally and chemically as in the case of a pure chemisorbed alanine on Ni{110}.

Alanine is thermally stable on Ni{110} up to 400-420 K, under both clean and wet conditions, a temperature range higher than the normal modification and

reaction conditions [16, 17]. The tridentate anionic form of alanine could induce chirality on the nickel surface through chiral reconstruction of the nickel atoms, in a similar way with the bitartrate(TA)/Ni{110} system in Ref.[34]. Adsorption of S-alanine on Cu{110} causes creation of chiral clusters of six or eight molecules, interspersed with chiral channels of metals which assemble into a chiral array without creation of its mirror domain on the surface [62]. This induced chirality is mirrored upon adsorption of R-alanine on the copper surface, which also generates similar chiral assemblies [62]. This structure was supported by generation of anionic alanine in both  $\mu_3$  and  $\mu_2$  adsorption geometries [62]. In the  $\mu_2$  anionic alanine the molecule interacted with the copper surface through its protonated amino group and through only one of the oxygen atoms of the carboxylate group [62]. The presence of an oxygen belonging to the deprotonated carboxyl group of alanine, dangled from the nickel surface, should have given a shift of  $\sim 0.3$ - $0.5$  eV towards high binding energies (with respect to the peak corresponding to the oxygen atoms of the  $\text{COO}^-/\text{COOH}_{(\text{ads})}$  groups) in the XP-spectra in the O 1s region, something that could not be resolved in our data. The presence of the neutral and anionic form of alanine in our study, can assist the generation these ordered structures on the Ni{110} surface since they can support a hydrogen bonding network. The presence of protonated carboxyl groups in the neutral form of alanine could also induce the interaction of the molecule with the  $\beta$ -ketoester reactant via hydrogen bonding and assisting its enantioselective hydrogenation through stabilising a pro-chiral configuration over the other.

In the presence of multilayer water, alanine partially converts in its zwitterionic form. Work on the interaction of (S)-glutamic acid and MAA on Ni{111} [40, 43, 44] provided evidence for a strong correlation between the increase of the keto:enol ratio of MAA, the protonation of the amino group of the modifier ((S)-glutamic acid) and the conditions that favour the generation of the R-product in excess. Under these conditions, it is possible, that the protonated amino group of the modifier ((S)-glutamic) can support an interaction with the  $\beta$ -ketoester reactant via hydrogen bonding in a configuration that will preferably produce the R-product during the hydrogenation reaction [40, 43, 44], as it was observed by Jones et al. (2006) [40] using RAIRS. The adsorption temperature ( $\sim 140$  K) and adsorption sequence ( $\text{H}_2\text{O}$  and then alanine) might not be exactly describe the exact reaction conditions, since at reaction temperatures we will expect the presence of only small amount of hydroxyls, however the multilayer  $\text{H}_2\text{O}$  can partially model the interaction of solvated alanine on Ni{110}. Further studies of the interaction of this molecule with the nickel surface under solution and high pressures of  $\text{H}_2\text{O}$  are essential to approach more realistic conditions.

## 5.5 Conclusions

Alanine plays an important role on the enantiomeric hydrogenation, since it is thermally stable on Ni{110} under reaction conditions (decomposes at  $\sim 400$ - $420$  K). Alanine chemisorbs on Ni{110} mainly in its anionic and neutral form. These chemical states support an  $\mu_3$  and  $\mu_2$  adsorption geometry, respectively. The XPS signal in the submonolayer regime, suggests also the presence of zwitterionic alanine, however it is not fully conclusive whether these zwitterionic species belong to the first chemisorbed layer or they are found in a second layer deposited on top of the chemisorbed layer. In the multilayer, alanine is present mainly in its zwitterionic form. The presence of multilayer water does not influence the decomposition temperature of the amino acid but it enhances its conversion to its zwitterionic form, a feature that is important for the generation of pure enantiomeric products under reaction conditions. The tilt angle of the C=O/COO<sup>-</sup> groups of the alanine molecule with respect to the surface plane was found to be  $\alpha \approx 42.1^\circ$  and did not change significantly upon co-adsorption of (S)-alanine with submonolayer H<sub>2</sub>O ( $\alpha \approx 42.0^\circ$ ).

# Chapter 6

## Adsorption of methyl acetoacetate (MAA) on Ni{100}

Reprinted (adapted) with permission from [170]. Copyright (2018) American Chemical Society.

### Abstract

The enantioselective hydrogenation of methyl acetoacetate (MAA) over modified Ni-based catalysts is a key reaction in the understanding of enantioselective heterogeneous catalysis as it represents the only example of this class of reactions catalysed by base metals. Yet, there is very little molecular-level information available about the adsorption complex formed by the reactants on Ni surfaces. Here, we report a combined experimental and theoretical study of the adsorption of MAA on the Ni{100} surface. X-ray photoelectron spectroscopy shows that MAA forms stable multilayers at low temperatures, which desorb between 200 K and 220 K. At higher temperatures a single chemisorbed layer is formed, which decomposes between 300 K and 350 K. Density functional theory modelling predicts an enolate species with bidentate coordination as the most stable chemisorbed species. Comparison of photoelectron spectroscopy and X-ray absorption data with simulations using this adsorption model show good qualitative and quantitative agreement. The molecular plane is tilted with respect to the surface plane by about 50°. This breaking of symmetry provides a mechanism for the enantioselective hydrogenation.

## 6.1 Introduction

The hydrogenation of  $\beta$ -ketoesters over modified Raney nickel opens up a pathway into enantioselective heterogeneous catalysis of bio-related molecules. Much of the characterisation of this reaction in terms of kinetics, modifier and solvent dependence was done by Izumi and coworkers in the 1960's [12, 16]. The quantitative characterisation at the molecular scale and the understanding of chiral and chirally-modified surfaces of model catalysts experienced a rapid growth over the last two decades, driven by the refinement of experimental surface characterisation techniques and theoretical modelling [2, 171–173]. This progress has also been driven by the increasing demand for enantiopure chemicals in drug manufacturing, where homogeneous catalytic processes are predominantly used [174]. However, the subsequent phase separation necessary in homogeneous catalysis is difficult and generally expensive. The use of heterogeneous catalysts avoids this problem; therefore, viable heterogeneous routes would make the production of pharmaceuticals greener and more economical.

In the case of one of the simplest  $\beta$ -ketoesters, methyl acetoacetate,  $\text{CH}_3\text{-O-C(O)-CH}_2\text{-C(O)-CH}_3$ , (MAA, see Fig. 6.1), the hydrogenation results in a racemic mixture of the *R* and *S* methyl-3-hydroxybutyrate (MHB) when carried out over an unmodified Raney Ni catalyst. However, the modification of the catalyst with chiral  $\alpha$ -amino acids or  $\alpha$ -hydroxy acids leads to optically active products. (R)-hydroxy acids (such as (R,R)-tartaric acid) or (S)-amino acids (such as (S)-glutamic acid) modifiers will produce (R)-product in excess, while (S)-hydroxy and (R)-amino-acid modifiers will generate (S)-products in excess [2, 11, 12, 16]. The reaction is well-characterised in terms of enantiomeric excess, temperature and solvent dependencies [16, 17, 24, 44]. Izumi (1983) [16] suggested that the surface modification is due to a combination of modifier and solvent molecules since the solvent has a significant influence on the enantiomeric excess of the catalyst. Furthermore, they showed that the enantioselective behaviour depends on how the reactant MAA adsorbs on the Ni surface and how it interacts with the modifier rather than on the transition state of the hydrogenation reaction [16]. Hence, determining the adsorption geometry of MAA at the molecular level and the influence modifiers have on it is a key step to understand and optimize the enantioselective behaviour of Ni-based catalysts.

On close-packed single crystal surfaces of many coinage and Pt-group metals chiral modifiers and/or reactants often form ordered adsorbate layers with well-defined chemical environments under UHV conditions [12]. On Ni surfaces,

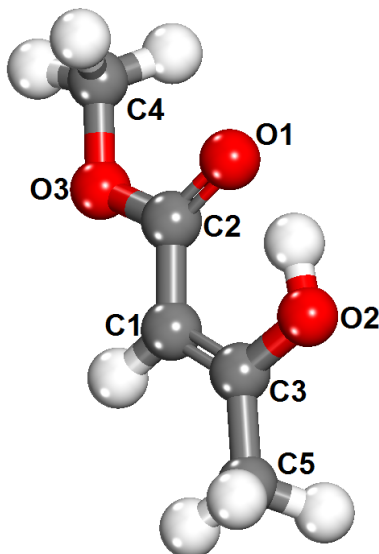


Figure 6.1: Molecular structure of MAA enol, which was found to be the most stable MAA tautomer in gas phase in Ref.[175].

such ordered structures are rare. Therefore little quantitative molecular-scale information is available on reactants and modifiers of enantioselective reactions on these surfaces. Raval and coworkers studied the adsorption of tartaric acid on Ni{110} and showed that the interaction with the modifier caused a chiral reconstruction of the surface [33–35]. Our group has studied the adsorption of alanine on Ni{111} using XPS and near-edge X-ray absorption fine structure (NEXAFS) spectroscopy [46]. In this and earlier studies, the combination of these two experimental techniques has proved very powerful for characterising the adsorption complex in terms of chemical state, bond coordination, and molecular orientation [46, 69–72].

The adsorption of MAA and several modifiers, including tartaric acid and glutamic acid, on Ni{111} was studied by Baddeley’s group using temperature-programmed desorption (TPD), IR spectroscopy and scanning tunneling microscopy (STM). There, the spatial configuration between the modifiers and the substrate depends on the coverage and adsorption temperature. Evidence was found for a one-to-one interaction between the chiral modifiers and MAA. In addition, it was shown that the experimental conditions, in particular temperature, influence the keto-to-enol ratio of MAA. [36, 37, 39, 40, 43, 44]. Recently, our group combined XPS and NEXAFS with DFT modelling to study the adsorption complex of MAA on Ni{111}. We found that the reactant MAA adsorbs on a flat surface forming deprotonated enolate species with bidentate coordination. The formation of energetically more favourable adatom adsorption complexes is kinetically hindered at low temperatures [175]. To our knowledge, no detailed study exists for

MAA adsorbed on the Ni{100} surface. The present study provides experimental data and theoretical modelling characterising the adsorption complex of MAA on Ni{100}. This study is published in Ref.[170]. The theoretical modelling of this study was performed by Dr.Jorge Ontaneda (University of Reading) and by Dr. Ricardo Grau-Crespo (University of Reading). The experimental data were collected by the author, by Prof. Georg Held (University of Reading) and by Dr. Roger Bennett (University of Reading) and analysed by the author. The overall contribution of the author to this study is  $\sim 50\%$  of the total work.

## 6.2 Methodology

The computational methods are described in Ref.[170]. The XPS and NEXAFS experiments were performed in the Elettra synchrotron in Trieste (Italy) in the UHV endstation of the SuperESCA beamline, which provides a horizontally polarized X-ray beam. The base pressures in the preparation and analysis chamber were in the  $10^{-10}$  mbar and  $10^{-11}$  mbar range, respectively. Sample cleaning was achieved by cycles of sputtering ( $3 \times 10^{-6}$  mbar / 1-1.5 kV) and oxygen treatment ( $1 \times 10^{-8}$  mbar for 1 min at room temperature with subsequent annealing to 900 K). Sample cleanliness was confirmed by XPS and LEED. The Ni single crystal was mounted at the base of the a liquid nitrogen-cooled cold finger and could be heated indirectly by a filament mounted close to the back face of the sample. Its temperature was measured through a spot-welded thermocouple and controlled using a programmable temperature controller. MAA was dosed via a leak valve. Prior to dosing, the liquid was purified by means of freeze-thaw cycles, until no bubbles were observed during thawing (4 cycles). A pressure rise to the low  $10^{-9}$  mbar range was observed during dosing of the molecule in the preparation chamber. Because of the small rise in pressure and differences in pumping speed, there was no good correlation between dosing time and surface coverage, hence the coverage was determined by XPS (see below).

The XP-spectra were acquired in the C 1s region ( $h\nu=400$  eV) and O 1s region ( $h\nu=650$  eV) using pass energies of 5 eV and 15 eV, which resulted in combined resolution of beamline and analyser of  $\sim 0.1-0.2$  eV for both photon energies. Spectra of the Fermi edge were obtained every time the monochromator was moved, for calibrating the offset of the binding energy axis. The spectra were normalised at low binding energy (BE) and the background was subtracted for quantitative analysis. The coverage (in ML) was calibrated by comparing O 1s spectra measured with a photon energy of  $h\nu=1000$  eV with those of CO ad-

sorbed to saturation at room temperature (0.5 ML, i.e. 1 molecule per 2 surface Ni atoms, [144]). Temperature-programmed XP-spectra were recorded by heating the sample at a constant rate of 12 K min<sup>-1</sup> in front of the analyser while measuring alternating C 1s and O 1s spectra ( $\sim 15$  s/spectrum). During the TP-XPS experiments the sample was moved under the beam to minimise any potential beam damage.

NEXAFS spectra were acquired in the O K-edge region detecting O KLL Auger electrons with kinetic energies of 507 eV. Three angles of incidence were used for determining the orientation of MAA on surface:  $\theta = 0^\circ$  (normal incidence),  $35^\circ$  and  $70^\circ$ , where  $\theta$  refers to the angle between the electric field vector and the surface plane. The photon energy was calibrated using the  $\pi^*$ -resonance in CO NEXAFS spectra [111]. The spectra were corrected for the transmission of the beamline through dividing by the photon flux,  $I_0$ , which was collected using the drain current of last refocusing mirror. Spectra of the clean surface, corrected in the same way, were subtracted as background. Finally, the spectra were normalised at 565 eV, which is above all oxygen absorption resonances.

## 6.3 Results

### 6.3.1 XPS Results

Figure 6.2 shows C 1s and O 1s XP-spectra of MAA on Ni{100}. The spectra were obtained after dosing MAA at 180 K for 1 min and 3 min, which led to coverages of 0.22 and 0.23 ML, respectively, and at 100 K for 6 min, which led to the growth of a “multilayer”. On the basis of modelling results (see below), it was estimated that a MAA molecule would block about 6 Ni atoms, i.e. the saturation coverage of the chemisorbed layer is around 0.17 ML. Above this value the coverage calibration by XPS is not linear anymore, as molecules in the second and higher layers attenuate the signal from the molecules below. This also depends on the growth kinetics / speed of growth and thus explains the differences between the 0.22 ML and 0.23 ML spectra despite the small difference in nominal coverage.

The O 1s spectrum, for 0.22 ML (Fig.6.2b) show two resolved peaks at  $\sim 531.3$  eV and  $\sim 533.2$  eV with an area ratio of 0.7:1. The low binding energy peak (peak A) can be attributed to deprotonated oxygen in contact with the nickel surface [46], while the peak at 533.2 eV (B) is related to oxygen atoms detached from the surface. The latter peak in the O 1s region broadens towards lower binding energies with increasing coverage, indicating the onset of multilayer formation. When the coverage increases and a thicker multilayer is formed, a third peak at

532.6 eV (C) can be resolved which is linked to the multilayer species. This species could be a protonated oxygen, implying the coexistence of two species of MAA in the multilayer regime.

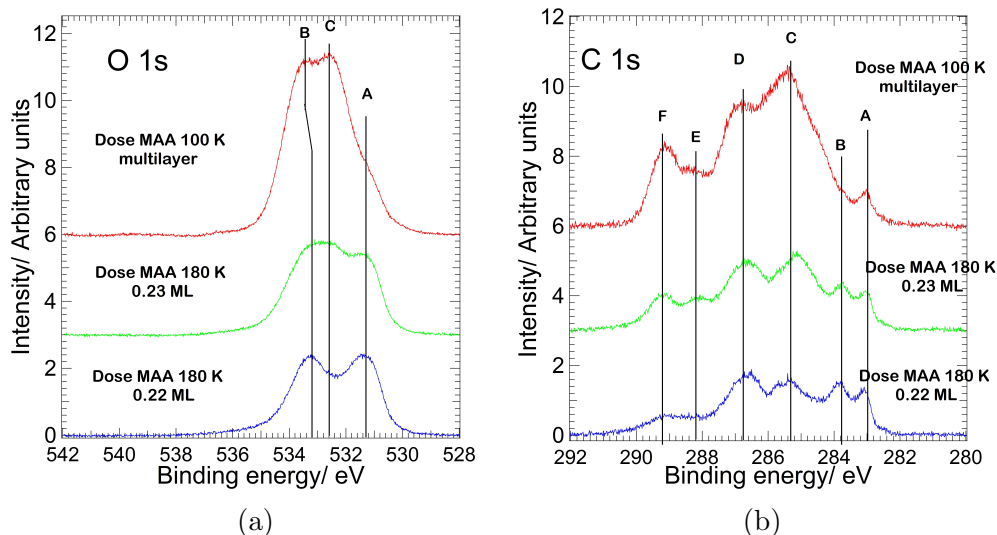


Figure 6.2: XP-spectra of MAA dosed onto Ni{100} at the indicated temperatures, in the (a) C 1s ( $h\nu=400$  eV) and (b) O 1s regions ( $h\nu=650$  eV).

In the C 1s region (Fig. 6.2a) we can detect six peaks at 283.0 eV (A), 283.8 eV (B), 285.3 eV (C), 286.8 eV (D), 288.2 eV (E) and 289.2 eV (F). Following previous work [46], the two peaks at the lowest binding energies (peak A and B) are associated with dissociation products of the MAA molecule. The remaining peaks are associated with intact MAA. Using calculated core-level shifts from DFT (see Tab. 6.2) the XPS signal 285-287 eV (peaks C and D) is assigned, in order of increasing binding energy, to the convoluted lines of C1 ( $C2=C1=C3$ ), C5 ( $C3-C5H_3$ ), C3 ( $C1=C3(-O_2)-C5$ ), C4 ( $H_3C4-O_3$ ) and C2 ( $O_3=C2(-O_1)=C1$ ) of the chemisorbed molecule (see also Fig. 6.7). The two peaks at high binding energies (E and F) are most likely multilayer and/or satellite features.

Figures 6.3a and 6.3b show temperature-programmed TP-XP-spectra after dosing MAA on Ni{100} for 3 min at 180 K (0.23 ML) while Fig. 6.3c and 6.3d show spectra of a MAA multilayer adsorbed at 100 K (3 min dose) and after successive annealing steps. The TP-XP-spectra are normalised at the low binding side without background subtraction, while the spectra in Fig. 6.3c-d have the background subtracted. Multilayer desorption occurs around 200-220 K, indicated by the disappearance of the peaks at 288.2 eV and 289.2 eV in the C 1s region (Figs 6.3a,c; peaks E and F) and 532.6 eV in the O 1s region (Fig. 6.3b,d; peak C), as well as by the shift of peak B in the O 1s region (Fig. 6.3d) to low binding

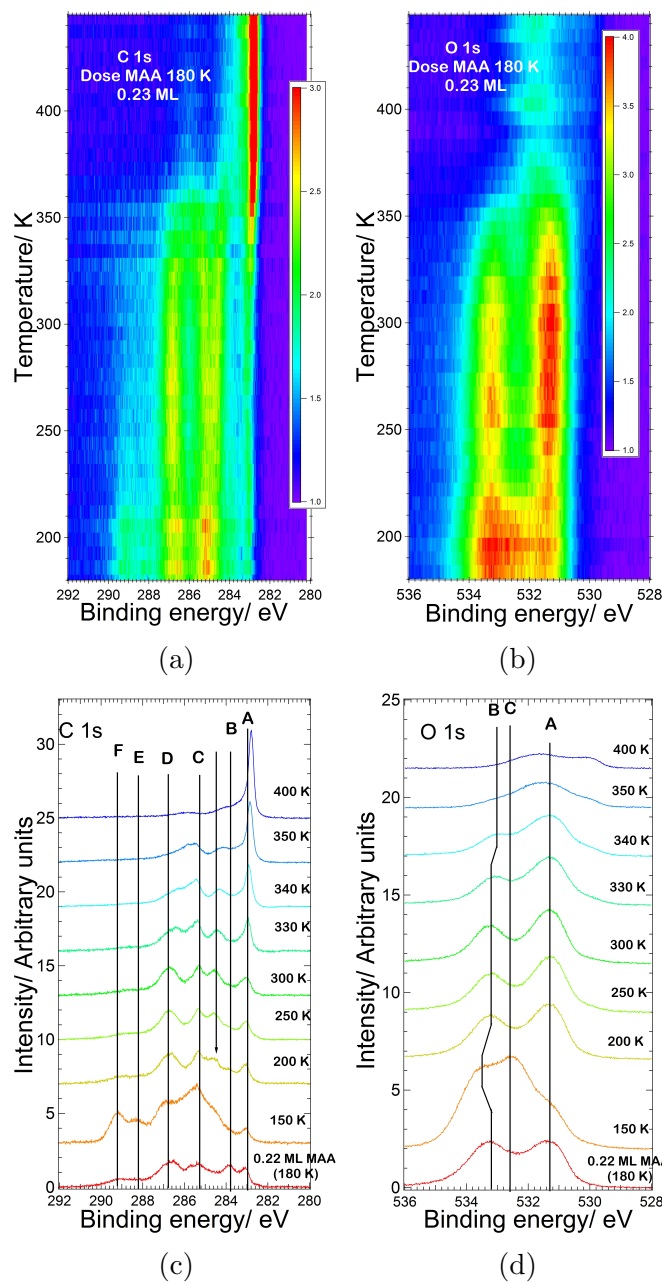


Figure 6.3: Temperature-dependent XPS-spectra of MAA on Ni{100}: TP-XPS of the (a) C 1s and (b) O 1s regions ( $h\nu=650$  eV) after dosing MAA onto on Ni{100} at 180 K for 3 min (heating rate  $12$  K  $\text{min}^{-1}$ ); (c) C 1s ( $h\nu=400$  eV); (d) O 1s ( $h\nu=650$  eV) XPS-spectra after dosing MAA at 100 K for 3 min and stepwise annealing as indicated.

energies. Above 200 K we can observe a clear splitting of peak C in the C 1s region and the appearance of a new peak at 284.5 eV (indicated by an arrow in Fig. 6.3c), which is assigned to the -C3-C1=C2- species. Heating from 300 K (0.21 ML) to 330 K (0.19 ML), causes a significant reduction in the signal corresponding to the intact molecule in both regions, accompanied by an increase in signal at 283.0 eV (peak A) in the C 1s region. This peak is associated with decomposition products, most likely atomic carbon. At 340 K we observe a significant shift of peak B in the O 1s region (O atoms not bound to the Ni surface) to lower binding energies (from 533.2 eV to 533.0 eV, Fig.6.3d). At this point the coverage is close to the saturation coverage (0.16 ML) and the intensity ratio between the O 1s peaks A (O atoms in contact with Ni) and B (O atoms not in contact with Ni) is 1.9:1, which indicates that MAA forms a bond with the Ni{100} surface through two oxygen atoms in a bidentate geometry. Above 350 K MAA is fully dissociated, leaving only decomposition fragments on the surface.

### 6.3.2 NEXAFS Results

Figure 6.4a shows angle dependent NEXAFS spectra after dosing MAA on Ni{100} for 1 min at 180 K (0.22 ML) and annealing to 250 K (0.21 ML). The corresponding XP-spectra are shown in Fig. 6.4b-6.4c. The experimentally determined coverage of 0.21 ML is close to the estimated saturation coverage of 0.17 ML. However, the presence of small peaks at 288.2 eV and 289.2 eV in the C 1s region (Fig. 6.4b) indicate that there is a small number of molecules adsorbed in the second layer which are not part of the chemisorbed layer.

The NEXAFS spectra (Fig. 6.4a) show a strong  $\pi^*$  resonance feature around 533.4 eV, a step at 536.4 eV and two  $\sigma^*$  resonances around 541 eV and 544 eV. The NEXAFS spectra were fitted using a linear background, a step function and Gaussian peaks representing the  $\sigma^*$  and  $\pi^*$  resonances of the molecule. The individual components of each function used for fitting the spectra are shown as red lines in Fig. 6.4a for each spectrum. The strong  $\pi^*$  resonance feature consists of three peaks at 532.5 eV, 533.5 eV and 535.3 eV. The intensities of these peaks show strong angular dependence, which allows the determination the molecular tilt angle  $\alpha$  for each resonance, according to the following equation [96] for surfaces with 4-fold symmetry:

$$I(\theta) = A[P(\sin\theta)^2 \cdot (1 - \frac{3}{2}\sin^2\alpha) + \frac{1}{2}\sin^2\alpha] \quad (6.1)$$

Where  $\theta$  is the angle between the electric field vector and the surface plane and P is the polarisation factor. Assuming P=1 for the SuperESCA beamline, the

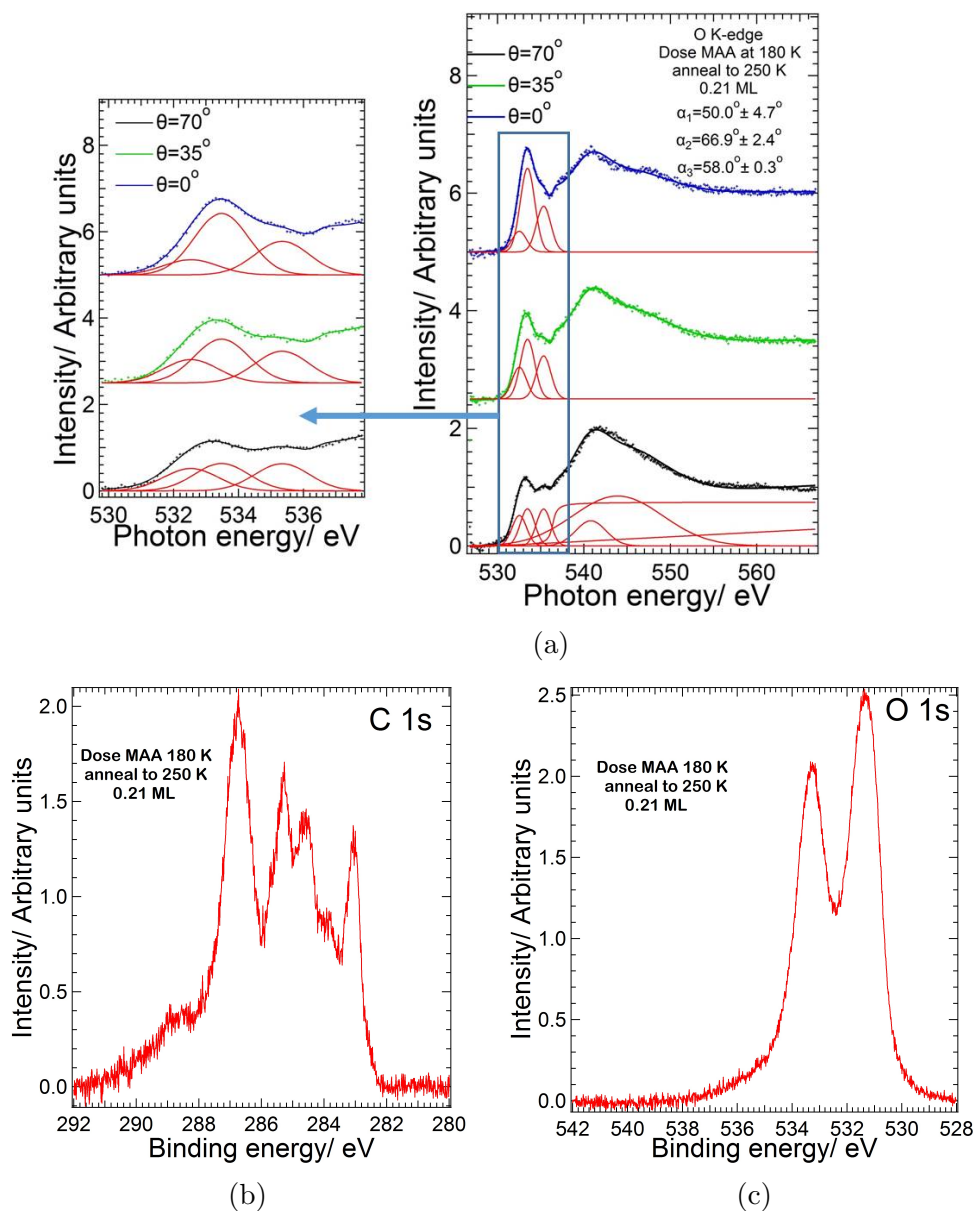


Figure 6.4: (a) Angle resolved O K-edge NEXAFS spectra after dosing MAA onto Ni{100} at 180 K for 1 min and annealing the layer to 250 K (0.21 ML). The dots represent the raw data and the solid lines the fitted curves. The red curves below the spectra indicate the individual Gaussian peaks, linear background, and the step function used for fitting. Right panel: complete spectra; Left panel: energy range of  $\pi^*$  resonances. (b+c) XP-spectra of the MAA layer used for the NEXAFS study: (b) C 1s region ( $h\nu=400$  eV) and in the (c) O 1s region ( $h\nu=650$  eV).

Eq. 6.1, is transformed to Eq. 6.2:

$$I(\gamma) = \frac{I_\alpha}{3} \left[ 1 + \frac{1}{2} (3\cos^2\gamma - 1)(3\cos^2\alpha - 1) \right] \quad (6.2)$$

Where  $\gamma=90^\circ-\theta$ . The values of tilt angles,  $\alpha$ , with respect to the surface plane, are  $50.0^\circ$ ,  $66.9^\circ$  and  $58.0^\circ$  for the peaks at 532.5 eV, 533.5 eV, 535.3 eV, respectively. The error margins stated in Fig. 6.4a refer to the fitting error. The two  $\sigma^*$  resonances can be assigned to C-C and C-O bonds respectively [46, 104].

### 6.3.3 DFT results

MAA belongs to the class of  $\beta$ -diketones of the type R-C(O)-CH<sub>2</sub>-C(O)-R. The keto-enol tautomerism of these compounds depends strongly on the substituent R. Symmetrically substituted  $\beta$ -diketones exist in the enol tautomeric form R-C(OH)-CH-C(O)-R when R is CH<sub>3</sub>, and in the diketo tautomeric form R-C(O)-CH<sub>2</sub>-C(O)-R when R is OCH<sub>3</sub> [176]. Both substituents are present in MAA, making its tautomeric behavior interesting: MAA vapor at 309 K exhibits a composition of 80% enol and 20% diketo form [177], whereas liquid MAA at room temperature exists exclusively in the diketo form [178]. In our previous work we found that DFT predicts the enol configuration as the most stable tautomer of MAA in the gas phase [175]. The diketo tautomer of MAA in its most stable configuration was found to be 0.24 eV above the enol ground state. Because the enol form is the most stable tautomer, we use it as the reference for the calculation of adsorption energies, regardless of the mode of adsorption. Both tautomeric forms of MAA have been considered, when we tested the adsorption geometries on the Ni{100} surface, however, the candidates with the MAA in its diketo form were less stable by at least 0.8 eV compared to the two most stable enol species shown in Fig. 6.5. The first local minimum corresponds to the *flat enol* configuration shown in Fig. 6.5a. The main molecular plane formed by the three carbons C2-C1-C3 (see Fig. 1.5 for numbering) is parallel to the surface with both oxygen atoms from the carbonyl and hydroxyl groups (O1 and O2) above atop sites. Unlike in the gas phase, the methyl and methoxy groups are not within this plane but bent away from the surface. The second global minimum (Fig. 6.5.b) corresponds to the *bidentate enolate* configuration, where O2 is deprotonated and the molecular plane is tilted with respect to the Ni surface. The surface bond is formed via the carbonyl groups sited located on bridge sites of non-adjacent rows. The dissociated hydrogen atom is adsorbed elsewhere on the surface on a four-hollow site. In this case, the methyl and methoxy groups remain aligned to

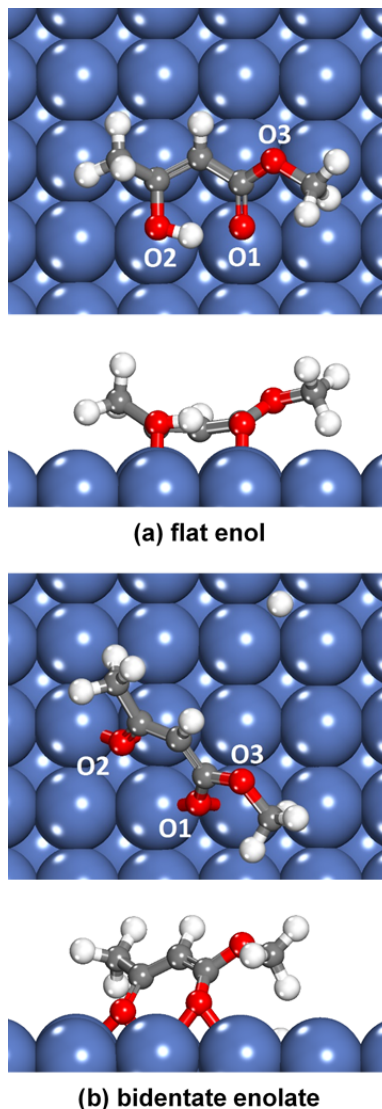


Figure 6.5: Top and side views of the two lowest-energy configurations found by DFT for the adsorption of MAA on the Ni{100} surface: (a) flat enol and (b) bidentate enolate (b) Key: red=O, gray=C, white=H and blue=Ni.

the plane of the molecule. The calculated adsorption energies without vibrational contributions are -1.91 eV for the *flat enol* and -1.82 eV for the *bidentate enolate* configuration. When vibrational contributions are included, the change in zero-point energy (ZPE) between gas phase and the adsorbed species stabilises the *bidentate enolate* by -0.20 eV but the *flat enol* only by -0.06 eV. This result is expected as the number of intra-molecular bonds in the latter is the same as in the gas-phase molecule, whereas with the enolate deprotonation occurs and the adsorbed species has one bond less and the vibrations of the dissociated hydrogen atom bound to Ni are much softer. This extra stabilisation yields a total adsorption energy (including electronic and vibrational contributions) of -2.02 eV for the *bidentate enolate* configuration compared to -1.97 eV for the *flat enol*, hence

rendering the enolate more stable.

## 6.4 Discussion

### 6.4.1 Comparison of Modelling and Experimental Data

In order to test whether the *bidentate enolate* conformation is indeed the predominant mode of adsorption, we compare the experimental XPS data with simulated spectra for the two candidate adsorption configurations. Core-level shifts for the O 1s photoemission peaks were calculated as described in Ref.[170]. The results are summarized in Tab. 6.1 together with some key geometrical data. For both adsorption geometries the BE shifts split into two groups, around  $\Delta BE_{O1s} = 0.00 - 0.29$  eV and  $\Delta BE_{O1s} = 1.29 - 1.86$  eV. For the *flat enol* conformation the oxygen of the carbonyl group (O1) falls into the lower BE group and the oxygen atoms of the hydroxyl and methoxy groups (O2 and O3) into the higher BE group. In the *bidentate enolate* configuration, the two oxygen atoms of the carbonyl groups (O1 and O2) have low BE and the methoxy oxygen (O3) has high BE.

For a further comparison with the experimental O 1s XPS data, spectra were modelled by the superposition of Gaussian functions of the same height, positioned according to the calculated binding energy shifts for each oxygen atom of the *flat enol* and *bidentate enolate* configurations (Tab. 6.1). A width (FWHM) of 1.5 eV was used for each Gaussian, which was determined by fitting the experimental data and is in accordance with our earlier work [175]. Figure 6.6 shows the individual Gaussians and their superposition alongside the experimental O 1s spectrum of MAA after annealing to 340 K. At this temperature, the coverage is 0.16 ML, close to the estimated saturation coverage of chemisorbed MAA on Ni{100} (0.17 ML). The coverage is different from the one used in the DFT calculations (0.04 ML), however strong lateral interaction, such as hydrogen bonding is not expected for MAA, therefore the adsorption geometry for chemisorbed molecules should be largely independent of coverage. The binding energy scale of the theoretical spectra has been shifted such that they coincide with the experimental data. Clearly, the simulated spectrum of the *bidentate enolate* conformation is in much better quantitative agreement with the experimental data than the one of the *flat enol*. Both the energy separation, 1.6 eV, and the relative heights of the two peaks fit the experimental data very well. As mentioned before in the Results Section, the intensity ratio between the low binding energy and high binding energy peaks (A and B) is close to 2:1, in the experimental spectrum for this layer, which sug-

Table 6.1: Key geometrical and spectroscopic parameters of the two candidate structures found by DFT<sup>α</sup>.

	<b>flat enol</b>	<b>bidentate enolate</b>
$E_{\text{ads}}^{\text{DFT}}$	-1.91 eV	-1.82 eV
$E_{\text{ads}}^{\text{DFT+ZPE}}$	-1.97 eV	-2.02 eV
$d(\text{C4-O3})$	1.447 Å	1.447 Å
$d(\text{C2-O3})$	1.367 Å	1.353 Å
$d(\text{C2-O1})$	1.322 Å	1.284 Å
$d(\text{C1-C2})$	1.467 Å	1.426 Å
$d(\text{C1-C3})$	1.461 Å	1.387 Å
$d(\text{C3-O2})$	1.423 Å	1.331 Å
$d(\text{C3-C5})$	1.507 Å	1.498 Å
$d(\text{O1-Ni})$	2.014 Å	2.093 Å / 2.134 Å
$d(\text{O2-Ni})$	2.071 Å	2.039 Å / 2.007 Å
$\angle \text{C2-O1-surface}$	0.0°	49.1°
$\angle \text{C3-O2-surface}$	0.7°	53.2°
$\angle \text{C2-C1-C3-surface}$	8.9°	54.3°
$\Delta z(\text{C})$	1.118 Å	0.640 Å
$\Delta BE_{\text{O}1\text{s}}(\text{O1})$	0.00 eV	0.29 eV
$\Delta BE_{\text{O}1\text{s}}(\text{O2})$	1.29 eV	0.00 eV
$\Delta BE_{\text{O}1\text{s}}(\text{O3})$	1.63 eV	1.86 eV

<sup>α</sup> $\Delta z(\text{C})$  is the maximum vertical height difference of the molecule's carbon atoms.

gests that MAA at this coverage is chemisorbed on Ni{100} in a bidentate form, through its two oxygen atoms, as in the *bidentate enolate* configuration.

C 1s spectrum (Fig. 6.7) was also modelled using the core level shifts values for the C 1s photoemission peaks for the *bidentate enolate* configuration (Tab. 6.2). Compared to the O 1s case (Fig. 6.6), the agreement between the simulated C 1s spectrum and the experiment (Fig. 6.7) was significantly worse. This is in agreement with previous findings on similar systems [104, 175] and is not fully understood yet. Nevertheless, there is little variation in the calculated C 1s binding energies between different adsorption geometries, as none of the carbon atoms is involved in any surface bond.

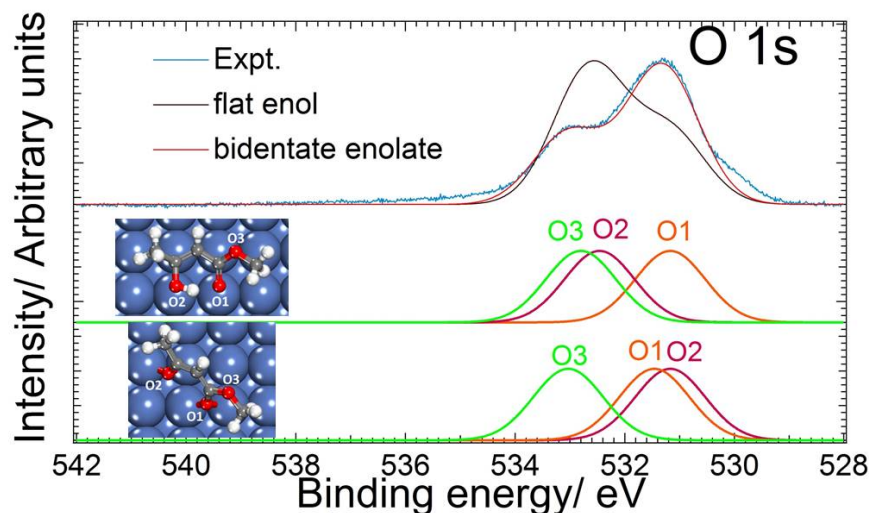


Figure 6.6: Comparison of experimental XPS data obtained after annealing the MAA layer to 340 K (0.16 ML) and modelled XP-spectra of the *flat enol* and *bidentate enolate* configurations. Top: direct comparison of experimental and modelled spectra; middle: individual Gaussian peaks centered at the calculated core level shifts for the *flat enol*; bottom: individual Gaussian peaks centered at the calculated core level shifts for the *bidentate enolate*.

Additional confirmation for the *bidentate enolate* adsorption geometry comes from the NEXAFS data. The DFT-optimised geometry predicts the molecular plane being tilted with respect to the surface plane. The inclination angles for the C-O bonds are  $\angle C3O2 = 53.2^\circ$  and  $\angle C2O1 = 49.1^\circ$ ; the plane of the carbon backbone has an angle of  $\angle C1C2C3 = 54.3^\circ$  with respect to the surface (Tab. 6.1).

The NEXAFS spectra consist of three peaks in the  $\pi^*$ -resonance region, at 532.5 eV, 533.5 eV, and 535.3 eV (Fig. 6.4a), which are most likely associated with these bonds, as they all are expected to be part of a resonant  $\pi$ -system. In order to make the correlation between the molecular geometry and these resonances, the density of states (DOS) near the Fermi energy was calculated for the bidentate

Table 6.2: Core-level shift values for the C 1s photoemission of the *bidentate enolate* configuration according to DFT. For numbering, refer to Fig.6.1.

Atom numbering	$\Delta BE$ (eV)
C1	0.00
C2	3.00
C3	1.56
C4	2.29
C5	0.83

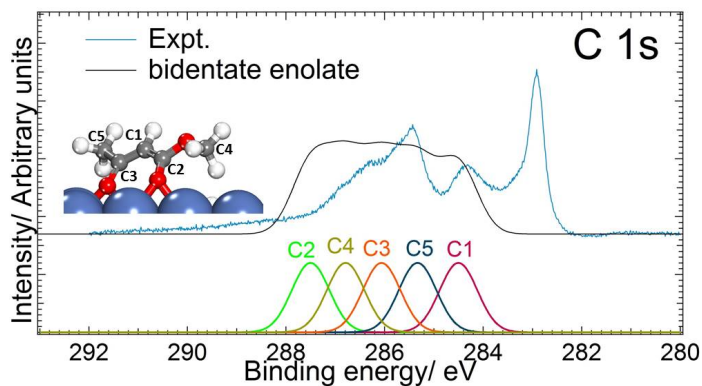


Figure 6.7: Top panel: Comparison of experimental C 1s XP-spectrum obtained upon annealed the MAA layer to 340 K (0.16 ML) with modelled XPS spectrum of the *bidentate enolate*. Bottom panel: individual Gaussian peaks of FWHM 0.9 eV placed at the core-level shift positions of Tab. 6.2.

enolate adsorption complex. Figure 6.8 shows the total DOS (black line), the DOS associated with the molecule (green), and the projections onto the Ni 3d, O 2p, C 2p states (blue, red, grey).

Figure 6.8 clearly shows a high density of empty states in the vicinity of C and O atoms around 1.7 eV and 4.8 eV above the Fermi level, which are associated with resonant  $\pi$ -like orbitals extending over most of the molecule. The main contribution to the states at 1.7 eV above the Fermi level are near the C3-O2 and C2-O1 bonds pointing towards the surface (see top panel of Fig. 6.8), while the empty states at 4.8 eV are located near the plane formed by C2, C1, and C3 (bottom panel of Fig. 6.8). The energy difference between the two DOS maxima ( $\sim 3.1$  eV) is very close to the energy difference between peak 1 (532.5 eV) and peak 3 (535.3 eV) in the NEXAFS spectra; we therefore assign the NEXAFS peaks 1 and 2 at 532.5 eV and 533.5 eV, respectively, to  $\pi$ -like orbital states associated with C-O bonds, while the peak at 535.33 eV is linked to the (C2C1C3) plane. The angles derived from the angular dependence of peaks 1 and 2 are  $50.0^\circ$  and  $66.9^\circ$  which is in fair agreement with the values from the DFT geometry ( $53.2^\circ$  and  $49.1^\circ$ ). The angle derived from the high photon energy peak 3 (535.33 eV) is  $58^\circ$  which also close to the theoretical value  $54.3^\circ$  for the angle of the (C2C1C3) plane. A closer look at the top and bottom panel of Fig. 6.8 shows that the respective orbitals are not exclusively associated with only one bond. Therefore, the angular dependence of the NEXAFS resonances, which is determined by the orientation of orbitals rather than bonds, must be expected to deviate somewhat from the bond

orientation. However, the experimental values are clearly not compatible with the *flat enol* adsorption complex where the molecular plane is essentially parallel to the surface (tilt angles between  $0.0^\circ$  and  $8.9^\circ$ , see Tab. 6.1).

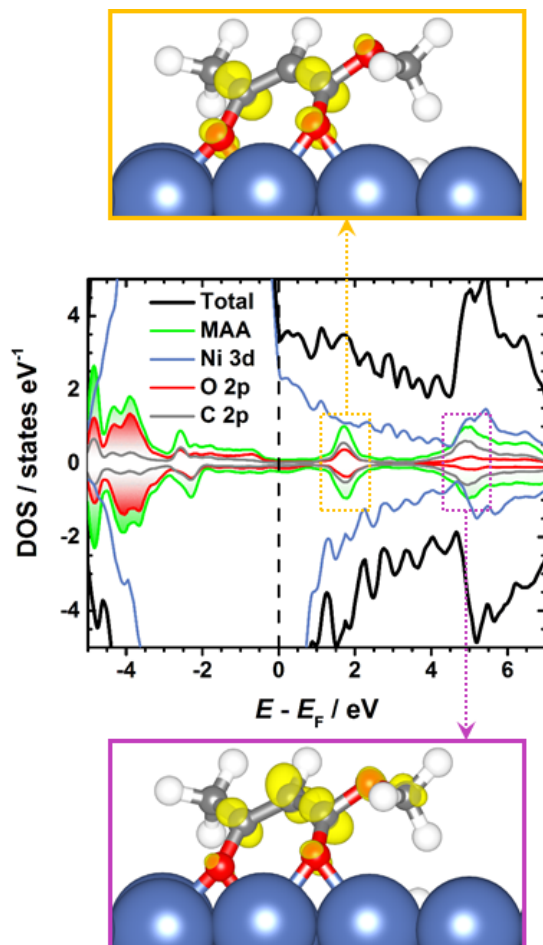


Figure 6.8: Electronic density of states (DOS) of the *bidentate enolate* conformation (center). The vertical dashed line marks the Fermi level ( $E_F$ ). The charge density isosurfaces, corresponding to electronic states with energies between 1.28 and 2.22 eV (top) and 4.38 and 5.32 eV (bottom) above the Fermi level, are highlighted with dotted rectangles.

Based on the above comparison of experimental and computational results we can confidently state that MAA adsorbs on Ni{100} in a *bidentate enolate* geometry. It should be stressed, that the small energy difference between the enolate and the enol adsorption species would not allow an unambiguous discrimination on the basis of DFT alone. Only the comparison with experimentally determined parameters, such as tilt angles and chemical shifts in XPS make a reliable determination of the adsorption complex possible.

## 6.4.2 Implications for Heterogeneous Catalysis

The TP-XPS experiments in this work show the onset of the decomposition of MAA on Ni{100} around 300-330 K; the molecule is fully decomposed at temperatures greater than 350 K. This decomposition temperature is within the temperature range of 273 K to 373 K typically used in enantioselective catalysis [16, 17]. In contrast, TP-XPS and step annealing experiments for MAA on Ni{111}, carried out under similar conditions, find the onset of decomposition at a significantly lower temperature of 270 K, but the decomposition process proceeds in two steps and is only complete at around 390 K [175].

Earlier TPD experiments by Jones et al. suggested that MAA on Ni{111} starts decomposing at 350 K [37]. However these experiments involved adsorption at 300 K (i.e. above the onset of the first decomposition step) and significantly higher heating rates ( $2 \text{ K s}^{-1}$ ) than in Ref.[175]. It is likely that Jones et al. only observed the second decomposition step. The same study also shows a delayed onset of decomposition when MAA is co-adsorbed with tartaric acid on Ni{111}. This indicates that the interaction with modifier molecules has a stabilising effect under reaction conditions, which is most likely also the case on Ni{100}. Nevertheless, it appears that the reactant MAA is intact over the range of typical reaction temperatures only on the Ni{100} surface, and not on Ni{111}.

The tilted *bidentate enolate* geometry found here is similar to the geometry found for MAA on Ni{111} earlier [175]. The most stable adsorption complex of MAA on Ni{100} is a enolate ( $=\text{C1H}^-$ ), whereas all diketo candidate structures ( $-\text{C1H}_2-$ ) tested in this study were found to be much less stable. Only the *flat enol* structure is similar in energy, but could be excluded by comparison with experimental data. The tilted adsorption geometry of the *bidentate enolate* offers an obvious mechanism for enantioselective hydrogenation. If we assume that the dissociation of  $\text{H}_2$  takes place on the Ni surface, it will be more likely for the hydrogen atoms to attach to the molecule on the side that is tilted towards the surface. On an unmodified Ni{100} surface, which has a mirror symmetry, the tilt can be in both directions. The role of a modifier is, therefore, to break the mirror symmetry and stabilise only one of two possible tilt directions. A similar mechanism would also explain enantioselectivity for the *flat enol* geometry or diketo structures that break the mirror symmetry of the surface in a similar way. Indeed, both enol and diketo conformers of MAA lead to enantioselective products, as a series of IR absorption studies has confirmed recently [40, 44], which investigated MAA on glutamic-acid-modified Ni{111} model catalysts under similar conditions as earlier experiments on Raney-nickel catalysts described by Izumi

[16]. When the surface is modified with (S)-glutamic acid the enol(ate) tautomer leads to the (S)-methyl-3-hydroxybutyrate product and the diketo form to the (R) product. When glutamic acid is used as modifier, the modification conditions (pH and temperature) have an influence on whether MAA assumes the enol or diketo conformer. Further studies with co-adsorbed reactant and modifier molecules will be necessary to determine the exact geometry of the modifier-MAA complex at the molecular level and establish the reaction mechanism that leads to the chiral product formation.

## 6.5 Summary

In summary, we have carried out a combined experimental and theoretical study of the interaction of MAA with the Ni{100} surface using XPS, NEXAFS, and DFT. The desorption of the multilayer MAA occurs at 200-220 K, leaving behind a stable chemisorbed layer which starts decomposing at 300-330 K and is completely dissociated at  $\sim 350$  K.

DFT calculations predict that the chemisorbed layer consists of a deprotonated enolate species with a tilted bidentate surface bond through two oxygen atoms. The enolate conformer and the tilt angle between  $49.1^\circ$  and  $54.3^\circ$  with respect to the surface plane is confirmed by comparison with spectroscopic data. A non-deprotonated enol tautomer is less stable by 50 meV, when vibrational zero-point energy contributions are taken into account. All diketo candidate structures were found to be significantly less stable.

# Chapter 7

## Conclusions

The interaction of (R,R)-tartaric acid, (S)-alanine and methyl acetoacetate (MAA) on Ni{100} and the co-adsorption of (S)-alanine and water on Ni{100}, under UHV conditions was investigated, using XPS, NEXAFS, TPD and LEED, in order to obtain fundamental insights into the mechanism of chiral modification of nickel catalyst, which causes the asymmetric hydrogenation of  $\beta$ -ketoesters. In order to bridge the pressure gap and approach more realistic reaction conditions, we have investigated the interaction of (R,R)-tartaric acid on the Ni{100} surface under the presence of elevated pressures of H<sub>2</sub> and H<sub>2</sub>O and the interaction of (S)-alanine on Ni{100} under the presence of elevated pressures of H<sub>2</sub> using AP-XPS. We have also investigated the interaction of (R,R)-tartaric acid on oxidised Ni{100}. The interaction of molecules on oxidised surfaces, also approaches the enantioselective catalysis conditions, since the modification occurs from aqueous solution and the catalyst itself is exposed to air before the modification [39].

The chemical state and adsorption geometry of (R,R)-tartaric acid on Ni{100} depends on the temperature of the crystal, the dosing rate of the TA molecule and its surface coverage. The bitartrate phase, in which both carboxyl groups of the TA molecule are deprotonated (TA<sup>2-</sup>) and chemisorbed on the nickel surface in an  $\mu_4$  adsorption geometry, is favoured as we increase the temperature of the crystal away from room temperature. Cooling the crystal towards room temperature while having high coverages of TA molecule, causes the formation of HTA<sup>-</sup> species (which support an  $\mu_2/\mu_3$  adsorption geometry). High deposition rates (deposition time  $\leq 24$  min/saturated layer) at T < 400 K also cause the formation of HTA<sup>-</sup> species.

Dosing (S)-alanine onto Ni{100} at (T  $\leq 330$  K) causes saturation of the XPS signal without formation of multilayer. At room temperature, ( $\Theta_{\text{Ala}} \geq 78\%$  sat), alanine chemisorbs on Ni{100} in both its anionic and neutral form. These species support an  $\mu_3$  (via the two oxygen atoms of the COO<sup>-</sup> group and nitrogen atom

of the amino group) and  $\mu_2$  (via the one oxygen atom of the carboxyl group and the nitrogen of the amino group) adsorption geometry, respectively. Dosing (S)-alanine at  $T_{\text{sample}}=250$  K causes also the formation of anionic and neutral alanine. At  $T_{\text{sample}}=250$  K and  $\Theta_{\text{Ala}}>0.10$  ML, some zwitterionic species (which also support an  $\mu_2$  adsorption geometry) are formed, which coexist with the anionic and neutral forms of alanine. It is not fully conclusive whether these zwitterionic species belong to the first chemisorbed layer or they are found in a second layer deposited on top of the chemisorbed layer. In the multilayer alanine is almost exclusively in its zwitterionic form. Similar results were observed upon depositing (S)-alanine onto Ni{110}. As in the case with the (S)-alanine/Ni{100} system, (S)-alanine chemisorbs on the Ni{110} surface in its neutral and anionic form, whereas in the multilayer alanine is in its zwitterionic form. Similar with the (S)-alanine/Ni{100} system, the XPS signal in the submonolayer regime, suggests also the presence of zwitterionic alanine, however it is not fully conclusive whether these zwitterionic species belong to the first chemisorbed layer or they are found in a second layer deposited on top of the chemisorbed layer. On Ni{111}[46] (S)-alanine chemisorbs in both zwitterionic and anionic form supporting a bidentate and tridentate geometry, respectively with the latter species being in majority on the nickel surface. The XPS signal in the O 1s region upon adsorbing the alanine molecule on the Ni{111}[46] show evidence of presence of protonated species of carboxyl group at  $T_{\text{sample}}=250$  K/ $\Theta_{\text{Ala}} \geq 0.11$  ML and at  $T_{\text{sample}}=300$  K/ $\Theta_{\text{Ala}} \geq 0.19$  ML at a fixed 10% relative intensity of the main peak at 531.5 eV. In the light of our results and the results of Nicklin et al. (2015) [46], we can safely conclude that the chemical state of (S)-alanine, under UHV conditions, does not change significantly between the three nickel facets ({110}, {111}, {100}).

Under UHV conditions, (R,R)-tartaric acid (TA) fully decomposes on Ni{100} at  $T>440$  K. Its thermal stability is further enhanced under the presence of  $P_{\text{H}_2}=6.4$  mbar, suggesting that TA remains intact on the Ni{100} facet during modification and reaction conditions [12, 16, 24].

Table 7.1 compares the decomposition temperature of (S)-alanine between the three nickel single crystals (Ni{100}, Ni{110}, Ni{111}[46]) On Ni{110}, alanine decomposes at  $\sim 400$ -420 K, while the presence of multilayer water does not influence the decomposition temperature of the amino acid on the Ni{110} surface. The situation is more complicated in the (S)-alanine/Ni{100} and (S)-alanine/Ni{111}[46] adsorption systems. TP-XP-spectra of (S)-alanine overlayers on Ni{100}, formed at  $T_{\text{sample}}=250$  K, suggest that the molecule decomposes at  $T\approx 330$ -390 K depending on the initial coverage of alanine. The increase in

the thermal stability of the molecule with increasing initial surface coverage, is most likely related to intermolecular interactions (hydrogen bonds), which become stronger as the surface becomes more crowded. On the other hand step anneal XP-spectra of alanine overlayers formed on Ni{100} at room temperature, show that the molecule fully decomposes on Ni{100} at  $T > 460$  K and  $T \geq 400$  K under UHV and elevated hydrogen pressure conditions ( $P_{\text{H}_2} = 6.3$  mbar), respectively. It seems that the presence of elevated pressures of  $\text{H}_2$  destabilise thermally the (S)-alanine molecule on the Ni{100} surface, which is the opposite effect with respect to the (R,R)-tartaric acid/Ni{100} system. On Ni{111} [46], the onset of decomposition of the (S)-alanine molecule, is around 320 K. The desorption and decomposition occurs in multistep processes between 300 K and 450 K [46]. According to previous work [16, 17], the temperature range used for modification of Raney nickel [16] and silica-supported nickel catalysts [17] using alanine as chiral modifier, as well as the temperatures used for the enantioselective hydrogenation of MAA using the aforementioned catalysts lies between 273 K and 373 K [16, 17]. It seems that, at least, under UHV conditions, (S)-alanine remains intact on the Ni{110} facet in the range of temperatures typically used in the enantioselective catalysis [16, 17] whereas on Ni{100} and Ni{111}, its not fully conclusive whether the molecule remains intact in the aforementioned temperature range. A further study, which will exploit the interaction of the molecule on the nickel surfaces under elevated solvent pressures, is essential, to obtain full conclusions about the thermal stability of the molecule on different nickel facets under modification and reaction conditions.

The decomposition species of the alanine molecule as well as the surface im-

Table 7.1: Comparison of the decomposition temperature of (S)-alanine (Ala) between the three nickel single crystals (Ni{100}, Ni{110}, Ni{111} [46]).

	Conditions	Method	Decomposition temperature
<b>Ala/Ni{110}</b> <b>this work</b>	UHV	TPD/TP-XPS	$T \approx 400-420$ K
<b>Ala/Ni{100}</b> <b>this work</b>	UHV UHV $P_{\text{H}_2} = 6.3$ mbar	TP-XPS step anneal XPS step anneal XPS	$T \approx 330-390$ K $T > 460$ K $T \geq 400$ K
<b>Ala/Ni{111}</b> [46]	UHV	TP-XPS	onset at $T \approx 320$ K

purities, present before dosing, behave differently among the three nickel facets ( $\{110\}$ ,  $\{111\}$  [46],  $\{100\}$ ). Upon dissociation of the alanine molecule on Ni $\{110\}$  and Ni $\{111\}$  [46], at  $T > 500$  K, the nickel surface is covered with  $H_xC_xN_x$  species and atomic C. According Nicklin et al. (2015) [46] the C 1s XPS signal of atomic carbon overlaps with the signal of  $H_xC_xN_x$ . Ref.[46] suggested that only  $H_xC_xN_x$  are present upon decomposition of (S)-alanine on Ni $\{111\}$ . At  $T \approx 730$  K (Ni $\{111\}$  [46]) and  $T \approx 770-780$  K (Ni $\{110\}$ ), the signals of the surface impurities and decomposition species of the alanine in the C 1s and N 1s disappear almost together (in the Ni $\{110\}$  facet the atomic carbon is thermally less stable than the CN species), leaving a nickel surface clean of impurities. At these temperatures, nitrogen species desorb from the surface as molecular  $N_2$ , whereas C diffuses into the bulk [46]. On Ni $\{100\}$ , at  $T > 500$  K, the XPS signal upon dissociation of the alanine molecule, is dominated with carbidic/surface carbon and atomic nitrogen. These species are quite resistive to high temperatures, with both being present on the Ni $\{100\}$  even upon heating to  $\sim 1050$  K, with their temperature trend suggesting that the atomic nitrogen is thermally more stable than the carbidic/surface carbon.

According to XPS, NEXAFS and DFT calculations methyl acetoacetate (MAA) one of the typical reactants in the asymmetric hydrogenation of  $\beta$ -ketoesters, chemisorbs on the Ni $\{100\}$  surface in a bidentate enolate geometry, through the two oxygen atoms. The chemisorbed layer starts decomposing at 300-330 K and is completely dissociated at  $\sim 350$  K. This decomposition temperature is within the temperature range of 273 K to 373 K typically used in enantioselective catalysis[16, 17]. A further study, which will exploit the interaction of the molecule on the nickel surfaces under elevated solvent pressures, is essential, to obtain full conclusions about the thermal stability of the molecule on different nickel facets under modification and reaction conditions.

Table 7.2 shows the tilt angles of the chemical groups of methyl acetoacetate (MAA), (S)-alanine (Ala), and (R,R)-tartaric acid (TA) with respect to the nickel surface plane, determined in our and previous studies [46, 47, 175]. According to DFT calculations the bidentate enolate form of MAA is tilted between  $49.1^\circ$  and  $54.3^\circ$  with respect to the Ni $\{100\}$  surface plane, confirmed also by angle dependent NEXAFS. XPS, angle dependent NEXAFS and DFT calculations performed by Ontaneda et al. 2016 [175], suggested a similar tilted geometry of the MAA molecule on the Ni $\{111\}$  surface ( $48-63^\circ$  with respect to the Ni $\{111\}$  surface plane). According to angle dependent NEXAFS, the C=O/COO $^-$  groups of the alanine molecule are tilted by  $\sim 48.5^\circ$  and  $\sim 42.1^\circ$  with respect to the surface plane of Ni $\{100\}$  and Ni $\{110\}$ , respectively. The tilt angle of (S)-alanine

Table 7.2: The tilt angles of the chemical groups of methyl acetoacetate (MAA), (S)-alanine (Ala), and (R,R)-tartaric acid (TA) with respect to the nickel surface plane.

	Angles determined	Values of the angles (range)
<b>MAA/Ni{100}</b> <b>this work</b>	$\angle$ C2-O1-surface <sup><math>\alpha</math></sup> $\angle$ C3-O2-surface $\angle$ C2-C1-C3-surface	49.1-54.3°
<b>MAA/Ni{111}</b> <b>[175]</b>	$\angle$ C2-O1-surface <sup><math>\alpha</math></sup> $\angle$ C3-O2-surface	48-63°
<b>Ala/Ni{100}</b> <b>this work</b>	C=O/COO <sup>-</sup> -surface	$\sim$ 48.5°
<b>Ala/Ni{110}</b> <b>this work</b>	C=O/COO <sup>-</sup> -surface	$\sim$ 42.0-42.1°
<b>Ala/Ni{111}</b> <b>[46, 47]</b>	COO <sup>-</sup> -surface	34-64°
<b>TA/Ni{100}</b> <b>TA/NiO/Ni{100}</b> <b>this work</b>	C=O/COO <sup>-</sup> -surface	$\sim$ 42-69°

<sup>$\alpha$</sup> See Ref.[170, 175] and chapter 6 for the numbering of the atoms.

on Ni{110} did not change significantly upon co-adsorption of (S)-alanine with submonolayer H<sub>2</sub>O ( $\alpha \approx 42.0^\circ$ ). According to angle dependent NEXAFS in the O K-edge region [46, 47], the tilt angle of the carboxylate group of (S)-alanine with respect to the Ni{111} surface plane is between 34° and  $\alpha = 64^\circ$ , depending on the chemical state of the molecule (anionic or zwitterionic) and the pressure in the chamber (UHV or elevated hydrogen pressures). Angle dependent NEXAFS of (R,R)-tartaric acid overlayers on Ni{100} and NiO/Ni{100}, suggested also similar molecular orientation. Depending on the chemical state, adsorption configuration of the TA molecule, and the substrate (Ni{100} or NiO/Ni{100}), the C=O/COO<sup>-</sup> groups of the TA molecule are tilted by  $\sim 42-69^\circ$  with respect to the surface plane of the nickel substrate. The tilted geometry of the MAA molecule on Ni{100} and Ni{111} [175] could lead to asymmetric hydrogenation in chirally modified nickel surface. If we assume that the dissociation of H<sub>2</sub> takes place on the Ni surface, it will be more likely for the hydrogen atoms to attach to the molecule on the side that is tilted towards the surface. On an unmodified nickel surface, which has a mirror symmetry, the tilt can be in both directions. The role

of a modifier is, therefore, to break the mirror symmetry of the crystal and stabilise only one of two possible tilt directions. The presence of elevated pressures of  $H_2$  and  $H_2O$  caused the formation of  $HTA^-$  species in the TA overlayer on the  $Ni\{100\}$  surface, while the presence of  $H_2$  also caused the formation of neutral and (perhaps) zwitterionic alanine on the  $Ni\{100\}$  surface. Formation of zwitterionic alanine was also observed upon exposing the saturated (0.25 ML) of alanine on the  $Ni\{111\}$  surface, to elevated pressures of  $H_2$  [46, 47]. The presence of multilayer water caused also the formation of zwitterionic species of alanine on the  $Ni\{110\}$  surface. Protonation of (S)-glutamic acid [40, 43, 44] and (R,R)-tartaric acid [37, 38] adsorbed on the  $Ni\{111\}$  surface, was observed, also, under conditions of optimum catalytic enantioselectivity for the production of R-product. The  $HTA^-$  species of the tartaric acid molecule, as well as the zwitterionic and neutral species of alanine, contain protonated species which are dangled from the surface and are free to form hydrogen bonds with the  $\beta$ -ketoester reactant, stabilising a pro-chiral configuration of the latter during the hydrogenation reaction. (S)-alanine and (R,R)-tartaric acid on  $Ni\{100\}$ , have similar molecular orientation with MAA on  $Ni\{100\}$  (as shown by the tilt angles in Tab. 7.2). The similar orientation of the modifiers ((S)-alanine and (R,R)-tartaric acid) with respect to the MAA reactant, could facilitate an interaction between the chiral modifier and  $\beta$ -ketoester reactant on the  $Ni\{100\}$  surface, since the dangled chemical groups of the two molecules will be in close distance to form hydrogen bonds. It is also possible that the protonation of (R,R)-tartaric acid and (S)-alanine at elevated pressures of hydrogen is an actual step in the hydrogenation reaction, with the modifiers acting as a hydrogen source for the  $\beta$ -ketoesters reactant [47]. A similar mechanism is known to occur during the (reversible) reduction of pyruvate to lactic acid, catalysed by lactate dehydrogenase, a natural enzyme [179].

Deposition of TA on oxidised  $Ni\{100\}$ , causes the generation of tartrate species whose thermal stability resembles the thermal behaviour of the nickel (II) tartrate complex, since they decomposed fully on  $NiO/Ni\{100\}$  substrate at  $T > 650$  K. Their presence under modification conditions could assist the etching of the nickel surface and induce the generation of chiral surfaces/arrangements.

The results of this study, highlight the need to approach more realistic reaction conditions in order to get a full understanding of the mechanism behind the chiral modification of nickel catalyst. The AP-XPS experiments of our study show that elevated  $H_2$  and  $H_2O$  pressures influence the chemical state, bond coordination and thermal stability (S)-alanine and (R,R)-tartaric acid on  $Ni\{100\}$  surface. The presence co-adsorbed water also change the chemical state of alanine on the  $Ni\{110\}$  surface, whereas adsorption of tartaric on oxidised  $Ni\{100\}$

generated species with increased thermal stability that could cause etching of the nickel surface. There are several ways to do surface chemistry while approaching the enantioselective catalysis conditions:

1. Use of elevated hydrogen and solvent pressures (AP-XPS and ambient pressure-X-ray absorption spectroscopy).
2. Co-adsorbing chiral modifiers, NaBr and  $\beta$ -ketoester reactants on nickel single crystals, polycrystalline nickel and oxidised nickel crystals.
3. Study the interaction of the aforementioned molecules on the nickel surface, in solution, following the procedure described in previous catalytic reaction studies, in similar fashion to the studies in Ref.[38, 42, 44, 48] and then expose the sample to elevated pressures of hydrogen. This will allow a direct correlation between the chemical state, bond coordination, molecular orientation, modifier-reactant adsorption complex and thermal stability of the molecules on different nickel facets with the conditions of optimum enantioselectivity. It will also be also interesting to link the coverage of the modifier upon modification and washing of the catalyst (prior to the hydrogen) and the conditions of optimum enantioselectivity, which will give us clear evidence of whether the reaction occurs in low concentration or absence of modifier as it was suggested by Ref.[42, 48], and if chiral metal arrangements generated from the modifier are the enantioselective sites in the asymmetric hydrogenation of  $\beta$ -ketoesters.
4. Study the interaction of the aforementioned molecules on more complex nickel systems such as Raney nickel, nickel powder and supported nickel catalyst, bridging the complexity gap.

This study showed that the progress of surface science techniques can provide endless possibilities to investigate catalytic systems under real reaction conditions, which will lead to the development of catalysts with high selectivities and activities.

# Bibliography

- [1] AR Ribeiro, PML Castro, and ME Tiritan. Chiral pharmaceuticals in the environment. *Environmental Chemistry Letters*, 10(3):239–253, 2012.
- [2] CJ Baddeley, TE Jones, AG Trant, and KE Wilson. Fundamental investigations of enantioselective heterogeneous catalysis. *Topics in Catalysis*, 54(19-20):1348–1356, 2011.
- [3] AN Collins, GN Sheldrake, and J Crosby. *Chirality in industry II: developments in the commercial manufacture and applications of optically active compounds*, volume 2. John Wiley & Sons, 1997.
- [4] A Baiker. Chiral catalysis on solids. *Current Opinion in Solid State and Materials Science*, 3(1):86–93, 1998.
- [5] RA Sheldon. *Chirotechnology: industrial synthesis of optically active compounds*. CRC press, 1993.
- [6] M Heitbaum, F Glorius, and I Escher. Asymmetric heterogeneous catalysis. *Angewandte Chemie International Edition*, 45(29):4732–4762, 2006.
- [7] HU Blaser, F Spindler, and M Studer. Enantioselective catalysis in fine chemicals production. *Applied Catalysis A: General*, 221(1):119–143, 2001.
- [8] CF McFadden, PS Cremer, and AJ Gellman. Adsorption of chiral alcohols on “chiral” metal surfaces. *Langmuir*, 12(10):2483–2487, 1996.
- [9] JM Fraile, JI García, CI Herrerías, JA Mayoral, and E Pires. Enantioselective catalysis with chiral complexes immobilized on nanostructured supports. *Chemical Society Reviews*, 38(3):695–706, 2009.
- [10] Li-X Dai. Chiral metal–organic assemblies—a new approach to immobilizing homogeneous asymmetric catalysts. *Angewandte Chemie International Edition*, 43(43):5726–5729, 2004.

- [11] B Minder, T Mallat, A Baiker, G Wang, T Heinz, and A Pfaltz. A novel aminoalcohol modifier for the enantioselective hydrogenation of ethyl pyruvate on Pt/alumina. *Journal of Catalysis*, 154(2):371–378, 1995.
- [12] G Webb and PB Wells. Asymmetric hydrogenation. *Catalysis Today*, 12(2):319–337, 1992.
- [13] PB Wells and AG Wilkinson. Platinum group metals as heterogeneous enantioselective catalysts. *Topics in Catalysis*, 5(1-4):39–50, 1998.
- [14] CJ Baddeley. Fundamental investigations of enantioselective heterogeneous catalysis. *Topics in catalysis*, 25(1-4):17–28, 2003.
- [15] JM Bonello, FJ Williams, and RM Lambert. Aspects of enantioselective heterogeneous catalysis: structure and reactivity of (S)-(-)-1-(1-naphthyl) ethylamine on Pt {111}. *Journal of the American Chemical Society*, 125(9):2723–2729, 2003.
- [16] Y Izumi. Modified Raney nickel (MRNi) catalyst: heterogeneous enantio-differentiating (asymmetric) catalyst. *Advances in Catalysis*, 32:215–271, 1983.
- [17] MA Keane. Adsorption of optically pure alanine on silica-supported nickel and the consequent catalytic enantioselectivity. *Langmuir*, 10(12):4560–4565, 1994.
- [18] E Klabunovskii, GV Smith, and A Zsigmond. *Heterogeneous enantioselective hydrogenation, theory and practice*.
- [19] T Osawa, T Kizawa, IYS Lee, S Ikeda, T Kitamura, Y Inoue, and V Borovkov. Durability enhancement of chirally modified metallic nickel catalysts for enantioselective hydrogenation. *Catalysis Communications*, 15(1):15–17, 2011.
- [20] T Osawa, T Kizawa, S Ikeda, T Kitamura, Y Inoue, and V Borovkov. Enhanced enantioselectivity in the heterogeneous catalytic hydrogenation of acetoacetate esters into the corresponding 3-hydroxybutyrates using commercial nickel powder. *Tetrahedron: Asymmetry*, 25(24):1630–1633, 2014.
- [21] T Osawa, Y Hayashi, A Ozawa, T Harada, and O Takayasu. Application of an in situ modification of nickel catalysts to the enantio-differentiating hydrogenation of methyl acetoacetate. *Journal of Molecular Catalysis A: Chemical*, 169(1):289–293, 2001.

- [22] T Osawa, S Sakai, K Deguchi, T Harada, and O Takayasu. High durability of asymmetrically modified nickel catalysts prepared by in situ modification. *Journal of Molecular Catalysis A: Chemical*, 185(1):65–69, 2002.
- [23] Chen, R Li, H Wang, J Liu, F Wang, and J Ma. Highly efficient enantioselective hydrogenation of methyl acetoacetate over chirally modified Raney nickel catalytic system. *Journal of Molecular Catalysis A: Chemical*, 269(1):125–132, 2007.
- [24] MA Keane. Interaction of optically active tartaric acid with a nickel- silica catalyst: role of both the modification and reaction media in determining enantioselectivity. *Langmuir*, 13(1):41–50, 1997.
- [25] P Kukula and L Červený. Preparation of tartaric acid modified Raney nickel catalysts: study of modification procedure. *Applied Catalysis A: General*, 210(1):237–246, 2001.
- [26] P Kukula and L Červený. Effects of reaction variables on enantioselectivity of modified Raney nickel catalyst. *Journal of Molecular Catalysis A: Chemical*, 185(1):195–202, 2002.
- [27] T Osawa, S Mita, A Iwai, O Takayasu, H Hashiba, S Hashimoto, T Harada, and I Matsuura. Enantio-differentiating hydrogenation of methyl acetoacetate over tartaric acid-NaBr-modified supported nickel catalyst prepared from nickel acetylacetonate. *Journal of Molecular Catalysis A: Chemical*, 157(1):207–216, 2000.
- [28] D Jo, JS Lee, and HL Lee. Enantio-differentiating hydrogenation of methyl acetoacetate over tartaric acid-modified nickel catalysts: effects of preparation method of supported nickel on activity and selectivity of catalysts. *Journal of Molecular Catalysis A: Chemical*, 222(1):199–205, 2004.
- [29] T Osawa, Y Amaya, T Harada, and O Takayasu. Enantio-differentiating hydrogenation of methyl acetoacetate over asymmetrically modified reduced nickel catalysts: the effects of the nickel sources on the enantio-differentiating ability. *Journal of Molecular Catalysis A: Chemical*, 211(1):93–96, 2004.
- [30] A Wolfson, S Geresh, MV Landau, and M Herskowitz. Enantioselective hydrogenation of methyl acetoacetate catalyzed by nickel supported on activated carbon or graphite. *Applied Catalysis A: General*, 208(1):91–98, 2001.

- [31] MA López-Martínez and IJ Shannon. Tartaric acid-Ni supported catalysts obtained from hydrotalcite-like compounds: effects of catalyst preparation variables on enantioselectivity. *Applied Catalysis A: General*, 435:123–130, 2012.
- [32] P Kukula and L Červený. Characterization of chirally modified Raney nickel and compounds of tartaric acid and nickel. *Applied Catalysis A: General*, 223(1):43–55, 2002.
- [33] V Humblot, S Haq, C Muryn, and R Raval. (R,R)- tartaric acid on Ni (110): the dynamic nature of chiral adsorption motifs. *Journal of Catalysis*, 228(1):130–140, 2004.
- [34] V Humblot, S Haq, C Muryn, WA Hofer, and R Raval. From local adsorption stresses to chiral surfaces:(R,R)- tartaric acid on Ni (110). *Journal of the American Chemical Society*, 124(3):503–510, 2002.
- [35] WA Hofer, V Humblot, and R Raval. Conveying chirality onto the electronic structure of achiral metals:(R,R)-tartaric acid on nickel. *Surface Science*, 554(2):141–149, 2004.
- [36] TE Jones and CJ Baddeley. A RAIRS, STM and TPD study of the Ni {111}/R,R-tartaric acid system: modelling the chiral modification of Ni nanoparticles. *Surface Science*, 513(3):453–467, 2002.
- [37] TE Jones and CJ Baddeley. Direct STM evidence of a surface interaction between chiral modifier and pro-chiral reagent: methylacetoacetate on R,R tartaric acid modified Ni {111}. *Surface Science*, 519(3):237–249, 2002.
- [38] TE Jones and CJ Baddeley. Influence of modification conditions on the interaction of methylacetoacetate with (R,R)-tartaric acid-modified Ni {111}. *The Journal of Physical Chemistry C*, 111(47):17558–17563, 2007.
- [39] TE Jones and CJ Baddeley. An investigation of the adsorption of (R,R)-tartaric acid on oxidised Ni {111} surfaces. *Journal of Molecular Catalysis A: Chemical*, 216(2):223–231, 2004.
- [40] TE Jones and CJ Baddeley. Investigating the mechanism of chiral surface reactions: the interaction of methylacetoacetate with (S)-glutamic acid modified Ni {111}. *Langmuir*, 22(1):148–152, 2006.

- [41] KE Wilson, AG Trant, and CJ Baddeley. Interaction of the pro-chiral molecule, methylacetoacetate, with (S)-aspartic acid modified Ni {111}. *The Journal of Physical Chemistry C*, 116(1):1092–1098, 2011.
- [42] KE Wilson and CJ Baddeley. Understanding the surface chemistry of enantioselective heterogeneous reactions: influence of modification variables on the interaction of methylacetoacetate with (S)-aspartic acid modified Ni {111}. *The Journal of Physical Chemistry C*, 113(24):10706–10711, 2009.
- [43] TE Jones, ME Urquhart, and CJ Baddeley. An investigation of the influence of temperature on the adsorption of the chiral modifier, (S)-glutamic acid, on Ni {111}. *Surface Science*, 587(1):69–77, 2005.
- [44] TE Jones, AE Rekas, and CJ Baddeley. Influence of modification pH and temperature on the interaction of methylacetoacetate with (S)-glutamic acid-modified Ni {111}. *The Journal of Physical Chemistry C*, 111(14):5500–5505, 2007.
- [45] AG Trant and CJ Baddeley. Surface chemistry underpinning enantioselective heterogeneous catalysis: supramolecular self-assembly of chiral modifiers and pro-chiral reagents on Ni {111}†. *The Journal of Physical Chemistry C*, 115(4):1025–1030, 2011.
- [46] REJ Nicklin, A Cornish, A Shavorskiy, S Baldanza, K Schulte, Z Liu, RA Bennett, and G Held. Surface chemistry of alanine on Ni {111}. *The Journal of Physical Chemistry C*, 119(47):26566–26574, 2015.
- [47] REJ Nicklin, A Shavorskiy, Aksoy AF, Z Liu, RA Bennett, M Sacchi, and G Held. “Pop-on and pop-off” Surface chemistry of alanine on Ni {111} under elevated hydrogen pressures. *The Journal of Physical Chemistry C*, 122(14):7720–7730, 2018.
- [48] KE Wilson and CJ Baddeley. XPS studies of the effects of modification pH on the interaction of methylacetoacetate with (S)-aspartic acid-modified Ni surfaces. *Journal of Catalysis*, 278(1):41–49, 2011.
- [49] AF Carley, MK Rajumon, MW Roberts, and PB Wells. XPS and LEED studies of 10, 11-dihydrocinchonidine adsorption at Pt (111). Implications for the role of cinchona alkaloids in enantioselective hydrogenation. *Journal of the Chemical Society, Faraday Transactions*, 91(14):2167–2172, 1995.
- [50] T Mallat, E Orglmeister, and A Baiker. Asymmetric catalysis at chiral metal surfaces. *Chemical Reviews*, 107(11):4863–4890, 2007.

- [51] DS Sholl, A Asthagiri, and TD Power. Naturally chiral metal surfaces as enantiospecific adsorbents. *The Journal of Physical Chemistry B*, 105(21):4771–4782, 2001.
- [52] A Ahmadi, G Attard, J Feliu, and A Rodes. Surface reactivity at “chiral” platinum surfaces. *Langmuir*, 15(7):2420–2424, 1999.
- [53] JD Horvath and AJ Gellman. Enantiospecific desorption of R- and S-propylene oxide from a chiral Cu (643) surface. *Journal of the American Chemical Society*, 123(32):7953–7954, 2001.
- [54] DJ Jenkins, AMS Alabdulrahman, GA Attard, KG Griffin, P Johnston, and PB Wells. Enantioselectivity and catalyst morphology: step and terrace site contributions to rate and enantiomeric excess in Pt-catalysed ethyl pyruvate hydrogenation. *Journal of Catalysis*, 234(1):230–239, 2005.
- [55] X Zhao. Fabricating homochiral facets on Cu (001) with L-lysine. *Journal of the American Chemical Society*, 122(50):12584–12585, 2000.
- [56] X Zhao, RG Zhao, and WS Yang. Adsorption of alanine on Cu (001) studied by scanning tunneling microscopy. *Surface Science*, 442(2):L995–L1000, 1999.
- [57] RB Rankin and DS Sholl. First-principles studies of chiral step reconstructions of Cu (100) by adsorbed glycine and alanine. *The Journal of Chemical Physics*, 124(7):074703–1–074703–6, 2006.
- [58] RB Rankin and DS Sholl. Structures of dense glycine and alanine adlayers on chiral Cu (3, 1, 17) surfaces. *Langmuir*, 22(19):8096–8103, 2006.
- [59] M Ortega Lorenzo, S Haq, T Bertrams, P Murray, R Raval, and CJ Baddeley. Creating chiral surfaces for enantioselective heterogeneous catalysis: R,R-tartaric acid on Cu (110). *The Journal of Physical Chemistry B*, 103(48):10661–10669, 1999.
- [60] M Ortega Lorenzo, V Humblot, P Murray, CJ Baddeley, S Haq, and R Raval. Chemical transformations, molecular transport, and kinetic barriers in creating the chiral phase of (R,R)-tartaric acid on Cu (110). *Journal of Catalysis*, 205(1):123–134, 2002.
- [61] M Ortega Lorenzo, CJ Baddeley, C Muryn, and R Raval. Extended surface chirality from supramolecular assemblies of adsorbed chiral molecules. *Nature*, 404(6776):376–379, 2000.

- [62] SM Barlow, S Louafi, D Le Roux, J Williams, C Muryn, S Haq, and R Raval. Supramolecular assembly of strongly chemisorbed size- and shape-defined chiral clusters: S- and R-alanine on Cu (110). *Langmuir*, 20(17):7171–7176, 2004.
- [63] SM Barlow, S Louafi, D Le Roux, J Williams, C Muryn, S Haq, and R Raval. Polymorphism in supramolecular chiral structures of R- and S-alanine on Cu (1 1 0). *Surface Science*, 590(2-3):243–263, 2005.
- [64] M Mahapatra, L Burkholder, Y Bai, M Garvey, JAI Boscoboinik, C Hirschmugl, and WT Tysoe. Formation of chiral self-assembled structures of amino acids on transition-metal surfaces: alanine on Pd (111). *The Journal of Physical Chemistry C*, 118(13):6856–6865, 2014.
- [65] DW Goodman. Model studies in catalysis using surface science probes. *Chemical Reviews*, 95(3):523–536, 1995.
- [66] KW Kolasinski. *Surface science: foundations of catalysis and nanoscience. Second edition.* John Wiley & sons, 2008.
- [67] A Cornish. *Investigations into chiral adsorption systems relevant to asymmetric heterogeneous catalysis on metal surfaces.* PhD thesis, University of Reading, 2011.
- [68] M Salmeron and R Schlögl. Ambient pressure photoelectron spectroscopy: a new tool for surface science and nanotechnology. *Surface Science Reports*, 63(4):169–199, 2008.
- [69] A Shavorskiy, T Eralp, K Schulte, H Bluhm, and G Held. Surface chemistry of glycine on Pt {111} in different aqueous environments. *Surface Science*, 607:10–19, 2013.
- [70] T Eralp, A Shavorskiy, and G Held. The adsorption geometry and chemical state of lysine on Cu {110}. *Surface Science*, 605(3-4):468–472, 2011.
- [71] T Eralp, A Ievins, A Shavorskiy, SJ Jenkins, and G Held. The importance of attractive three-point interaction in enantioselective surface chemistry: stereospecific adsorption of serine on the intrinsically chiral Cu {531} surface. *Journal of the American Chemical Society*, 134(23):9615–9621, 2012.
- [72] S Baldanza, A Cornish, REJ Nicklin, ZV Zheleva, and G Held. Surface chemistry of alanine on Cu {111}: adsorption geometry and temperature dependence. *Surface Science*, 629:114–122, 2014.

- [73] S Baldanza. *Model studies for chiral modification of heterogeneous catalysts: amino acids and tartaric acid on Cu and Ni surfaces*. PhD thesis, University of Reading, 2014.
- [74] G Held. *Photoelectron spectroscopy of metal surfaces for potential heterogeneous catalysis*. 2011.
- [75] REJ Nicklin. *Emulation of chiral hydrogenation catalysts by adsorption of small molecules onto Ni surfaces*. PhD thesis, University of Reading, 2014.
- [76] T Eralp. *Fundamental enantiospecific interactions of amino acids on metal surfaces*. PhD thesis, University of Reading, 2010.
- [77] G Hähner. Near edge X-ray absorption fine structure spectroscopy as a tool to probe electronic and structural properties of thin organic films and liquids. *Chemical Society Reviews*, 35(12):1244–1255, 2006.
- [78] S Hüfner, S Schmidt, and F Reinert. Photoelectron spectroscopy—an overview. *Nuclear Instruments and Methods in Physics Research Section A: Accelerators, Spectrometers, Detectors and Associated Equipment*, 547(1):8–23, 2005.
- [79] Website of the SuperESCA beamline. <https://www.elettra.trieste.it/lightsources/elettra/elettra-beamlines/superesca/specifications.html>, 2011.
- [80] Website of the HE-SGM beamline. [https://www.helmholtz-berlin.de/pubbin/igama\\_output?modus=einzel&sprache=en&gid=1606&typoid=](https://www.helmholtz-berlin.de/pubbin/igama_output?modus=einzel&sprache=en&gid=1606&typoid=)
- [81] Private communication with Alexei Preobrajenski (staff member in the D1011 beamline).
- [82] Private communication with Alex Walton (staff member in the University of Manchester).
- [83] S Hüfner. *Photoelectron spectroscopy: principles and applications. Third edition*. Springer, 2003.
- [84] G Attard and C Barnes. *Surfaces*. Oxford University Press, 1998.
- [85] A Shavorskiy. *Chemistry of amino acids at the water-metal interfaces*. PhD thesis, University of Reading, 2010.

- [86] U Gelius, S Svensson, H Siegbahn, E Basilier, Å Faxälv, and K Siegbahn. Vibrational and lifetime line broadenings in ESCA. *Chemical Physics Letters*, 28(1):1–7, 1974.
- [87] D Nordlund. *Core level spectroscopy of water and ice*. PhD thesis, Stockholm University, 2004.
- [88] DP Woodruff. Adsorbate structure determination using photoelectron diffraction: methods and applications. *Surface Science Reports*, 62(1):1–38, 2007.
- [89] DF Ogletree, H Bluhm, ED Hebenstreit, and M Salmeron. Photoelectron spectroscopy under ambient pressure and temperature conditions. *Nuclear Instruments and Methods in Physics Research Section A: Accelerators, Spectrometers, Detectors and Associated Equipment*, 601(1-2):151–160, 2009.
- [90] DA Shirley. High-resolution X-ray photoemission spectrum of the valence bands of gold. *Physical Review B*, 5(12):4709–4714, 1972.
- [91] J Stöhr. *NEXAFS spectroscopy*. Springer, 1992.
- [92] RO Ansell, T Dickinson, AF Povey, and PMA Sherwood. X-ray photoelectron spectroscopic studies of electrode surfaces using a new controlled transfer technique: part II. Results for a molybdenum electrode and the curve fitting procedure. *Journal of Electroanalytical Chemistry and Interfacial Electrochemistry*, 98(1):79–89, 1979.
- [93] I Kojima and M Kurahashi. Application of asymmetrical Gaussian/Lorentzian mixed function for X-ray photoelectron curve synthesis. *Journal of Electron Spectroscopy and Related Phenomena*, 42(2):177–181, 1987.
- [94] C Nicolas and C Miron. Lifetime broadening of core-excited and-ionized states. *Journal of Electron Spectroscopy and Related Phenomena*, 185(8-9):267–272, 2012.
- [95] JG Chen. NEXAFS investigations of transition metal oxides, nitrides, carbides, sulfides and other interstitial compounds. *Surface Science Reports*, 30(1):1–152, 1997.
- [96] J Stöhr and DA Outka. Determination of molecular orientations on surfaces from the angular dependence of near-edge X-ray-absorption fine-structure spectra. *Physical Review B*, 36(15):7891–7905, 1987.

- [97] V Humblot and R Raval. Chiral metal surfaces from the adsorption of chiral and achiral molecules. *Applied Surface Science*, 241(1):150–156, 2005.
- [98] V Humblot, M Ortega Lorenzo, CJ Baddeley, S Haq, and R Raval. Local and global chirality at surfaces: succinic acid versus tartaric acid on Cu (110). *Journal of the American Chemical Society*, 126(20):6460–6469, 2004.
- [99] S Baldanza, J Ardini, A Giglia, and Georg Held. Stereochemistry and thermal stability of tartaric acid on the intrinsically chiral Cu {531} surface. *Surface Science*, 643:108–116, 2016.
- [100] M Mahapatra and WT Tysoe. Structure and decomposition pathways of D-(-)-tartaric acid on Pd {111}. *Surface Science*, 629:132–138, 2014.
- [101] R Neubauer, CM Whelan, R Denecke, and H-P Steinrück. The thermal chemistry of saturated layers of acetylene and ethylene on Ni (100) studied by in situ synchrotron X-ray photoelectron spectroscopy. *The Journal of Chemical Physics*, 119(3):1710–1718, 2003.
- [102] Q Zhao, R Deng, and F Zaera. Thermal activation and reaction of allyl alcohol on Ni (100). *Surface Science*, 605(13-14):1236–1242, 2011.
- [103] A Wiltner and Ch Linsmeier. Thermally induced reaction and diffusion of carbon films on Ni (1 1 1) and Ni (1 0 0). *Surface Science*, 602(23):3623–3631, 2008.
- [104] G Jones, LB Jones, F Thibault-Starzyk, EA Seddon, R Raval, SJ Jenkins, and G Held. The local adsorption geometry and electronic structure of alanine on Cu {110}. *Surface Science*, 600(9):1924–1935, 2006.
- [105] J Hasselström, O Karis, M Weinelt, N Wassdahl, A Nilsson, M Nyberg, LGM Pettersson, MG Samant, and J Stöhr. The adsorption structure of glycine adsorbed on Cu (110); comparison with formate and acetate/Cu (110). *Surface Science*, 407(1):221–236, 1998.
- [106] DJ Watson, S Acharya, REJ Nicklin, and G Held. Observing the in situ chiral modification of Ni nanoparticles using scanning transmission X-ray microspectroscopy. *Surface Science*, 629:108–113, 2014.
- [107] O Plashkevych, V Carravetta, O Vahtras, and H Ågren. Theoretical study of X-ray circular dichroism of amino acids. *Chemical Physics*, 232(1-2):49–62, 1998.

- [108] L Yang, O Plashkevych, O Vahtras, V Carravetta, and H Ågren. Near-edge X-ray absorption and dichroism in amino acids. *Journal of Synchrotron Radiation*, 6(3):708–710, 1999.
- [109] A Shavorskiy, F Aksoy, ME Grass, Z Liu, H Bluhm, and G Held. A step toward the wet surface chemistry of glycine and alanine on Cu {110}: destabilization and decomposition in the presence of near-ambient water vapor. *Journal of the American Chemical Society*, 133(17):6659–6667, 2011.
- [110] MJ Gladys, AV Stevens, NR Scott, G Jones, D Batchelor, and G Held. Enantiospecific adsorption of alanine on the chiral Cu {531} surface. *The Journal of Physical Chemistry C*, 111(23):8331–8336, 2007.
- [111] J Stöhr and R Jaeger. Absorption-edge resonances, core-hole screening, and orientation of chemisorbed molecules: CO, NO, and N<sub>2</sub> on Ni (100). *Physical Review B*, 26(8):4111–41131, 1982.
- [112] OL Warren and PA Thiel. Structural determination of a NiO (111) film on Ni (100) by dynamical low-energy electron-diffraction analysis. *The Journal of Chemical Physics*, 100(1):659–663, 1994.
- [113] E Kopatzki and RJ Behm. Step faceting: origin of the temperature dependent induction period in Ni (100) oxidation. *Physical Review Letters*, 74(8):1399–1402, 1995.
- [114] MA Munoz-Marquez, RE Tanner, and DP Woodruff. Surface and subsurface oxide formation on Ni (1 0 0) and Ni (1 1 1). *Surface Science*, 565(1):1–13, 2004.
- [115] W-D Wang, NJ Wu, and PA Thiel. Structural steps to oxidation of Ni (100). *The Journal of Chemical Physics*, 92(3):2025–2035, 1990.
- [116] PH Holloway and JB Hudson. Kinetics of the reaction of oxygen with clean nickel single crystal surfaces: I. Ni (100) surface. *Surface Science*, 43(1):123–140, 1974.
- [117] DF Mitchell, PB Sewell, and M Cohen. A kinetic study of the initial oxidation of the Ni (001) surface by RHEED and X-ray emission. *Surface Science*, 61(2):355–376, 1976.
- [118] PR Norton, RL Tapping, and JW Goodale. A photoemission study of the interaction of Ni (100), (110) and (111) surfaces with oxygen. *Surface Science*, 65(1):13–36, 1977.

- [119] G Dalmai-Imelik, JC Bertolini, and J Rousseau. Relationship between vibrational states of O-Ni systems and their superficial structure on (100) face of nickel single crystal. *Surface Science*, 63:67–78, 1977.
- [120] J Stöhr, R Jaeger, and T Kendelewicz. Structure of p ( $2 \times 2$ ) and c ( $2 \times 2$ ) oxygen on Ni (100): a surface extended-X-ray absorption fine-structure study. *Physical Review Letters*, 49(2):142–146, 1982.
- [121] DE Taylor and RL Park. Phase diagram of oxygen on Ni (100). *Surface Science Letters*, 125(1):L73–L79, 1983.
- [122] RS Saiki, AP Kaduwela, J Osterwalder, CS Fadley, and CR Brundle. Observation and characterization of a strained lateral superlattice in the oxidation of Ni (001). *Physical Review B*, 40(3):1586–1592, 1989.
- [123] JG Chen, MD Weisel, and RB Hall. A vibrational investigation of the stability, morphology and surface reactivity of NiO on Ni (100). *Surface Science*, 250(1-3):159–168, 1991.
- [124] TD Pope, SJ Bushby, K Griffiths, and PR Norton. Correlated LEED, work function and absolute coverage measurements of the oxidation of Ni (100) at 325 K. *Surface Science*, 258(1-3):101–106, 1991.
- [125] M Bäumer, D Cappus, H Kuhlenbeck, H-J Freund, G Wilhelmi, A Brodde, and H Neddermeyer. The structure of thin NiO (100) films grown on Ni (100) as determined by low-energy-electron diffraction and scanning tunneling microscopy. *Surface Science*, 253(1-3):116–128, 1991.
- [126] RS Saiki, AP Kaduwela, M Sagurton, J Osterwalder, DJ Friedman, CS Fadley, and CR Brundle. X-ray photoelectron diffraction and low-energy electron diffraction study of the interaction of oxygen with the Ni (001) surface: c ( $2 \times 2$ ) to saturated oxide. *Surface Science*, 282(1-2):33–61, 1993.
- [127] D Cappus, C Xu, D Ehrlich, B Dillmann, CA Ventrice Jr, K Al Shamery, H Kuhlenbeck, and H-J Freund. Hydroxyl groups on oxide surfaces: NiO (100), NiO (111) and Cr<sub>2</sub>O<sub>3</sub> (111). *Chemical Physics*, 177(2):533–546, 1993.
- [128] W-D Wang, NJ Wu, PA Thiel, and MC Tringides. Epitaxial growth in a strained system: Ni (100)- O ( $7 \times 7$ ). *Surface science*, 282(3):229–236, 1993.
- [129] MA Langell and MH Nassir. Stabilization of NiO (111) thin films by surface hydroxyls. *The Journal of Physical Chemistry*, 99(12):4162–4169, 1995.

- [130] MA Langell, CL Berrie, MH Nassir, and KW Wulser. Adsorption of acetic acid on hydroxylated NiO (111) thin films. *Surface Science*, 320(1-2):25–38, 1994.
- [131] JC de Jesús, J Carrazza, P Pereira, and F Zaera. Hydroxylation of NiO films: the effect of water and ion bombardment during the oxidation of nickel foils with O<sub>2</sub> under vacuum. *Surface Science*, 397(1-3):34–47, 1998.
- [132] N Kitakatsu, V Maurice, C Hinnen, and P Marcus. Surface hydroxylation and local structure of NiO thin films formed on Ni (111). *Surface Science*, 407(1-3):36–58, 1998.
- [133] M Pedio, JC Fuggle, J Somers, E Umbach, J Haase, Th Lindner, U Höfer, M Grioni, FMF De Groot, B Hillert, L Becker, and A Robinson. Covalency in oxygen chemisorption as probed by X-ray absorption. *Physical Review B*, 40(11):7924–7927, 1989.
- [134] D Norman, J Stöhr, R Jaeger, PJ Durham, and JB Pendry. Determination of local atomic arrangements at surfaces from near-edge X-ray-absorption fine-structure studies: O on Ni (100). *Physical Review Letters*, 51(22):2052–2055, 1983.
- [135] M Pedio, L Becker, B Hillert, S D’Addato, and J Haase. Oxygen on Ni (111): A multiple-scattering analysis of the near-edge X-ray-absorption fine structure. *Physical Review B*, 41(11):7462–7466, 1990.
- [136] A Cornish, T Eralp, A Shavorskiy, RA Bennett, G Held, SA Cavill, A Potenza, H Marchetto, and SS Dhesi. Oxidation of polycrystalline Ni studied by spectromicroscopy: phase separation in the early stages of crystallite growth. *Physical Review B*, 81(8):085403–1–085403–4, 2010.
- [137] S Johnson and RJ Madix. Desorption of hydrogen and carbon monoxide from Ni (100), Ni (100) p (2 × 2) s, and Ni (100) c (2 × 2) s surfaces. *Surface Science*, 108(1):77–98, 1981.
- [138] M Kiskinova and DW Goodman. Modification of chemisorption properties by electronegative adatoms: H<sub>2</sub> and CO on chlorided, sulfided, and phosphided Ni (100). *Surface Science*, 108(1):64–76, 1981.
- [139] JA Switzer, HM Kothari, P Poizot, S Nakanishi, and EW Bohannan. Enantiospecific electrodeposition of a chiral catalyst. *Nature*, 425(6957):490–493, 2003.

- [140] Ci Egawa, H Iwai, M Kabutoya, and S Oki. STM study of dl-alanine array structure on Cu (0 0 1). *Surface Science*, 532:233–236, 2003.
- [141] RB Rankin and DS Sholl. Structures of glycine, enantiopure alanine, and racemic alanine adlayers on Cu (110) and Cu (100) surfaces. *The Journal of Physical Chemistry B*, 109(35):16764–16773, 2005.
- [142] H Iwai and C Egawa. Molecular orientation and intermolecular interaction in alanine on Cu (001). *Langmuir*, 26(4):2294–2300, 2009.
- [143] F Gao, Z Li, Y Wang, L Burkholder, and WT Tysoc. Chemistry of alanine on Pd (111): temperature-programmed desorption and X-ray photoelectron spectroscopic study. *Surface Science*, 601(15):3276–3288, 2007.
- [144] J Lauterbach, M Wittmann, and J Küppers. Adsorption of CO at Ni (100) surfaces: a FTIRAS-TDS study. *Surface Science*, 279(3):287–296, 1992.
- [145] F Gao, Z Li, Y Wang, L Burkholder, and WT Tysoc. Chemistry of glycine on Pd (111): temperature-programmed desorption and X-ray photoelectron spectroscopic study. *The Journal of Physical Chemistry C*, 111(27):9981–9991, 2007.
- [146] H Tillborg, A Nilsson, and N Mårtensson. Studies of the CO-H<sub>2</sub>-Ni (100) system using photoelectron spectroscopy. *Surface Science*, 273(1-2):47–60, 1992.
- [147] G Held, J Schuler, W Sklarek, and H-P Steinrück. Determination of adsorption sites of pure and coadsorbed CO on Ni (111) by high resolution X-ray photoelectron spectroscopy. *Surface Science*, 398(1-2):154–171, 1998.
- [148] X Zhao and J Rodriguez. Photoemission study of glycine adsorption on Cu/Au (111) interfaces. *Surface Science*, 600(10):2113–2121, 2006.
- [149] J Williams, S Haq, and R Raval. The bonding and orientation of the amino acid L-alanine on Cu {110} determined by RAIRS. *Surface Science*, 368(1-3):303–309, 1996.
- [150] M Polcik, F Allegretti, DI Sayago, G Nisbet, CLA Lamont, and DP Woodruff. Circular dichroism in core level photoemission from an adsorbed chiral molecule. *Physical Review Letters*, 92(23):236103–1–236103–4, 2004.

- [151] DI Sayago, M Polcik, G Nisbet, CLA Lamont, and DP Woodruff. Local structure determination of a chiral adsorbate: alanine on Cu (1 1 0). *Surface Science*, 590(1):76–87, 2005.
- [152] Rees B Rankin and David S Sholl. Structure of enantiopure and racemic alanine adlayers on Cu (1 1 0). *Surface Science*, 574(1):L1–L8, 2005.
- [153] C Benndorf and TE Madey. Adsorption of H<sub>2</sub>O on clean and oxygen-pre-dosed Ni{110}. *Surface Science*, 194:63–91, 1988.
- [154] BW Callen, K Griffiths, U Memmert, DA Harrington, SJ Bushby, and PR Norton. The adsorption of water on Ni (110): monolayer, bilayer and related phenomena. *Surface Science*, 230(1):159–174, 1990.
- [155] BW Callen, K Griffiths, and PR Norton. Reorientation of chemisorbed water on Ni (110) by hydrogen bonding to second layer. *Physical Review Letters*, 66(12):1634–1637, 1991.
- [156] BW Callen, K Griffiths, RV Kasza, MB Jensen, PA Thiel, and PR Norton. Structural phenomena related to associative and dissociative adsorption of water on Ni (110). *The Journal of Chemical Physics*, 97(5):3760–3774, 1992.
- [157] N Pangher, A Schmalz, and J Haase. Structure determination of water chemisorbed on Ni (110) by use of X-ray absorption fine-structure measurements. *Chemical Physics Letters*, 221(3):189–193, 1994.
- [158] G Pirug, O Knauff, and HP Bonzel. Structural and chemical aspects of H<sub>2</sub>O adsorption on Ni(110). *Surface Science*, 321(1):58–70, 1994.
- [159] A Hodgson and S Haq. Water adsorption and the wetting of metal surfaces. *Surface Science Reports*, 64(9):381–451, 2009.
- [160] J Reichert, A Schiffrin, W Auwärter, A Weber-Bargioni, M Marschall, M Dell’Angela, D Cvetko, G Bavdek, A Cossaro, A Morgante, and JV Barth. L-tyrosine on Ag (111): universality of the amino acid 2D zwitterionic bonding scheme? *ACS Nano*, 4(2):1218–1226, 2010.
- [161] S Tanuma, CJ Powell, and DR Penn. Calculations of electron inelastic mean free paths. V. data for 14 organic compounds over the 50–2000 ev range. *Surface and Interface Analysis*, 21(3):165–176, 1994.
- [162] I Powis, EE Rennie, U Hergenbahn, O Kugeler, and R Bussy-Socrate. Investigation of the gas-phase amino acid alanine by synchrotron radiation

- photoelectron spectroscopy. *The Journal of Physical Chemistry A*, 107(1): 25–34, 2003.
- [163] G Tzvetkov, MG Ramsey, and FP Netzer. Glycine-ice nanolayers: morphology and surface energetics. *The Journal of Chemical Physics*, 122(11): 114712–1–114712–7, 2005.
- [164] Y Zubavichus, O Fuchs, L Weinhardt, C Heske, E Umbach, JD Denlinger, and M Grunze. Soft X-ray-induced decomposition of amino acids: an XPS, mass spectrometry, and NEXAFS study. *Radiation Research*, 161(3):346–358, 2004.
- [165] DE Gardin and GA Somorjai. Vibrational spectra and thermal decomposition of methylamine and ethylamine on Ni(111). *The Journal of Physical Chemistry*, 96(23):9424–9431, 1992.
- [166] MG Campo. Molecular dynamics simulation of glycine zwitterion in aqueous solution. *The Journal of Chemical Physics*, 125(11):114511–1–114511–8, 2006.
- [167] K Leung and SB Rempe. Ab initio molecular dynamics study of glycine intramolecular proton transfer in water. *The Journal of Chemical Physics*, 122(18):184506, 2005.
- [168] K Chuhev and JJ BelBruno. Computational treatment of the microsolvation of neutral and zwitterionic forms of alanine. *Journal of Molecular Structure: THEOCHEM*, 850(1):111–120, 2008.
- [169] LM Ghiringhelli, P Schravendijk, and L Delle Site. Adsorption of alanine on a Ni (111) surface: a multiscale modeling oriented density functional study. *Physical Review B*, 74(3):035437–1–035437–8, 2006.
- [170] P Tsaousis, J Ontaneda, L Bignardi, RA Bennett, R Grau-Crespo, and G Held. Combined experimental and theoretical study of methyl acetoacetate adsorption on Ni {100}. *The Journal of Physical Chemistry C*, 122(11):6186–6194, 2018.
- [171] A Baiker. Progress in asymmetric heterogeneous catalysis: design of novel chirally modified platinum metal catalysts. *Journal of Molecular Catalysis A: Chemical*, 115(3):473–493, 1997.

- [172] A Baiker. Transition state analogues—a guide for the rational design of enantioselective heterogeneous hydrogenation catalysts. *Journal of Molecular Catalysis A: Chemical*, 163(1-2):205–220, 2000.
- [173] CJ Baddeley and G Held. Chiral molecules on surfaces. *Handbook of Nanofabrication*, page 91, 2010.
- [174] KB Sharpless. Searching for new reactivity (nobel lecture). *Angewandte Chemie International Edition*, 41(12):2024–2032, 2002.
- [175] J Ontaneda, REJ Nicklin, A Cornish, A Roldan, R Grau-Crespo, and G Held. Adsorption of methyl acetoacetate at Ni {111}: experiment and theory. *The Journal of Physical Chemistry C*, 120(48):27490–27499, 2016.
- [176] NV Belova, VV Sliznev, H Oberhammer, and GV Girichev. Tautomeric and conformational properties of  $\beta$ -diketones. *Journal of Molecular Structure*, 978(1-3):282–293, 2010.
- [177] NV Belova, H Oberhammer, and GV Girichev. Tautomeric and conformational properties of methyl acetoacetate,  $\text{CH}_3\text{OC}(\text{O})\text{-CH}_2\text{-C}(\text{O})\text{CH}_3$ : electron diffraction and quantum chemical study. *The Journal of Physical Chemistry A*, 108(16):3593–3597, 2004.
- [178] MM Schiavoni, HE Di Loreto, A Hermann, H-G Mack, SE Ulic, and CO Della Vedova. Keto–enol tautomerism in  $\beta$ -ketoesters:  $\text{CH}_3\text{C}(\text{O})\text{CHXC}(\text{O})\text{OY}$  ( $\text{X} = \text{H, Cl}$ ;  $\text{Y} = \text{CH}_3, \text{C}_2\text{H}_5$ ). Vibrational analyses, NMR spectra and quantum chemical calculations. *Journal of Raman Spectroscopy*, 32(5):319–329, 2001.
- [179] SV Antonyuk, RW Strange, MJ Ellis, Y Bessho, S Kuramitsu, Y Inoue, S Yokoyama, and SS Hasnain. Structure of D-lactate dehydrogenase from *Aquifex aeolicus* complexed with  $\text{NAD}^+$  and lactic acid (or pyruvate). *Acta Crystallographica Section F: Structural Biology and Crystallization Communications*, 65(12):1209–1213, 2009.